Universidad de Oviedo

Universidá d'Uviéu

University of Oviedo

Programa de Doctorado en Materiales

Preparación y modificación de láminas bidimensionales de grafeno y MoS_2 para aplicaciones energéticas y medioambientales.

Preparation and modification of two-dimensional graphene and MoS_2 nanosheets for energy and environmental applications.

TESIS DOCTORAL

Sergio García Dalí

Abril 2021

Universidad de Oviedo

Universidá d'Uviéu

University of Oviedo

Programa de Doctorado en Materiales

Preparación y modificación de láminas bidimensionales de grafeno y MoS_2 para aplicaciones energéticas y medioambientales.

Preparation and modification of two-dimensional graphene and MoS_2 nanosheets for energy and environmental applications.

TESIS DOCTORAL

Dr. Juan Ignacio Paredes Nachón
Dra. Silvia Villar Rodil

Universidad de Oviedo
Universidá d'Uviéu
University of Oviedo

RESUMEN DEL CONTENIDO DE TESIS DOCTORAL

1.- Título de la Tesis	
Español: Preparación y modificación de láminas bidimensionales de grafeno y MoS_2 para aplicaciones energéticas y medioambientales	Inglés: Preparation and modification of two-dimensional graphene and MoS_2 nanosheets for energy and environmental applications.

2.- Autor	
Nombre: Sergio García Dalí	DNI
Programa de Doctorado: Materiales	
Órgano responsable: Comisión Académica Programa de Doctorado en Materiales	

RESUMEN (en español)

El objetivo de esta tesis consiste en la preparación y procesado, mediante métodos en fase líquida, de nanoláminas bidimensionales de grafeno y MoS_2 para aplicaciones energéticas y medioambientales.

Utilizando como cátodo piezas de grafito y MoS_2 se obtuvieron, mediante exfoliación electroquímica en medio acuoso, grafeno y nanoláminas de MoS_2, respectivamente.

Se optimizaron diferentes parámetros del proceso, como los distintos tipos de grafito de partida o el electrolito utilizado (sales de amonio cuaternario), obteniendo rendimientos de cerca del 50%. El grafeno obtenido mediante este proceso posee un bajo grado de oxidación, una alta calidad estructural y una buena conductividad eléctrica. Siendo útil como electrodo para supercondensadores, fabricando un híbrido mediante la adición de una pequeña cantidad de óxido de cobalto en forma de nanoláminas verticalmente orientadas, y como adsorbente de contaminantes acuosos, tales como aceites y colorantes.

La exfoliación electroquímica catódica de MoS_2 se llevó a cabo utilizando como electrolitos sales comunes, como el KCl, en las condiciones adecuadas. La exfoliación no provoca cambio de fase (se conserva la fase 2H) ni oxidación del material. Las nanoláminas de MoS_2 obtenidas se estudiaron como catalizador para la reducción de nitroarenos y como electrodo para supercondensadores.

Además, se llevaron a cabo tratamientos de modificación (activación) de nanoláminas de MoS_2 con vistas a mejorar su actividad como catalizadores en la reducción de nitroarenos y colorantes orgánicos en agua.

Universidad de Oviedo
Universidá d'Uviéu
University of Oviedo

RESUMEN (en Inglés)

The main aim of this thesis is the preparation by liquid-phase methods of two-dimensional materials, such as graphene and MoS_2 nanosheets, as well as the exploration of their use in energy and environmental applications.

Using *bulk* graphite and MoS_2 pieces as the starting materials, two-dimensional graphene and MoS_2 nanosheets were obtained, respectively, via cathodic exfoliation in aqueous medium.

Different parameters of the process were optimized, such as the starting graphite and the electrolytes used (quaternary ammonium salts), affording graphene yields close to 50 wt% in optimal conditions. Graphene obtained by this process has a low content of oxygen, a high structural quality and a good electrical conductivity, so it was useful as an electrode for supercapacitors and as an absorbent of aqueous pollutants, such as oils and dyes.

The cathodic exfoliation of *bulk* MoS_2 was carried out using common salts, such as KCl, as the electrolyte in apropiate conditions. The resulting two-dimensional MoS_2 nanosheets retained the original 2H phase of the starting material and do not undergo oxidation at any substantial extent. The obtained material was studied as catalyst for the reduction of nitroarenes and as an electrode for supercapacitors.

Moreover, MoS_2 nanosheets were subjected to activation treatments in order to improve their catalytic activity towards the reduction of nitroarenes and organic dyes in water.

SR. PRESIDENTE DE LA COMISIÓN ACADÉMICA DEL PROGRAMA DE DOCTORADO EN MATERIALES

Agradecimientos

La realización de esta tesis no hubiera sido posible sin la ayuda y el apoyo de todas las personas que me rodean día tras día y que incluso desde la distancia siempre han estado ahí.

Pocas personas pueden presumir de tener unos directores de tesis como los que he tenido. Gracias Nacho y Silvia, por todo lo que me habéis enseñado y de la forma en la que lo habéis hecho.

A todas las personas con las que he compartido mi día a día, tanto en el trabajo como fuera de él, haciendo más profundas las conversaciones del café, más interesantes las partidas de pádel y haciendo valorar nuestra vida, gracias Laura, Cristina y Noe, respectivamente. Gracias Raúl y Alberto C. (el auténtico, el guapo) por contribuir haciendo un poco el payaso en vídeos de dudosa moral. A los que pasaron por aquí y a los que cada día se les echa de menos, allá donde estéis, gracias Jose, Luis Adrián y Julián. Gracias a las personas que, voluntariamente o no (más bien no), fueron víctimas de mis bromas. A mis amigos Carloss, cuya amistad perdura más allá de la distancia y del tiempo. Pero en especial, gracias a Dani y Alberto M. (el otro, el feote) por hacer tan divertidos los momentos en el laboratorio.

Gracias a mi familia, a mis padres y a mi hermano, que desde el principio me apoyaron y me ayudaron en todo lo que necesitaba, así como a mi familia política, de las que pocos pueden decir tener. A todos por aguantarme.

Y por supuesto a mi vida, a Mercedes, cuya sonrisa ilumina el camino hasta en la más oscura noche.

Gracias a todos por hacerme ser quién soy.

“Vincit qui partitur”

Índice

Contenido

Resumen

El objetivo de esta tesis consiste en la preparación y procesado, mediante métodos en fase líquida, de nanoláminas bidimensionales de grafeno y MoS_2 para aplicaciones energéticas y medioambientales.

Utilizando como cátodo piezas de grafito y MoS_2 se obtuvieron, mediante exfoliación electroquímica en medio acuoso, grafeno y nanoláminas de MoS_2, respectivamente. Se optimizaron diferentes parámetros del proceso.

Entre los distintos tipos de grafito de partida utilizados para la producción de grafeno (grafito flexible, barras de grafito y grafito pirolítico altamente orientado), el grafito flexible es el que condujo a mayor rendimiento en producto expandido. En cuanto al electrolito, ciertas sales de amonio cuaternario de tamaño apropiado resultaron óptimas para maximizar la expansión del electrodo y el rendimiento en grafeno, alcanzándose valores de cerca del 50%. El grafeno obtenido mediante este proceso posee un bajo grado de oxidación, una alta calidad estructural y una buena conductividad eléctrica.

Se empleó el grafeno obtenido por exfoliación catódica como electrodo para supercondensadores, fabricando un híbrido mediante la adición de una pequeña cantidad de óxido de cobalto en forma de nanoláminas verticalmente orientadas. Éstas últimas proporcionan pseudocapacitancia y funcionan como espaciador, impidiendo el reapilamiento del grafeno.

El alto grado de hidrofobicidad del grafeno obtenido lo hace también útil como adsorbente de contaminantes acuosos, tales como aceites y colorantes. En este caso, se recubrió una esponja de melamina con el grafeno exfoliado, evitando así el reapilamiento de las láminas y la consecuente pérdida de superficie específica, obteniéndose una estructura macroscópica de baja densidad y fácilmente manejable, lo que a su vez facilitaba su regeneración tras el uso.

La exfoliación electroquímica catódica de MoS_2 se llevó a cabo utilizando como electrolitos sales comunes, como el KCl, en las condiciones adecuadas. La exfoliación no provoca cambio de fase (se conserva la fase 2H) ni oxidación del material. Las nanoláminas de MoS_2 obtenidas se estudiaron como catalizador para la reducción de nitroarenos y como electrodo para supercondensadores, formando híbridos con nanotubos de carbono de capa simple, que proporcionan conductividad eléctrica y

actúan como espaciadores. Los materiales resultaron competitivos en ambas aplicaciones, comparando con materiales similares preparados mediante otros métodos.

Además, se llevaron a cabo tratamientos de modificación (activación) de nanoláminas de MoS_2 con vistas a mejorar su actividad como catalizadores en la reducción de nitroarenos y colorantes orgánicos en agua. En este caso, se obtuvieron las nanoláminas mediante sonicación de MoS_2 *bulk* en polvo en isopropanol y se generaron vacantes de azufre (centros activos) en ellas mediante tratamiento con hidracina. Las nanoláminas activadas mostraron valores de actividad catalítica hasta 3-4 veces mayores que los del material sin tratar.

Abstract

The main aim of this thesis is the preparation by liquid-phase methods of two-dimensional materials, such as graphene and MoS_2 nanosheets, as well as the exploration of their use in energy and environmental applications.

Using *bulk* graphite and MoS_2 pieces as the starting materials, two-dimensional graphene and MoS_2 nanosheets were obtained, respectively, via cathodic exfoliation in aqueous medium. Different parameters of the process were optimized.

Among the different starting graphite materials used to produce graphene (graphite foil, graphite rod and highly oriented pyrolytic graphite), graphite foil shows the highest yields, while electrolytes comprising quaternary ammonium salts of intermediate size afford graphene yields close to 50 wt% in optimal conditions. Graphene obtained by this process has a low content of oxygen, a high structural quality and a good electrical conductivity.

The cathodically exfoliated graphene was used as an electrode for supercapacitors in the form of a hybrid that incorporated a small amount of vertically oriented cobalt oxide nanosheets. The latter provide pseudocapacitance and act as a spacer, thus preventing the re-stacking of graphene.

The hydrophobic graphene obtained by cathodic exfoliation was used as an absorbent of aqueous pollutants, such as oils and dyes. A low-density, easy-to-handle macroscopic structure was prepared by coating melamine foam with cathodic graphene. This strategy prevents the re-stacking of the nanosheets and thus a dramatic loss of specific surface area, thus facilitating the regeneration of the adsorbent.

The cathodic exfoliation of *bulk* MoS_2 was carried out using common salts, such as KCl, as the electrolyte in apropiate conditions. The resulting two-dimensional MoS_2 nanosheets retained the original 2H phase of the starting material and do not undergo oxidation at any substantial extent. The obtained material was studied as catalyst for the reduction of nitroarenes and as an electrode for supercapacitors. In the latter case, a hybrid made up of the exfoliated MoS_2 nanosheets and single walled carbon nanotubes, which provide electrical conductivity and act as spacer, was used. Cathodic MoS_2 nanosheets were found to be very competitive for both applications in comparison with similar materials obtained through other methods.

Moreover, MoS_2 nanosheets were subjected to activation treatments in order to improve their catalytic activity towards the reduction of nitroarenes and organic dyes in water. Colloidal dispersions of nanosheets were first obtained by sonication of *bulk* MoS_2 powder in isopropanol, and then treated with hydrazine to generate sulfur vacancies (active sites). The MoS_2 nanosheets activated in such a way show catalytic activity values three o four times higher than those of their non-activated counterparts.

ACRÓNIMOS

Por orden alfabético:

-2-NA: 2-nitroanilina
-4-NA: 4-nitroanilina
-4-NP: 4-nitrofenol
-ACl: cloruro de amonio (*ammonium chloride*)
-AFM: microscopía de fuerza atómica (*atomic force microscopy*)
-AM: antimoneno (*antimonene*)
-AMP: adenosín monofosfato
-B NSs: nanoláminas de boro (*boron nanosheets*)
-BP: fósforo negro (*black phosphorous*)
-BzTMACl: cloruro de benciltrimetilamonio (*benzyltrimethylammonium chloride)*
-CVD: depósito químico en fase vapor (*chemical vapor deposition*)
-DDTMABr: bromuro de dodeciltrimetilamonio (*dodecyltrimethylammonium bromide*)
-DMF: dimetilformamida
-DMSO: dimetilsulfóxido
-EDLC: condensadores de doble capa eléctrica (*electrostatic double layer capacitors*)
-EIS: espectroscopía de impedancia electroquímica (*electrochemical impedance spectroscopy)*
-EPR: resonancia paramagnética electrónica (*electron paramagnetic resonance)*
-FMN: flavín mononucleótido
-g-C_3N_4: nitruros de carbono grafíticos (*graphitic carbon nitride*)
-GMP: guanosín monofosfato
-GO: óxido de grafeno (*graphene oxide*)
-h-BN: nitruro de boro hexagonal (*hexagonal boron nitride*)
-HDTMABr: bromuro de hexadeciltrimetilamonio (*hexadecyltrimethylammonium bromide)*
-HER: reacción de evolución de hidrógeno (*hydrogen evolution reaction*)
-HOPG: grafito pirolítico altamente orientado (*highly oriented pyrolitic graphite*)
-HR-TEM: microscopía electrónica de transmisión de alta resolución (*high resolution transmission electron microscopy)*
-HTMABr: bromuro de hexiltrimetilamonio (*hexyltrimethylammonium bromide*)
-IR: infrarrojo
-IPA: isopropanol
-LDHs: hidróxidos de capa doble (*Layered double hydroxides*)
-MB: azul de metileno (*methylene blue*)
-MO: naranja de metilo (*methyl orange*)
-NEP: N-etil-2-pirrolidona
-NMP: N-metil-2-pirrolidona
-NMR: resonancia magnética nuclear (*nuclear magnetic resonance*)
-NSs: nanoláminas (*nanosheets*)
-NVP: N-vinil-2-pirrolidona
-ORR: reacción de reducción de oxígeno (*oxygen reduction reaction*)
-OTMABr: bromuro de octiltrimetilamonio (*octyltrimethylammonium bromide*)
-PhTMACl: cloruro de feniltrimetilamonio (*phenyltrimethylammonium chloride)*
-rGO: óxido de grafeno reducido (*reduced graphene oxide*)

-SEM: microscopía electrónica de barrido (*scanning electron microscopy*)
-SnTe NSs: nanoláminas de telururo de estaño (*SnTe nanosheets*)
-STEM: microscopía electrónica de barrido por transmisión (*scanning tranmission electron microscopy)*
-SWCNTs: nanotubos de carbono de capa simple (*single-walled carbon nanotubes*)
-TBACl: cloruro de tetrabutilamonio (*tetrabutylammonium chloride*)
-TBAHCl: cloruro de tributilamonio (*tributylammonium chloride*)
-TBMACl: cloruro de tributilmetilamonio (*tributylmethylammonium chloride*)
-TEACl: cloruro de tetraetilamonio (*tetraethylammonium chloride*)
-TEM: microscopía electrónica de transmisión (*transmission electron microscopy)*
-TMACl: cloruro tetrametilamonio (*tetramethylammonium chloride*)
-TMAHCl: cloruro de trimetilamonio (*trimethylammonium chloride)*
-TMDs: dicalcogenuros de metales de transición (*transition metal dichalcogenides*)
-TMO: óxidos de metales de transición (*transition metal oxides*)
-TPACl: cloruro de tetrapropilamonio (*tetrapropylammonium chloride*)
-UV: ultravioleta
-XPS: Espectroscopía fotoelectrónica de rayos X (XPS, *X-ray photoemission spectroscopy*

1. Introducción

1.1. Materiales bidimensionales (2D)

Los materiales nanoestructurados son sólidos que presentan al menos una de sus dimensiones en la escala de los nanómetros. De esta forma, los materiales con 3 dimensiones nanométricas se denominan cero-dimensionales (0D, como los puntos cuánticos), con dos de ellas nanométricas son materiales unidimensionales (1D, como los nanotubos) y bidimensionales (2D) son aquellos sólidos con una dimensión nanométrica, (como las nanoláminas) [1]. La estructura nanométrica que presentan estos materiales afecta a las propiedades de éstos, distinguiéndolos de los sólidos no nanoestructurados. Un ejemplo sería el grafito, que no presenta una alta dureza en su estado *bulk*, pero sí al ser exfoliado hasta monocapas de grafeno [2]. En muchas ocasiones, los materiales 2D están directamente relacionados con los materiales laminares, que son una familia de sólidos (naturales y artificiales) compuestos por capas apiladas, unidas entre sí por interacciones débiles tipo van der Waals y por fuertes enlaces (como los covalentes) dentro del mismo plano [3]. A raíz del descubrimiento del grafeno, por Geim y Novoselov [4], se ha desatado una enorme actividad investigadora en torno a los materiales 2D (Figura 1), que continúa hasta el día de hoy.

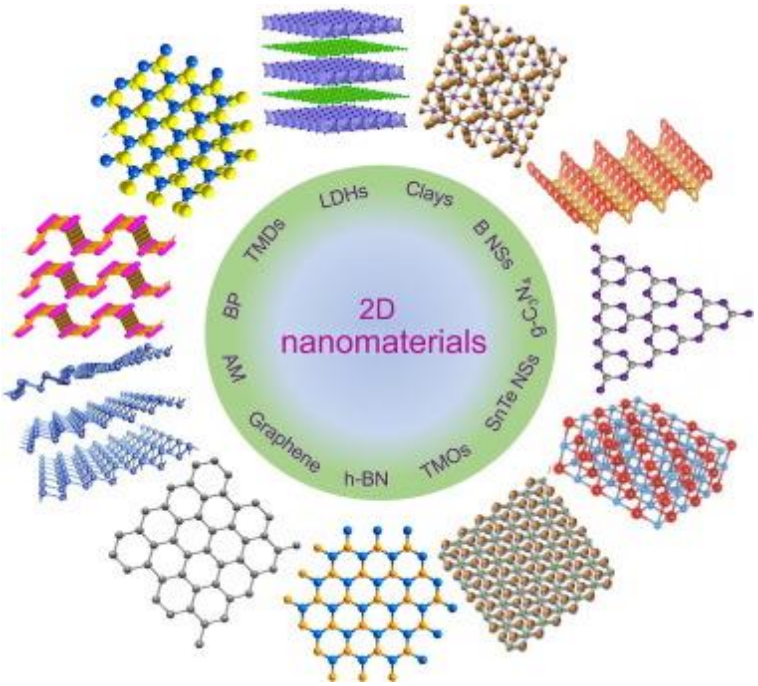

Figura 1: Ejemplos de materiales bidimensionales: Hidróxidos de capa doble (*Layered double hydroxides*, LDHs), Arcillas (*Clays*), Nanoláminas de Boro (*Boron nanosheets*, B NSs), Nitruros de carbono grafíticos (*Graphitic carbon nitride*, g-C_3N_4), Nanoláminas de telururo de estaño (*SnTe nanosheets*, SnTe NSs), Óxidos de metales de transición (*Transition metal oxides*, TMO), Nitruro de boro hexagonal (*Hexagonal boron nitride*, h-BN), Grafeno (*Graphene*), Antimoneno (*Antimonene*, AM), Fósforo negro (*Black phosphorous*, BP), Dicalcogenuros de metales de transición (*Transition metal dicalcogenides*, TMDs) . Adaptado de [5].

A lo largo de esta tesis se ha trabajado fundamentalmente con materiales 2D, en especial el grafeno y nanoláminas de disulfuro de molibdeno.

1.1.1. Grafeno

El grafeno consiste, por definición, en una monocapa de átomos de carbono unidos covalentemente en estructura hexagonal, formando anillos de 6 átomos en hibridación sp^2, cuyo espesor es 0.34 nm (Figura 2a). Sin embargo, se puede considerar también grafeno a láminas de entre 2 y 10 capas, debido a que las propiedades de éstas son diferentes a las del grafito *bulk*, generando por tanto, un gran interés práctico en diferentes aplicaciones [6-10].

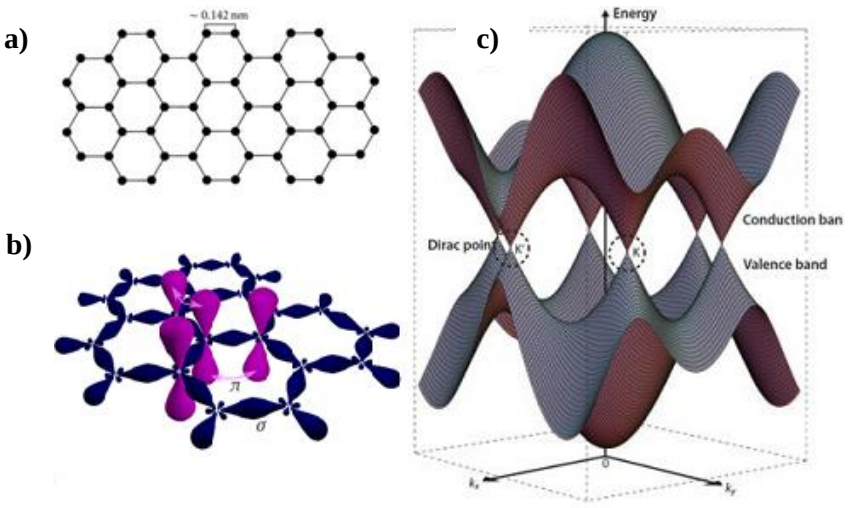

Figura 2: Representación de una lámina (a), de la hibridación e interacción de los orbitales atómicos de los de carbono (b) y de la estructura de bandas (c) del grafeno [11].

A partir de esta estructura, podemos derivar y explicar varias propiedades importantes del grafeno, descritas a continuación:

1.1.1.1. Propiedades electrónicas

Los átomos de carbono interaccionan entre sí formando tres enlaces covalentes sencillos en el plano con 3 átomos de carbono vecinos debido a la hibridación sp^2 de cada uno de ellos, a partir de orbitales atómicos 2s, $2p_x$ y $2p_y$. Cada átomo de carbono tiene, además, un orbital $2p_z$ perpendicular al plano que interacciona lateralmente con los mismos orbitales de los átomos vecinos, formando enlaces dobles que se conjugan a lo largo de la estructura en una nube electrónica π a ambos lados del plano basal (Figura 2b). Esta deslocalización de los electrones permite una gran movilidad de cargas (2.5×10^5 cm^2 V^{-1} s^{-1}) y una conductividad eléctrica un millón de veces superior a la del cobre [12]. Esta movilidad viene dada por su estructura de bandas, en la que la estructura de la celda unitaria del grafeno hace que las bandas de valencia y conducción intersecten en un punto (el punto de Dirac, Figura 2c), donde está situado el nivel de Fermi de los electrones, convirtiendo al grafeno en un semiconductor de *gap* de banda cero con características que pueden ser modificadas a través de su funcionalización [13].

1.1.1.2. Efecto Hall cuántico

Este fenómeno consiste en la aparición de una diferencia de potencial en un material sometido a una corriente eléctrica y un campo magnético perpendiculares. Clásicamente, existe una relación lineal entre el voltaje de Hall y el campo magnético aplicado, siendo escalonado en el fenómeno cuántico. Particularmente, para el caso del grafeno, está cuantizada en números semienteros [14,15].

Debido a estas propiedades, y a su estabilidad química y las posibilidades de modificación y funcionalización, se han documentado aplicaciones del grafeno en baterías, condensadores de doble capa eléctrica (*electrostatic double layer capacitors* EDLC, denominados habitualmente supercondensadores), pilas de combustible, celdas solares, transistores y sensores electroquímicos y de efecto Hall [16-18].

1.1.1.3. Propiedades ópticas

Una monocapa de grafeno posee una transmitancia del 97.7% de luz visible y una reflectancia del 0.1%, disminuyendo la primera linealmente con el espesor, hasta un 70% para 10 nm [19]. El grafeno absorbe radiación en el espectro visible e infrarrojo (IR) cercano sin rasgos distintivos, de forma casi constante entre 300 y 2500 nm. Sin embargo, presenta una banda característica de absorción en el ultravioleta (UV) a ~270 nm, correspondiente a transiciones $\pi \rightarrow \pi^*$ [19]. Estas características, junto a la conductividad eléctrica mencionada antes, hacen que el grafeno sea un buen candidato como conductor transparente, un posible sustituto del óxido de indio y estaño (ITO, *indium tin oxide*), comúnmente utilizado a día de hoy en dispositivos electrónicos (pantallas táctiles) [20]. Por otro lado, modificando las dimensiones de las láminas de grafeno (para tener nanocintas o puntos cuánticos) o la estructura del plano basal, es posible modificar características como el gap de banda, permitiendo obtener materiales luminiscentes para la fabricación de sensores y visualizar tejidos vivos [21].

1.1.1.4. Propiedades mecánicas

De entre las propiedades mecánicas del grafeno, destaca particularmente su excepcional rigidez, siendo el módulo de Young de este material de ~1 TPa, 5 veces superior al del acero estructural estándar. Además, su resistencia a la tracción es de 130 GPa, muy superior a la de ese mismo acero (0.4 GPa) o la del kevlar (0.38 GPa) [22].

Estas propiedades hacen que el grafeno sea un gran candidato como refuerzo de materiales compuestos con diferentes matrices (poliméricas, cerámicas, metálicas), lo que permitiría mejorar sus propiedades mecánicas con cargas de grafeno relativamente bajas [23].

1.1.1.5. Propiedades térmicas

En su forma prístina, este material posee una conductividad térmica de ~5000 W m^{-1} K^{-1}, siendo más de 10 veces superior a la del cobre [24], haciéndolo idóneo como componente disipador de calor en dispositivos electrónicos [25]. También es posible incorporarlo en materiales compuestos para mejorar su conductividad y estabilidad térmicas, además de modificar las temperaturas de transición de fase [26]. Por otro lado, estas propiedades térmicas y de absorción IR permiten la aplicación de dichas láminas en nanomedicina, siendo útil para la destrucción de células cancerígenas mediante calentamiento por láser (terapia fototérmica), reduciendo el daño a los tejidos colindantes en comparación con el uso de otros materiales [27].

1.1.1.6. Propiedades químicas

Al tratarse el grafeno de láminas constituidas por carbono con enlaces saturados en su plano basal y por tanto con una baja energía superficial, podemos deducir el alto grado de hidrofobicidad que presenta dicho material. Esta propiedad hace que el grafeno sea muy útil para recubrimientos hidrofóbos o adsorción de aceites o hidrocarburos [28]. Sin embargo, el procesado del grafeno en fase líquida, para diferentes fines prácticos, requiere que el material sea estable coloidalmente en dispersión en disolventes orgánicos o en agua, siendo necesaria para ello, en general, su modificación superficial (funcionalización) con el objetivo de facilitar su estabilidad coloidal y modificar sus propiedades (hidrofobia/hidrofilia, *gap* de banda, superficie específica, actividad catalítica, almacenamiento de carga, etc.).

1.1.2. Disulfuro de molibdeno (MoS_2)

Los dicalcogenuros de metales de transición (*transition metal dichalcogenides* TMDs) son compuestos cuya fórmula general es MX_2, siendo M un metal de transición (Mo, W, Ti, Nb, etc.) y X un calcógeno (S, Se, Te). A raíz del auge del grafeno, ha surgido un gran interés en los últimos años en esta familia de materiales laminares dentro de la investigación de los materiales 2D, debido a que presentan una gran

variedad de combinaciones y diferentes características. Por ejemplo, existen TMDs semiconductores (MoS_2, WS_2, etc.), metálicos (p. e. NbS_2 y VSe_2), semimetálicos (p. e. WTe_2 y $TiSe_2$), magnéticos ($CrSe_2$) y superconductores ($PdTe_2$). De todos ellos, el MoS_2 es el material que más intensamente está siendo investigado, en parte debido a su mayor abundancia y disponibilidad pero también a sus propiedades químicas, ópticas, mecánicas y sus posibles aplicaciones [29-31].

El MoS_2 *bulk* posee estructura tridimensional compuesta por láminas formadas por una monocapa de átomos de molibdeno situada entre dos monocapas de átomos de azufre, estando las láminas unidas débilmente entre sí por fuerzas de van der Waals. Los átomos de azufre pueden coordinarse alrededor del molibdeno en dos configuraciones diferentes (Figura 3), coordinación trigonal prismática (fase 2H, termodinámicamente estable) y octaédrica (fase 1T, metaestable) [32,33].

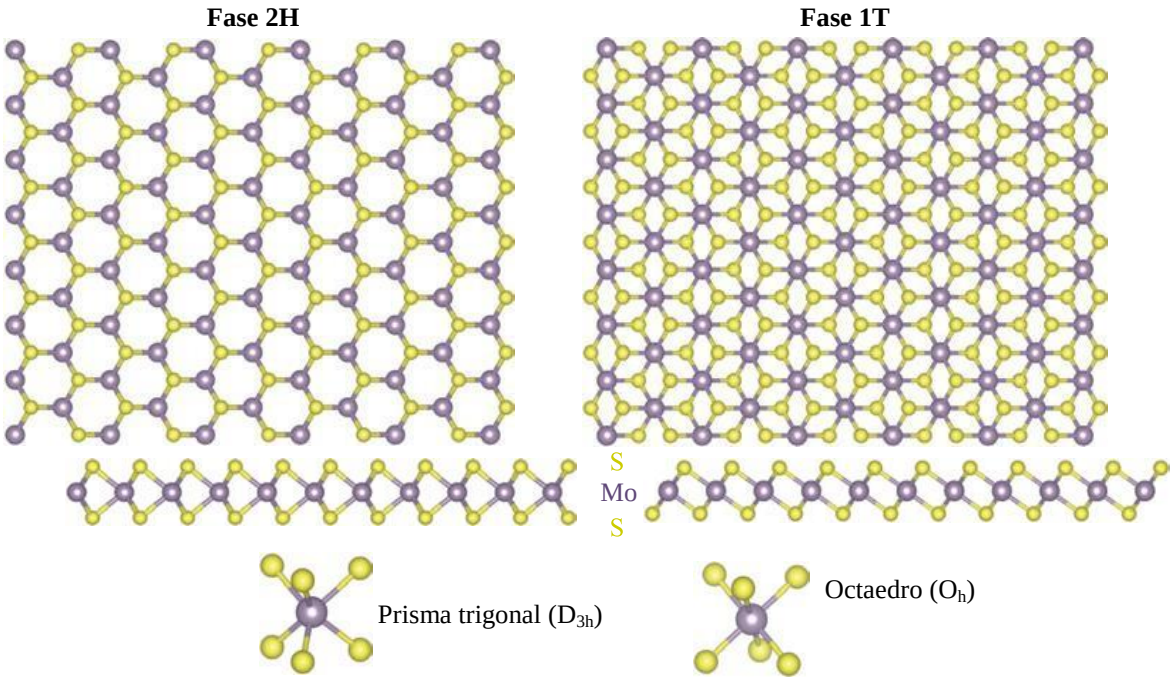

Figura 3. Fases **(a)** 2H y **(b)** 1T del MoS_2. Adaptado de [32].

Al igual que todos los materiales bidimensionales, las propiedades del material *bulk* cambian cuando reducimos de 3 a 2 sus dimensiones, siendo sensibles al número de capas que presenten.

1.1.2.1. Propiedades electrónicas y ópticas

En su forma *bulk* este material es un semiconductor de *gap* de banda indirecto de 1.29 eV, mientras que al ser exfoliado en monocapas el gap se hace directo y tiene un valor de ~1.9 eV [34], lo que lo hace interesante para su uso en dispositivos electrónicos, como transistores de efecto de campo [35], dispositivos bioelectrónicos [36] y sensores [37].

1.1.2.2. Propiedades mecánicas

Su módulo de Young es comparable al del acero (270 frente a 400 GPa) [38], y los filmes de MoS_2 2D son marcadamente elásticos, con deformaciones de 10 nm para espesores de 5 a 25 láminas [39], lo que lo hace apropiado para su uso en dispositivos electrónicos flexibles [40] y como refuerzo en materiales compuestos [41].

1.1.2.3. Propiedades térmicas

Su conductividad térmica a lo largo del plano es de ~ 18 $W\ m^{-1}\ K^{-1}$, aunque varía con el grado de exfoliación [42]. Esto lo convierte en un relleno útil para mejorar tanto las propiedades térmicas como la estabilidad a altas temperaturas de materiales compuestos [43].

1.1.2.4. Propiedades químicas

Los bordes en las láminas de MoS_2 y las vacantes de azufre en su plano basal, éstas últimas relativamente abundantes debido a su baja energía de formación, son centros catalíticamente activos en reacciones como la evolución de hidrógeno (*hydrogen evolution reaction*, HER) [44], la hidrodesulfuración [45], la reducción de óxido de azufre [46] y la reducción de nitroarenos [47]. Al igual que el grafeno, el MoS_2 prístino presenta un carácter hidrófobo, que impide su dispersión coloidal en agua en ausencia de surfactantes [48,49] o funcionalización.

1.2. Métodos de obtención de materiales 2D

Debido a que las propiedades de los materiales 2D suelen ser sustancialmente diferentes de las de sus equivalentes *bulk* 3D y dependen del número de capas, resulta crucial controlar el grado de exfoliación en los materiales 2D obtenidos a partir de materiales laminares. No existe un único método de preparación de materiales 2D, sino que se han ido desarrollando técnicas basadas en diferentes estrategias y que tienen diferentes características en términos de coste, cantidad obtenida, rendimiento, escalabilidad, control de las características del material (espesor, tamaño lateral, oxidación, defectos, grupos funcionales, morfología, etc.), rapidez y subproductos contaminantes generados. Resulta, por tanto, importante conocer los requisitos necesarios para que el material sea útil para una determinada aplicación y así seleccionar en consecuencia el método apropiado de preparación de láminas 2D. En general, los métodos de obtención de materiales 2D se pueden clasificar en dos grandes familias: los métodos *bottom-up* o ascendentes y *top-down* o descendentes (Figura 4).

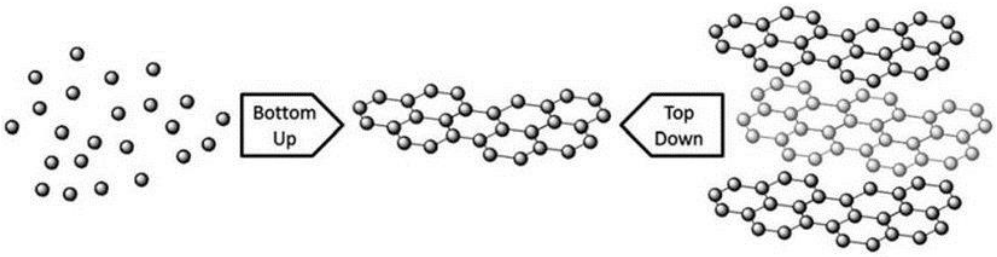

Figura 4: Esquema de los procesos top-down y bottom-up. Adaptado de [50].

1.2.1. Métodos *bottom-up*

Esta familia de métodos de preparación se basa en la síntesis de láminas 2D a partir de estructuras aún más pequeñas, como precursores atómicos o moleculares, que mediante reacciones químicas van formando el material con morfología 2D. De entre todos los métodos que componen esta familia, destacan la formación en fase líquida de TMDs y de óxidos metálicos a partir de precursores moleculares por vía solvotérmica, y de grafeno y TMDs en fase gas por medio de depósito químico en fase vapor.

1.2.1.1 Depósito químico en fase vapor (*Chemical vapor deposition*, CVD)

Este método consiste en la descomposición y reacción de un precursor, que se encuentra en estado gaseoso, generándose un producto depositado sobre un sustrato, normalmente metálico, en una cámara de reacción [51,52], como se muestra en la Figura 5. Mediante este método se obtienen generalmente materiales 2D, como grafeno y TMDs, con una alta calidad estructural, pero requiere utilizar equipos especializados y es lento.

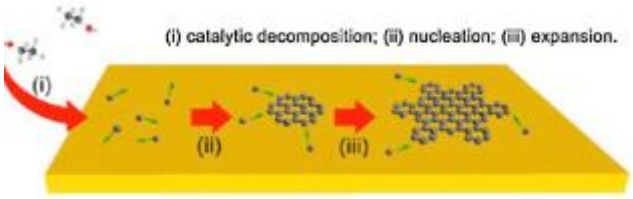

Figura 5: Representación esquemática de crecimiento de grafeno sobre Cu mediante CVD. Adaptado de [53].

1.2.1.2. Síntesis de TMDs a partir de precursores moleculares por vía solvotérmica

Jugando con la ventaja de que su estructura en capas favorece el crecimiento en forma laminar, es posible sintetizar láminas 2D de TMDs, como MoS_2, a partir de precursores moleculares en fase líquida y a temperatura moderadas [54]. Además, mediante este método se puede controlar la proporción de las fases 1T y 2H en función de las condiciones de síntesis [55], siendo una técnica muy versátil para la preparación de estos materiales.

1.2.1.3. Síntesis de láminas 2D controlada por fases micelares

Si los materiales 2D que se quieren sintetizar no presentan estructura laminar por naturaleza, como ocurre con muchos óxidos metálicos, es necesario modular el medio de síntesis para favorecer la formación de estructuras 2D. Esto se puede conseguir utilizando agentes directores de la estructura tipo surfactante que, en presencia de los precursores necesarios y por tratamiento solvotérmico, dan lugar a láminas nanométricas del material buscado [56]. Estos agentes directores forman fases micelares laminares en

las que tiene lugar la nucleación y crecimiento a partir de los precursores, de manera que los productos obtenidos son láminas 2D. Actualmente existen procedimientos generales para la preparación de óxidos metálicos 2D o laminares basados en el uso de estas fases micelares, utilizándose como agentes directores polímeros anfifílicos [56], surfactantes [57] u otros materiales 2D como óxido de grafeno [58]. Por este método se obtienen láminas que se han empleado como fotodetectores [56], catalizadores para la reacción de reducción de oxígeno (*Oxygen reduction reaction*, ORR) [57] y en almacenamiento de carga eléctrica [58].

1.2.2. Métodos *top-down*

En esta estrategia, se parte de un material laminar *bulk* que es exfoliado para obtener láminas 2D, tanto monocapa como multicapa. Esto es posible al estar formados dichos materiales por láminas individuales unidas por interacciones débiles tipo van der Waals, lo que facilita su deslaminación mediante la aplicación de algún tipo de estímulo o fuerza externa, como cambios de temperatura, intercalación de especies químicas, ultrasonidos o fuerzas de cizalla, que aumentan el espaciado interlaminar. La exfoliación se ve facilitada por el hecho de que las interacciones interlaminares son proporcionales a $1/d^6$ (siendo d la distancia interlaminar) y se vuelven despreciables por encima de distancias de ~5 Å [59].

El primer método utilizado para aislar monocapas de un material 2D a partir de un material *bulk* fue el método de la cinta adhesiva (*Scotch tape*, o de forma general, exfoliación micromecánica), mediante el cual se obtuvieron láminas de grafeno pegando y despegando la cinta adhesiva de una pieza de HOPG en 2004 [2]. Aunque este proceso permite obtener grafeno de altísima calidad estructural y es aplicable a otros muchos materiales laminares (MoS_2, WS_2, $NbSe_2$, fósforo negro, hBN, etc [60]), su productividad y rendimientos son muy bajos, por lo que ha sido necesario desarrollar otras estrategias que permiten producir mayores cantidades de materiales 2D. Los métodos más habituales son los que se llevan a cabo en fase líquida, ya que dan lugar con frecuencia a cantidades considerables del material 2D en dispersión coloidal, facilitando su procesado. Los métodos en fase líquida más relevantes se describen a continuación.

1.2.2.1. Exfoliación por ultrasonidos y por fuerzas de cizalla

La exfoliación por ultrasonidos, una de las vías más extendidas para la preparación de dispersiones coloidales de láminas 2D, se realiza mediante la aplicación de fuerzas laterales y verticales a los planos basales, separando las capas del material *bulk* y provocando su exfoliación hasta obtener láminas 2D de pocas capas de espesor [49]. Al aplicar ultrasonidos en fase líquida, se generan burbujas de cavitación que provocan diversas fuerzas sobre el material que permiten su exfoliación (Figura 6). Por otro lado, puede producirse la exfoliación de un material mediante la aplicación de fuerzas de cizalla mediante un rotor que gira sumergido en un disolvente [61,62]. Para poder llevar a cabo ambos procesos, es necesario que el medio líquido en el que se encuentra el material tenga una energía superficial similar a la del plano basal del material a exfoliar, de tal forma que se minimice la energía requerida para la exfoliación y solvatación de las láminas 2D. Debido a esto, es común el uso de disolventes orgánicos como la N-metil-2-pirrolidona (NMP), el isopropanol (IPA) y la N,N-dimetilformamida (DMF), tanto para la exfoliación de grafito [61] como de otros materiales laminares, como MoS_2, WS_2, $MoSe_2$, $MoTe_2$, $TaSe_2$, $NbSe_2$, $NiTe_2$, BN, y Bi_2Te_3 [63]. También se pueden utilizar mezclas de agua y otras sustancias, como otros disolventes o moléculas anfifílicas, para minimizar la energía requerida en la exfoliación, usándose de esta forma mezclas agua/alcohol [64] así como surfactantes [65], polímeros [66] y biomoléculas [67].

Como resultado de estos procesos de exfoliación en fase líquida se obtienen dispersiones coloidales de láminas 2D formadas por pocas capas (entre 3 y 10 capas, en diferente proporción) aunque con un bajo rendimiento de exfoliación (en torno al 1% en peso) [61]. Por otro lado, la calidad estructural de estos materiales 2D es muy alta, ya que la exfoliación solo ocurre mediante fenómenos mecánicos que rasgan los planos basales pero que no implican una modificación química significativa de la estructura, siendo además las dispersiones obtenidas fácilmente procesables y útiles para preparar, entre otros, materiales compuestos [68], electrodos de supercondensadores [69] o transistores [70].

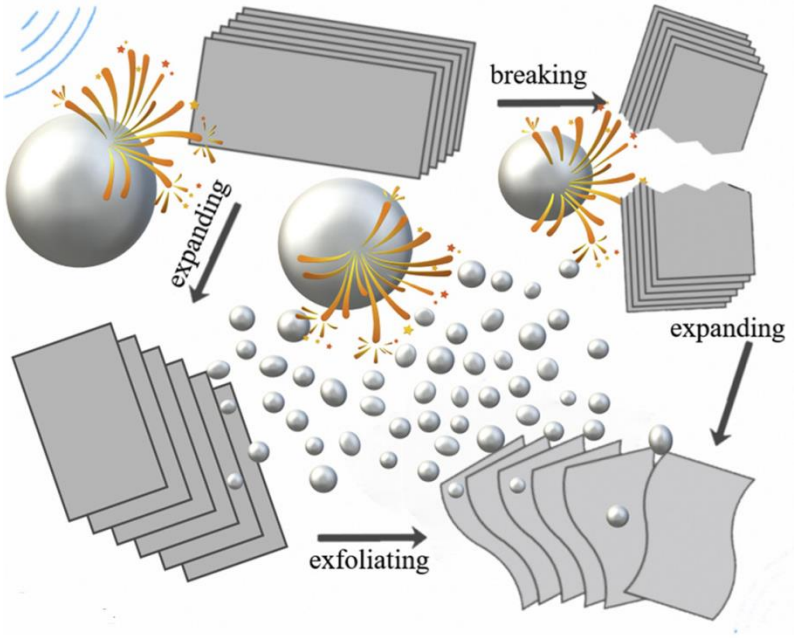

Figura 6: Representación esquemática del proceso de exfoliación por ultrasonidos de un material laminar. Adaptado de [71].

1.2.2.2. Ruta del óxido de grafeno

Es posible obtener láminas 2D en dispersión coloidal a través de la modificación química del material laminar de partida. El ejemplo más conocido es la ruta del óxido de grafeno (*graphene oxide*, GO), el cual puede prepararse mediante oxidación de grafito por el método de Hummers o modificaciones del mismo [72,73]. En dicho método el grafito es expuesto a oxidantes fuertes, como $KMnO_4$, en medio ácido. Los grupos oxigenados generados en el material resultante, denominado óxido de grafito, aumentan su espaciado interlaminar y disminuyen la energía requerida para separar unas capas de otras. Además, la presencia de grupos oxigenados capaces de desprotonarse hace que el material tenga buena dispersabilidad coloidal en agua, obteniéndose fácilmente suspensiones de láminas monocapa de GO mediante sonicación o fuerzas de cizalla [73,74]. A continuación, se lleva a cabo una reducción del GO para obtener el denominado óxido de grafeno reducido (*reduced graphene oxide*, rGO) con objeto de recuperar así la estructura y propiedades del grafeno prístino, siendo esto solo posible parcialmente, ya que para obtener una conversión completa a grafeno prístino es necesario normalmente alcanzar altas temperaturas [75]. Este proceso de reducción se puede llevar a cabo de diferentes formas, por ejemplo mediante el uso de reductores

químicos como la hidracina [76], vitamina C [77], hidrógeno [78] o biomoléculas [79], o con procesos de reducción térmica [80], electroquímica [81] o fotoquímica [82].

Se ha utilizado rGO preparado por estos métodos en materiales híbridos para aplicaciones como el almacenamiento y conversión de energía [83,84], electrocatálisis [81] y descontaminación de aguas [82].

1.2.2.3. Exfoliación química

Este método se usa comúnmente en la exfoliación de MoS_2 y otros TMDs y consiste en la intercalación de metales alcalinos en forma de compuestos, como el n-butillitio, de manera que se obtienen compuestos de intercalación (p. e. Li_xMoS_2) en los que tiene lugar una transferencia de electrones del litio al sólido y que en muchos casos induce un cambio de la fase original 2H (semiconductora) a la 1T (metálica) [85-87]. La formación de estos compuestos de intercalación tiene como objetivo aumentar el espaciado interlaminar y la reactividad del material, facilitando por tanto su exfoliación al debilitar las interacciones cohesivas [88]. En particular, estos compuestos de intercalación suelen ser altamente reactivos en medio acuoso, dando lugar a la formación de LiOH e hidrógeno gaseoso y favoreciendo así la exfoliación del material. Mediante este proceso se obtienen láminas 2D formadas por monocapas del TMD cargadas negativamente debido al exceso remanente de electrones, lo que les proporciona estabilidad coloidal en el medio acuoso, y las vuelve más reactivas, tendiendo a oxidarse por reacción con el agua, lo que les hace perder la carga eléctrica y precipitar irreversiblemente en cuestión de pocas semanas [89].

La obtención de TMDs en fase metálica 1T hace que estos materiales sean aptos en aplicaciones como el almacenamiento de energía en supercondensadores [86], catalizador de HER [87] y de reducción de nitroarenos [49].

1.2.2.4. Exfoliación electroquímica

De entre todos los procesos existentes para la obtención de materiales 2D, la exfoliación electroquímica es uno de los métodos más recientes y prometedores para este fin de forma escalable [90,91]. Este método ha sido ampliamente utilizado para la obtención de grafeno, aunque no se limita a la producción de éste, sino que también puede ser aplicado en otros materiales laminares, como los TMDs. Mediante la aplicación de un potencial eléctrico a un electrodo (del material a exfoliar) sumergido en un electrolito en un medio líquido, las especies iónicas solvatadas son atraídas por el electrodo de carga opuesta, produciéndose la intercalación de dichas especies en la

estructura del material, aumentando el espaciado interlaminar y facilitando por tanto su deslaminación para obtener el material 2D, frecuentemente con la ayuda de reacciones electrolíticas adicionales que tienen lugar en los espacios interlaminares (Figura 7). Por su propia naturaleza, es posible realizar esta técnica en modos diferentes, en función del signo positivo o negativo del potencial aplicado al electrodo de trabajo.

En la **exfoliación anódica** se aplica un potencial positivo a un electrodo de grafito (u otro material laminar), produciéndose la intercalación de los aniones presentes en el medio. En este modo se suele utilizar agua como disolvente y electrolitos como ácido sulfúrico [92], ácido fosfórico [93], sales de sulfato [94], sulfonatos orgánicos [95], o incluso líquidos iónicos [96]. Cuando se somete a un electrodo de grafito a un potencial positivo en medio acuoso (entre 4 y 30 V, siendo lo más común aplicar 10 V), se produce la oxidación de los bordes de grano y lámina del grafito, facilitando la intercalación de los aniones presentes en la disolución. Además, como el potencial aplicado es superior al de oxidación del agua, el proceso genera especies altamente reactivas, como el radical OH·, que oxida el ánodo de grafito no solo en los bordes sino también en el plano basal, y se generan especies gaseosas, como O_2, que inducen una fuerte expansión del ánodo, dando lugar a un grafito deslaminado que puede terminar de ser exfoliado en láminas de grafeno mediante tratamiento de sonicación en medio líquido. Los materiales obtenidos mediante este proceso están compuestos generalmente por láminas muy delgadas (entre 1 y 3 monocapas en su mayoría) y con un alto contenido en oxígeno (entre el 10 y el 30%) [91].

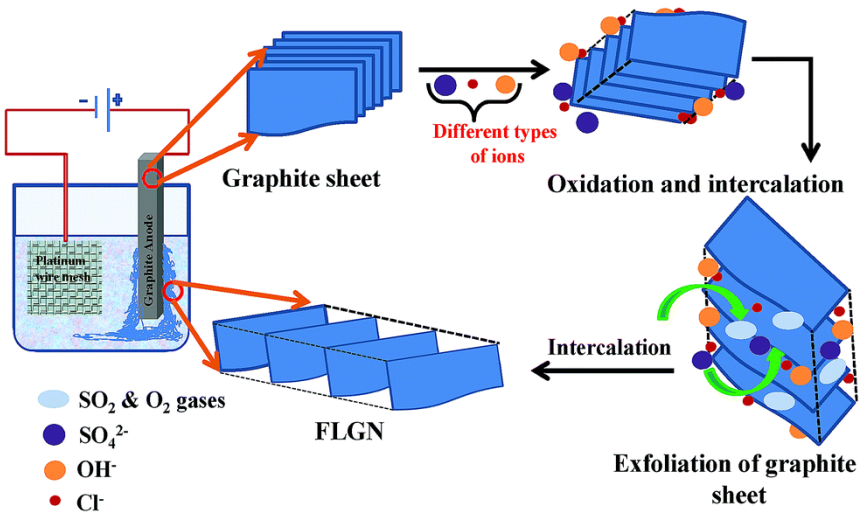

Figura 7: Esquema del proceso de exfoliación electroquímica anódica de grafito. Adaptado de [97].

En un proceso de **exfoliación catódica** se aplica un potencial negativo sobre un electrodo de grafito (típicamente de -2 a -10 V), produciéndose la atracción de los iones positivos presentes en el medio por parte de éste, que se intercalan en la estructura [98]. Este proceso se suele llevar a cabo empleando electrolitos de sales de Li^+ [99], de alquilamonio [100,101] o líquidos iónicos [102], disueltos en disolventes orgánicos como dimetilsulfóxido (DMSO) o carbonato de propileno (PC). Posteriormente, y al igual que en la exfoliación anódica, el material expandido se somete a un proceso de sonicación para completar la exfoliación del material. En general, los materiales obtenidos están formados por láminas relativamente delgadas (entre 5 y 10 capas), y con un bajo contenido en defectos y oxígeno [98], ya que se obtienen en condiciones reductoras. Son utilizados en aplicaciones como el almacenamiento y la conversión de energía [97], sensores y LEDs [98].

1.3. Métodos de modificación de materiales 2D

Puesto que los materiales 2D descritos en esta tesis poseen propiedades químicas que les permiten interaccionar con otras sustancias y modificar su estructura y propiedades, se ha estudiado una gran variedad de tratamientos de dichos materiales con el fin de modificar o mejorar sus prestaciones en diferentes aplicaciones, entre los que se encuentran los siguientes:

1.3.1. Cambio de fase

Para materiales que presentan más de una fase, puede resultar más interesante la presencia de una fase que otra debido a las diferentes propiedades que cada una presenta y a la aplicación en la que se vaya a utilizar. Para ello, puede ser necesario realizar una transformación de fase para acceder a la fase deseada. Esto ocurre, por ejemplo, cuando se transforma la fase 2H a la 1T del MoS_2 mediante el proceso de intercalación de Li^+. La fase 1T es eléctricamente conductora y estable en dispersión acuosa, resultando en principio, más útil para catálisis [47] o almacenamiento de energía [103].

1.3.2. Modificación no covalente

Se basa en la adsorción de especies químicas sobre la superficie de las láminas 2D, como surfactantes, polímeros o biomoléculas. Por ejemplo los surfactantes, pueden mejorar la estabilidad coloidal de las láminas [32,48,49], mientras que con el uso de biomoléculas es posible mejorar su biocompatibilidad [104].

1.3.3. Modificación covalente

Por un lado, es posible formar enlaces covalentes entre la superficie del material 2D y determinadas especies químicas [28,29], haciendo al material más reactivo o estable coloidalmente. Por otro lado, es posible también realizar modificaciones en la propia estructura del material 2D mediante sustitución atómica, dopándolo con heteroátomos. Un ejemplo lo constituye el dopaje de MoS_2 con Nb para para la fabricación de transistores y dispositivos optoelectrónicos [105], o la sustitución de átomos de C por N en el grafeno para aplicaciones de catalizador de la ORR, electrodos de baterías y de pilas de combustible [30,31]. También es posible la eliminación de átomos de la estructura del material 2D para generar vacantes atómicas, que generalmente están asociadas a una mayor reactividad química. Por ejemplo, la formación de vacantes de S en el MoS_2 hace que el material sea más activo para la HER [33] (Figura 8).

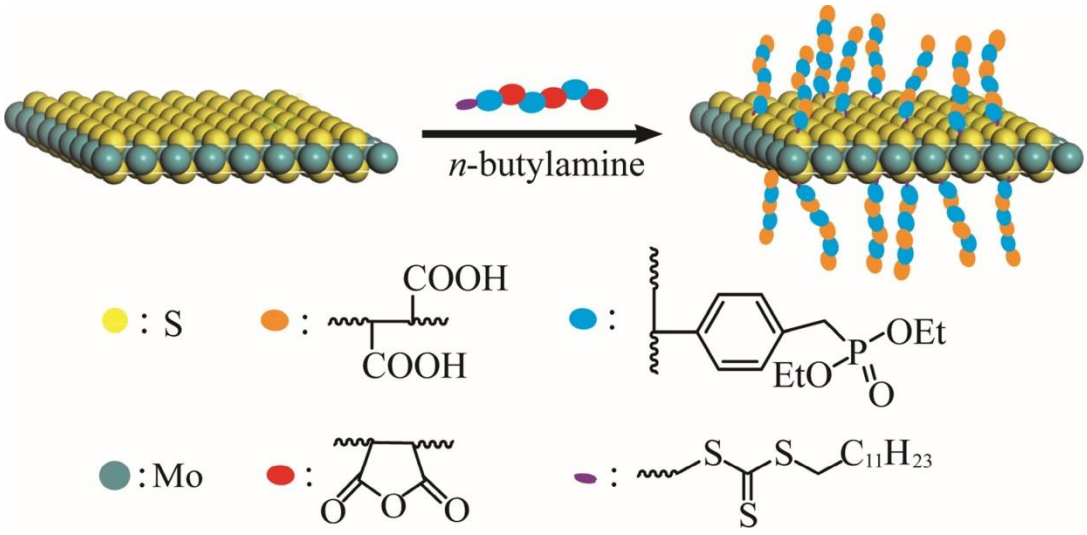

Figura 8: Esquema de un ejemplo de modificación superficial covalente de MoS_2. Adaptado de [106].

Bibliografía

[1] International Organization for Standardization, ISO/TS 80004:2015 Nanotechnologies- Vocabulary.

[2] Lee, J.-U.; Yoon, D.; Cheong, H. Estimation of Young's modulus of graphene by Raman spectroscopy. Nano Lett., 2012, 12, 4444-4448.

[3] Butler, S. Z.; Hollen, S. M.; Cao, L.; Cui, Y.; Gupta, J.A.; Gutiérrez, H.R.; Heinz, T.F.; Hong, S. S.; Huang, J.; Ismach, A. F.; Johnston-Halperin, E.; Kuno, M.; Plashnitsa, V. V.; Robinson, R. D.; Ruoff, R. S.; Salahuddin, S.; Shan, J.; Shi, L.; Spencer, M. G.; Terrones, M.; Windl, W.; Goldberger, J. E. Progress, Challenges, and Opportunities in Two-Dimensional Materials Beyond Graphene. ACS Nano, 2013, 7, 2898-2926.

[4] Novoselov, K. S.; Geim, A. K.; Morozov, S. V.; Jiang, D.; Zhang, Y.; Dubonos, S. V.; Grigorieva, I.V.; Firsov, A.A. Electric field in atomically thin carbon films. Science, 2004, 306, 666-669.

[5] Hu, T.; Mei, X.; Wuang, Y.; Weng, X.; Liang, R.; Wei, M. Two-dimensional nanomaterials: fascinating materials in biomedical field. Science Bulletin, 2019, 64, 1707-1727.

[6] Rao, C. N. R.; Sood, A. K.; Subrahmanyam, K. S .; Govindaraj, A. Graphene: The new two- dimensional nanomaterial. Angew. Chem. Int. Ed., 2009, 48, 7752-7777.

[7] Ohta, T.; Bostwick, A.; Seyller, T.; Horn, K.; Rotenberg, E. Controlling the Electronic Structure of Bilayer Graphene. Science, 2006, 313, 951-954.

[8] Zhang, Y.; Tang, T.-T.; Girit, C.; Hao, Z.; Martin, M. C.; Zettl, A.; Crommie, M. F.; Shen, Y. R.; Wang, F. Direct observation of a widely tunable bandgap in bilayer graphene. Nature, 2009, 459, 820-823.

[9] Shahil, K. M. F.; Balandin, A. A. Graphene-Multilayer Graphene Nanocomposites as Highly Efficient Thermal Interface Materials. Nano Lett., 2012, 12, 861-867.

[10] Tan, P. H.; Han, W. P.; Zhao, W. J.: Wu, Z. H.; Chang, K.; Wang, H.; Wang, Y. F.; Bonini, N.; Marzari, N.; Pugno, N.; Savini, G.; Lombardo, A.; Ferrari, A.C. The shear mode of multilayer graphene. Nat. Mat., 2012, 11, 294-300.

[11] Roberts, M. W.; Clemons, C. B.; Wilber, J. P.; Young, G. W.; Buldum, A.; Quinn, D. D. Continuum Plate Theory and Atomistic Modeling to Find the Flexural Rigidity of a Graphene Sheet Interacting with a Substrate, Journal of Nanotechnology, 2010, 2010.

[12] Novoselov, K. S.; Fal'Ko, V. I.; Colombo, L.; Gellert, P. R.; Schwab, M. G.; Kim, K. A roadmap for graphene. Nature, 2012, 490, 192-200.

[13] Weiss, N. O.; Zhou, H.; Liao, L.; Liu, Y.; Jiang, S.; Huang, Y.; Duan, X. Graphene: An emerging electronic material. Adv, Mater., 2012, 24, 5782-5825.

[14] Zhang, Y.; Tan, Y.-W.; Stormer, H. L.; Kim, P. Experimental observation of the quantum Hall effect and Berry's phase in graphene. Nature, 2005, 438, 201-204.

[15] Novoselov, K. S.; Jiang, Z.; Zhang, Y.; Morozov, S. V.; Stormer, H. L.; Zeitler, U.; Maan, J. C.; Boebinger, G. S.; Kim, P.; Geim, A. K. Room-temperature quantum hall effect in graphene. Science, 2007, 315, 1379.

[16] Sun, Y.; Wu, Q.; Shi, G. Graphene based new energy materials, Energy Environ. Sci., 2011, 4, 1113-1132.

[17] Bonaccorso, F.; Colombo, L.; Yu, G.; Stoller, M.; Tozzini, V.; Ferrari, A. C.; Ruoff, R. S.; Pellegrini, V. Graphene, related two-dimensional crystals, and hybrid systems for energy conversion and storage. Science, 2017, 347, 1246501.

[18] Schwierz, F. Graphene transistors, Nat. Nanotechnol., 2010, 5, 487-496

[19] Bonaccorso, F.; Sun, Z.; Hasan, T.; Ferrari, A. C. Graphene photonics and optoelectronics. Nat. Photonics, 2010, 4, 611-622.

[20] Shuping Pang, S.; Hernandez, Y.; Feng, X.; Müllen, K. Graphene as Transparent Electrode Material for Organic Electronics. Adv. Mater., 2011, 23, 2779-2795.

[21] Prezzi, D.; Varsano, D.; Ruini, A.; Marini, A.; Molinari, E. Optical properties of graphene nanoribbons: The role of many-body effects. Phys. Rev. B. 2008, 77, 041404(R).

[22] Lee, C.; Wei1, X.; Kysar, J. W.; Hone1, J. Measurement of the Elastic Properties and Intrinsic Strength of Monolayer Graphene. Science, 2008, 321, 385-388.

[23] Graphene Reinforced Metal Matrix Composite (GRMMC): A Review. Procedia Eng., 2014, 97, 1033-1040.

[24] Balandin, A. A. Thermal properties of graphene and nanostructured carbon materials. Nat. Mater., 2011, 10, 569-581.

[25] Weiss, N.O.; Zhou, H.; Liao, L.; Liu Y.; Jiang, S.; Huang, Y.; Duan, X. Graphene: an emerging electronic material. Adv Mater., 2012, 24, 5782-5825.

[26] Pottsa, J. R.; Dreyerb, D. R.; Bielawski, C. W.; Ruoff, R. S. Graphene-based polymer nanocomposites. Polymer, 2011, 52, 5-25.

[27] Yang, K.; Feng, L.; Shi, X.; Liu, Z. Nano-graphene in biomedicine: theranostic applications. Chem. Soc. Rev., 2013, 42, 530-547

[28] Wang, X.; Nie, S.; Zhang, P.; Song, L.; Hu, Y. Superhydrophobic and superoleophilic graphene aerogel for ultrafast removal of hazardous organics from water. J. Mater. Res. and Tech., 2020, 9, 667-674.

[29] Ganatra, R.; Zhang, Q. Few-layer MoS_2: A promising layered semiconductor. ACS Nano, 2014, 4074-4099.

[30] Huang, X.; Zeng, Z.; Zhang, H. Metal dichalcogenide nanosheets: preparation, properties and applications. Chem. Soc. Rev., 2013, 42, 1934-1946.

[31] Winer, W.O. Molybdenum disulfide as a lubricant: A review of the fundamental knowledge. Wear, 1967, 10, 422-452.

[32] Chhowalla, M.; Shin, H. S.; Eda, G.; Li, L.-J.; Loh, K. P.; Zhang, H. The chemistry of two- dimensional layered transition metal dichalcogenide nanosheets. Nat. Chem., 2013, 5, 263-275.

[33] Benavente, E.; Santa Ana, M.A.; Mendizábal, F.; González, G. Intercalation chemistry of molybdenum disulfide. Coord. Chem. Rev., 2002, 224, 87-109.

[34] Mak, K.F.; Lee, C.; Hone, J.; Shan, J.; Heinz, T.F. Atomically thin MoS_2: a new direct-gap semiconductor. Phys Rev Lett., 2010, 105, 136805.

[35] Ghatak, S.; Pal, A.N.; Ghosh, A. Nature of electronic states in atomically thin MoS_2 field- effect transistors. ACS Nano, 2011, 5, 7707-7712.

[36] Kang, P.; Wang, M. C.; Nam, S. Bioelectronics with two-dimensional materials, Microelectron. Eng., 2016, 161, 18–35.

[37] Zhang, W.; Zhang, P.; Su, Z.; Wei, G. Synthesis and sensor applications of MoS2-based nanocomposites. Nanoscale, 2015, 7, 18364-18378.

[38] Bertolazzi, S.; Brivio, J.; Kis, A. Stretching and breaking of ultrathin MoS_2. ACS Nano, 2011, 5, 9703-9709.

[39] Castellanos-Gomez, A.; Poot, M.; Steele, G.A.; van der Zant, H.S.J.; Agraït, N.; Rubio-Bollinger, G. Elastic properties of freely suspended MoS_2 nanosheets, Adv. Mater, 2012, 24, 772-775.

[40] Lembke, D.; Bertolazzi, S.; Kis, A. Single-Layer MoS_2 Electronics. Acc. Chem. Res., 2015, 48, 100-110.

[41] Wang, X.; Kalali, E. N.; Wang, D-Y. An in situ polymerization approach for functionalized MoS_2/nylon-6 nanocomposites with enhanced mechanical properties and thermal stability. J. Mater. Chem. A, 2015, 3, 24112-24120.

[42] Kim, J.-Y.; Choi, S.M.; Seo, W.-S.; Cho, W.-S. Thermal and Electronic Properties of Exfoliated Metal Chalcogenides. Bull. Korean Chem. Soc., 2010, 31, 3225-3227.

[43] Zhou, K.; Liu, J.; Zeng, W.; Hu, Y.; Gui, Z. In situ synthesis, morphology, and fundamental properties of polymer/MoS_2 nanocomposites. Compos. Sci. Technol., 2015, 107, 120-128.

[44] Jaramillo, T.F.; Jørgensen, K.P.; Bonde, J.; Nielsen, J.H.; Horch, S.; Chorkendorff, I. Identification of active edge sites for electrochemical H_2 evolution from MoS_2 nanocatalysts. Science, 2007, 317, 100-102.

[45] Grange, P.; Delmon, B. The role of cobalt and molybdenum sulphides in hydrodesulphurisation catalysts: A review. J. Less Common. Met., 1974, 36, 353-360.

[46] Zhang, X.; Hayward, D.O.; Lee, C.; Mingos, D.; Michael, P. Microwave assisted catalytic reduction of sulfur dioxide with methane over MoS_2 catalysts. Appl. Catal. B, 2001, 33, 137-148.

[47] Guardia, L.; Paredes, J. I.; Munuera, J. M.; Villar-Rodil, S.; Ayán-Varela, M.; Martínez- Alonso, A.; Tascón, J. M. D. Chemically exfoliated MoS_2 nanosheets as an efficient catalyst for reduction reactions in the aqueous phase. ACS Appl. Mater. Interfaces, 2014, 6, 21702−21710.

[48] Varrla, E.; Backes, C.; Paton, K.R.; Harvey, A.; Gholamvand, Z.; McCauley, J.; Coleman, J.N. Large-Scale Production of Size-Controlled MoS_2 Nanosheets by Shear Exfoliation. Chem. Mater., 2015, 27, 1129-1139.

[49] Guardia, L.; Paredes, J.I.; Rozada, R.; Villar-Rodil, S.; Martínez-Alonso, A.; Tascón, J.M.D. Production of aqueous dispersions of inorganic graphene analogues by exfoliation and stabilization with non-ionic surfactants. RSC Adv., 2014, 4, 14115-14127.

[50] Chaitoglou, S. Growth Study and Characterization of Single Layer Graphene Structures Deposited on Copper Substrate by Chemical Vapor Deposition. 2016.

[51] Li, W.; Hongwei Zhu, H.; Two-dimensional MoS_2: Properties, preparation, and applications. J. Materiomics, 2015, 1, 33-44.

[52] Reina, A.; Jia, X.; Ho, J.; Nezich, D.; Son, H.; Bulovic, V.; Dresselhaus, M. S.; Jing, K. Large area, Few-layer Graphene Films on Arbitrary Substrates by Chemical Vapor Deposition. Nano Lett., 2009, 9, 30-35.

[53] Chen, X.; Zhang, L.; Chen, S. Large area CVD growth of graphene. Synth. Met. 2015, 2010, 95-108.

[54] Chua, C. K.; Loo, A. H.; Pumera, M. Top-Down and Bottom-Up Approaches in Engineering 1 T Phase Molybdenum Disulfide (MoS_2): Towards Highly Catalytically Active Materials. Chem. Eur. J., 2016, 22, 14336-14341.

[55] Sun, K.; Liu, Y.; Pan, Y.; Zhu, H.; Zhao, J.; Zeng, L.; Liu, Z.; Liu, C. Targeted bottom-up synthesis of 1T-phase MoS_2 arrays with high electrocatalytic hydrogen evolution activity by simultaneous structure and morphology engineering. Nano Research, 2018, 11, 4368–4379.

[56] Sun, Z.; Liao, T.; Dou, Y.; Hwang, S. M.; Park, M.-S.; Jiang, L.; Kim, J. H.; Dou, S. X. Generalized self-assembly of scalable two-dimensional transition metal oxide nanosheets. Nat. Commun., 2014, 5, 3813-3822.

[57] Zhuang, L.; Ge, L.; Yang, Y.; Li, M.; Jia, Y.; Yao, X.; Zhu, Z. Ultrathin iron-cobalt oxide nanosheets with abundant oxygen vacancies for the oxygen evolution reaction. Adv. Mater., 2017, 1606793.

[58] Chen, P.-Y.; Liu, M.; Valentin, T. M.; Wang, Z.; Steinberg, R. S.; Sodhi, J.; Wong, I. Y.; Hurt, R. H. Hierarchical metal oxide topographies replicated from highly textured graphene oxide by intercalation templating. ACS Nano, 2016, 10, 10869-10879.

[59] Du, W.; Jiang, X.; Zhu, L. From graphite to graphene: direct liquid-phase exfoliation of graphite to produce single- and few layered pristine graphene. J. Mater. Chem. A, 2013, 1, 10592-10606.

[60] Novoselov, K.S.; Jiang, D.; Schedin, F.; Booth, T.J.; Khotkevich, V.V.; Morozov, S.V.; Geim, A.K. Two-dimensional atomic crystals. Proc. Natl. Acad. Sci. U.S.A., 2005, 102, 10451-10453.

[61] Hernandez, Y.; Nicolosi, V.; Lotya, M.; Blighe, F. M.; Sun, Z.; De, S.; McGovern, I. T.; Holland, B.; Byrne, M.; Gun'Ko, Y. K.; Boland, J. J.; Niraj, P.; Duesberg, G.; Krishnamurthy, S.; Goodhue, R., Hutchison, J.; Scardaci, V.; Ferrari, A. C.; Coleman, J. N. High-yield production of graphene by liquid-phase exfoliation of

graphite. Nat. Nanotechnol., 2008, 3, 563–568.

[62] Paton, K. R.; Varrla, E.; Backes, C.; Smith, R. J.; Khan, U.; O'Neill, A.; Boland, C.; Lotya, M.; Istrate, O. M.; King, P.; Higgins, T.; Barwich, S.; May, P.; Puczkarski, P.; Ahmed, I.; Moebius, M.; Pettersson, H.; Long, E.; Coelho, J.; O'Brien, S. E.; McGuire, E. K.; Sanchez, B. M.; Duesberg, G. S.; McEvoy, N.; Pennycook, T. J.; Downing, C.; Crossley, A.; Nicolosi, V.; Coleman, J. N. Scalable production of large quantities of defect-free few-layer graphene by shear exfoliation in liquids. Nat. Mat., 2014, 13, 624–630.

[63] Coleman, J.N.; Lotya, M.; O'Neill, A.; Bergin, S.D.; King, P.J.; Khan, U.; Young, K.; Gaucher, A.; De, S.; Smith, R.J.; Shvets, I.V.; Arora, S.K.; Stanton, G.; Kim, H.-Y.; Lee, K.; Kim, G.T.; Duesberg, G.S.; Hallam, T.; Boland, J.J.; Wang, J.J.; Donegan, J.F.; Grunlan, J.C.; Moriarty, G.; Shmeliov, A.; Nicholls, R.J.; Perkins, J.M.; Grieveson, E.M.; Theuwissen, K.; McComb, D.W.; Nellist, P.D.; Nicolosi, V. Two-dimensional nanosheets produced by liquid exfoliation of layered materials. Science, 2011, 331, 568-571.

[64] Halim, U.; Zheng, C. R.; Chen, Y.; Lin, Z.; Jiang, S.; Cheng, R.; Huang, Y.; Duan, X. A rational design of cosolvent exfoliation of layered materials by directly probing liquid–solid interaction. Nature Commun., 2013, 4, 2213-2020.

[65] Lotya, M.; Hernandez, Y.; King, P. J.; Smith, R. J.; Nicolosi, V.; Karlsson, L. S.; Blighe, F. M.; De, S.; Zhiming, W.; McGovern, I. T.; Duesberg, G. S.; Coleman, J. N. Liquid phase production of graphene by exfoliation of graphite in surfactant/water solutions. J. Am. Chem. Soc., 2009, 131, 3611-3620.

[66] Bourlinos, A. B.; Georgakilas, V.; Zboril, R.; Steriotis, T. A.; Stubos, A. K.; Trapalis, C. Aqueous-phase exfoliation of graphite in the presence of polyvinylpyrrolidone for the production of water-soluble graphenes. Solid State Commun., 2009, 149, 2172-2176.

[67] Caridad, B.; Paredes, J. I.; Pérez-Vidal, O.; Villar-Rodil, S.; Pagán, A.; Cenis, J. L.; Martínez-Alonso, A.; Tascón, J. M. D. A biosupramolecular approach to graphene: Complementary nucleotide-nucleobase combinations as enhanced stabilizers towards aqueous-phase exfoliation and functional graphene-nucleotide hydrogels.

Carbon, 2018, 129, 321-334.

[68] Shahil, K. M. F.; Balandin, A. A. Graphene-multilayer graphene nanocomposites as highly efficient thermal interface materials. Nano Letters, 2012, 12, 861-867.

[69] Bissett, M. A.; Kinloch, I. A.; Dryfe, R. A. W. Characterization of MoS_2-Graphene Composites for High-Performance Coin Cell Supercapacitors. ACS Appl. Mater. Interfaces, 2015, 7, 17388-17398.

[70] Kelly, A. G.; Hallam, T.; Backes, C.; Harvey, A.; Esmaeily, A. S.; Godwin, I.; Coelho, J.; Nicolosi, V.; Lauth, J.; Kulkarni, A.; Kinge, S.; Siebbeles, L. D. A.; Duesberg, G. S.; Coleman, J. N. All-printed thin-film transistors from networks of liquid-exfoliated nanosheets. Science, 2017, 356, 69–73.

[71] Tyurnina, A. V.; Tzanakis, I.; Morton, J.; Mi, J.; Porfyrakis, K.; Maciejewska, B. M.; Grobert, N.; Eskin, D. G. Ultrasonic exfoliation of graphene in water: A key parameter study. Carbon, 2020, 168, 737-747.

[72] Dreyer, D.R.; Park, S.; Bielawski, C.W.; Ruoff, R.S. The chemistry of graphene oxide. Chem. Soc. Rev., 2010, 39, 228-240.

[73] Zhu, Y.; Murali, S.; Cai, W.; Li, X.; Suk, J.W.; Potts, J.R.; Ruoff, R.S. Graphene and Graphene Oxide: Synthesis, Properties, and Applications. Adv. Mater., 2010, 22, 3906-3924.

[74] Paredes, J. I.; Villar-Rodil, S.; Martínez-Alonso, A.; Tascón, J. M. D. Graphene oxide dispersions in organic solvents. Langmuir, 2008, 24, 10560-10564.

[75] Rozada, R.; Paredes, J. I.; López, M. J.; Villar-Rodil, S.; Cabria, I.; Alonso, J. A.; Martínez-Alonso, A.; Tascón, J. M. D. From graphene oxide to pristine graphene: Revealing the inner workings of the full structural restoration. Nanoscale, 2015, 7, 2374-2390.

[76] Stankovich, S.; Dikin, D.A.; Piner, R.D.; Kohlhaas, K.A.; Kleinhammes, A.; Jia, Y.; Wu, Y.; Nguyen, S.T.; Ruoff, R.S. Synthesis of graphene-based nanosheets via chemical reduction of exfoliated graphite oxide. Carbon, 2007, 45, 1558-1565.

[77] Fernández-Merino, M.J.; Guardia, L.; Paredes, J.I.; Villar-Rodil, S.; Solís-Fernández, P.; Martínez-Alonso, A.; Tascón, J.M.D. Vitamin C Is an Ideal Substitute for Hydrazine in the Reduction of Graphene Oxide Suspensions. J. Phys. Chem. C, 2010, 114, 6426-6432.

[78] Pham, V.H.; Pham, H.D.; Dang, T.T.; Hur, S.H.; Kim, E.J.; Kong, B.S.; Kim, S.; Chung, J.S. Chemical reduction of an aqueous suspension of graphene oxide by nascent hydrogen. J. Mater. Chem., 2012, 22, 10530-10536.

[79] Aunkor, M.T.H.; Mahbubul, I.M.; Saidur, R.; Metselaar, H.S.C. The green reduction of graphene oxide. RSC Adv., 2016, 6, 27807–27828.

[80] Acik, M.; Lee, G.; Mattevi, C.; Pirkle, A.; Wallace, R.M.; Chhowalla, M.; Cho, K.; Chabal, Y. The Role of Oxygen during Thermal Reduction of Graphene Oxide Studied by Infrared Absorption Spectroscopy. J. Phys. Chem. C, 2011, 115, 19761-19781.

[81] Guo, H.-L.; Wang, X.-F.; Qian, Q.-Y.; Wang, F.-B.; Xia, X.-H. A Green Approach to the Synthesis of Graphene Nanosheets. ACS Nano, 2009, 3, 2653-2659.

[82] Guardia, L.; Villar-Rodil, S.; Paredes, J.I.; Rozada, R.; Martínez-Alonso, A.; Tascón, J.M.D. UV light exposure of aqueous graphene oxide suspensions to promote their direct reduction, formation of graphene–metal nanoparticle hybrids and dye degradation. Carbon, 2012, 50, 1014-1024.

[83] Huang, X.; Qi, X.; Boey, F.; Zhang, H. Graphene-based composites. Chem. Soc. Rev., 2012, 41, 666-686.

[84] Huang, X.; Yin, Z.; Wu, S.; Qi, X.; He, Q.; Zhang, Q.; Yan, Q.; Boey, F.; Zhang, H. Graphene-based materials: Synthesis, characterization, properties, and applications. Small, 2011, 7, 1876-1902.

[85] Joensen, P.; Frindt, R. F.; Morrison, S. R. Single-layer MoS_2. Materials Research Bulletin, 1986, 21, 457-461.

[86] Acerce, M., Voiry, D., Chhowalla, M. Metallic 1T phase MoS2 nanosheets as supercapacitor electrode materials. Nat. Nanotechnol., 2015, 10, 313-318.

[87] Lukowski, M.A., Daniel, A.S., Meng, F., Forticaux, A., Li, L., Jin, S. Enhanced hydrogen evolution catalysis from chemically exfoliated metallic MoS_2 nanosheets. J. Am. Chem. Soc., 2013, 135, 10274-10277.

[88] Nicolosi, V.; Chhowalla, M.; Kanatzidis, M. G.; Strano, M. S.; Coleman, J. N. Liquid Exfoliation of Layered Materials. Science, 2013, 340, 1226419.

[89] Chou, S. S.; De, M.; Kim, J.; Byun, S.; Dykstra, C.; Yu, J.; Huang, J.; Dravid, V. P. Ligand conjugation of chemically exfoliated MoS_2. J. Am. Chem. Soc., 2013, 135, 4584−4587.

[90] Abdelkader, A. M.; Cooper, A. J.; Dryfe, R. A. W.; Kinloch, I A. How to get between the sheets: a review of recent works on the electrochemical exfoliation of graphene materials from bulk graphite. Nanoscale, 2015, 7, 6944-6956.

[91] Yang, S.; Lohe, M. R.; Müllen, K.; Feng, X. New-generation graphene from electrochemical approaches: production and applications. Adv. Mater., 2016, 28, 6213–6221.

[92] Parvez, K.; Li, R.; Puniredd, S. R.; Hernandez, Y.; Hinkel, F.; Wang, S.; Feng, X.; Müllen, K. Electrochemically exfoliated graphene as solution-processable, highly conductive electrodes for organic electronics. ACS Nano, 2013, 7, 3598–3606.

[93] Liu, J. L.; Yang, H. P.; Zhen, S. G.; Poh, C. K.; Chaurasia, A.; Luo, J. S.; Wu, X. Y.; Yeow, E. K. L.; Sahoo, N. G.; Lin, J. Y.; Shen, Z. X. A green approach to the synthesis of high-quality graphene oxide flakes via electrochemical exfoliation of pencil core. RSC Adv., 2013, 3, 11745-11750.

[94] Parvez, K.; Wu, Z.-S.; Li, R.; Liu, X.; Graf, R.; Feng, X.; Müllen, K. Exfoliation of graphite into graphene in aqueous solutions of inorganic salts. J. Am. Chem. Soc., 2014, 136, 6083−6091.

[95] Alanyalıoğlu, M.; Segura, J. J.; Oró-Solè, J.; Casañ-Pastor, N. The synthesis of graphene sheets with controlled thickness and order using surfactant-assisted electrochemical processes. Carbon, 2012, 50, 142-152.

[96] Liu, N.; Luo, F.; Wu, H.; Liu, Y.; Zhang, C.; Chen, J. One-step ionic-liquid-assisted electrochemical synthesis of ionic-liquid-functionalized graphene sheets directly from graphite. Adv. Funct. Mater., 2008, 18, 1518–1525.

[97] Parveen, N.; Omaish Ansari, N.; Hwan Cho, M. Simple route for gram synthesis of less defective few layered graphene and its electrochemical performance. RSC Adv., 2015, 5, 44920-44927.

[98] Low, C. T. J.; Walsh, F. C.; Chakrabarti, M. H.; Hashim, M. A.; Hussain, M. A. Electrochemical approaches to the production of graphene flakes and their potential applications. Carbon, 2013, 54, 1-21.

[99] Wang, J.; Manga, K. K.; Bao, Q.; Loh, K. P. High-yield synthesis of few-layer graphene flakes through electrochemical expansion of graphite in propylene carbonate electrolyte. J. Am. Chem. Soc., 2011, 133, 23, 8888-8891.

[100] Cooper, A. J.; Velický, M.; Kinloch, I. A.; Dryfe, R. A. W. On the controlled electrochemical preparation of R_4N^+ graphite intercalation compounds and their host structural deformation effects. J. Electroanal. Chem., 2014, 730, 34-40.

[101] Cooper, A. J.; Wilson, N. R.; Kinloch, I. A.; Dryfe, R. A. W. Single stage electrochemical exfoliation method for the production of few-layer graphene via intercalation of tetraalkylammonium cations. Carbon, 2014, 66, 340-350.

[102] Yang, Y.; Lu, F.; Zhou, Z.; Song, W.; Chen, Q.; Ji, X. Electrochemically cathodic exfoliation of graphene sheets in room temperature ionic liquids N-butyl, methylpyrrolidinium bis(trifluoromethylsulfonyl)imide and their electrochemical properties. Electrochim. Acta, 2013, 113, 9–16.

[103] Acerce, M.; Voiry, D.; Chhowalla, M. Metallic 1T phase MoS_2 nanosheets as supercapacitor electrode materials. Nat. Nanotech., 2015, 10, 313-318.

[104] Chen, L.; Feng, W.; Zhou, X.; Qiu, K.; Miao, Y.; Zhang, Q.; Qin, M.; Li, L.; Zhang, Y.; He, C. Facile synthesis of novel albumin-functionalized flower-like MoS_2 nanoparticles for in vitro chemophotothermal synergistic therapy. RSC Adv., 2016, 6, 13040-13049.

[105] Suh, J.; Park, T.-E.; Lin, D.-Y.; Fu, D.; Park, J.; Jung, H.J.; Chen, Y.; Ko,

C.; Jang, C.; Sun, Y.; Sinclair, R.; Chang, J.; Tongay, S.; Wu, J. Doping against the Native Propensity of MoS_2: Degenerate Hole Doping by Cation Substitution. Nano Lett., 2014, 14, 6976-6982.

[106] Yang, S.; Hua, M.; Shen, L.; Han, X.; Xu, M.; Kuang, L.; Hua, D. Phosphonate and carboxylic acid co-functionalized MoS_2 sheets for efficient sorption of uranium and europium: Multiple groups for broad-spectrum adsorption. J. Hazard. Mater., 2018, 354, 191-197.

2. Objetivos

Como se ha explicado en la introducción, debido a las atractivas propiedades de los materiales bidimensionales (térmicas, eléctricas, mecánicas, etc) y a sus múltiples aplicaciones potenciales (almacenamiento de energía, dispositivos electrónicos, recubrimientos, descontaminación de aguas, etc), y conocidas las limitaciones de los métodos disponibles para su preparación, se hace necesario desarrollar nuevos métodos de preparación que aborden dichos problemas y permitan además obtener materiales con alta calidad estructural.

Por ello, se plantea como objetivo principal de esta tesis la obtención de materiales bidimensionales, como grafeno y nanoláminas de MoS_2, mediante métodos potencialmente escalables llevados a cabo en fase líquida. Se ha utilizado principalmente la exfoliación electroquímica, ya que se trata de una técnica prometedora debido a su bajo coste, su escalabilidad y la corta duración del proceso. Se ha elegido la modalidad catódica frente a la anódica, ya que las características de la primera permiten evitar más fácilmente problemas como la oxidación del producto exfoliado, dando lugar a nanoláminas de mejor calidad estructural. Además, se ha llevado a cabo la modificación de MoS_2 bidimensional para activarlo de cara a su uso como catalizador.

Los objetivos específicos se detallan a continuación:

- Preparación de grafeno por exfoliación electroquímica catódica de grafito *bulk*, concretamente utilizándose electrodos de grafito como cátodo en medio acuoso y optimizándose parámetros como la concentración y el tipo de electrolito, el potencial aplicado, la duración del proceso y el tipo de grafito de partida.

- Caracterización del grafeno catódico obtenido y estudio del material en aplicaciones de almacenamiento de energía (supercondensadores) y medioambientales (absorción de contaminantes en agua).

- Preparación de nanoláminas de MoS_2 por exfoliación electroquímica catódica del correspondiente material *bulk* en medio acuoso y estudiando el efecto de las mismas variables de exfoliación que en el caso del grafeno catódico.

- Caracterización y estudio del MoS_2 catódico obtenido con vistas a su aplicación como electrodo de supercondensador y catalizador de reacciones de reducción de nitroarenos y colorantes orgánicos.

- Activación de nanoláminas bidimensionales de MoS_2 para aplicaciones catalíticas en base a la generación de vacantes de azufre por tratamiento con hidracina, así como la optimización del proceso estudiando el efecto de parámetros como la concentración de hidracina y la temperatura del tratamiento.

3. Materiales y métodos

3.1. Grafeno

3.1.1. Exfoliación electroquímica catódica con sales de amonio cuaternario

Se ha llevado a cabo la preparación de grafeno a través de la exfoliación electroquímica catódica de grafito. Dicho proceso requiere la utilización de una celda electroquímica con configuración de dos electrodos, en la que se emplea grafito como cátodo, una placa de platino como ánodo y una disolución acuosa de una sal de amonio cuaternario como electrolito.

Se usaron piezas tanto de grafito flexible, de 55×30×0.5 mm^3 (Papyex I980, Mersen), como de HOPG, de 10×5×0.5 mm^3 (grado ZYH, Advanced Ceramics) y de grafito en barra, de diámetro 3.05 mm y densidad 1.7 g cm^{-3} (Alfa Aesar). Las piezas de grafito se conectan a través de pinzas de cocodrilo a la fuente de corriente (Agilent 6614C DC power supply) y se sigue el mismo procedimiento para la placa de platino, de 25×25×0.025 mm^3, como ánodo.

Los electrodos se preparan disolviendo diferentes sales de amonio cuaternario a concentraciones de 0.02, 0.1 y 0.3 M, en 80 mL de agua Milli-Q (resistividad: 18.2 MΩ cm, Millipore Corporation). Se usaron las siguientes sales: cloruro de amonio (ACl, *ammonium chloride*), cloruro de trimetilamonio (TMAHCl, *trimethylammonium chloride*), cloruro de tetrametilamonio (TMACl, *tetramethylammonium chloride*), cloruro de tetraetilamonio (TEACl, *tetraethylammonium chloride*), cloruro de tetrapropilamonio (TPACl, *tetrapropylammonium chloride*), cloruro de tributilamonio (TBAHCl, *tributylammonium chloride*), cloruro de tributilmetilamonio (TBMACl, *tributylmethylammonium chloride*), cloruro de tetrabutilamonio (TBACl, *tetrabutylammonium chloride*), bromuro de hexiltrimetilamonio (HTMABr, *hexyltrimethylammonium bromide*), bromuro de octiltrimetilamonio (OTMABr, *octyltrimethylammonium bromide*), bromuro de dodeciltrimetilamonio (DDTMABr, *dodecyltrimethylammonium bromide*), bromuro de hexadeciltrimetilamono (HDTMABr, *hexadecyltrimethylammonium bromide*), cloruro de feniltrimetilamonio (PhTMACl, *phenyltrimethylammonium chloride*) y cloruro de benciltrimetilamonio (BzTMACl,

benzyltrimethylammonium chloride) (todas de Sigma Aldrich). En el caso del HDTMABr no ha sido posible la preparación de la disolución a 0.3 M debido a limitaciones de solubilidad. Debido a los mayores rendimientos de grafeno catódico obtenidos, se ha usado HTMABr y TPACl, a una concentración de 0.3 M, como electrolitos estándar para usos posteriores de este material.

Los electrodos se sumergen en cada una de las disoluciones anteriores, paralelos entre sí a una distancia de aproximadamente 2 cm y se aplica un potencial de -10 V con una densidad de corriente máxima de 0.5 A durante 2 h. Durante este tiempo se observa como el grafito flexible se hincha progresivamente a la vez que se desprenden algunas partículas del mismo. La magnitud del hinchamiento varía en función del electrolito utilizado.

Tras el proceso electrolítico, se separa el grafito expandido del resto rascando la superficie con una espátula. Este grafito expandido se lava por filtración, utilizando 1.5 L de agua Milli-Q y se seca posteriormente a vacío a 60 ºC durante 18 h.

Para extraer láminas de grafeno del grafito expandido catódicamente, se toma el producto expandido, lavado y seco, se le añade un disolvente orgánico, tal como NMP, N-etil-2-pirrolidona (NEP), N-vinil-2-pirrolidona (NVP), DMF, dimetilsulfóxido (DMSO), 1,3-dioxolano y piridina, o agua con el surfactante no iónico Pluronic P-123 (0.7 mg mL^{-1}) y se le realiza un proceso de sonicación durante 3 h usando un baño de ultrasonidos (JP Selecta Ultrasons, 40 kHz). La dispersión resultante se deja reposar 24 h o se centrifuga a 100 g durante 20 min (microcentrífuga Eppendorf 5424 y 5430) con el fin de sedimentar todo aquel material que no ha quedado bien exfoliado.

La concentración de grafeno en dispersión fue estimada utilizando espectroscopía de absorción UV-Vis en base a la ley de Lambert-Beer: $A = \varepsilon\, l\, c$, siendo A la absorbancia medida a una longitud de onda de 660 nm, l el camino óptico que debe seguir el haz de luz (1 cm), ε el coeficiente de extinción a esa longitud de onda (2440 mL mg^{-1} m^{-1}) y c la concentración de grafeno en dispersión.

3.1.2. Híbrido de grafeno con óxido de cobalto

El procedimiento de preparación del híbrido de grafeno con óxido de cobalto se realizó a través de una síntesis solvotérmica de láminas 2D de óxido de cobalto contralado por fases micelares (apartado 1.2.1.3 de la introducción), en la que se añade el grafito exfoliado catódicamente en un determinado paso del proceso. En primer lugar, se disuelven 200 mg de Pluronic P-123 en 17.5 mL de una mezcla etanol/agua (33/2 v/v) con ayuda de agitación magnética. A continuación, se añaden a la disolución resultante 250 mg de acetato de cobalto (II) tetrahidratado, 70 mg de hexametilentetramina y 50 mg de grafito exfoliado catódicamente. Tras dejar mezclar durante 15 min, se añaden 13 mL de etilenglicol, se agita la mezcla durante 30 min y se deja envejecer 24 h. Se transfiere la suspensión a un autoclave de Teflón y se calienta a 170 ºC durante 2 h. El producto sólido obtenido se lava mediante repetidos ciclos de centrifugación a 2000 g durante 20 min (J.P. Selecta Meditronic), eliminación de sobrenadante y resuspensión en agua y, posteriormente, en etanol.

3.2. MoS_2

3.2.1. Exfoliación electroquímica con iones alcalinos

El procedimiento de exfoliación electroquímica del disulfuro de molibdeno es similar al de grafeno descrito anteriormente, salvo algunas particularidades. La pieza de MoS_2 (SPI Supplies) utilizada como cátodo en la celda electroquímica de dos electrodos tiene unas dimensiones de 5×5×0.5 mm^3. Como electrolitos se emplean 20 mL de disoluciones de KCl y NaCl, a concentraciones de 0.1, 0.5, 1, 2 y 4 M, de LiCl a 4 M y de TEACl, TPACl y TBACl a 0.3 M. Se aplica una diferencia de potencial de -10 V para todas las concentraciones de las sales alcalinas y también -20 V para la concentración 4 M de cada una de ellas. Para las sales de amonio cuaternario se aplica una diferencia de potencial de -20 V. En todos los casos el tiempo de aplicación del voltaje es de 30 min, durante el cual se observa cómo se abre la pieza de MoS_2 desde el extremo sumergido en el electrolito hasta el extremo sujetado por la pinza en forma de abanico. Se utiliza como electrolito KCl 4 M y diferencia de potencial de -20 V como condiciones estándar para preparar este material, debido al mayor rendimiento en producto expandido del proceso.

El secado a vacío del producto expandido tiene lugar a temperatura ambiente y posteriormente la pieza expandida se trocea con la ayuda de un bisturí. Se toma una parte de este material y se transfiere a una disolución (inicialmente 0.3-0.4 mg mL^{-1} del MoS_2 troceado) utilizando como estabilizantes adenosín monofosfato (AMP) o guanosín monofosfato (GMP) (5 mg mL^{-1}) en IPA, agua, DMF o NMP y se introduce en un baño ultrasonidos durante 3 h. La dispersión resultante se centrifuga (microcentrífuga Eppendorf 5424 y 5430) a 20000 g durante 20 min, eliminando el sobrenadante y añadiendo nuevo disolvente, repitiendo este proceso 2 veces para eliminar el exceso de estabilizante.

La concentración de MoS_2 en dispersión fue estimada utilizando espectroscopía de absorción UV-Vis en base a la ley de Lambert-Beer: $A = \varepsilon\, l\, c$, siendo A la absorbancia medida a una longitud de onda de 345 nm, l el camino óptico que debe seguir el haz de luz (1 cm), ε el coeficiente de extinción a esa longitud de onda (6900 mL mg^{-1} m^{-1}) y c la concentración de MoS_2 en dispersión.

3.2.2. Formación de vacantes por tratamiento con hidracina

En primer lugar, se toman 3 g de MoS_2 en polvo (Sigma Aldrich) y se añaden a 200 mL de IPA, sonicándose la mezcla resultante durante 5 h en un baño de ultrasonidos. La dispersión resultante se centrifuga (2000 g, 20 min), tomando el sobrenadante, y determinando su concentración por espectroscopía de absorción UV-Vis.

A continuación, se añade un volumen de hidracina monohidratada (Sigma Aldrich), 1, 2, 4, 6, 8 y 10 % v/v, a una dispersión de MoS_2 de concentración 0.1 mg mL^{-1} en IPA, obtenida como se explica en el apartado anterior. Esta mezcla se somete a una temperatura dada (70º C, 150º C o temperatura ambiente) durante 2 h, realizando un proceso de lavado posterior consistente en 2 ciclos de centrifugación a 20000 g durante 20 min, eliminación del sobrenadante y redispersión en el mismo volumen de IPA. Para utilizar el material en forma de polvo seco, el sedimento de la última centrifugación se recoge y se seca a vacío a temperatura ambiente durante una noche.

3.3. Preparación de electrodos para estudios como supercondensadores

3.3.1. Electrodos de grafeno catódico, híbrido de grafeno catódico con óxido de cobalto

Ambos electrodos se prepararon prensando (1 t durante 10 s) el material a estudiar (grafeno catódico con y sin óxido de cobalto) sobre una pieza circular (1 cm de diámetro) de grafito flexible (sin tratar), utilizando una prensa hidráulica. La cantidad de material activo en el electrodo es de aproximadamente 1 mg cm^{-2}.

Las medidas electroquímicas se llevaron a cabo en una celda tipo Swagelok de 3 electrodos, donde el electrodo de trabajo y el contraelectrodo están separados por un filtro de membrana de Nylon circular (~1.3 cm de diámetro, 0.45 µm de tamaño de poro, Whatman), utilizando el material de grafeno como electrodo de trabajo, una pasta formada por una mezcla de fibra de carbón activo, politetrafluoroetileno (como aglomerante) y negro de carbono (como aditivo conductor) en proporción másica 90:5:5 como contraelectrodo, un electrodo de referencia de Hg/HgO y KOH 6 M como electrolito. Previamente, los electrodos y el separador de Nylon se sumergen por separado en el electrolito y la celda es desgasificada en la estufa a vacío durante 1 min. Las medidas se llevan a cabo con un potenciostato VSP (Biologic).

3.3.2. Electrodos de MoS_2 exfoliado catódicamente

Se prepararon los electrodos de MoS_2 descritos a continuación prensando los correspondientes materiales sobre una pieza circular (1 cm de diámetro) de grafito flexible (sin tratar), utilizando una prensa hidráulica (1 t durante 10 s). La cantidad de material activo en el electrodo es de aproximadamente 1-1.3 mg cm^{-2}.

1) MoS_2 expandido catódicamente utilizando KCl 4 M a -20 V, sin tratamiento posterior. Lavado por filtración con abundante agua destilada y secado a vacío a 60 ºC durante una noche.
2) MoS_2 expandido catódicamente utilizando KCl 4 M a -20 V, agitado en una disolución de GMP (5 mg mL^{-1}) y secado a vacío a 60 ºC durante una noche.

3) Láminas de MoS_2 obtenidas por exfoliación catódica y posterior sonicación en una disolución de GMP en IPA (5 mg mL^{-1}). El material se sedimenta por centrifugación (20000 g, 20 min) y el precipitado se seca a vacío a 60º C durante una noche.
4) Láminas de MoS_2 combinadas con con nanotubos de carbono de capa simple (SWCNTs, *single-walled carbon nanotubes*) en proporción másica 2:1. Las láminas de MoS_2 se preparan como se ha descrito en el punto anterior. Los SWCNTs se preparan por sonicación del material comercial (1 mg mL^{-1}, 0.7-1.3 nm de diámetro, de Sigma-Aldrich) en una disolución acuosa de flavín mononucleótido (FMN) (1 mg mL^{-1}) y posterior centrifugación (20000 g, 40 min). El sobrenadante se mezcla con una pequeña cantidad de etanol y el aglomerado se recoge y se seca a vacío a 60º C durante una noche. Finalmente, ambos polvos se mezclan físicamente en la proporción deseada en un mortero hasta homogeneidad.
5) Láminas de MoS_2 combinadas con SWCNTs en proporción másica 7:1, siguiendo el protocolo descrito en el punto anterior.
6) SWCNTs en ausencia de MoS_2, preparado de igual forma que en el punto 4.

Las medidas electroquímicas de 3 electrodos se llevan a cabo realizando el mismo montaje descrito para los electrodos de grafito.

Además, se usaron las láminas de MoS_2 combinadas con SWCNTs en proporción másica 2:1 (punto 4) como electrodo positivo en un sistema de 2 electrodos asimétrico, utilizando como electrodo negativo una pasta formada por carbón activo comercial (YP-50F, de Kuraray), politetrafluoroetileno (como aglomerante) y negro de carbono (como aditivo conductor) en proporción másica 90:5:5, y KOH 6 M como electrolito.

3.4. Preparación de esponjas para estudios de absorción y catálisis

3.4.1. Esponja de melamina recubierta con grafeno

Se utiliza una esponja de melamina comercial de forma cúbica (1 cm^3), que se sumerge repetidamente (3 o 4 veces durante 1 min) en una dispersión (sonicada 3 h) de grafeno obtenido por exfoliación catódica (con TPACl 0.3 M) en piridina (0.25 mg mL^{-1}), calentándose posteriormente durante 5 min para eliminar el disolvente. Dicha esponja se utilizará para los estudios de absorción de aceites y disolventes orgánicos.

3.4.2. Esponja de melamina recubierta con MoS_2

Se corta una esponja de melamina comercial en forma cúbica (1 cm^3), se sumerge en una dispersión en IPA de MoS_2 tratado con hidracina (0.1 mg mL^{-1}) y se deja secar a temperatura ambiente y presión reducida. Este proceso se repite varias veces (normalmente 3) hasta que la esponja cambia de color blanco a un color verdoso, indicativo de la presencia de MoS_2. Esta esponja se utilizará en estudios cinéticos de catálisis.

3.5. Evaluación de la actividad catalítica en reacciones de reducción de nitroarenos y colorantes

Se han realizado estudios de actividad catalítica tanto de MoS_2 obtenido catódicamente como de MoS_2 tratado con hidracina para generar vacantes. Para ello, se ha estudiado la reacción de reducción de nitroarenos con $NaBH_4$, así como la reducción de colorantes (para el caso del MoS_2 con vacantes). Estas reacciones se han seguido mediante espectroscopía de absorción UV-Vis, ya que dichos reactivos presentan una absorbancia característica a una determinada longitud de onda que es distinta de la de los productos, de modo que la variación (disminución) de dicha absorbancia puede relacionarse con el consumo de los reactivos a medida que la reacción avanza. Los experimentos se llevaron a cabo tomando una cantidad fija de reactivo y de catalizador (MoS_2), con un exceso de $NaBH_4$. Se midió la absorbancia a la longitud de onda característica del reactivo en función del tiempo de reacción. La actividad catalítica del catalizador se calculó a partir del tiempo de reacción y las cantidades de reactivo y catalizador presentes. En la sección de espectroscopía UV-vis del capítulo de técnicas de caracterización se describe detalladamente el protocolo utilizado y se muestra un ejemplo de estas cinéticas en la Figura 10.

3.6. Evaluación como absorbentes de aceites y disolventes orgánicos

Se realizaron estudios de absorción de aceites y disolventes orgánicos sobre grafeno, tanto del material expandido, utilizando TPACl 0.3M y HxTMABr 0.3M como electrolitos (sin un proceso de sonicación posterior) y lavando posteriormente para eliminar los restos de dichos electrolitos, como del material exfoliado (tras sonicación) y depositado sobre una esponja de melamina, tal y como se describe en el apartado 3.4.2.

Para realizar dicho estudio, se toma una cierta masa de polvo de material expandido (entre 10 y 15 mg) y se introduce en un vial de 1.5 mL. A continuación, se añaden pequeñas cantidades del aceite o disolvente orgánico en cuestión, unos 50 µL, de manera sucesiva hasta que el material queda saturado, observándose que el líquido sobresale del material. Determinándose en este punto la masa de aceite o disolvente orgánico absorbido por una cierta cantidad de material expandido, teniendo en cuenta el volumen absorbido y la densidad de cada aceite o disolvente. De la misma forma se procede con la esponja, sin ser necesaria su introducción en un vial.

Los aceites y disolventes orgánicos utilizados en este estudio fueron: tolueno, n-hexano, dodecano, tetrahidrofurano, acetona, cloroformo, aceite de oliva y aceite de bomba.

Además, se realizaron estudios de reusabilidad del grafeno depositado sobre sobre la esponja de melamina, en los que la esponja se presionaba manualmente para extraer el líquido absorbido y se volvía a reutilizar para un nuevo proceso de absorción, repitiendo este proceso hasta 10 veces.

4. Técnicas de Caracterización

4.1. Espectroscopías

La disciplina que se encarga del estudio del intercambio de energía producido por interacciones de la radiación electromagnética con la materia se denomina espectroscopía. Esta interacción es posible debido a que los estados energéticos de la materia se encuentran cuantizados, pudiendo solo absorberse o emitirse radiación con determinados valores de energía [1], tal y como se expresa en la ecuación de Plank-Einstein:

$$E_{superior} - E_{inferior} = \Delta E = h\upsilon \qquad (1)$$

siendo $E_{superior}$ la energía del estado más alto, $E_{inferior}$, la energía del estado más bajo, h la constante de Plank y υ la frecuencia de la radiación emitida o absorbida. Cada material posee frecuencias de radiación específicas, y por tanto, características de cada uno de ellos, siendo útil esta técnica para la obtención de información cualitativa. Por otro lado, se puede relacionar la absorción de radiación de un material a cualquier frecuencia dada con su concentración en un medio según la ley de Lambert-Beer [2]:

$$A = \varepsilon\, l\, c \qquad (2)$$

representando A la absorbancia a una determinada frecuencia o longitud de onda, ε el coeficiente de extinción molar a dicha longitud de onda, l la longitud de paso óptico y c la concentración. De esta forma, es posible cuantificar la concentración de un material a partir de la medida de la absorbancia, siempre y cuando la medida se realice dentro del rango lineal de aplicación de la ecuación.

4.1.1 Espectroscopía de absorción ultravioleta-visible (UV-Vis)

En esta tesis, se ha realizado caracterización por espectroscopía de absorción UV-Vis mediante un espectrofotómetro dispersivo de doble haz Hελios α (Thermo Spectronic). Tal y como se muestra en la Figura 9, el equipo funciona midiendo al mismo tiempo el haz que atraviesa la muestra de referencia (P_0) y el haz que atraviesa la muestra de interés (P), permitiendo calcular la absorbancia a través de la ecuación $A=-log\ (P/P_0)$. Para realizar las medidas de absorbancia, hay que diluir las dispersiones coloidales hasta alcanzar el rango lineal de la ecuación de Lambert-Beer.

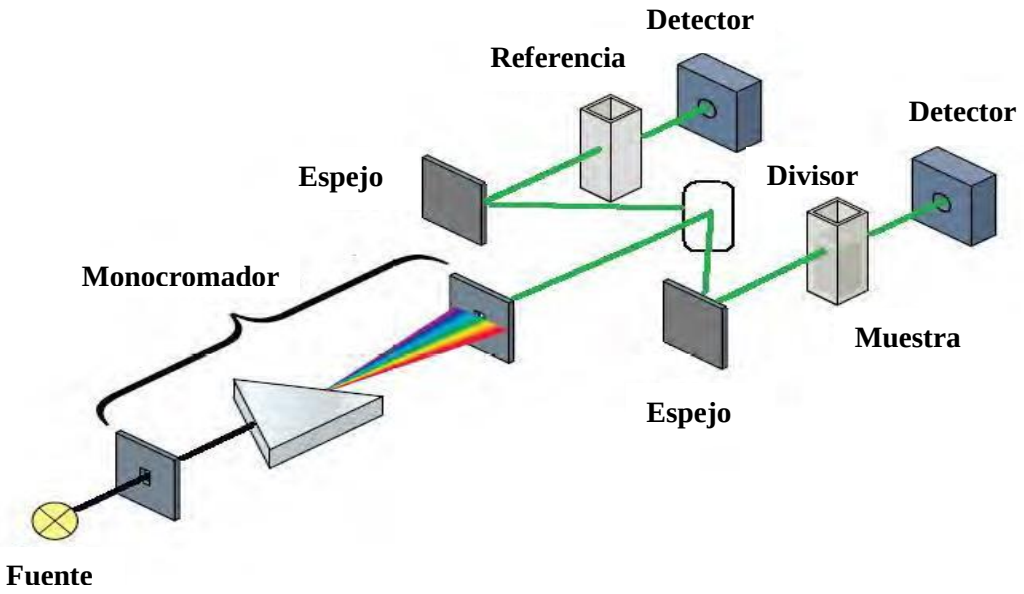

Figura 9. Esquema de funcionamiento de un espectrofotómetro UV-Vis de doble haz.

Con este tipo de equipos se suele medir la absorbancia de radiación en longitudes de onda entre 200 y 1100 nm, correspondiéndose a energías comprendidas entre ~1 y 6 eV. Estas energías comprenden transiciones electrónicas entre niveles energéticos próximos en energía, tales como los orbitales moleculares tipo π insaturados, pares de electrones no enlazantes u orbitales *d* y *f* [3].

Estos niveles energéticos electrónicos, a su vez, se combinan con diferentes estados vibracionales y rotacionales, habiendo por tanto, para cada salto energético, diferentes transiciones entre dichos estados. Esto se traduce en que los espectros de absorción obtenidos de las especies que poseen niveles vibracionales y rotacionales no

muestren longitudes de onda de absorción perfectamente definidas, sino bandas ensanchadas debido a las diferentes combinaciones de transiciones [4]. Además, debido a la interacción de los materiales con el medio, por ejemplo, con el disolvente en fase líquida, se producen modificaciones en los niveles energéticos, produciendo también un ensanchamiento en la señal obtenida [1,5]. Todo esto hace que la técnica tenga una resolución limitada, haciendo que por sí sola sea insuficiente para identificar unívocamente una sustancia. Es, sin embargo, una técnica ampliamente utilizada para detectar la presencia de ciertos grupos funcionales [6,7], complejos organometálicos [8,9] o nanoestructuras [10,11], teniendo en cuenta la forma y posición de las bandas del espectro de absorción. En esta tesis se han realizado los siguientes estudios cualitativos de materiales bidimensionales obtenidos en dispersión coloidal utilizando la espectroscopía UV-Vis:

- Observación del pico característico a 270 nm de las transiciones $\pi \rightarrow \pi^*$ para dispersiones de grafeno obtenidas por exfoliación electroquímica catódica (Figura 10a). Esta transición se produce a 270 nm cuando el material posee amplios dominios conjugados, es decir, cuando el grafeno tiene un bajo grado de oxidación.

- Determinación de la fase, 2H o 1T, tanto de dispersiones de MoS_2 exfoliado electroquímicamente, como de las de MoS_2 tratado con hidracina. Dado que estas dos fases implican diferentes coordinaciones de los átomos de azufre alrededor del molibdeno en la estructura (trigonal prismática en 2H (Figura 10b) y octaédrica en 1T (Figura 10c), se originan diferentes niveles energéticos para cada estructura, dando lugar a diferentes transiciones posibles y obteniéndose diferentes espectros.

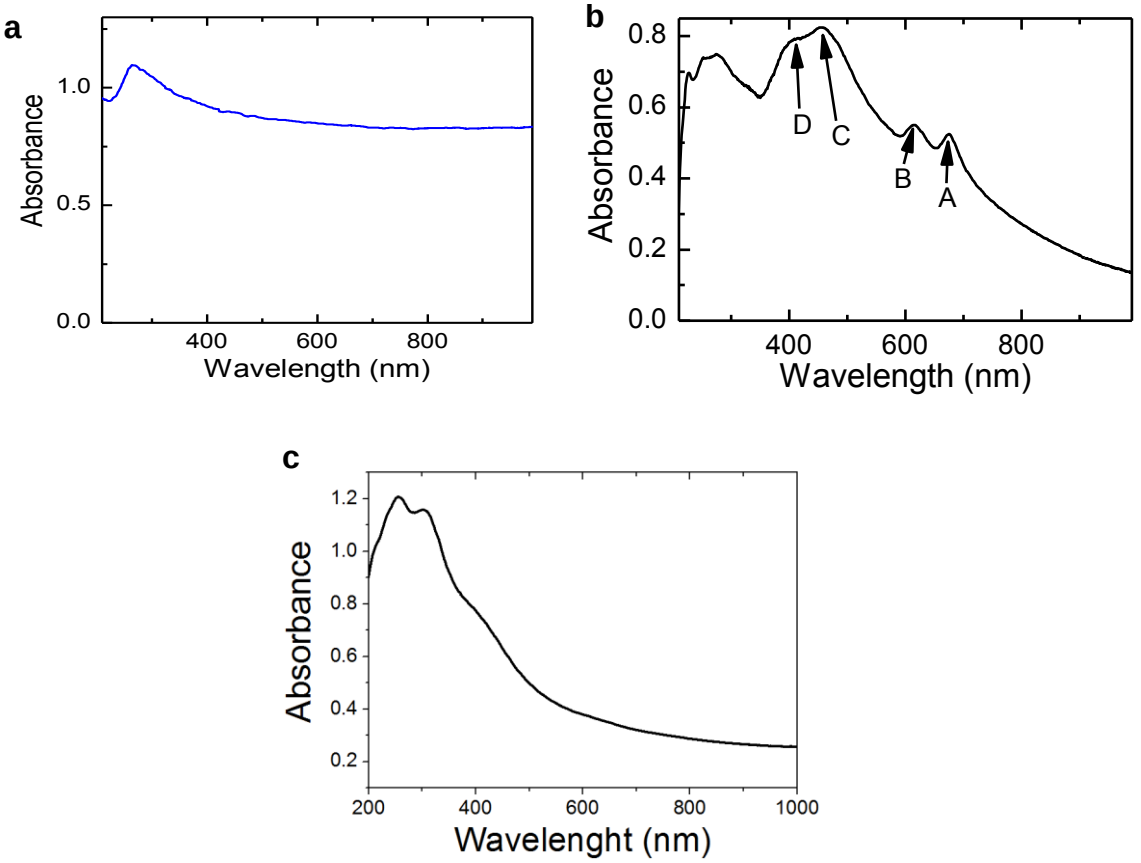

Figura 10: Espectros UV-Vis de una dispersión de grafeno en agua con Pluronic P-123 (**a**), de una dispersión de MoS_2 de fase 2H en IPA (**b**), en el que se identifican los picos característicos de la fase 2H (A, B, C y D), ambos obtenidos por exfoliación electroquímica catódica y de una dispersión de MoS_2 1T en agua (**c**).

Por otro lado, debido a su alta sensibilidad, esta técnica resulta muy apropiada para la cuantificación de especies adsorbentes, utilizándose, por tanto, para cuantificar:

- La concentración de grafeno y MoS_2 en dispersión coloidal obtenidos por exfoliación electroquímica, así como el MoS_2 tratado con hidracina. Dicha concentración puede ser calculada en base a la ecuación de Lambert-Beer y utilizando los coeficientes de extinción molar documentados en la literatura a diferentes longitudes de onda [12,13].

- Seguimiento de reacciones en las cuales alguno de los reactivos o productos tienen un espectro característico. En concreto, se siguió la reducción catalítica de de diferentes nitroarenos, específicamente 4-nitrofenol (4-NP), 4-nitroanilina (4-NA), 4-nitrobenceno

y 2-nitroanilina (2-NA), que poseen bandas características de absorción a ~400, ~380, ~270 y ~410 nm respectivamente. Dichas bandas son diferentes de las bandas de absorción características de las especies reducidas, permitiendo por tanto realizar un seguimiento cinético de la reacción [6], tal y como se ejemplifica en la Figura 11. Por el mismo método se realizó el seguimiento catalítico de la reducción de algunos colorantes orgánicos, como el naranja de metilo (MO, *methyl orange*) y azul de metileno (MB, *methylene blue*) y cuyas bandas de absorción características aparecen a ~460 y ~675 nm, respectivamente.

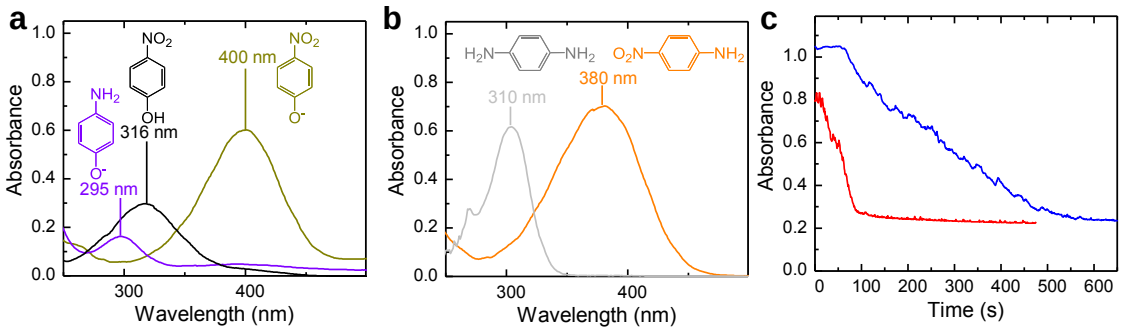

Figura 11: Espectros de absorción UV-Vis del **(a)** 4-NP (negro), ión 4-nitrofenóxido (verde) y su forma reducida, el ión 4-nitrofenóxido (violeta); **(b)** 4-NA (naranja) y su forma reducida, *p*-fenilendiamina (gris). **(c)** Perfiles cinéticos típicos para la reducción del 4-NP (azul) y 4-NA (rojo) con nanoláminas de MoS_2 catódicamente exfoliadas y estabilizadas con GMP.

4.1.2. Espectroscopía Raman

La espectroscopía Raman estudia las transiciones entre niveles vibracionales en la materia [1,5,14] al hacer incidir radiación de energía de la región del espectro visible sobre la muestra y midiendo la radiación dispersada inelásticamente. En este proceso, al no producirse transición energética electrónica debido a la relativa baja energía de la radiación electromagnética incidente, la mayoría de los fotones incidentes serán dispersados elásticamente (sin cambio en su frecuencia), constituyendo la dispersión Rayleigh (Figura 12). Por otro lado, una pequeña fracción de la radiación incidente experimenta dispersión inelástica, constituyendo la dispersión Raman, la cual puede

producir fotones de menor energía que la luz incidente (transición Stokes) o, si la población de estados excitados vibracionales es alta, puede dar lugar a fotones de mayor energía (anti-Stokes). Estas transiciones solo pueden ocurrir, y por tanto observarse, cuando el modo de vibración indicado produce un cambio en la polarizabilidad de la muestra.

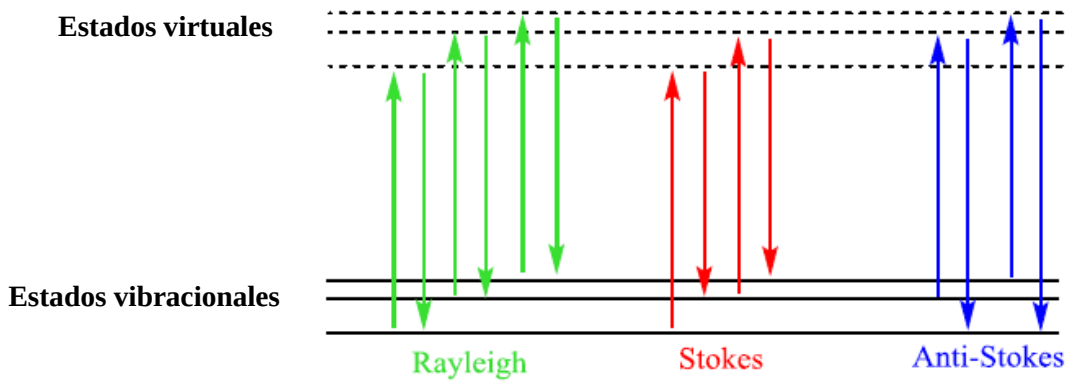

Figura 12: Transiciones entre niveles energéticos que dan lugar a los fenómenos Rayleigh, Stokes y anti-Stokes.

Esta técnica se usa habitualmente para caracterizar las propiedades de materiales carbonosos [15-19] y materiales bidimensionales como el grafeno [18,20], donde las bandas del espectro Raman corresponden a modos de vibración colectivos o fonones.

Las medidas de espectroscopía Raman en esta tesis fueron realizadas en un espectrómetro Horiba Jobin-Yvon LabRam con radiación incidente generada por una fuente láser de 532 nm y 2 mW de potencia para las muestras de grafeno, y 0.2-0.5 mW para las muestras de MoS_2. Se utilizaron muestras depositadas a partir de dispersiones coloidales mediante la evaporación del disolvente sobre discos de acero inoxidable calentados previamente a 50–60 ºC (para las muestras de grafeno) o sin calentar (para las muestras de MoS_2 tratadas con hidracina) y secados posteriormente a temperatura ambiente, o bien en forma de filmes preparados mediante filtración de las dispersiones (para las muestras de MoS_2 exfoliadas catódicamente).

En esta tesis, la espectroscopía Raman se ha utilizado para:

- Evaluar la calidad estructural de las láminas de grafeno midiendo la relación de intensidades integradas de las bandas denominadas G (característica de materiales grafito/grafeno) y D (asociada a defectos), las cuales aparecen en números de onda en torno a 1582 cm^{-1} y 1350 cm^{-1}, respectivamente. Se toma la relación entre las intensidades de ambas bandas (I_D/I_G) como medida del desorden estructural presente en el material [21-27].

- Identificar las bandas E^1_{2g} y A_{1g}, características de la fase 2H del MoS_2, que aparecen a ~383 y 408 cm^{-1} respectivamente, así como la ausencia de las bandas características de la fase 1T (~150, 200, 280 y 320 cm^{-1}) y de los óxidos de molibdeno (~285-295 cm^{-1}), indicando de esta forma la pureza de dicha fase.

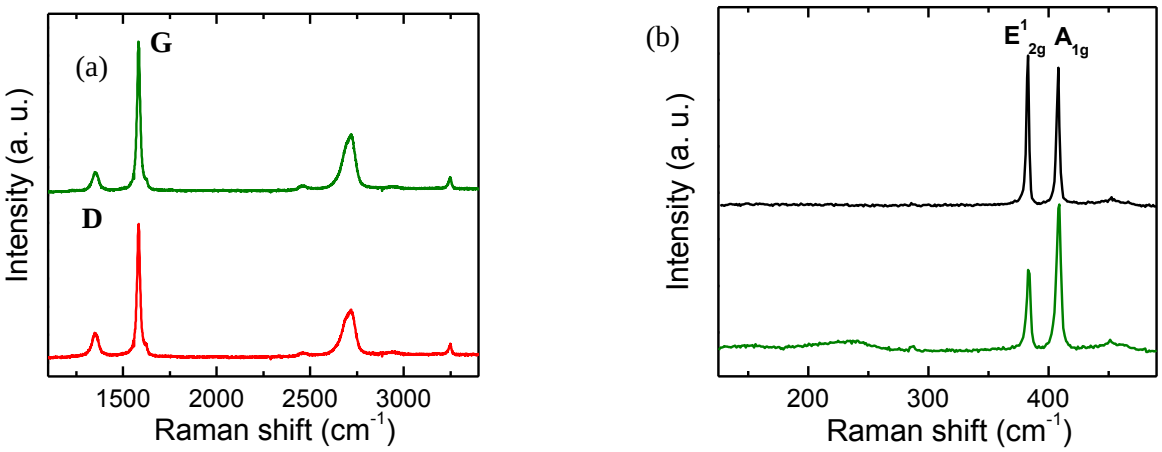

Figura 13: Espectros Raman de grafenos (**a**) preparados por exfoliación catódica con TPACl 0.3 M (verde) y HxTMABr 0.3 M (rojo) como electrolitos y del MoS_2 (**b**) de partida (negro) y exfoliado catódicamente con KCl 4 M (verde).

4.1.3. Espectroscopía fotoelectrónica de rayos X (XPS, *X-ray photoemission spectroscopy*)

La espectroscopía fotoelectrónica de rayos X (XPS), mide la energía necesaria para arrancar electrones desde niveles internos del átomo debido al efecto fotoeléctrico [1,5,28]. Este efecto se consigue cuando se irradia la muestra con fotones de energía superior a la suma de la energía de ligadura del electrón al átomo (*binding energy*, BE) y la función de trabajo del equipo (Φ, la energía necesaria para llevar el electrón al nivel de Fermi del vacío cercano a la muestra), transfiriéndose el resto de la energía al

electrón en forma de energía cinética (*kinetic energy*, KE). Todo ello puede ser expresado según la ecuación de Plank-Einstein:

$$\Delta E = h\nu = BE + \Phi + KE \qquad (3)$$

A partir de esta ecuación, se obtiene la energía de ligadura de un electrón de una capa interna a través de la medida de su energía cinética, al ser conocida la energía $h\nu$ de los fotones de rayos X que expulsan a dicho electrón. En el espectro XPS se representa la intensidad de la señal (número de electrones emitidos) en función de la energía de ligadura, pudiendo solo estudiarse aquellos electrones procedentes de átomos situados en las capas más superficiales de la muestra, es decir, aquellos que abandonan el material sin sufrir colisiones y, por tanto, sin perder energía cinética. Los generados a mayores profundidades pierden energía al sufrir colisiones inelásticas y pasan a formar parte del *background* o incluso pueden ser reabsorbidos por la muestra. Esto implica que los espectros de XPS solamente proporcionan información de la superficie de la muestra, con un espesor de análisis de unos pocos nanómetros. Además, esta técnica también es útil para obtener información acerca de los estados de oxidación y los enlaces entre átomos a partir de la forma detallada del espectro correspondiente a cada elemento, puesto que la energía de ligadura de los electrones internos se ve afectada por el entorno químico de los átomos.

Para esta tesis, se ha utilizado un espectrómetro XPS de la casa SPECS que utiliza fuentes de rayos X tanto Al Kα monocromática como Mg Kα no monocromática. El equipo se opera a presiones inferiores a 10^{-7} Pa durante las medidas, y las muestras analizadas fueron preparadas de la misma manera que las utilizadas para análisis por espectroscopía Raman. En esta tesis se ha empleado XPS para:

- Estudiar el contenido en oxígeno de los grafenos preparados mediante exfoliación catódica, para determinar el grado de oxidación de éstos, así como el contenido en nitrógeno, para determinar la presencia de electrolito de amonio cuaternario adsorbido durante el proceso de exfoliación electroquímica (Figura 14a).

- Determinar la presencia de las fases 2H y 1T del MoS_2 exfoliado catódicamente, así como del tratado con hidracina (Figura 14b y 14c), pudiendo estimarse la presencia y proporción de ambas mediante el análisis del espectro de alta resolución del Mo 3d [29].

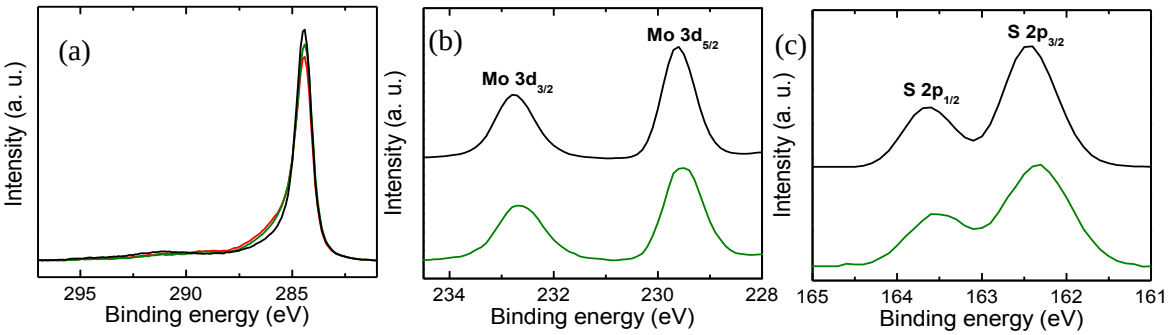

Figura 14: Espectro de alta resolución de XPS de C 1s para el grafeno obtenido catódicamente con HTMABr 0.3 M (rojo) y TPACl 0.3 M (verde) **(a)** y de Mo 3d **(b)** y S 2p **(c)** del MoS_2 de partida (negro) y MoS_2 exfoliado catódicamente con KCl 4 M (verde)

4.1.4. Resonancia paramagnética electrónica (EPR, *electron paramagnetic resonance*)

La resonancia paramagnética electrónica (EPR, *electron paramagnetic resonance*) es una técnica espectroscópica basada en la detección de la absorción de radiación en el rango de microondas, que puede ser producida cuando se aplica un intenso campo magnético externo a una sustancia o material que contenga radicales o electrones desapareados. A diferencia de la resonancia magnética nuclear (NMR, *nuclear magnetic resonance*), ésta no se basa en el carácter magnético de los núcleos atómicos, sino en el de los electrones no apareados.

Mientras que en NMR se pueden producir diferentes desdoblamientos en la señal debido a los diferentes valores que pueda mostrar el spín nuclear, en EPR, al tratarse de spin electrónico, solo se tiene el número cuántico de spín (½) y solo puede haber, por tanto, un desdoblamiento en dos niveles energéticos en presencia de un campo magnético.

Asimismo, mientras que en NMR se mide directamente un campo magnético, en EPR se aplica un gradiente magnético y se mide la primera derivada del campo magnético.

Los resultados obtenidos por esta técnica aportan información sobre el número y tipo de radicales o electrones desapareados de la muestra analizada.

En esta tesis, se ha utilizado un espectómetro Bruker EMX equipado con un puente de microondas de banda X (frecuencia ~9 GHz) EMX premium X. Los espectros se tomaron con una amplitud de modulación del campo magnético de 1.86 G, una frecuencia de modulación de 100 kHz y una potencia de microondas de ~20 mW. El tratamiento de los datos de EPR se llevó a cabo con el software Bruker WinEPR Processing.

Se ha utilizado el EPR para determinar la presencia de vacantes de azufre en MoS_2 tratado con hidracina. Esto es posible debido a que el molibdeno no enlazado a azufre en MoS_2 presenta electrones desapareados, dando lugar a una señal a un campo magnético de ~3500 G, siendo en principio más pronunciada dicha señal cuanto mayor sea el número de átomos de molibdeno no enlazados, y por tanto cuanto mayor sea el número de vacantes de azufre en la red del MoS_2 [30,31]. Puede observarse dicho efecto en la Figura 15.

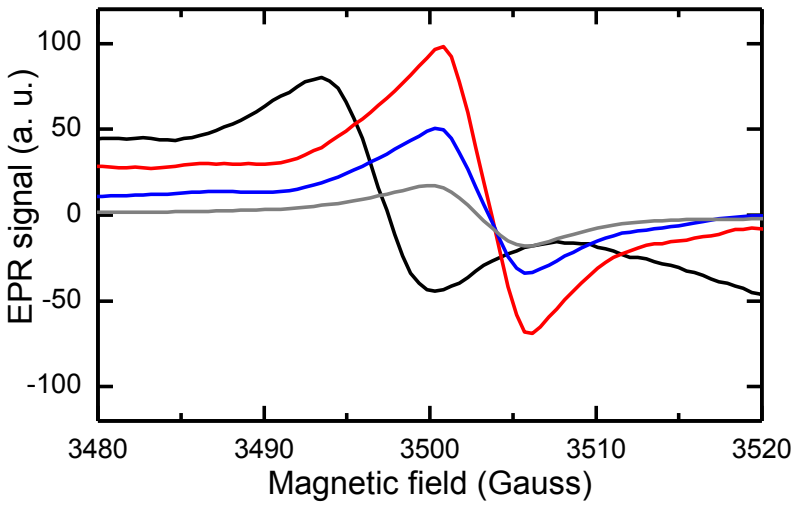

Figura 15: Espectro EPR del MoS_2 2D inicial (negro), MoS_2 4% hidracina (rojo), MoS_2 10% hidracina (azul) y MoS_2 sin exfoliar (gris).

4.2. Microscopías

4.2.1. Microscopía electrónica de transmisión (TEM, *transmission electron microscopy*)

Debido a que la microscopía óptica presenta limitaciones significativas en términos de resolución (resolución del orden de la longitud de onda de la luz visible, ~400 nm), se hace necesario disponer de una técnica con un mayor poder de resolución para el estudio de materiales nanoestructurados. Esto se puede conseguir sustituyendo los fotones por electrones como elementos sonda que interaccionan con la materia, ya que los electrones pueden comportarse de manera similar a los fotones cuando son emitidos por un filamento y acelerados por un campo electromagnético (a voltajes de 100-1000 kV), constituyendo así la base de la microscopía electrónica [1]. Los electrones pueden ser transmitidos a través de láminas delgadas (espesor menor de 200 nm) de igual forma que ocurre con los fotones en microscopía óptica, lo cual permite obtener imágenes con mucha mayor resolución que dicha técnica. En la Figura 16 se representa, de manera esquemática, los componentes de un equipo de microscopía electrónica de transmisión (*transmission electron microscopy*, TEM). En la parte superior se encuentra la fuente de electrones, que son enfocados sobre la muestra mediante el uso de lentes electromagnéticas. Tras atravesar la muestra, los electrones transmitidos pasan por otro juego de lentes que los dirigen al detector, donde se registran. El equipo utilizado en las medidas para esta tesis es un microscopio de alta resolución (HR-TEM, *High resolution transmission electron microscopy*) JEM-2100F system (JEOL) con un voltaje de 200 kV y condiciones criogénicas (-180 ºC) para evitar el daño causado por el bombardeo de electrones de alta energía sobre la muestra. Para realizar las medidas, las muestras se preparan depositando 40 µL de dispersión coloidal del material a estudiar, en este caso en IPA, sobre rejillas de cobre recubiertas de un filme delgado de carbono (Electron Microscopy Sciences), dejando evaporar el disolvente a temperatura ambiente.

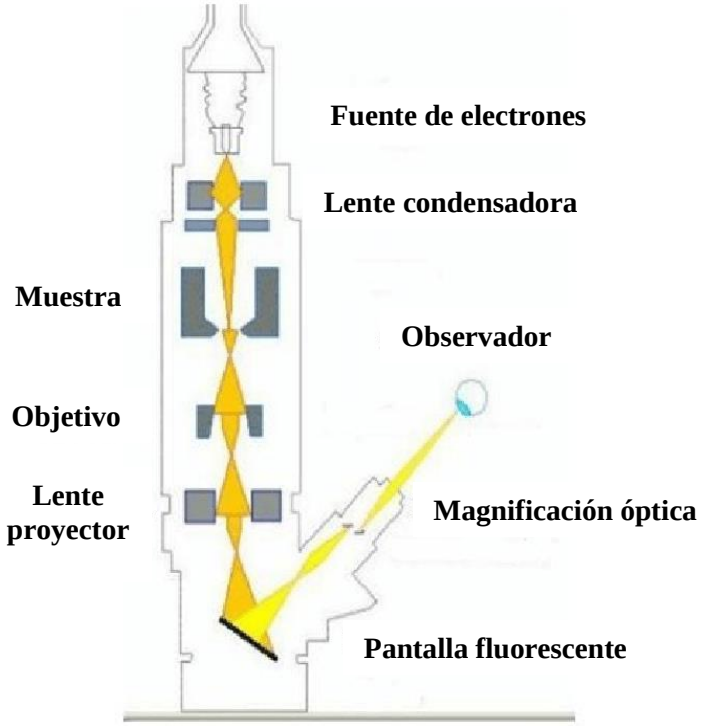

Figura 16: Esquema de un microscopio electrónico de transmisión

En esta tesis se han realizado análisis mediante TEM de las láminas de MoS_2 obtenidas por exfoliación catódica y las tratadas con hidracina. Las imágenes obtenidas para ambas muestras permiten observar la morfología de las láminas, así como la presencia y distribución de defectos estructurales. Algunos ejemplos de las muestras tratadas con hidracina pueden verse en la Figura 17.

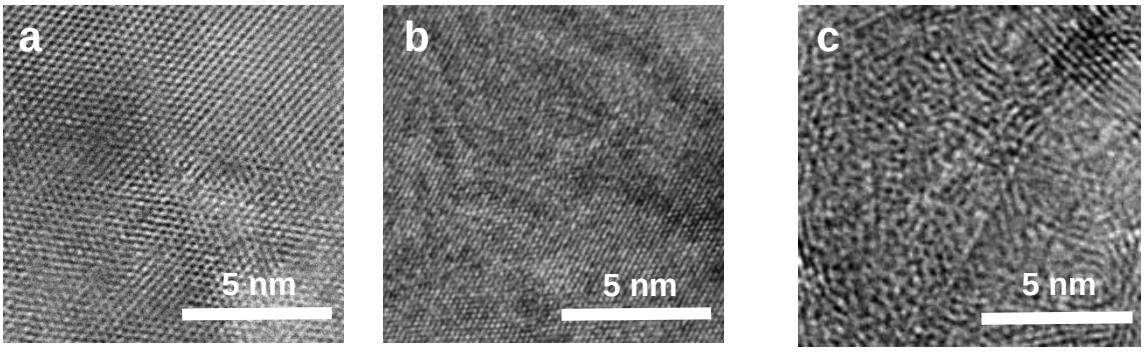

Figura 17: Imágenes de HR-TEM del MoS_2 exfoliado (a), del tratado con un 4 % de hidracina (b) y del tratado con un 10 % de hidracina (c).

4.2.2. Microscopía electrónica de barrido (SEM, *scanning electron microscopy*)

Al igual que un microscopio TEM, un equipo de microscopía electrónica de barrido (SEM, *scanning electron microscopy*) utiliza una fuente de electrones (acelerados en este caso por voltajes menores, de ~40 kV) que son concentrados mediante lentes electromagnéticas sobre la muestra [1,32]. Los detectores recogen diferentes señales, sean electrones o fotones, y construyen la imagen de la superficie de la muestra punto por punto. Debido a su capacidad para enfocar superficies de tamaños muy diferentes (desde pocas decenas de nm a varios mm), esta técnica es tremendamente útil para estudiar la morfología de materiales a distintas escalas. Los electrones que inciden sobre la muestra pueden:

- Experimentar choques elásticos, es decir, "rebotar" en la superficie de la muestra sin perder energía. Estos son los llamados electrones retrodispersados.
- Interaccionar con los electrones de la banda de conducción de la muestra, produciendo su expulsión (electrones secundarios). Estos electrones secundarios tienen mucha menor energía que los retrodispersados, siendo por tanto solo detectables los que proceden de la superficie, permitiendo obtener imágenes de la superficie de sólidos.
- Excitar electrones de capas internas de los átomos de la muestra, que se relajan mediante su vuelta a los niveles internos produciendo la emisión de fotones de rayos X. Éstos, al sufrir menos interacciones con la materia que los electrones, salen de la muestra sin ser alterados desde profundidades mayores.

Cuando el equipo SEM incorpora un detector de electrones situado bajo la muestra, es decir, del otro lado de la fuente de electrones, y la muestra es suficientemente delgada como para permitir la transmisión de electrones (como en el caso de láminas de materiales bidimensionales), es posible registrar imágenes de microscopía electrónica de barrido por transmisión (STEM, *scanning tranmission electron microscopy*,) con muy alta resolución [33]. Este estudio ha sido posible con el microscopio SEM del que se disponía y para las nanoláminas obtenidas en esta tesis.

Para tomar las imágenes de SEM de esta tesis se ha utilizado un microscopio Quanta FEG 650 (FEI Company), operado a 25 kV y utilizando la señal de electrones

secundarios. Los materiales sólidos utilizados, tanto grafito como MoS_2, no requieren ninguna preparación especial para su estudio por STEM. Las muestras de dispersiones coloidales se prepararon de la misma manera que aquellas medidas en TEM, salvo las de grafeno, en cuyo caso se depositaron 150 µL de una dispersión del material en una mezcla agua-IPA en proporción 2:1.

Se ha estudiado por SEM la morfología de:

- Diferentes tipos de grafito (HOPG y grafito flexible) (Figura 18a), así como las piezas de MoS_2 utilizadas como material de partida en la exfoliación catódica.
- Los mismos materiales después del tratamiento electroquímico, es decir, expandidos (Figura 18b).

También se ha estudiado por STEM la morfología de:

- Ambos materiales obtenidos en dispersión coloidal a partir de los materiales anteriores, tras un proceso de sonicación (Figura 18c).
- Láminas MoS_2 en dispersión, tras un proceso de sonicación partiendo del polvo comercial.
- Láminas anteriores tras ser tratadas con hidracina (Figura 18d).

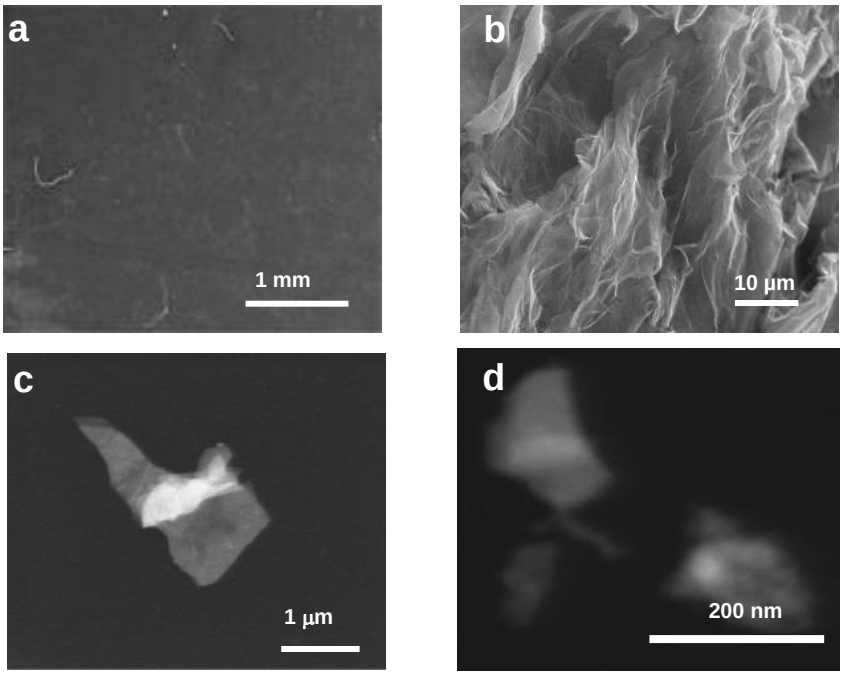

Figura 18: Imágenes de SEM de grafito flexible antes (**a**) y después del tratamiento electroquímico (**b**), imágenes de STEM de láminas de grafeno obtenidas tras sonicar el grafito expandido catódicamente (**c**) y láminas de MoS_2 tratadas con hidracina (**d**).

4.2.3. Microscopía de fuerza atómica (AFM, *atomic force microscopy*)

Se denominan microscopías de proximidad a aquellas técnicas microscópicas que permiten obtener imágenes de una superficie al medir las interacciones que resultan de acercar una punta afilada (sonda) a la muestra a distancias de nanómetros o angstroms. En el caso de la microscopía de fuerza atómica (AFM, *atomic force microscopy*), se detecta la fuerza que experimenta una punta al interactuar con la superficie de la muestra en función de la distancia que las separa, tal y como se representa en la Figura 19a [1]. La punta se encuentra situada de manera perpendicular al final de una palanca flexible (*cantilever*), pudiendo oscilar verticalmente. Sobre el cantilever se hace incidir un haz láser que se refleja sobre un fotodetector dividido en 4 secciones, de manera que el movimiento de flexión del *cantilever* en cualquier dirección como consecuencia de la interacción de la punta con la superficie de la muestra queda registrado y puede ser representado en un mapa topográfico al hacer barridos sobre la superficie de una muestra (Figura 19b).

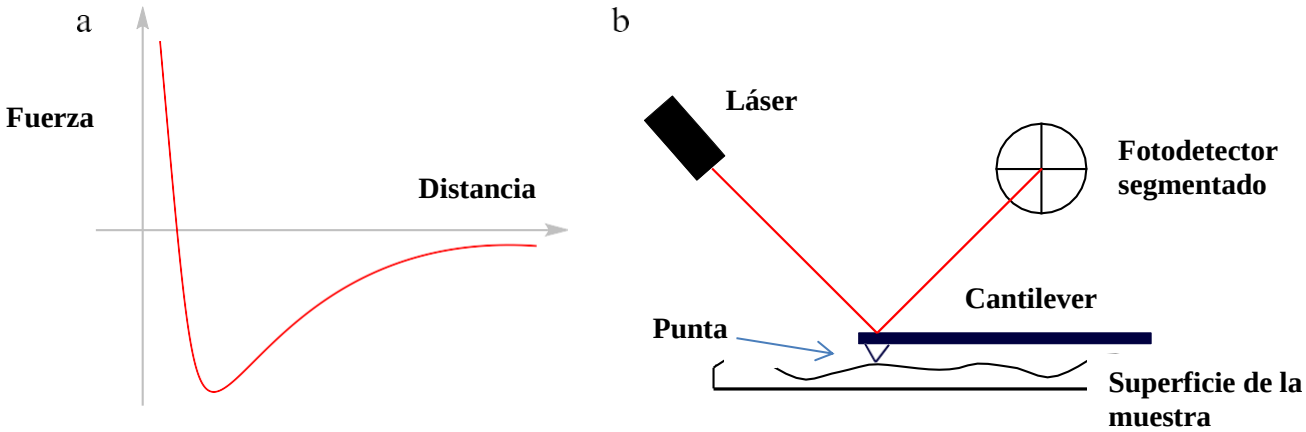

Figura 19: (a) Perfil típico de la interacción punta-muestra en función de la distancia de separación entre ambas. **(b)** Esquema de operación de un microscopio AFM.

Esta técnica se utiliza para el estudio de superficies de materiales y, debido a que la interacción de fuerzas puede darse con cualquier sólido, es aplicable a cualquier muestra con una superficie relativamente plana [34-37]. La interacción punta-muestra medida en AFM puede ser repulsiva, cuando la distancia es extremadamente pequeña, o atractiva, cuando la distancia es mayor. Por ello, en esta técnica se puede trabajar en modo de contacto, donde la interacción punta-muestra es repulsiva, o en modo de contacto intermitente (*tapping*) [38], donde el contacto es mucho menos agresivo con la superficie de la muestra al hacer oscilar periódicamente al *cantilever* (y, por tanto, a la punta con él) de manera vertical sobre la superficie de la muestra. El AFM es muy útil para estudiar materiales bidimensionales depositados sobre sustratos planos, como grafeno sobre HOPG [39]. En el modo *tapping*, se aplica un voltaje a un elemento piezoeléctrico situado en el extremo del cantilever que lo hace oscilar con una amplitud de ~100-200 nm. Cuando la distancia entre la punta y la superficie de la muestra es inferior a esta oscilación, se produce una reducción de la amplitud de ésta. Si mantenemos la amplitud de oscilación constante y registramos los cambios en la posición vertical del *cantilever* sobre la muestra necesarios para mantener constante dicha amplitud de oscilación, esta variante permite generar mapas topográficos de la superficie de la muestra mediante barridos lineales.

A diferencia de las microscopías TEM y SEM, la microscopía AFM posee un gran poder de resolución en la dirección perpendicular a la superficie de la muestra, lo que permite determinar el espesor de láminas 2D de grosor atómico, además de su morfología y tamaño lateral [39].

En esta tesis se ha utilizado un microscopio Nanoscope IIIa Multimode de Veeco Instruments, utilizando *cantilevers* de silicio de constante de fuerza ~40 N m^{-1} y frecuencia de resonancia ~250–300 kHz (Bruker Corporation). Para la preparación de muestras, se depositaron pequeños volúmenes (10 µL) de una dispersión acuosa diluida (~0.05 $mg{\cdot}mL^{-1}$) del material sobre un sustrato de HOPG, mica o silicio recubierto de SiO_2 (300 nm de espesor) precalentado a 50-60 ºC.

En esta tesis se ha utilizado el AFM para obtener imágenes de láminas de materiales bidimensionales (grafeno y MoS_2) depositadas a partir de una dispersión coloidal, para de esta manera determinar su grosor, número de capas y dimensiones laterales, como se aprecia en la Figura 20.

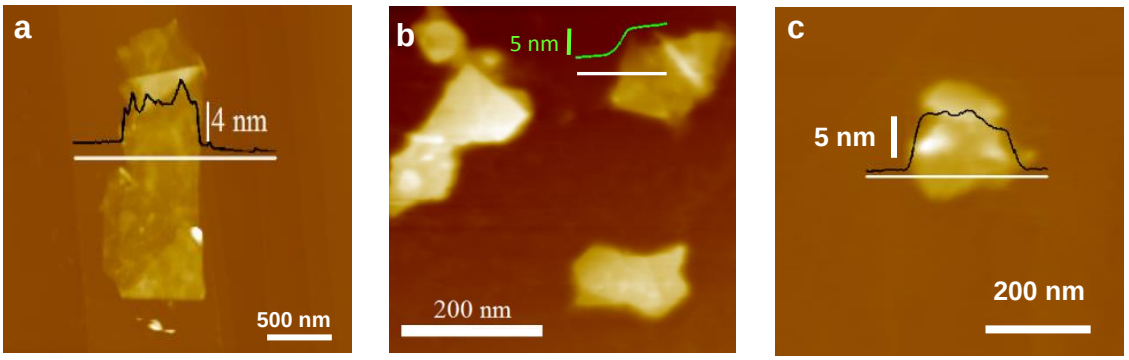

Figura 20: Imágenes de AFM de grafeno obtenido catódicamente sobre HOPG (**a**), MoS_2 obtenido catódicamente sobre mica (**b**) y MoS_2 tratado con hidracina sobre SiO_2/Si (**c**).

4.3. Técnicas electroquímicas

4.3.1. Espectroscopía de impedancia electroquímica (EIS, *electrochemical impedance spectroscopy*)

En la espectroscopía de impedancia electroquímica (EIS, *electrochemical impedance spectroscopy*) se somete una muestra en el interior de una celda a un potencial que varía sinusoidalmente en un rango de frecuencias, registrándose la corriente que circula por dicha celda y calculando el cociente entre el potencial aplicado V y la corriente I que circula ($Z = V/I$) [40,41]. Como el valor de la impedancia depende da la frecuencia de la onda sinusoidal, se puede obtener diferente información en función de la región de la frecuencia estudiada de los procesos de transferencia de carga y masa que puedan tener lugar en el electrodo. En esta tesis se usó la EIS para caracterizar los procesos que tienen lugar en los dispositivos de almacenamiento de energía de manera complementaria a las otras técnicas electroquímicas que se comentarán posteriormente. Se utilizó un potenciostato VSP, de Bio-Logic Science Instruments, y celdas preparadas en configuración de dos electrodos simétricos y asimétricos, así como de tres electrodos. Para la configuración de tres electrodos, se usaron electrodos de trabajo con el material activo, contraelectrodos de pasta de carbón activado y electrodos de referencia de Hg/HgO en medio básico (KOH 6 M). Los materiales utilizados como electrodos de trabajo se utilizaron en estado sólido (polvo)

presionados contra grafito flexible a 1 t durante 10 s. En la Figura 21 se representan espectros típicos de EIS de muestras de MoS_2.

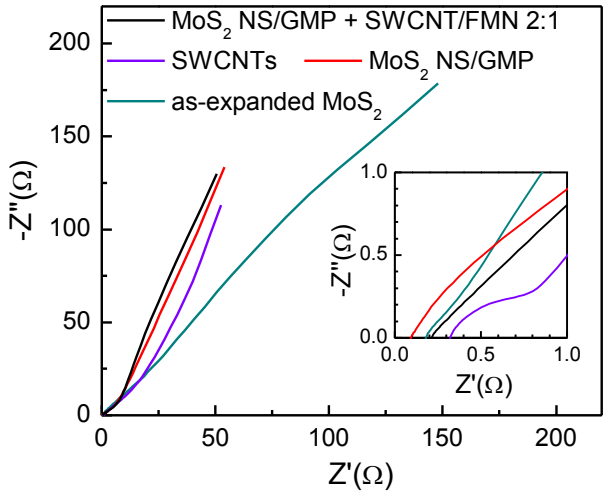

Figura 21: Estudios de EIS para diferentes muestras de MoS_2 obtenido por exfoliación catódica. En **negro**: híbrido de nanoláminas de MoS2 estabilizado en GMP con SWCNTs estabilizados en FMN en proporción 2:1, en azul: SWCNTs por separado, en rojo: nanoláminas de MoS2 por separado y en verde: MoS2 expandido.

4.3.2. Voltamperometría

La voltamperometría consiste en medir la intensidad de corriente (I) que se genera al aplicar un potencial (V), que varía de manera constante con el tiempo entre dos valores fijos n entre un electrodo de trabajo y un contraelectrodo sumergidos en una disolución con un electrolito. Al representarse I en función de V, se obtiene lo que se denomina voltamperograma [40,41]. La voltamperometría puede ser lineal, si se realiza un proceso de barrido en sentido creciente o decreciente de potencial, o cíclica, si se realizan ciclos de barrido en ambos sentidos, permitiendo explorar la evolución de las curvas con el tiempo debido a procesos que pueden ocurrir por acción del potencial aplicado. Esta técnica constituye la base del análisis electroquímico, ya que permite, entre otras cosas, estudiar procesos rédox, adsorción sobre superficies, intercalación de iones, procesos catalíticos, cinéticas de reacción y almacenamiento de energía [40,41], siendo además muy versátil debido a la facilidad con la que se pueden modificar sus parámetros.

Las medidas de voltamperometría cíclica se realizaron en el mismo equipo que el usado para las medidas de impedancia.

En esta tesis la voltamperometría se utilizó para caracterizar la respuesta electroquímica y la capacidad de almacenamiento de energía de materiales de grafeno y MoS_2 obtenidos catódicamente, así como sus híbridos con óxido de cobalto y SWCNTs, respectivamente, tal y como se ilustra en la Figura 22.

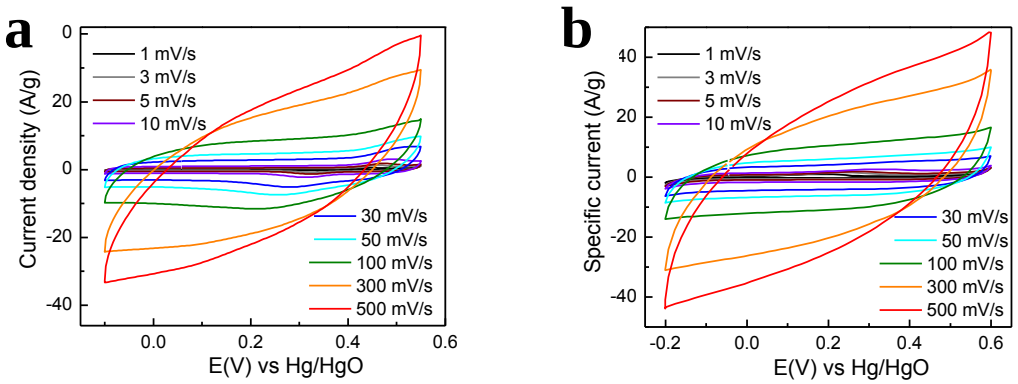

Figura 22: Voltamperometrías cíclicas de grafeno catódico con óxido de cobalto (**a**) y de MoS_2-SWCNTs a una relación 2:1 en masa (**b**).

4.3.3. Carga-descarga galvanostática

Al contrario que en la voltamperometría, una curva de carga-descarga galvanostática se obtiene al aplicar al electrodo de trabajo una intensidad de corriente constante (habitualmente entre 0.1 y 20 A g^{-1}), midiendo el voltaje de la celda en función del tiempo. Durante este proceso tienen lugar procesos de adsorción del electrolito y/o rédox que implican el almacenamiento de carga eléctrica en el material (procesos denominados capacitivos y pseudocapacitivos, respectivamente), los cuales dependen de las características químicas, morfológicas y superficiales del electrodo [40,41]. El análisis de estas curvas de carga y descarga permite caracterizar el tipo de procesos que tienen lugar en el electrodo, así como evaluar su capacitancia bajo diferentes condiciones.

Estos experimentos fueron llevados a cabo utilizando el mismo potenciostato y las mismas condiciones que las usadas para las voltamperometrías cíclicas, siendo útiles para determinar la capacitancia de los materiales preparados en esta tesis (grafeno y MoS_2), así como sus híbridos (Figura 23).

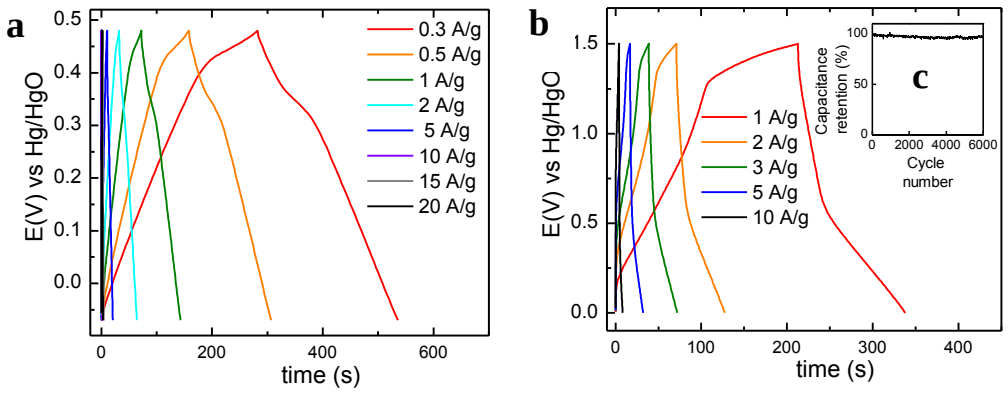

Figura 23: Carga/descarga galvanostática del híbrido de grafeno-óxido de cobalto (**a**) y de la mezcla MoS_2-SWCNTs a una relación 2:1 en masa (**b**). Estudio de la variación de la capacitancia con el número de ciclos (**c**).

4.4. Medida de conductividad eléctrica de filmes

Se define la conductividad eléctrica de un material como la facilidad que tiene este para dejar fluir la corriente eléctrica a través de él cuando está sometido a un potencial eléctrico externo. Es, por tanto, dependiente de su composición y morfología. De entre todos los métodos existentes para medir la conductividad de materiales, en esta tesis se ha utilizado el de van der Pauw, ya que es de gran utilidad para medidas precisas de muestras altamente conductoras, puesto que su diseño minimiza la influencia de la resistencia de los puntos de contacto del equipo con la muestra [42]. Con este método, se ha determinado la conductividad eléctrica de filmes de grafeno obtenidos catódicamente (12×12 mm^2, con espesores del orden de micras), utilizando como fuente de corriente continua un equipo Agilent 6614C y un multímetro Fluke 45 para medir voltajes, tal y como se describe en la Figura 24.

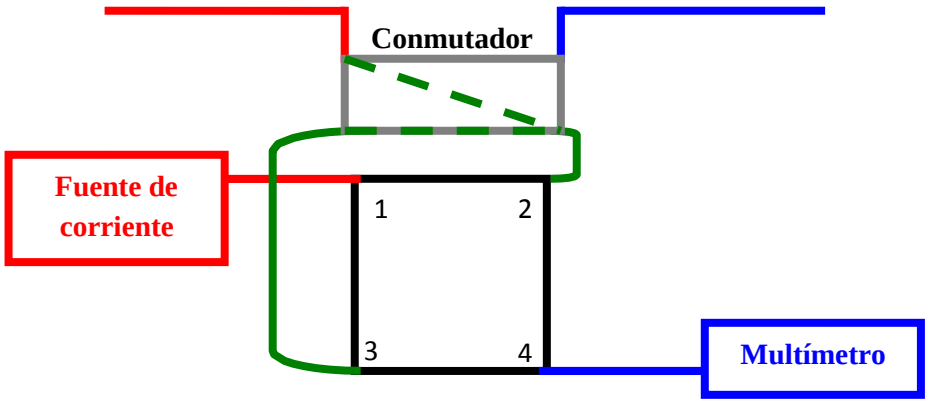

Figura 24: Esquema para la medida de la conductividad eléctrica de filmes mediante el método de Van der Pauw.

Utilizando la configuración representada en la Figura 24, se aplica una corriente entre los puntos 1 y 2 y se mide el voltaje inducido (por el efecto Hall) entre los puntos 3 y 4. A continuación, se aplica corriente entre los puntos 1 y 3, y se mide el voltaje entre 2 y 4. De esta forma, se obtienen los valores $R_A=V_{43}/I_{12}$ y $R_B=V_{42}/I_{13}$, y se puede obtener la resistencia del material (Rs) según la siguiente ecuación:

$$e^{-\pi \cdot R_A/Rs} + e^{-\pi \cdot R_B/Rs} = 1 \qquad (4)$$

Calculada la resistencia y conocidas la longitud (L) y el área de la sección (A) del filme es posible calcular la conductividad σ según la siguiente ecuación:

$$\sigma = L/(Rs \cdot A) \qquad (5)$$

Bibliografía

[1] Faraldos, M.; Goberna C. Técnicas de análisis y caracterización de materiales. Madrid: Consejo Superior de Investigaciones Científicas, 2011.

[2] Beer, A. Determination of the absorption of red light in colored liquids, Annalen der Physik und Chemie, 1852, 86, 78–88.

[3] Jentoft, F. C. Characterization of solid materials and heterogeneous catalysts: from structure to surface reactivity. Wiley-VCH, 2012, Volume 1.

[4] Pino, F.; Pérez, M. D., Análisis de elementos-traza por espectrofotometría de absorción molecular ultravioleta-visible. Universidad de Sevilla. 1983.

[5] Skoog, D. A.; Holler, F. J.; Nieman, T. A. Principles of instrumental analysis. Belmont (USA): Thomson Brooks/cole. 2007.

[6] Hervés, P.; Pérez-Lorenzo, M.; Liz-Marzán, L.M.; Dzubiella, J.; Lu, Y.; Ballauff, M. Catalysis by metallic nanoparticles in aqueous solution: Model reactions. Chem. Soc. Rev., 2012, 41, 5577-5587.

[7] Preat, J.; Michaux, C.; Jacquemin, D.; Perpèt, E. A. Enhanced efficiency of organic dye- sensitized solar cells: triphenylamine derivatives. J. Phys. Chem. C, 2009, 113, 16821-16833.

[8] Liu, M.; Wang, L.; Meng, Y.; Chen, Q.; Li, H.; Zhang, Y.; Yao, S. (4-Ferrocenylethyne) phenylamine functionalized graphene oxide modified electrode for sensitive nitrite sensing. Electrochim. Acta, 2014, 116, 504-51.

[9] Deka, M. J.; Chowdhury, D. Tuning electrical properties of graphene with different π- stacking organic molecules. J. Phys. Chem. C, 2016, 120, 4121-4129.

[10] Panáček, A.; Kvítek, L.; Prucek, R.; Kolář, M.; Večeřová, R.; Pizúrová, N.; Sharma, V. K.; Nevěčná, T.; Zbořil, R. Silver colloid nanoparticles: synthesis, characterization, and their antibacterial activity. J. Phys. Chem. B, 2006, 110, 16248-16253.

[11] Haiss, W.; Thanh, N. T. K.; Aveyard, J.; Fernig, D. G. Determination of size and concentration of gold nanoparticles from UV−Vis spectra. Anal. Chem., 2007, 79, 4215-4221.

[12] Hernandez, Y.; Nicolosi, V.; Lotya, M.; Blighe, F. M.; Sun, Z.; De, S.; McGovern, I. T.; Holland, B.; Byrne, M.; Gun'ko, Y. K.; Boland, J. J.; Niraj, P.; Duesberg, G.; Krishnamurthy, S.; Goodhue, R.; Hutchison, J.; Scardaci, V.; Ferrari, A. C.; Coleman, J. N.; High-yield production of graphene by liquid-phase exfoliation of graphite. Nat. Nanotechnol., 2008, 3, 563- 568.

[13] Ayán–Varela, M.; Paredes, J. I.; Guardia, L.; Villar–Rodil, S.; Munuera, J. M.; Díaz– González, M.; Fernández–Sánchez, C.; Martínez–Alonso, A.; Tascón, J. M. D. Achieving extremely concentrated aqueous dispersions of graphene flakes and catalytically efficient graphene-metal nanoparticle hybrids with flavin mononucleotide as a high-performance stabilizer. ACS Appl. Mater. Interfaces, 2015, 7, 10293–10307.

[14] Smith, E; Dent, G. Modern Raman spectroscopy: a practical approach. John Wiley & Sons, 2005.

[15] Ferrari, A. C.; Robertson J. Interpretation of Raman spectra of disordered and amorphous carbon. Phys. Rev. B, 2000, 61, 14095.

[16] Kataura, H.; Maniwa, Y.; Kodama, T.; Kikuchi, K.; Hirahara, K.; Suenaga, K.; Iijima, S.; Suzuki, S.; Achiba, Y.; Krätschmer, W. High-yield fullerene encapsulation in single-wall carbon nanotubes. Synth. Met., 2001, 121, 1195-1196.

[17] Dresselhaus, M. S.; Dresselhaus, G.; Saito, R.; Jorio, A. Raman spectroscopy of carbon nanotubes. Phys. Rep., 2005, 409, 47-99.

[18] Ferrari, A.C. Raman spectroscopy of graphene and graphite: Disorder, electron-phonon coupling, doping and nonadiabatic effects. Solid State Commun., 2007, 143, 47-57.

[19] Knight, D.S.; White, W.B. Characterization of diamond films by Raman spectroscopy. J. Mater. Res., 1989, 4, 385-393.

[20] Ferrari A. C.; Meyer, J. C.; Scardaci, V.; Casiraghi, C.; Lazzeri, M.; Mauri, F.; Piscanec, S.; Jiang, D.; Novoselov, K. S.; Roth, S.; Geim A. K. Raman spectrum of graphene and graphene layers. Phys Rev Lett., 2006, 97, 187401.

[21] Paton, K. R.; Varrla, E.; Backes, C.; Smith, R. J.; Khan, U.; O'Neil, A.; Boland, C.; Lotya, M.; Istrate, O. M.; King, P.; Higgins, T.; Barwich, S.; May, P.; Puczkarski, P.; Ahmed, I.; Moebius, M.; Pettersson, H.; Long, E.; Coelho, J.; O'Brien, S. E.; McGuire, E. K.; Mendoza Sanchez, B.; Duesberg, G. S.; McEvoy, N.; Pennycook, T. J.; Downing, C.; Crossley, A.; Nicolosi, V.; Coleman, J. N. Scalable production of large quantities of defect-free few-layer graphene by shear exfoliation in liquids. Nature Mater., 2014, 13, 624-630.

[22] Guardia, L.; Fernández-Merino, M. J.; Paredes, J. I.; Solís-Fernández, P.; Villar-Rodil, S.; Martínez-Alonso, A.; Tascón, J. M. D. High-throughput production of pristine graphene in an aqueous dispersion assisted by non-ionic surfactants. Carbon, 2011, 49, 1653-1662.

[23] Sun, Z.; Masa, J.; Liu, Z.; Schuhmann, W.; Muhler, M. Highly concentrated aqueous dispersions of graphene exfoliated by sodium taurodeoxycholate: dispersion behavior and potential application as a catalyst support for the oxygen-reduction reaction. Chem. Eur. J. 2012, 18, 6972-6978.

[24] Zhang, L.; Zhang, Z.; He, C.; Dai, L.; Liu, J., Wang L. Rationally designed surfactants for few-layered graphene exfoliation: ionic groups attached to electron deficient π-conjugated unit through alkyl spacers. ACS Nano, 2014, 8, 6663-6670.

[25] Buzaglo, M.; Shtein, M.; Kober, S.: Lovrinčić, R.: Vilan, A.; Regev, O. Critical parameters in exfoliating graphite into graphene. Phys. Chem. Chem. Phys., 2013, 15, 4428-4435.

[26] Bourlinos, A. B.; Georgakilas, V.; Zboril, R.; Steriotis, T. A.; Stubos, A. K.; Trapalis, C. Aqueous-phase exfoliation of graphite in the presence of polyvinylpyrrolidone for the production of water-soluble graphenes. Solid State Commun., 2009, 149, 2172- 2176.

[27] Notley, S. M. Highly Concentrated suspensions of graphene through ultrasonic exfoliation with continuous surfactant addition. Langmuir, 2012, 28, 14110-14113.

[28] Van der Heide, P. X-ray photoelectron spectroscopy: an introduction to the principles and practices; John Wiley & Sons: Hoboken, NJ, 2012.

[29] Eda, G.; Yamaguchi, H.; Voiry, D.; Fujita, T.; Chen, M.; Chhowalla, M. Photoluminescence from chemically exfoliated MoS_2. Nano Lett., 2011, 11, 5111-5116

[30] L. Cai, J. He, Q. Liu, T. Yao, L. Chen, W. Yan, F. Hu, Y. Jiang, Y. Zhao, T. Hu, Z. Sun, S. Wei, Vacancy-induced ferromagnetism of MoS_2 nanosheets, J. Am. Chem. Soc. 137 2015, 2622-2627.

[31] L. Li, Z. Qin, L. Ries, S. Hong, T. Michel, J. Yang, C. Salameh, M. Bechelany, P. Miele, D. Kaplan, M. Chhowalla, D. Voiry, Role of sulfur vacancies and undercoordinated Mo regions in MoS_2 nanosheets toward the evolution of hydrogen, ACS Nano 13 2019, 6824-6834.

[32] Spence, J. C. H. High-Resolution Electron Microscopy, Oup Oxford, 2014.

[33] Egerton, R. F. Physical principles of electron microscopy. Springer. 2008.

[34] Biris, A. R.; Dervishi, E.; Ardelean, S.; Lazar, M. D.; Watanabe, F.; Biris, G. L.; Misan, I.; Biris, A. S.; Giessibl, F. J. Advances in atomic force microscopy. Rev. Mod. Phys., 2003, 75, 949-983.

[35] Abu-Lail, N. I., Camesano, T. A. Polysaccharide properties probed with atomic force microscopy. J. Microsc., 2003, 212, 217-238.

[36] Kuznetsov, Y. G.; Malin, A. J.; Lucas, R. W.; Plomp, M.; McPherson, A. Imaging of viruses by atomic force microscopy. J. Gen. Virol., 2001, 82, 2025-2034.

[37] Jalili, N.; Laxminarayana, K. A review of atomic force microscopy imaging systems: Application to molecular metrology and biological sciences. Mechatronics, 2004, 14, 907-945.

[38] Haugstad, G. Atomic Force Microscopy: Understanding Basic Modes and Advanced Applications. Wiley. 2012.

[39] Paredes, J. I.; Villar-Rodil, S.; Solís-Fernández, P.; Martínez-Alonso, A.; Tascón, J. M. D. Atomic force and scanning tunneling microscopy imaging of graphene nanosheets derived from graphite oxide. Langmuir, 2009, 25, 5957-5968.

[40] Scholz, F. Electroanalytical methods: guide to experiments and applications. Springer. 2010.

[41] Zoski, C. G. Handbook of electrochemistry. Elsevier. 2007.

[42] Van der Paw, L. A method of measuring the resistivity and Hall coefficient on lamellae of arbitrary shape. Philips Tech. Rev., 1958, 20, 220-224.

5. Resúmenes y artículos

5.1. Exfoliación electroquímica catódica

Artículo I

An aqueous cathodic delamination route towards high quality grapheme flakes for oil sorption and electrochemical charge storage applications, Sergio García-Dalí, Juan I. Paredes, José M. Munuera, Silvia Villar-Rodil, Amelia Martínez-Alonso, Juan M.D. Tascón, *Chemical Engineering Journal*, 2019, 372, 1226–1239.

Artículo II

Aqueous Cathodic Exfoliation Strategy toward Solution-Processable and Phase-Preserved MoS_2 Nanosheets for Energy Storage and Catalytic Applications, Sergio García-Dalí, Juan I. Paredes, José M. Munuera, Silvia Villar-Rodil, Alaa Adawy, Amelia Martínez-Alonso, Juan
M.D. Tascón, *ACS Applied Materials and Interfaces*, 2019, 11, 36991–37003.

La exfoliación electroquímica en medio acuoso es un método de preparación de grafeno y otros materiales bidimensionales, que posee una serie de características atractivas, como la escalabilidad, bajo coste, simplicidad y bajo impacto medioambiental y que permite la producción de este material para su uso en diferentes aplicaciones. En particular, la exfoliación catódica en agua permitiría obtener un grafeno de alta calidad estructural y bajo grado de oxidación, características que no se consiguen fácilmente con la exfoliación anódica. Sin embargo, en los estudios previos, la intercalación de cationes acuosos y, por tanto, la eficiencia de la exfoliación catódica era muy pobre. En consecuencia, uno de los objetivos principales de esta tesis fue la mejora de dicha eficiencia, lo que constituyó el tema central de estudio del **artículo I.**

La exfoliación catódica acuosa resulta interesante no solo para la obtención de grafeno, sino también para la preparación de otros materiales bidimensionales de gran interés, como el MoS_2 nanoestructurado. Hasta el presente, la preparación por exfoliación electroquímica de este material ha conllevado el uso de disolventes orgánicos o sales orgánicas sintéticas, o ha implicado la oxidación del material durante el proceso. Por ello, en el **artículo II** se realiza el estudio de obtención de MoS_2 2D mediante exfoliación electroquímica catódica en agua, estudiando variables como el tipo de electrolito y su concentración, el potencial y el tiempo aplicados.

Estudios previos han demostrado que la exfoliación anódica de grafito en medio acuoso tiene lugar por un mecanismo mediante el que se produce la oxidación inicial del material en los bordes, límites de grano y otros tipos de defectos, debido a la formación de radicales altamente reactivos (p. e., ·OH) por la oxidación anódica del agua. La oxidación local del grafito provoca un aumento en el espaciado interlaminar y la consecuente intercalación de aniones hidratados procedentes del electrolito. La oxidación de las moléculas del agua co- intercaladas con los aniones genera oxígeno molecular que favorece la expansión y delaminación del grafito. Esto hace que la exfoliación anódica tenga un buen rendimiento. Sin embargo, cabe esperar que este mecanismo no ocurra al aplicar potenciales negativos en una exfoliación catódica, bajo los que el grafito se mantiene en condiciones intrínsecamente reductoras, que no facilitan por tanto ni la oxidación ni la expansión interlaminar y en consecuencia, tampoco la intercalación de cationes hidratados.

Por ello, en el **artículo I** la primera variable a estudiar es el tipo de grafito de partida (HOPG, barra de grafito o grafito flexible), con el fin de evaluar cómo afecta la estructura del grafito a la exfoliación catódica. Por microscopía SEM se observó que, al contrario que el HOPG, el grafito flexible presenta de entrada muchos bordes y huecos interlaminares que, a priori, facilitarían la penetración del electrolito y del agua sin necesidad de oxidar el material, permitiendo a su vez su expansión. Los resultados demostraron que sólo cuando se utiliza grafito flexible como material de partida se obtiene un grafito deslaminado, siendo por tanto la elección del grafito de partida una variable crucial en el proceso de exfoliación catódica en medio acuoso.

La segunda variable a estudiar es el electrolito, tanto el tipo como la concentración utilizada. Para ello, se estudió una amplia variedad de iones de amonio cuaternario como electrolito. Otros estudios han demostrado que, al menos en disolventes orgánicos, estos iones son capaces de intercalarse entre las láminas de grafito, produciendo su exfoliación en condiciones catódicas. Aplicando un potencial de -10 V durante 2 h, y usando una placa de Pt como ánodo y el grafito flexible como cátodo, se utilizaron como electrolito tanto sales de amonio con grupos alquilo (ACl, TMAHCl, TMACl, TEACl, TPACl, TBAHCl, TBMACl, TBACl, HTMABr, OTMABr, DDTMABr, HDTMABr), como arilo (PhTMACl y BzTMACl) a concentraciones de 0.02, 0.1 y 0.3 M.

Se observa que durante el tratamiento catódico el electrodo de grafito se va hinchando progresivamente en diferente medida dependiendo del electrolito concreto y su concentración. El material deslaminado obtenido se recoge y se lava por filtración, se seca a vacío a 60 ºC durante 18 h, se pesa para determinar el rendimiento (en comparación con la masa inicial de grafito) y se analiza por SEM, observando que el grafito expandido presenta una morfología tipo “acordeón”, característica de procesos eficientes de exfoliación electroquímica, con muchas láminas parcialmente separadas y con huecos entre ellas en su superficie.

Para entender por qué unos iones funcionan mejor que otros en el proceso de exfoliación electroquímica acuosa debemos tener en cuenta varias consideraciones. Por un lado, la presencia de átomos de hidrógeno directamente enlazados con el átomo de nitrógeno hace que estos iones tengan un rendimiento prácticamente nulo. Ello es debido a que, al entrar en contacto con el electrodo de grafito cargado negativamente, son fácilmente reducibles, formando un producto eléctricamente neutro e hidrógeno molecular

(p. e., 2 NH_4^+ + 2 e^- → 2 NH_3 + H_2 en el caso del ACl), y perdiendo por tanto la carga que les permite ser atraídos hacia el interior del electrodo, evitándose la intercalación. Por otro lado, el diferente rendimiento obtenido cuando se utilizan iones de amonio que no presentan ningún átomo de hidrógeno directamente enlazado al átomo de nitrógeno (amonio cuaternario) puede explicarse por la combinación del efecto de la movilidad electroforética y del tamaño/masa molecular. En principio, los electrolitos con grupos orgánicos enlazados al nitrógeno que poseen un mayor número de átomos de carbono y, por tanto, mayores dimensiones permitirían una mayor eficiencia en la separación de las láminas, pero también dificultarían su entrada en los espacios interlaminares. Por un lado, su mayor tamaño conllevaría efectos estéricos. Por otro, dado que todos poseen la misma carga eléctrica, una masa molecular mayor implica una menor movilidad electroforética. Por tanto, debe alcanzarse un compromiso entre ambos efectos, consiguiéndose rendimiento máximo utilizando iones de tamaño intermedio. Ello puede observarse claramente al comparar el rendimiento en producto deslaminado de una serie de sales de cloruros de alquilamonio con grupos alquilo de longitud creciente (TMACl, TEACl, TPACl y TBACl). Efectivamente, el rendimiento aumenta inicialmente con la longitud de la cadena de aquilo (TMACl < TEACl < TPACl), pero disminuye cuando el ión es demasiado grande (TPACl > TBACl). Un comportamiento similar puede observarse cuando se aumenta la longitud de solo uno de los cuatro grupos alquilo unidos al nitrógeno (TMACl, HTMABr, OTMABr, DDTMABr, HDTMABr). Para los electrolitos que permiten deslaminar el grafito el rendimiento aumenta con la concentración, hasta alcanzar un valor máximo (0.3 M) consiguiéndose, un rendimiento de casi el 50% en dichas condiciones, utilizando como electrolito HTMABr. Por último, al utilizar grupos arilo (PhTMACl y BzTMACl) en lugar de grupos alquilo con el mismo número de átomos de carbono (HTMABr), se observa cómo disminuye el rendimiento del proceso. Esto se interpreta en base al hecho de que los iones con grupos arilo adoptan una conformación plana con la que interaccionan mejor con la superficie del grafito, pero que es menos eficiente en el proceso de expansión.

Tras el tratamiento catódico, se toma una cierta cantidad del material expandido lavado y secado y se sonica utilizando un disolvente adecuado (NMP, NEP, NVP, DMF, DMSO, 1,3- dioxolano, piridina, o agua con Pluronic P-123) para obtener el grafeno exfoliado en dispersión. Se realizaron estudios de caracterización para conocer las

características y propiedades del material obtenido. Con espectroscopía de absorción UV-Vis de la dispersión de grafeno, se observa la banda característica a 270 nm de las transiciones $\pi \rightarrow \pi^*$, posición que indica la presencia de dominios conjugados relativamente grandes y asociados a un bajo grado de oxidación. Las imágenes de STEM y AFM demuestran que efectivamente se ha producido la exfoliación, al observarse láminas de grafeno con un tamaño lateral de varios cientos de nm y un grosor de unos 4–5 nm. Los resultados de XPS muestran una pequeña cantidad de N (<1% at.), lo que indica la presencia de moléculas de electrolito adsorbidas sobre el grafeno. Además, la relación atómica O/C es de 0.05–0.08, similar a los valores documentados para la exfoliación catódica en medio orgánico. Los espectros de alta resolución del C 1s para los grafenos obtenidos con TPACl y HTMABr, que fueron los electrolitos más eficientes en cuanto a rendimiento de grafeno, indican que no hay diferencias significativas en cuanto a su grado de oxidación entre ambos. Se midió la calidad estructural del grafeno mediante espectroscopía Raman, a través de la relación de las intensidades de las señales D y G (dando valores de I_D/I_G en el rango de 0.2–0.3), similar a los de grafenos obtenidos por exfoliación directa en fase líquida por ultrasonidos. También se realizaron estudios de conductividad eléctrica de filmes obtenidos por filtración, arrojando valores de $1.5 \cdot 10^4$ $S \cdot m^{-1}$, superiores a la mayoría de valores documentados para exfoliación directa en fase líquida ($\sim 2 \cdot 10^2$–$5 \cdot 10^4$ $S \cdot m^{-1}$) y muy similares a los de grafenos de alta calidad y bajo grado de oxidación obtenidos por exfoliación anódica con electrolitos que previenen la oxidación ($\sim 1 \cdot 10^4$–$4.6 \cdot 10^4$ $S \cdot m^{-1}$).

Debido a su alta calidad estructural, bajo grado de oxidación y buena conductividad eléctrica, este material ha sido estudiado para aplicaciones de absorción de aceites y como electrodo para supercondensador.

Para la absorción de aceites, es necesario que el material no sólo tenga carácter hidrófobo, sino que además tenga baja densidad, con el fin de maximizar la cantidad absorbida por unidad de masa. Por ello, el material exfoliado si es procesado en estructuras tridimensionales de baja densidad es en principio más útil para este propósito. Una manera de conseguir esto es utilizar una estructura tridimensional preformada de baja densidad sobre la que depositar las láminas. Concretamente en este trabajo se usó una esponja de melamina como soporte para depositar el grafeno exfoliado. Se observa que la esponja recubierta con grafeno se vuelve hidrófoba y presenta buena capacidad de absorción (60–

150 g/g).

Para usar como electrodo de supercondensador, se estudió el grafito expandido catódicamente como electrodo de trabajo en un sistema de tres electrodos. Las curvas obtenidas en voltametría cíclica muestran una forma rectangular sin ningún pico redox, indicando el almacenamiento de carga sobre el electrodo al formarse una doble capa eléctrica, sin procesos faradaicos (pseudocapacitancia). Este es el comportamiento esperable para materiales carbonosos sin heteroátomos ni especies electroactivas (grupos funcionales). Las curvas de carga/descarga galvanostáticas muestran perfiles casi simétricos y lineales, y dan unos valores de capacitancia de ~25 F/g a 0.3 A/g de densidad de corriente, siendo un valor bajo en comparación con lo que se encuentra en la literatura para materiales de grafeno. Este comportamiento tiene su origen muy posiblemente en la preparación del electrodo para su estudio electroquímico, que implica un prensado del grafito expandido y por tanto un reapilamiento de las láminas, lo que hace disminuir por tanto la superficie expuesta.

Para mejorar los valores de capacitancia, el grafito expandido catódicamente se combina con una pequeña cantidad de óxido de cobalto (~5%), crecido vertical y laminarmente sobre su superficie. El óxido aporta pseudocapacitancia (característica de este material) y evita el reapilamiento del grafito durante el prensado para formar el electrodo. Las imágenes de SEM de la superficie así como el análisis elemental corroboran la presencia del óxido de cobalto en la superficie. Los procesos redox son claramente visibles tanto en la voltametría cíclica como en los perfiles de carga/descarga galvanostática, viéndose incrementada la capacitancia hasta 140 F/g a 0.3 A/g de densidad de corriente.

En el caso del MoS_2, material de trabajo en el **artículo II**, no se disponía de distintos tipos de MoS_2 de partida apropiados para su uso como electrodos en exfoliación catódica, por lo que no se realizó un estudio de la influencia del material de partida, utilizándose cristales naturales de MoS_2 como cátodos. Se estudiaron otras variables, como el tipo de electrolito y su concentración, el tiempo del tratamiento y el potencial aplicado.

En primer lugar, se utilizó el mismo tipo de electrolito que dió buen resultado en la exfoliación catódica de grafito, es decir, sales de amonio cuaternario, concretamente TEACl, TPACl y TBACl. Estos electrolitos permitieron expandir el material y obtener

MoS_2 exfoliado en dispersión coloidal con un rendimiento de hasta un 18 % usando TPACl. Sin embargo, también se probaron electrolitos de sales de cloruros alcalinos, debido a su alta disponibilidad, bajo coste y solubilidad en agua, tales como LiCl, NaCl y KCl, logrando un rendimiento de hasta el 30% con KCl.

El uso de estos electrolitos fue optimizado utilizando concentraciones de hasta 4 M en el caso de los cloruros alcalinos y 0.3 M para las sales de amonio, aplicando un potencial de -20 V durante 30 min. Durante el proceso se observa cómo la pieza de MoS_2 se va hinchando progresivamente desde el extremo sumergido en el electrolito hasta el extremo sujetado por la pinza, en forma de abanico.

Al igual que con el grafito, el proceso de expansión del MoS_2 puede ser explicado debido a una intercalación de cationes hidratados del electrolito, en una primera etapa, seguida de la reducción de las moléculas de agua cointercaladas para dar lugar a gas hidrógeno, produciendo así la expansión del material. Esta explicación es corroborada por el hecho de que en ausencia de electrolito no se produce expansión, ya que el agua no se intercala y se reduce solo en la superficie del electrodo, así como por el seguimiento del proceso que se realizó por voltametría en un potenciostato. Se observó un pico abrupto solo en el primer ciclo del proceso y no en los siguientes, lo que indica que inicialmente tiene lugar la intercalación del electrolito, la expansión del material por reducción del agua y posteriormente solo la reducción del agua en el material ya deslaminado.

Para explicar por qué con KCl se consigue un mayor rendimiento que con LiCl y NaCl, hay que tener en cuenta que estas especies iónicas se encuentran hidratadas en medio acuoso, siendo necesario tener en cuenta el tamaño de su esfera de hidratación. Se sabe que el tamaño de los cationes alcalinos hidratados disminuye en el orden $Li^+ > Na^+ > K^+$, deduciéndose que los iones K^+ tendrán mayor movilidad en medio acuoso en presencia de un campo eléctrico externo. Además, la conductividad molar de las disoluciones de estos iones en agua (25º C) es de 38.69, 50.11 y 73.5 S cm^2 mol^{-1}, respectivamente. Por tanto, es de esperar que los iones K^+ en medio acuoso con mayor movilidad y conductividad se intercalen entre las láminas de MoS_2 de manera más eficiente.

El MoS_2 expandido catódicamente fue caracterizado por SEM, observándose láminas o conjuntos de ellas separadas por pequeños huecos y espacios de menos de 1 µm, tal y como ocurría con el grafito expandido catódicamente. También se caracterizaron las

láminas extraídas posteriormente por sonicación, utilizando GMP en IPA, por STEM, AFM y TEM, en las que se observaban láminas de pocos cientos de nanómetros de tamaño lateral y entre 5 y 8 nm de grosor, indicando que obtenemos un MoS_2 de entre 6 y 11 monocapas. Por otro lado, los resultados de XPS, espectroscopía Raman y espectroscopía UV-Vis muestran los picos característicos de MoS_2 en fase 2H, lo que demuestra que la exfoliación catódica no indujo un cambio de fase.

Debido a su alta área superficial y a su capacidad para intercalar iones, se estudia el MoS_2 exfoliado catódicamente como electrodo para supercondensadores. Sin embargo, el MoS_2 2H es un semiconductor y, por tanto, presenta una conductividad eléctrica limitada, lo que hace necesario usar este material en combinación con un material conductor, como los nanotubos de carbono. Se realizaron estudios preliminares en ausencia de nanotubos de carbono para el MoS_2 expandido, MoS_2 expandido y agitado en una disolución de GMP, así como para láminas de MoS_2 extraídas por sonicación en isopropanol con GMP, dando éste último los mejores resultados con una capacitancia de ~145 F/g a 1 A/g y ~50 F/g a 20 A/g. Por ello, se combina éste último con diferentes proporciones de nanotubos de carbono, produciendo un incremento en la capacitancia hasta ~175 F/g a 1 A/g y ~75 F/g a 20 A/g. Se estudia también el comportamiento de una celda asimétrica formada por un electrodo positivo de MoS_2 combinado con nanotubos de carbono y carbón activo comercial (Kurarai YP-50F) como electrodo negativo. La densidad de energía máxima que es capaz de almacenar esta celda es de 26 W h kg^{-1}, demostrando ser un material razonablemente competitivo en el almacenamiento de energía en comparación con los resultados obtenidos hasta la fecha utilizando MoS_2 2D obtenido por otros métodos.

También se estudian las láminas de MoS_2 exfoliadas catódicamente y dispersadas en agua con GMP como catalizador para la reducción de nitroarenos (4-NP y 4-NA). Como el GMP adsorbido sobre las láminas puede competir por los centros catalíticos activos del MoS_2 y degradar por tanto su actividad catalítica, se realizan los estudios cinéticos tras sucesivos lavados de la dispersión acuosa de MoS_2, con el fin reducir la cantidad de GMP adsorbido. Se observa que la actividad catalítica aumenta tras realizar un primer lavado, obteniéndose valores de actividad competitivos, pero ésta disminuye radicalmente al hacer posteriores lavados, ya que se elimina gran parte del GMP adsorbido impidiendo la estabilización coloidal del MoS_2 en el medio de reducción acuoso.

ARTÍCULO I

An aqueous cathodic delamination route towards high quality graphene flakes for oil sorption and electrochemical charge storage applications

Sergio García-Dalí, Juan I. Paredes,* José M. Munuera, Silvia Villar-Rodil,* Amelia Martínez-Alonso, Juan M.D. Tascón

Instituto Nacional del Carbón, INCAR-CSIC, C/Francisco Pintado Fe 26, 33011 Oviedo, Spain

* Corresponding author: paredes@incar.csic.es

* Corresponding author: silvia@incar.csic.es

Abstract

The electrochemical exfoliation of graphite in aqueous medium stands out as an attractive, scalable approach for the production of graphenes for different applications, due to its simplicity, cost-effectiveness and environmental friendliness. In particular, cathodic exfoliation in water should allow access to high quality, non-oxidized graphene flakes, as it avoids the intrinsic oxidizing conditions that typically plague the anodic route, but this possibility has been limited by a poor intercalation ability of aqueous cations. Here, we demonstrate that with a proper choice of starting graphite and electrolyte, high quality graphene flakes can be obtained in substantial yields via cathodic delamination in water. Graphites having some pre-expanded edges and interlayer voids (e.g., graphite foil) were found to be critical for a successful exfoliation. Large differences in the efficiency of a range of aqueous quaternary ammonium-based electrolytes were observed, quantitatively compared and rationalized on the basis of their chemical structure. Graphene yields up to 40–50 wt% were attained with the most efficient cations (tetrapropylammonium and hexyltrimethylammonium). Hydrophobic sponges made up of cathodic graphene-coated melamine foam exhibited a notable capacity towards the sorption of oils and organic solvents from water with good re-usability. Hybrids comprised of cathodically exfoliated graphite and a small amount of vertically oriented cobalt oxide nanosheets displayed good electrochemical charge storage behavior. Overall, the ability to access graphene flakes in considerable yields by the aqueous cathodic route disclosed here should raise the prospects of cathodic exfoliation as a competitive method for the industrial manufacturing of high quality graphene for practical applications.

Keywords: two-dimensional (2D) material, graphene, cobalt oxide, electrochemical exfoliation, cathodic exfoliation, water remediation, energy storage.

1. Introduction

More than a decade after it was first isolated and its outstanding physical properties uncovered, graphene still retains a broad appeal to the research community worldwide and continues to be one of the most intensively investigated materials.[1–3] Different to the early days of this two-dimensional form of carbon, which were dominated by fundamental enquiry, current efforts are mostly focused on translating its attractive features to a

plethora of relevant technological applications. Indeed, the areas where graphene and graphene-derived materials have a strong potential to contribute incremental or disruptive advances are wide-ranging, encompassing the fields of energy conversion and storage,[4–6] electronics,[7] photonics,[8] biomedicine[9,10] and chemical sensing/biosensing,[11] among others. An obvious pre-requisite for the fulfillment of these prospects, however, is the availability of graphenes in large quantities, obtained by cost-effective means and having characteristics (lateral size, thickness, presence of defects or functional groups, doping, etc) that can be specifically adjusted to meet the needs of each intended use of the material.

Although great progress has been made over the last years in the development of scalable technologies for the production of graphenes, it is also true that most of the currently known approaches, if not all, suffer from their own limitations and shortcomings.[3,12,13] Thus, the idea of resorting to a single, versatile method for the manufacture of graphenes with virtually any specification that could be demanded in real-life applications remains at present an unrealistic option. Instead, researchers are pushing to advance and improve a pool of very different top- down and bottom-up production strategies to choose from when a certain type of graphene will be required in large amounts under industrially competitive conditions. [3] Among such strategies, those based on the electrochemical exfoliation of graphite have received considerable attention in recent years.[14–18] This top-down approach relies on the delamination of a graphite electrode triggered by intercalation of ions from an electrolytic medium upon application of a DC bias voltage, and boasts a number of alluring qualities, such as simplicity and speed of operation, cost-effectiveness and scalability.

By its own nature, the electrochemical exfoliation method can be implemented under two distinct operation modes, namely, the anodic mode and the cathodic mode. The former is typically carried out in aqueous electrolytes of common inorganic acids (e.g., H_2SO_4) or their salts [$(NH_4)_2SO_4$, Na_2SO_4, etc], and generally affords well exfoliated graphene nanosheets (< 5 monolayers thick) in high yields.[16,17] Nonetheless, these electrolytes tend to give anodically exfoliated graphene that is substantially oxidized due to attack by highly reactive oxygen radicals (e.g., ·OH) generated from the anodic oxidation of water molecules, thus compromising its utility in applications that demand high quality materials. Although recent work has demonstrated that such an oxidative attack can be avoided to a considerable degree, it normally requires resorting to more complex and

expensive electrolytes and/or electrolyte additives, which act as oxygen radical scavengers,[19–21] but this strategy can also risk a lower efficiency of the intercalation/exfoliation process itself.[20,22] On the other hand, extensive oxidation of graphene is inherently averted in cathodic exfoliation due to the fact that the graphite electrode is subjected to reducing conditions (negative potential). This delamination mode has been demonstrated to yield high quality, largely defect-free graphenes using electrolytic media that are typically based on lithium,[23,24] sodium,[25] alkylammonium,[26–28] alkylimidazolium[29,30] or alkylpyrrolidinium[29,31,32] salts in such organic solvents as propylene carbonate, acetonitrile, dimethyl sulfoxide or *N*,*N*- dimethylformamide. However, carrying out cathodic exfoliation in aqueous (rather than organic) electrolytic media would be highly desirable, as it would make the production process easier to scale-up as well as more environmentally friendly and affordable, but unfortunately this possibility has been seldom reported.[33] A likely reason behind this state of affairs is that because the graphite electrode does not oxidize under the applied cathodic potential, its hydrophobic interlayer spaces cannot be efficiently intercalated by the hydrated cations from the electrolyte (as opposed to the case of the hydrated anions in anodic exfoliation). As a result, only "naked", de-hydrated cations will be probably able to intercalate the graphite cathode, and if they cannot enter in sufficient numbers and/or they do not have the right molecular size, the graphite layers will not be pushed apart from each other to an extent enough to allow exfoliation.

When cathodic exfoliation is accomplished in organic solvents, the efficiency of graphite delamination is known to depend not only on the specific type of intercalating cation used, but also on the organic solvent itself, i.e., the success of exfoliation is determined by the choice of a proper cation/organic solvent combination.[34,35] We hypothesized that a similar situation could be in place for aqueous electrolytes, implying that, among other possible factors, the selection of the intercalating cation should be crucial for an effective exfoliation in water. Indeed, there is some evidence in the recent literature suggesting that this hypothesis is correct.[36] More specifically, aqueous tetrabutylammonium cations were shown to increase the delamination yield of graphite electrodes in conjunction with sulfate anions in a combined anodic/cathodic process, whereas such an effect was much weaker or even not present at all with other tested cations (i.e., tetramethylammonium and ammonium). However, to the best of our knowledge a thorough survey aimed at identifying the most efficient cations in purely

cathodic exfoliation processes has not yet been undertaken.

We have investigated a broad range of ammonium-based cations as prospective intercalating/exfoliating agents for the cathodic delamination of graphite into graphene in aqueous medium, the results of which are reported here. Very large differences in the ability of these chemical species to intercalate and expand the graphite electrode were observed, quantitatively compared and rationalized on the basis of their chemical make-up. More significantly, the tested cations that turned out to be the most efficient in terms of their expanding power were shown to afford graphene nanosheets in competitive yields, which should facilitate the future industrial implementation of the cathodic route as a method of choice for the manufacturing of high quality graphenes. We demonstrate the potential of this type of graphene nanosheets in practical applications with two specific examples, namely, (1) the sorption of oils and organic solvents either using the as-prepared, stand-alone graphene material directly obtained from the cathodic process or using melamine foam coated with the cathodically exfoliated nanosheets, and (2) the use of the cathodic graphene in combination with cobalt oxide nanosheets as an electrode for electrochemical charge storage.

2. Results and discussion

2.1. Screening of efficient electrolytes for the cathodic exfoliation of graphite in water

The electrochemical exfoliation of graphite in aqueous medium to afford graphene nanosheets is usually accomplished under anodic conditions, whereby the graphite electrode is efficiently delaminated upon application of a positive voltage in the presence of a proper electrolyte (typically, a sulfate-based one).[16,17] This process is believed to be driven, at least in its early stages, by the oxidation of graphite at edges, grain boundaries and other defects, which in turn is induced by highly reactive oxygen radicals generated from the oxidation of water molecules at the graphite anode.[37,38] In particular, the oxidative attack of graphite edges and their subsequent decoration with hydrophilic oxygen functional groups can be expected to lead to a local increase in the interlayer spacing, thus facilitating the intercalation of hydrated anions from the electrolyte (i.e., anions surrounded by a bound shell of water molecules) into the interlayer galleries of the material. These intercalated species could then act as a sort of molecular wedge to trigger the separation of the constituting graphene sheets from one another (i.e., to trigger their exfoliation), probably assisted by the electrolytic decomposition of the water molecules

into gaseous products (e.g., O_2).

On the other hand, such a course of events is not expected to occur in a prospective cathodic exfoliation with an aqueous electrolyte, because in this case water-derived oxygen radicals will not be generated at the graphite cathode under the applied reducing conditions. As a result of the lack of oxidative attack, the graphite edges will remain unexpanded and hydrophobic, therefore hindering the intercalation of hydrated cations and so the electrode exfoliation. A possible way to circumvent this issue and allow cathodic exfoliation in water could be to use graphite materials with pre-expanded edges and interlayer voids, which would expedite the entrance of ionic species from the electrolyte without the need to resort to oxidation processes. To this end, graphite foil appeared to be a good candidate.[39] Indeed, prior studies have indicated that anodic intercalation and exfoliation processes are promoted in graphite foil compared to other graphite types, such as highly oriented pyrolytic graphite (HOPG) or graphite rod, powder and flakes,[22,39] suggesting that similar effects could be in place for cathodic processes. As will be discussed and rationalized below, the choice of graphite foil as the electrode material turned out to be one of the critical factors for the success of cathodic exfoliation in water.

As potential electrolytes for the exfoliation experiments, we selected a number of ammonium-based salts, where the ammonium cation was derivatized with different alkyl or phenyl groups and the counterion was typically a halide (Cl^- or Br^-). We note that at least in organic solvents, several ammonium-based cations are known to intercalate and exfoliate graphite efficiently under cathodic potentials.[26–28,34,40] Table 1 lists the names, acronyms used and chemical structures of the tested species. To provide an initial, quantitative proxy for the ability of these electrolytes to intercalate/exfoliate the graphite electrode, we carried out benchmark experiments whereby a piece of graphite foil of fixed dimensions (55 × 30 × 0.5 mm^3) was subjected to cathodic treatment (bias voltage: -10 V) for 2 h in a two-electrode setup using Pt foil as the counter electrode in an aqueous solution of a given electrolyte at a certain molar concentration (see Experimental section for details of the treatment and Table 1 for the molar concentrations tested with each electrolyte). In many cases, the graphite cathode was seen to progressively swell and expand upon application of the negative potential, to an extent that depended on the particular electrolyte and electrolyte concentration tested. To illustrate this point, Fig. 1a shows digital photographs of the cross-section of graphite foil pieces before (left) as well as after cathodic treatment in 0.3 M PhTMACl (middle) and 0.3 M HTMABr (right). Upon

completion of the electrolytic step, the expanded products were collected, thoroughly washed with water to remove remnants of the ammonium-based salt, dried under reduced pressure and finally the resulting fluffy, low density (30–45 mg cm^{-3}) powders were weighed to estimate the efficiency (yield) of the expansion process. Comparison of field-emission scanning electron microscopy (FE-SEM) images of the starting graphite foil, which appeared mostly planar and featureless on the millimeter scale (Fig. 1b), with those recorded for the expanded material obtained with an efficient electrolyte, such as 0.3 M HTMABr (Fig. 1c and d), revealed that the cathodic treatment led to a dramatic expansion of micrometer-sized graphite particles (presumably along the *c* axis of their atomic lattice) to give worm-like objects (Fig. 1c). Closer inspection of the latter indicated that they were made up of thin, corrugated sheets separated by micrometer- to nanometer-wide voids (Fig. 1d). Such a morphology was very similar to that previously reported in efficient processes of anodic[19,22,37,41,42] and cathodic (in organic solvent)[23,26,28] delamination of graphite to give graphene nanosheets, suggesting that a satisfactory exfoliation can also be attained in aqueous medium under cathodic conditions. This point will be corroborated further below.

Table 1. Name, acronym, chemical structure and the different molar concentrations assayed for each ammonium-based salt tested as an electrolyte in the cathodic exfoliation of graphite. The corresponding yields of expanded graphite obtained after 2 h of electrochemical treatment, calculated as the weight of expanded graphite relative to the weight of the starting graphite foil piece, are also indicated.

Electrolyte (acronym)	Structure	Conc (M)	Yield of expanded graphite (wt%)
Ammonium chloride (ACl)	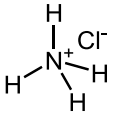	0.02 0.1 0.3	0 0 0
Trimethylamine hydrochloride (TMAHCl)	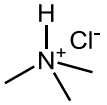	0.02 0.1 0.3	0 0 0.5
Tetramethylammonium chloride (TMACl)	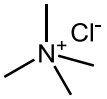	0.02 0.1 0.3	2.0 8.7 15
Tetraethylammonium chloride (TEACl)	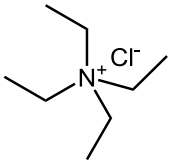	0.02 0.1 0.3	3.3 12 28
Tetrapropylammonium chloride (TPACl)	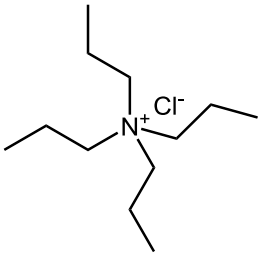	0.02 0.1 0.3	7.0 13 44
Tributylamine hydrochloride (TBAHCl)	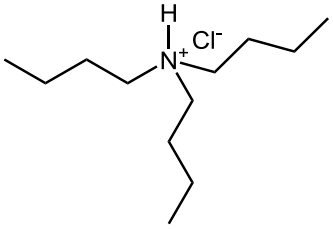	0.02 0.1 0.3	0 0 0

Tributylmethylammonium chloride (TBMACl)	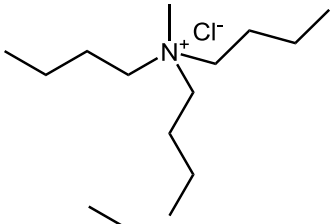	0.02 0.1 0.3	5.3 12 25
Tetrabutylammonium chloride (TBACl)	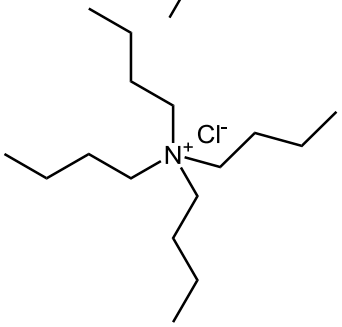	0.02 0.1 0.3	5.7 13 33
Hexyltrimethylammonium bromide (HTMABr)	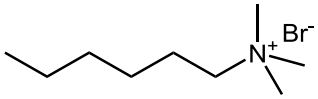	0.02 0.1 0.3	0.4 18 46
Octyltrimethylammonium bromide (OTMABr)	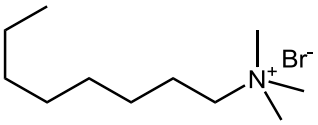	0.02 0.1 0.3	1.8 13 26
Dodecyltrimethylammonium bromide (DDTMABr)	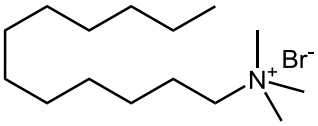	0.02 0.1 0.3	2.9 8.0 13
Hexadecyltrimethylammonium bromide (HDTMABr)	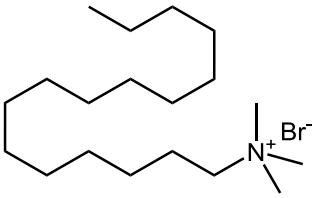	0.02 0.1	0 4.6
Phenyltrimethylammonium chloride (PhTMACl)	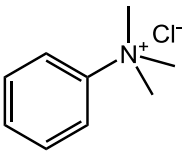	0.02 0.1 0.3	2.2 2.8 14

Benzyltrimethylammonium chloride (BzTMACl)	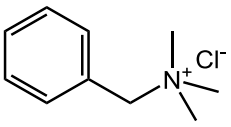	0.02 0.1 0.3	0.7 7.5 25

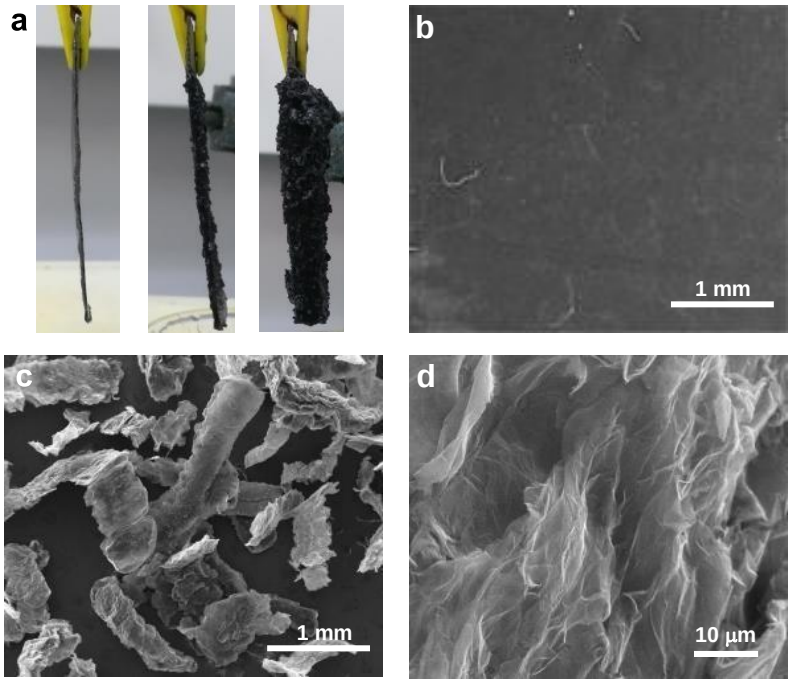

Figure 1. (a) Digital photographs of the cross-section of graphite foil pieces before (left) and after cathodic treatment in 0.3 M PhTMACl (middle) and 0.3 M HTMABr (right). **(b-d)** Typical FE-SEM images of **(b)** the starting graphite foil and **(c,d)** the cathodically expanded material obtained from it after cathodic treatment for 2 h using 0.3 M HTMABr as the electrolyte.

The yield of expanded product, calculated as its weight relative to the weight of the starting graphite foil piece, was taken as a quantitative measure of the efficiency of the cathodic treatment, and the values determined for the tested electrolytes at different concentrations are given in Table 1. First of all, we note that for almost any given electrolyte the yield of expanded material tended to increase with the electrolyte concentration, which was a clear indication of the central role played by these ionic species in the expansion of the material. Second, large differences in yield values were

noticed between the different electrolytes. In particular, some of the tested species, i.e. ACl, TMAHCl and TBAHCl, gave very small or even virtually negligible yields. We interpret this result to be related to the fact that one or more hydrogen atoms were directly connected to the N^+ site in the corresponding cation. This type of cation should be readily reduced at the graphite cathode to afford a stable, electrically neutral product and molecular hydrogen (e.g., $2NH_4^+ + 2e^- \rightarrow 2NH_3 + H_2$ in the case of ACl).[43,44] If the cation is reduced promptly to a neutral species after contacting the electrode, it will lose its electrophoretic mobility and hence most of its ability to intercalate the graphite material. As a result, no or very little expansion of the latter should take place. On the other hand, the electroreduction of cations without bound hydrogen atoms (i.e., with only alkyl or phenyl moieties bound to the N^+ site) can be expected to be a less likely event, so that their intercalation into the graphite electrode would not be so much hampered by the loss of electrophoretic mobility. Such an interpretation was supported by the observation that when the TMAHCl and TBAHCl electrolytes were replaced by TMACl and TBMACl, respectively, which only differ from the former in the substitution of a methyl group for the N^+-bound hydrogen, very substantial yields of expanded product could be attained.

The results collected in Table 1 also provided some insight into the effect that the size of the alkyl groups appended to the N^+ site of the electrolyte has on its ability to induce expansion of the graphite cathode. In principle, larger alkyl chains should be more conducive to an efficient separation of neighboring sheets in the graphite electrode upon cation intercalation, as a stronger wedge effect can be expected for bulkier species. However, the ability of cations from the electrolyte to enter the interlayer space of graphite in the first instance should be limited by their size, both in a direct way (i.e., if the cations are too large, steric effects should prevent them from penetrating the interlayer spaces) and indirectly through constraints on their electrophoretic mobility, which is largely determined by their charge/mass ratio.[21] For instance, the mobility of tetraalkylammonium cations in water is known to decrease with the alkyl chain length (i.e., methyl > ethyl > propyl > butyl).[45,46] Based on these considerations, it can be anticipated that the intercalation and expansion of the graphite cathode should be most effective with ammonium-based cations of a certain intermediate size. This conclusion was substantiated by comparing the yields of expanded material within specific sets of the electrolytes from Table 1. More specifically, for the case of the tetraalkylammonium-based electrolytes with the four alkyl chains in the cation being identical (i.e., TMACl, TEACl, TPACl and

TBACl), the measured yields clearly increased in the order TMACl < TEACl < TPACl, but the performance of their butyl-based counterpart (TBACl) was similar or even lower (at the higher electrolyte concentration) than that of TPACl. Indeed, TPACl turned out to be a very efficient electrolyte, boasting yields up to 44 wt% (i.e., almost half of the graphite foil piece was converted to expanded product).

A similar behavior was noticed for the series of electrolytes with the cation comprising three methyl groups and a fourth alkyl chain of variable length, namely, methyl, hexyl, octyl, dodecyl or hexadecyl (i.e., TMACl, HTMABr, OTMABr, DDTMABr and HDTMABr). For these alkyltrimethylammonium species, the highest expansion efficiency was attained with the hexyl-based cation and was similar to that of TPACl (e.g., a yield of 46 wt% at 0.3 M HTMABr), declining significantly for cations with longer chains. Likewise, replacing the alkyl group in the ammonium cation with an aryl moiety was detrimental to its ability to intercalate and expand the graphite cathode. This can be seen by comparing the yields of expanded product obtained with HTMABr (hexyl group) to those afforded by PhTMACl (phenyl group), where both groups possess the same number of carbon atoms (and thus the cations have very similar molecular weights) but the latter gave substantially lower yields. As a tentative explanation for such a result, it can be argued that the phenyl moiety forces the cation to take on a relatively flat conformation upon intercalation into graphite, in order to maximize its interaction with the carbon surface. With a flat configuration, the ability of the intercalated cation to act as a molecular wedge and expand the graphite cathode would be decreased. This interpretation was supported by the observation that when the phenyl group was replaced by a benzyl moiety (i.e., the BzTMACl electrolyte), which can be expected to hinder the adoption of flat configurations by the cation, higher yields of expanded material were attained.

Nevertheless, we note that the ability of some of the alkyltrimethyl-based electrolytes to intercalate and expand the graphite cathode could be affected by their tendency to form micelles above a certain concentration (referred to as the critical micelle concentration, or cmc), giving rise to more complex behaviors. This should be particularly the case for the two longer-chain species (DDTMABr and HDTMABr), which are broadly used cationic surfactants and have cmc values lying below the range of concentrations tested here for the cathodic expansion experiments.[47,48] More specifically, at concentrations above the cmc threshold, the number of surfactant monomers in the solution (i.e., those molecules that remain as stand-alone, non-associated entities) is known to be approximately invariant

with respect to surfactant concentration, whereas the number of molecules associated in micelles increases monotonically with surfactant concentration.[47] It is reasonable to assume that the monomeric entities contribute most effectively to the expansion of the graphite cathode, as they are readily available cations for intercalation. On the other hand, the actual contribution of surfactant cations assembled into micelles to the graphite expansion is much less obvious: while surfactant micelles are dynamic objects, with individual molecules continuously incorporating to and detaching from the assembly, intercalation of a molecule (cation) from a micelle into graphite should involve overcoming first a certain barrier associated to its detachment from the micelle. As a result, the micelle-assembled cations should be less available for intercalation than their stand-alone, monomeric counterparts. Consequently, at least part of the mediocre to poor performance of DDTMABr and HDTMABr as electrolytes for the cathodic expansion of graphite (Table 1) should be ascribed to this effect. Such a situation was not believed to be in place in the case of the shorter chain alkyltrimethyl- ammonium cations (octyl, hexyl and methyl), since their corresponding cmc values were above the tested range of electrolyte concentrations.[48] Nonetheless, the extent to which micellization of DDTMABr and HDTMABr limited their ability to intercalate and expand the graphite cathode is currently unknown and its determination lies beyond the scope of the present work.

2.2.Physicochemical characteristics of the cathodically exfoliated graphenes

While some of the tested aqueous electrolytes (e.g., HTMABr and TPACl) demonstrated a good ability to intercalate the graphite cathode and give high yields of expanded product, the actual amount as well as the characteristics of graphene nanosheets that could be extracted from the latter were a priori unknown and needed to be determined. Nanosheet extraction from electrochemically exfoliated graphites is typically accomplished through a sonication step in proper solvents.[16,49] To this end, a certain amount of expanded material was transferred to a solvent medium, where it was subjected to mild sonication to separate loosely attached, thin nanosheets from poorly exfoliated, relatively thick platelets, and finally either centrifuged at 50 g for 20 min or allowed to stand undisturbed overnight, with the resulting supernatant (dispersion) being collected for further studies and the sediment being discarded (see Experimental section for details). Fig. 2a shows a digital photograph of several successful dispersing solvents, where the

supernatant material could be stably suspended for days to weeks, as denoted by their dark grey or black tone. These solvents included *N*-methyl-2- pyrrolidone, *N*-vinyl-2-pyrrolidone, *N*-ethyl-2-pyrrolidone, *N*,*N*-dimethylformamide, pyridine, 1,3-dioxolane, dimethyl sulfoxide, ethlylene glycol and water with the non-ionic surfactant Pluronic P123 (triblock copolymer). Other tested solvents that turned out to be ineffective for dispersion comprised pure water (as could be expected for low-oxidized nanosheets), water/isopropanol mixtures and ethanol. A representative UV-vis absorption spectrum of the material suspended in water/P123 is presented in Fig. 2b. It is dominated by a strong absorption peak located at about ~270 nm, together with substantial, slowly decreasing absorbance at longer wavelengths. These features are known to be characteristic of graphitic, sp^2-based carbon nanostructures with limited oxidation, including pristine graphene and well reduced graphene oxide nanosheets, but not (unreduced) graphene oxide.[39,50,51] In particular, the peak at ~270 nm has been ascribed to $\pi \rightarrow \pi^*$ transitions in electronically conjugated domains of carbon materials with sizes larger than those typical of the conjugated domains in graphene oxide (i.e., larger than a couple of nanometers).[39,52]

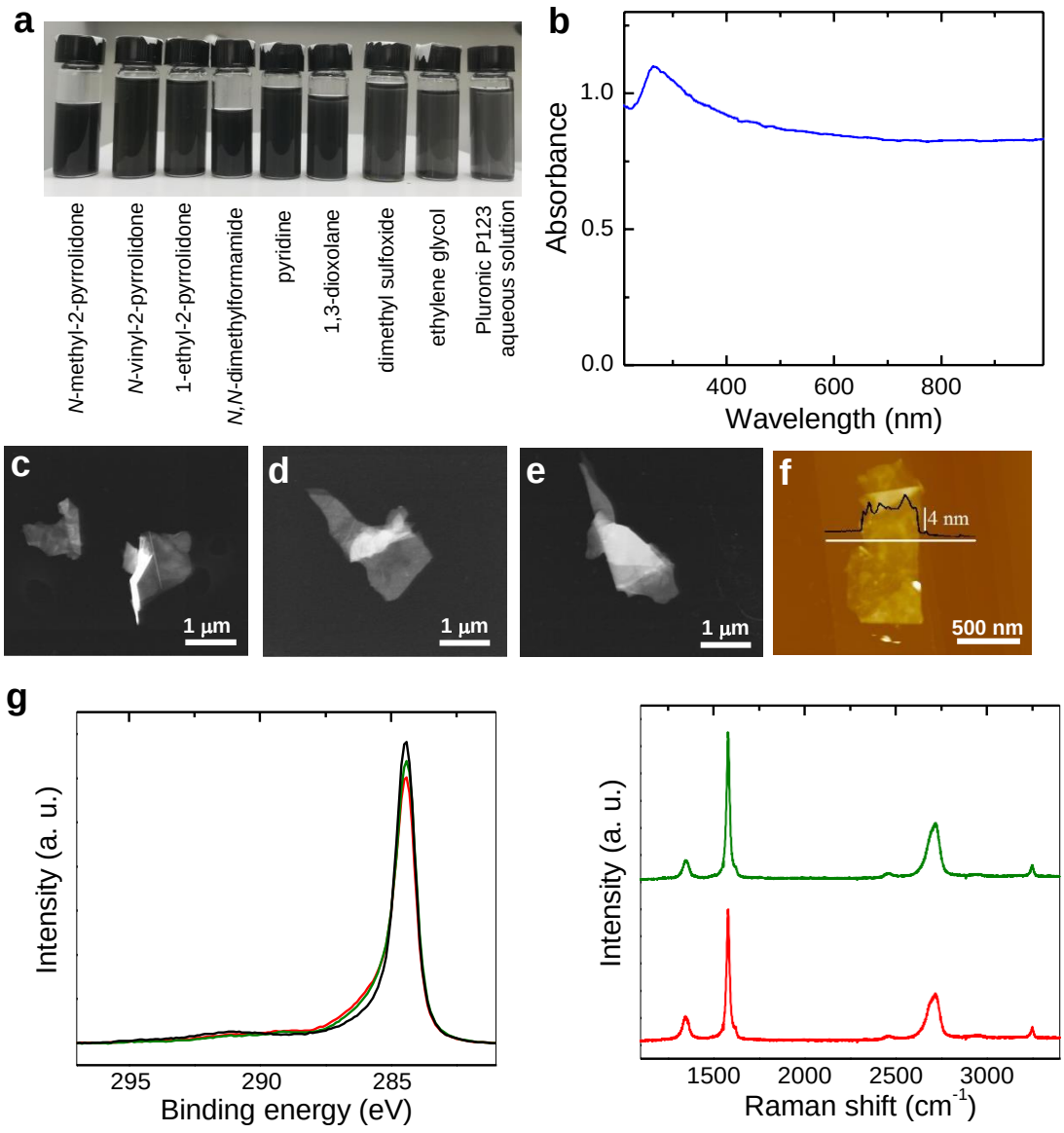
a
N-methyl-2-pyrrolidone
N-vinyl-2-pyrrolidone
1-ethyl-2-pyrrolidone
N,N-dimethylformamide
pyridine
1,3-dioxolane
dimethyl sulfoxide
ethylene glycol
Pluronic P123 aqueous solution
b
Absorbance
1.0
0.5
0.0
400
600
800
Wavelength (nm)
c
1 µm
d
1 µm
e
1 µm
f
4 nm
500 nm
g
Intensity (a. u.)
295
290
285
Binding energy (eV)
Intensity (a. u.)
1500
2000
2500
3000
Raman shift (cm-1)

Figure 2. Physicochemical characterization of the cathodically exfoliated graphenes isolated by ultrasonication of the expanded product in solvent media: **(a)** Digital picture of graphene dispersions in different solvents. From left to right: *N*-methyl-2-pyrrolidone, *N*-vinyl-2- pyrrolidone, *N*-ethyl-2-pyrrolidone, *N*,*N*-dimethylformamide, pyridine, 1,3-dioxolane, dimethyl sulfoxide, ethylene glycol and water with the non-ionic surfactant Pluronic P123 (0.5 wt%). **(b)** UV-vis absorption spectrum of a water/P123 dispersion of cathodic graphene obtained with 0.3 M HTMABr. **(c-e)** Representative STEM images recorded for cathodic graphene flakes. **(f)** Typical AFM image of graphene flakes deposited onto HOPG substrate from their dispersion. A representative line profile (black line) taken along the marked white line is shown overlaid on the image. **(g)** High resolution XPS C 1s core level spectra recorded for graphene obtained with 0.3 M HTMABr (red trace) and 0.3 M TPACl (green trace). The spectrum of the starting graphite foil has been added as a reference (black trace). **(h)** Raman spectra of graphene obtained with 0.3 M HTMABr (red trace) and with 0.3 M TPACl (green trace).

The physicochemical characteristics of the solvent-dispersed objects (e.g., lateral size and thickness, presence of structural defects and chemical composition) were analyzed by both microscopic and spectroscopic techniques. Direct evidence of the efficient generation of graphene nanosheets from the aqueous cathodic process was gathered by scanning transmission electron microscopy (STEM) and atomic force microscopy (AFM). Figure 2c-e shows typical STEM images recorded for graphene flakes obtained using 0.3 M HTMABr as. In all cases, the observed flakes exhibited an irregular polygonal shape with typical lateral sizes between several hundreds of nanometers and a few micrometers. The apparent thickness of the flakes derived from representative AFM height profiles was ~3–5 nm (Fig. 2f). However, detailed inspection of the AFM images revealed that the flakes were decorated by discrete features about 1 nm high, which could be ascribed to remnants of electrolyte and/or organic solvent molecules that remain adsorbed on the graphene surface despite the washing. The detection of small amounts of nitrogen (<1 at%) by X-ray photoelectron spectroscopy (XPS) analysis of paper-like films prepared by filtration of the graphene dispersions (see Fig. S1 of the Supporting Information) provided further evidence of the presence of electrolyte and/or organic solvent molecules adsorbed on their surface.

Indeed, this effect has been previously reported for cathodically exfoliated graphite obtained with ammonium-based salts in organic medium.[26] It was thus reasonable to assume that the measured apparent thickness of the flakes included a contribution of up to about 2 nm (i. e., ~1 nm from each face of the flake) from adsorbed electrolyte/organic solvent. Consequently, the actual thickness of the flakes would be ~1–3 nm, thus typically comprising between 3 and 10 layers. Chemical analysis by XPS of the graphene flakes processed into films revealed that carbon was the dominant element, although some amount of oxygen and nitrogen, as mentioned above, was also found (see Fig. S1 of the Supporting Information). The O/C atomic ratio was 0.05–0.08, similar to the values reported for prior cathodically exfoliated graphenes obtained in organic media.[24,26] Fig. 2g shows high resolution C 1s core level spectra for graphene obtained with

0.3 M HTMABr (red trace) and 0.3 M TPACl (green trace). For comparison purposes, the corresponding spectrum for the starting graphite foil is also shown (black trace). The C 1s band for the cathodically exfoliated graphenes was sharp and centered at ~284.6 eV (C=C structures in non-oxidized graphitic domains), and displayed only a minor contribution from oxidized species (e. g., hydroxyl or epoxide C-O groups) centered at ~286.5 eV.[39] These results corroborated that the cathodic graphenes obtained in aqueous medium were oxidized only to a rather limited extent.

The structural quality of the cathodic graphenes was evaluated by Raman spectroscopy, as illustrated in Fig. 2h for materials obtained with 0.3 M HTMABr (red trace) and 0.3 M TPACl (green trace) as electrolytes. The spectra were dominated by three bands: the G band characteristic of graphite/graphene materials (~1582 cm^{-1}), the defect-related D band (~1350 cm^{-1}) and its overtone, the 2D band (~2700 cm^{-1}).[53] The integrated intensity ratio of the D and G bands (I_D/I_G ratio), which is widely adopted as a quantitative measure of the amount of defects present in graphitic structures,[53] yielded values of 0.2–0.3 for the cathodically exfoliated graphenes. These values are comparable to, or even lower than, those usually reported for graphenes obtained by direct liquid-phase exfoliation of graphite. Although such I_D/I_G ratios were significantly larger than that of the starting graphite foil (~0.03), they are not thought to arise from a greater number of basal plane defects in the exfoliated graphene flakes, but from the relatively small lateral dimensions of the flakes. Given that the diameter of the Raman laser spot (a few micrometers) was larger than the typical flake size (see Fig. 2c–f and

discussion above), the flake edges must have contributed substantially to the intensity of the defect-related D band.[54,55]

Taken together, the characterization results allow concluding that the dispersions obtained via aqueous cathodic exfoliation were comprised of few- to several-layer graphene flakes that largely retained the chemical and structural integrity of their parent material. Such high structural quality and limited oxidation was expected to imply the retention of high electrical conductivity. Indeed, the conductivity of films obtained by vacuum-filtration of the present cathodic graphene dispersions obtained using, e. g., 0.3 M HTMABr as the electrolyte was 1.5×10^4 S m^{-1}. This figure compared favorably with the values previously reported for graphene films obtained by direct exfoliation of graphite via ultrasonication in organic solvents or water-surfactant systems (~2×10^2–5×10^4 S m^{-1})[54–58] and was similar to the values obtained beforehand for films of high-quality, low-oxidized anodic graphene obtained with oxidation-preventing electrolytes or electrolyte additives (~1×10^4 –4.6×10^4 S m^{-1}).[20,21,38]

2.3. Overall yield of the exfoliation process and relevance of the starting graphite type

The overall yield of graphene nanosheets produced with the best-performing aqueous electrolytes (i.e., the mass of graphene extracted from the expanded material relative to the mass of the starting graphite foil piece) was estimated by determining the concentration of the corresponding dispersions in a good solvent such as *N*-methyl-2-pyroolidone. Dispersion concentrations were assessed following previously reported protocols based on the use of UV- vis absorption spectroscopy (Lambert-Beer law).[21,56] For many electrolytes, roughly one third to one half of the mass of the expanded product could be extracted as graphene nanosheets, implying that the overall graphene yield was about one third to one half of the corresponding yield of expanded material. This was particularly the case of the best electrolytes, namely, TPACl and HTMABr, which boasted overall yields of ~15–20 wt%. It is important to note that the yield of expanded product and thus the overall graphene yield were highly dependent on the thickness of the graphite foil piece used in the experiments, thinner foils affording higher yields of expanded material. The yields of expanded product collected in Table 1 were obtained with ~500 μm thick graphite foil, whereas in many instances in the literature

substantially thinner foils (e.g., between 100 and 250 μm) have been used for electrochemical exfoliation experiments (both anodic and cathodic).[20,24,30,36,37,59] Indeed, carrying out the cathodic treatment in 0.3 M TPACl or HTMABr with ~70 μm thick foil pieces led to yields of expanded product close to 100 wt%, and thus to overall graphene yields of ~40–50 wt%. These overall yields were commensurate with, or even better than, the graphene yields previously reported for the cathodic exfoliation of different types of graphite (foil, rod, powder, etc) in organic solvents,[23,29,31,32,60–62] indicating that the present water-based cathodic approach is competitive with those implemented in non-aqueous media.

As briefly noted above, a critical issue for the successful attainment of graphene through cathodic exfoliation in water was a proper choice of the graphite type to be used as an electrode. While substantial amounts of expanded product and then graphene nanosheets could be generated with certain electrolytes and graphite foil as the cathode (Table 1), the same was not true when graphite foil was replaced by other types of graphite, such as graphite rod or HOPG. In these cases, almost no expansion of the cathode was observed even if using the best-performing electrolytes (for HOPG, a very slight expansion could be noticed), so that graphene nanosheets could not be extracted in any significant quantities. We believe the ultimate origin of such a discrepancy between graphite foil and other graphite types to be in the different packing configurations of the graphene layers in the materials. For HOPG, graphite rod and other graphite varieties (powder, flakes), the graphene layers are very tightly stacked onto each other, leaving essentially no interlayer voids or openings.[39] In the absence of oxidation processes at the graphite electrode during the electrolytic treatment, which are only expected to occur under anodic conditions, the interlayer spaces adjacent to the graphite edges should remain mostly hydrophobic and unexpanded, thus preventing the entry of hydrated cations from the electrolyte and thus the electrode expansion (Fig. 3a).

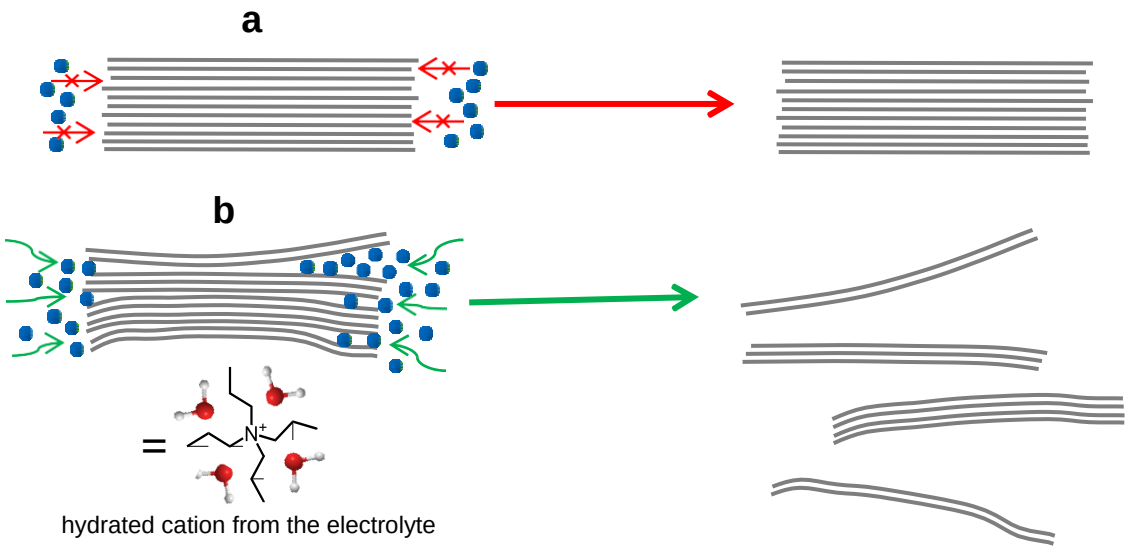

Figure 3. Schematic of the cathodic exfoliation process for **(a)** graphite with tightly stacked graphene layers, such as graphite powder, flakes, rod, etc. and **(b)** graphite containing local areas with expanded interlayer spacing, such as graphite foil. In (a), hydrated cations from the electrolyte are not able to enter the interlayer spaces, as the latter remain hydrophobic and unexpanded due to the absence of oxidizing conditions in the electrolytic treatment. As a result, no expansion and exfoliation of the material is attained. In (b), pre-formed interlayer openings and voids in the graphite material facilitate the entry of hydrated cations, then triggering its expansion and exfoliation.

On the other hand, graphite foil is known to possess a large number of nanometer-sized interlayer voids and packing imperfections, i.e., local areas with expanded interlayer spacing, which arise from its production process (roll compaction of expanded graphite particles).[39] In particular, the interlayer voids located adjacent to graphite edges should act as selective entry points and facilitate the initial intercalation of a number of hydrated cations from the electrolyte (Fig. 3b). The latter would then behave as a sort of advance party, playing the role of a molecular wedge and triggering a further expansion of the interlayer spacing at increasing distances from the edges into the graphite particle. In turn, this process should favor the subsequent intercalation of more hydrated cations, which would continue cleaving the layers to finally give expanded products from which graphene nanosheets can be readily extracted. Overall, it

can be concluded that a pre-requisite for the successful exfoliation of graphite in water under both anodic and cathodic conditions is the presence of expanded edges that facilitate the intercalation of hydrated ions. However, whereas expanded edges can be generated *in situ* under anodic conditions as a result of built-in oxidation processes,[17,37] they have to be pre-formed by some means for cathodic exfoliation, for instance, by applying a proper pre-expansion step to the graphite material, as was the case of graphite foil. We also note that the need to use this type of graphite should not constitute a significant problem with a view to the industrial implementation of cathodic exfoliation in water for the production of high quality graphene. Graphite foil is manufactured annually by the ton as a modestly priced commodity (less than U.S. $0.1 per gram, compared to about U.S. $100 per gram for HOPG), which should contribute to the affordability of the aqueous cathodic route.

2.4. Application of cathodically exfoliated graphene as sorbent in oil absorption and electrochemical energy storage

The high-quality, low-oxidized, and electrically conductive graphene obtained here by aqueous cathodic exfoliation could find use, e. g., as a sorbent in water/oil remediation, where hydrophobicity is a requisite, or as an electrode for energy storage, where a high electrical conductivity is needed. A large specific surface area would be an additional requirement for both applications that graphene-based materials could in principle fulfill. Among our materials, those subjected to sonication after cathodic expansion would in principle display higher exposed surface areas in liquid media. However, when these well-separated graphene nanosheets are removed from their dispersing solvent or when the (non-sonicated) cathodically expanded graphite materials are removed from their electrolytic and washing media to handle them as bulk solid products for practical uses, they tend to re-stack into more compact configurations, with the subsequent decrease in surface area and performance in such uses.[63] To alleviate this issue, proper assembling strategies must be put in place, which frequently involve the construction of three-dimensional structures with the aid of components other than graphene.[64] Here, we have investigated two such protocols for the present cathodic graphene in the context of its use as a sorbent for oils/organic solvents and as an electrode for energy storage (supercapacitors). Fig. 4a shows the sorption capacity of as-expanded (non-sonicated) materials obtained via cathodic exfoliation of graphite using

0.3 M HTMABr (red bars) and 0.3 M TPACl (green bars) towards several organic solvents and oils, namely, toluene, heptane, dodecane, tetrahydrofuran, acetone, chloroform, olive oil and pump oil. As expected from their hydrophobic nature, these materials were good sorbents for such liquids, with measured sorption capacities ranging between ~8 and 20 g/g, comparable to those reported for light weight graphene-based sorbents of similar density (30–45 mg cm^{-3})[22] (see Table S1 in the Supporting Information for a comparative list). Nevertheless, it is noteworthy that the much simpler and faster preparation of the present materials constitutes an asset over those prior graphene-based sorbents. To improve these sorption figures with cathodic graphene, though, it is clear that macroscopic structures of a lower density must be used. To this end, we resorted to commercial melamine foam (density: ~8–10 mg cm^{-3}) as a scaffold that was coated with a thin layer of graphene nanosheets.[65] Coating was accomplished by repeatedly soaking the foam into a (sonicated) dispersion of cathodic graphene nanosheets in pyridine and drying at moderate temperature, giving rise to graphene loadings on the foam of up to 4 mg cm^{-3} (see Experimental section for details). Fig. 4b shows digital photographs of the starting melamime foam (white dices) and the graphene-coated one (blackish dices) after casting droplets of acetone and water with yellow and magenta dye, respectively, to facilitate observation of their fate. The neat, non-coated melamine foam, which was originally both hydrophilic and oleophilic, became highly hydrophobic after coating with graphene. Indeed, the water contact angle for the graphene-coated material was determined to be ~120° (inset to bottom panel of Fig. 4b). FE-SEM imaging provided insight into the structural origin of the observed change: the starting (hydrophilic) surface of the foam (Fig. 4c) became largely covered with the (hydrophobic) graphene nanosheets after dip- coating (Fig. 4d). These results indicate that the graphene-coated foam can be used as a selective sorbent for, e. g., removing oil spills from water, as illustrated by the series of successive (from left to right) digital photographs shown in Fig. 4e, where the oil phase originally floating on water was removed by dipping the graphene-coated foam. The measured sorption capacities of the graphene-coated foam towards the different solvents ans oils are given in Fig. 4f, with typical values ranging between 60 and 150 g/g, i. e., 3 to 10 times larger than those determined for by the as-expanded material (compare Figs. 4a and f). This improvement must come from the lower density (~12–14 mg cm^{-3}) of the former sorbent. Another advantage of the graphene-coated foam over the as-obtained powdery

solid lies in its easier handling. Indeed, as seen in the digital photographs in Fig. 4e, oil contamination could readily be removed from water just by dipping the coated foam sorbent into the liquid for a few seconds. The regeneration of the foam could be performed very conveniently as well, just by squeezing it and gathering the desorbed liquid on absorbent paper. Furthermore, the sorption capacity for the oils after ten sorption/desorption cycles was retained to a large extent, as indicated by the re-usability tests gathered in Fig. 4g. We note that the ability of the cathodic graphene-coated foam to retain its oil sorption capacity after repeated use was much better than that of previously reported melamine foam coated with graphene derived from chemically expanded graphite, where an ~80% decrease in oil sorption capacity was measured during the first few cycles,[65] thus highlighting the practical advantage of the present materials.

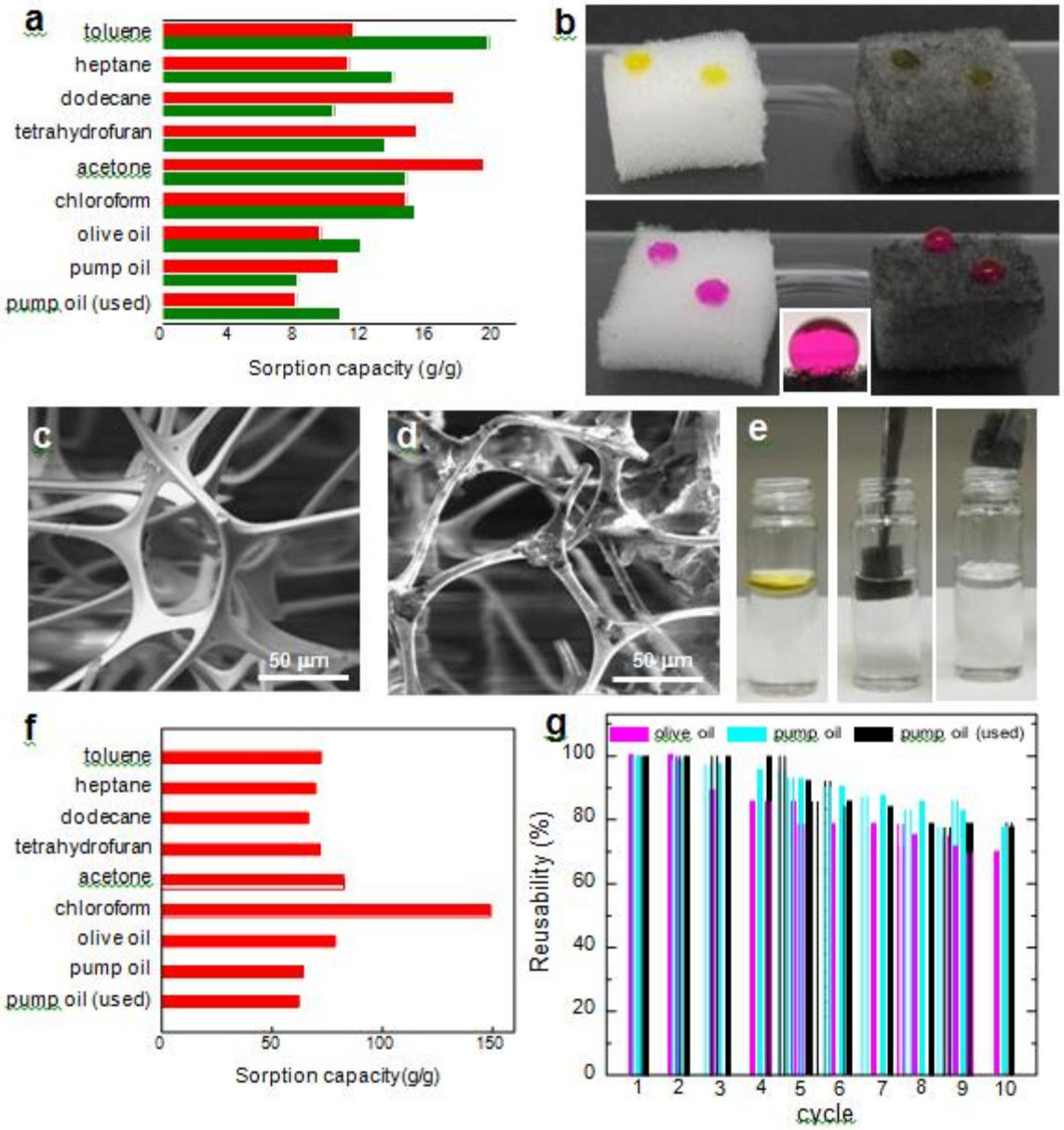

Figure 4. (a) Sorption capacity for different organic solvents and oils of as-expanded graphite materials obtained via cathodic exfoliation of graphite foil using 0.3 M HTMABr (red bars) or 0.3 M TPACl (green bars) as the electrolyte. **(b)** Digital pictures of droplets of acetone (top) and water (bottom) deposited on the surface of melamine foam (white dice) and graphene- coated melamine foam (blackish dice). A dye (yellow for acetone and magenta for water) has been added to the droplets to render them more readily visible. Inset: magnified photograph of a water droplet on the surface of graphene-coated melamine foam. **(c,d)** FE-SEM images of the neat, non-coated

melamine foam **(c)** and melamine foam coated with graphene **(d)**. **(e)** Digital photographs of: olive oil floating on water (left), a graphene-coated melamine foam adsorbing the oil phase (middle), and the final oil-free water after extraction of the sorbent (right). **(f)** Sorption capacity of graphene-coated melamine foam towards different organic solvents and oils. **(g)** Histogram for the re-usability of the graphene-coated foam for the sorption of oils.

The cathodically exfoliated material was also tested as an electrode for capacitive energy storage. Again in this case, the dried, as-expanded non-sonicated graphite material (0.3 M HTMABr) was preferred to the its solvent-sonicated counterpart for direct use as the electrode material, due to its easier processing and handling. The electrochemical charge storage experiments were carried out in a three-electrode configuration with aqueous 6M KOH as the electrolyte (see Experimental Section for details). Fig. 5a shows the cyclic voltammetry (CV) curves recorded for the as-expanded material at different potential scan rates. The voltammograms exhibited nearly rectangular shape with no redox peaks, indicating that charge storage in the electrode was dominated by the formation of an electric double layer, with no significant contribution from Faradaic processes (i. e., pseudocapacitance). This is the expected behavior for carbon materials with low heteroatom content (including the present cathodic graphene), and thus low amounts of electroactive species (e.g., certain oxygen- containing functional groups).[63] Fig. 5b shows typical galvanostatic charge/discharge curves recorded at different current densities for the as-expanded material. The curves displayed nearly symmetrical shapes and linear slopes, which is again consistent with electrochemical double-layer capacitive processes as the prevailing charge storage mechanism. As displayed in Fig. 5e (red squares), the gravimetric capacitance values calculated from the discharge curves for this material were ~25 F g^{-1} at 0.3 A g^{-1} and decreased down to ~5 F g^{-1} at a current density of 20 A g^{-1}. These figures were rather low in comparison with those reported for other graphene materials previously tested as electrodes for capacitive energy storage (see Table S2 in the Supporting Information for a comparative list). We interpret such a poor performance to be the result of significant re-stacking taking place in the material during its processing to form the electrodes. More specifically, re-stacking could readily arise from the drying and pressing of the cathodically expanded graphite. This re-

stacking, together with the hydrophobic nature of the low-oxidized cathodic graphene layers, should prevent an effective wetting of interlayer spaces by the electrolyte, hence seriously limiting the capacitance of the electrode.

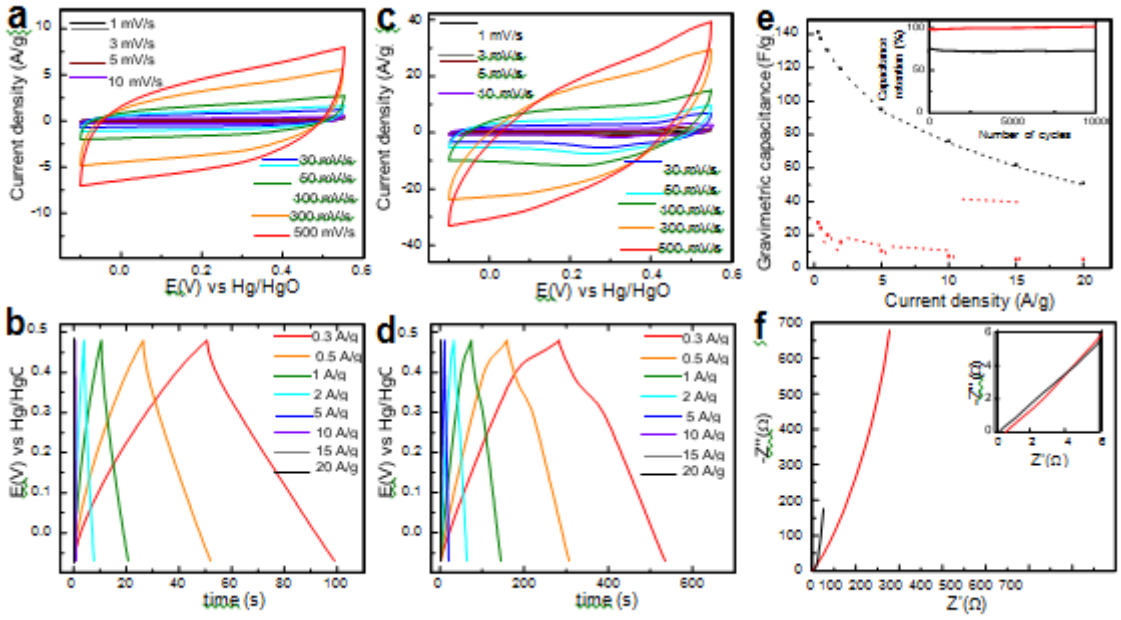

Figure 5. Electrode performance tests for catodically exfoliated graphite both alone and in combination with cobalt oxide nanosheets. Cyclic voltamograms recorded at potential scan rates between 1 and 500 mV/s for cathodic graphene alone **(a)** and cathodic graphene combined with cobalt oxide **(c)**. Galvanostatic charge/discharge curves recorded at current densities between 0.3 and 20 A/g for cathodic graphene alone **(b)** and cathodic graphene combined with cobalt oxide **(d)**. **(e)** Gravimetric capacitance values determined at different current densities from the discharge curves in b (red squares) and d (black squares). Inset to e: capacitance retention (in percentage) measured at a current density of 2 A/g for consecutive charge/discharge cycles (up to 10000) of the electrodes prepared from cathodic graphene alone (red trace), and cathodic graphene in combination with cobalt oxide (black trace). **(f)** Electrochemical impedance spectra of cathodic graphene alone (red trace) and cathodic graphene combined with cobalt oxide (black trace). Inset to f: detailed view of the high frequency region of the spectra.

To improve the capacitive performance of the cathodically expanded material, we combined it with a small amount of an electroactive material (cobalt oxide) in nanosheet morphology, which could provide a two-fold benefit: (1) to contribute pseudocapacitance to the hybrid electrode, and (2) to act as a spacer material within the expanded graphite, thus alleviating to some extent the issue of re-stacking during the electrode processing.[63,66] We synthesized cobalt oxide nanosheets following the general solvothermal method originally proposed by Sun et al for the preparation of stand-alone transition metal oxide nanosheets,[67] but with the novelty that here the wet synthesis was performed in the presence of cathodically expanded graphite (see Experimental Section for details). The fact that the originally grey material acquired a slightly greenish tone after the process pointed to the successful generation of cobalt oxide.[68] Indeed, the amount of metal oxide present in the hybrid structure was determined to be ~5 wt% by elemental analysis. By comparison of the FE-SEM images of the surface of the as-expanded graphite before (Fig. 6a and c) and after (Fig. 6b and d) the solvothermal synthesis, we inferred that the small elongated features that uniformly decorated the surface of the latter correspond to cobalt oxide lamellae. Indeed, the nanosheets were seen to be attached sideways on to the expanded graphite plane, instead of lying flat on its surface. This morphology should be beneficial for the use of the material for capacitive energy storage, as it should increase the surface exposed to the electrolyte and improve accessibility of the ions. The presence of cobalt oxide on the expanded graphite was confirmed by XPS. Indeed, the recorded high resolution Co $2p_{3/2}$ core level spectrum (Fig. 6d) was that expected for cobalt in an oxidation state of +2.[69] Indeed, the Co $2p_{3/2}$ band comprised a main peak located at a binding energy of ~781 eV, and a second, less intense satellite band at ~786 eV typical of cobalt (II) species.

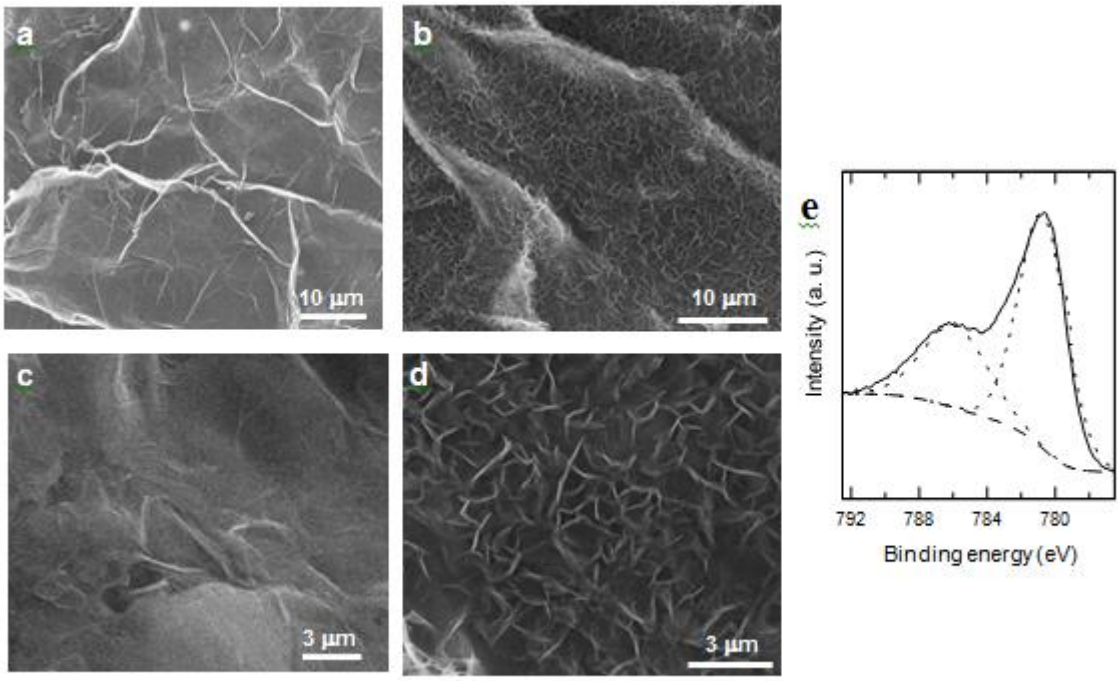

Figure 6. FE-SEM images of cathodically espanded graphite alone **(a,c)** and the same material coated with cobalt oxide nanosheets **(b,d)**. **(e)** High resolution Co $2p_{3/2}$ XPS spectrum of the expanded graphite-cobalt oxide hybrid. The background (dashed line), and the two components obtained upon peak-fitting of the spectrum (dotted lines) are also indicated.

The performance of the cathodicaly expanded graphite as an electrode was significantly improved by the small amount of cobalt oxide nanosheets, both in terms of delivered current (see Fig. 5c) and gravimetric capacitance values (Fig. 5e), the latter being 50–140 F g^{-1} for current densities ranging between 20 and 0.3 A g^{-1}. The occurrence of Faradaic redox reactions, in addition to purely capacitive processes, was confirmed by the appearance of oxidation and reduction humps visible in the CVs recorded at low potential scan rates (Fig. 5c) at potentials of ~0.45 V and ~0.3 V vs Hg/HgO, respectively. The corresponding galvanostatic charge/discharge curves (Fig. 5d) were less symmetrical than those of its cobalt oxide-free counterpart (Fig. 5b), which was expected from the fact that some of the charge will be stored by ionic intercalation (pseudocapacitance) into the electrode and not just by the formation of an electrical double layer on its surface. This hybrid electrode was also stable, retaining its capacitance after 10,000 consecutive charge/discharge cycles at 2 A g^{-1} (black trace in the inset to Fig. 5e).

Information on ionic diffusion and electronic conductivity of the tested electrodes (with and without cobalt oxide), was obtained by electrochemical impedance spectroscopy. Fig. 5f shows Nyquist plots of the two electrodes. At high frequencies (inset to Fig. 5f) both materials behaved similarly, showing a negligible equivalent series resistance (i. e., a high conductivity), as indicated by the absence of a semicircle in that region. In the case of the cobalt oxide-containing materials, there was a short segment at 45° phase angle related to diffusion-controlled Faradaic reactions, followed by a nearly vertical line, indicative of an almost ideal capacitive behavior. However, the curve for the cobalt oxide-free material (red trace) exhibited a lower, similar phase angle largely independent of the frequency. This behavior has been previously observed for some porous carbon-based double-layer capacitors and is thought to have a non-diffusional origin related to the presence of a distributed resistor- capacitor network due to the porous nature of the electrode, where slit- and/or wedge-shaped pores lead to the kind of curve envelope observed here. Indeed, such types of pore shape are the ones expected for graphenes obtained through electrochemical exfoliation (see Fig. 3).

3. Conclusions

We have demonstrated that high quality graphene nanosheets can be obtained in substantial yields (up to ~40-50 wt%) through cathodic exfoliation of graphite in water-based electrolytes. Two aspects were found to be critical for a successful and efficient aqueous cathodic exfoliation, namely, the type of starting graphite and the electrolyte. In the absence of oxidizing conditions during the electrolytic treatment such as those typically found in anodic exfoliation processes, the use of graphite materials having pre-expanded edges and interlayer voids (e.g., graphite foil) was seen to be essential for an effective intercalation of the material by aqueous cations. As for the electrolyte, quaternary ammonium-based cations of a certain intermediate size (e.g., tetrapropylammonium or hexyltrimethylammonium) exhibited an optimum ability to expand the graphite cathode and give graphene nanosheets in competitive yields. The exfoliated material could be colloidally dispersed in different media and was made up of few- to several-layer nanosheets with low defect content and limited oxidation. Melamine foam coated with cathodic graphene nanosheets was tested as a hydrophobic sorbent for the removal of oils and organic solvents from water, exhibiting good sorption capacities and a high re-usability. Likewise, combination of the cathodically exfoliated material with a small amount of vertically oriented cobalt oxide nanosheets

afforded hybrids with good capacitive charge storage characteristics. Overall, we believe that the water-based route developed here should raise the prospects of cathodic exfoliation as a competitive approach in the efforts to industrialize the production of high quality graphene for use in different practical applications.

4.1. Experimental section

4.1. Materials and reagents

Three types of high-purity graphite were used in the electrochemical exfoliation experiments, namely, graphite foil, graphite rod and highly oriented pyrolytic graphite (HOPG). Graphite foil (Papyex I980) with a thickness and mass density of ~500 μm and 1.1 g cm^{-3}, respectively, was acquired from Mersen. Graphite rod (diameter: 3.05 mm; density: 1.7 g cm^{-3}) was purchased from Alfa Aesar, whereas HOPG (grade ZYH, density: 2.25 g cm^{-3}) was obtained from Advanced Ceramics. Unless stated otherwise, all the chemicals used throughout the study (salts, organic solvents, reagents, etc) were received from Sigma- Aldrich. The following salts were used for the preparation of the aqueous electrolytic media for cathodic exfoliation: ammonium chloride (ACl), trimethylamine hydrochloride (TMAHCl), tetramethylammonium chloride (TMACl), tetraethylammonium chloride (TEACl), tetrapropylammonium chloride (TPACl), tributylamine hydrochloride (TBAHCl), tributylmethylammonium chloride (TBMACl), tetrabutylammonium chloride (TBACl), hexyltrimethylammonium bromide (HTMABr), octyltrimethylammonium bromide (OTMABr), dodecyltrimethylammonium bromide (DDTMABr), hexadecyltrimethylammonium bromide (HDTMABr), phenyltrimethylammonium chloride (PhTMACl) and benzyltrimethylammonium chloride (BzTMACl). Organic solvents for colloidal dispersion of the cathodic graphene nanosheets: *N*-methyl-2-pyrrolidone (NMP), N-ethyl-2-pyrrolidone (NEP), N-vinyl-2-pyrrolidone (NVP), *N*,*N*-dimethylformamide (DMF), dimethyl sulfoxide (DMSO), 1,3-dioxolane and pyridine. Organic liquids for sorption tests: toluene, heptane, dodecane, tetrahydrofuran, acetone and chloroform. Oils for sorption tests: Commercial olive oil, commercial rotary vane pump. Commercial melamine foam (density

~8–10 mg cm^{-3}) was used as a scaffold for graphene in sorption tests. Other chemical reagents, surfactants and salts for synthesis: cobalt (II) acetate tetrahydrate, hexamethylenetetramine and Pluronic P123 (block copolymer surfactant). Milli-Q

deionized water (resistivity: 18.2 MΩ·cm; Millipore Corporation) was used in all the experiments.

4.2. Cathodic exfoliation experiments

The cathodic exfoliation tests were undertaken in a two-electrode configuration, using a graphite piece as the cathode, platinum foil (dimensions: 25 × 25 × 0.025 mm^3) as the anode, and an aqueous solution of a given ammonium-based salt as the electrolytic medium. Most of the experiments were carried out with graphite foil (55 × 30 × 0.5 mm^3), although for comparative purposes HOPG (10 × 5 × 0.5 mm^3) and graphite rod (diameter: 3.05 mm; length: 40 mm) were also employed. The graphite cathode and platinum foil were immersed in the electrolytic solution (80 mL) at a distance of ~2 cm from each other and connected to the current source (Agilent 6614C DC power supply) through crocodile clips. A negative potential (typically -10 V) was subsequently applied to the graphite electrode for 2 h, during which the material was generally seen to swell and expand in different proportions depending on the specific salt used as an electrolyte, with some expanded graphite fragments of millimeter dimensions detaching from the cathode and being left to float on the aqueous solution. After the electrolytic treatment, the fraction of the graphite foil that was expanded was gently scraped from the cathode with a spatula and collected together with the detached graphite fragments. This product was then extensively washed with water (1.5 L) through filter paper to remove remnants of the ammonium-based salt, and finally allowed to dry at room temperature in air for one day and overnight under reduced pressure at 60 °C. To extract individual graphene nanosheets from the expanded product, the latter product was transferred to a certain organic solvent (NMP, NEP, NVP, DMF, DMSO, 1,3-dioxolane or pyridine) or to an aqueous solution of the surfactant Pluronic P123 (0.7 mg mL^{-1}) and sonicated for 3 h in an ultrasound bath cleaner (J.P. Selecta Ultrasons system, 40 kHz). The resulting suspension was left to stand undisturbed for 24 h or, alternatively, centrifuged at 100g for 20 min, after which the supernatant was collected and stored for further use, with the sediment being discarded. Following previously reported procedures,[56] the concentration of graphene nanosheets in the supernatant dispersion was estimated by means of UV-vis absorption spectroscopy on the basis of the Lambert-Beer law, measuring the absorbance of the dispersion at a wavelength of 660 nm and using an extinction coefficient value of α_{660} =

2440 mL mg^{-1} m^{-1}.

4.3. Characterization techniques

The samples were characterized by UV-vis absorption spectroscopy, field-emission scanning electron microscopy (FE-SEM), scanning transmission electron microscopy (STEM), atomic force microscopy (AFM), Raman spectroscopy and X-ray photoelectron spectroscopy (XPS). UV-vis absorption spectra were obtained with a double-beam Heλios α spectrophotometer (Thermo Spectronic). FE-SEM and STEM images were recorded on a Quanta FEG 650 apparatus (FEI Company) working at a voltage of 20–25 kV. Specimens for FE-SEM were directly mounted onto metallic sample holders using double-sided carbon adhesive tape, whereas for STEM the samples were first dispersed in a water/isopropanol mixture (50/50, v/v) by bath-sonication for 3 h (J.P. Selecta Ultrasons system, 40 kHz, power

~20 W L^{-1}) and then drop-cast (~150 μL) onto a copper grid (200 square mesh) covered with a thin, continuous carbon film (Electron Microscopy Sciences). AFM imaging was carried out in the tapping mode of operation with a Nanoscope IIIa Multimode microscope (Veeco), using silicon cantilevers with nominal spring constant and resonance frequency of ~40 N m^{-1} and 250–300 kHz, respectively. HOPG was employed as a supporting substrate for AFM, onto which an aqueous dispersion of the sample (prepared by bath-sonication) was deposited by drop-casting. Raman spectroscopy was conducted in a LabRam apparatus (Horiba Jobin Yvon) with a laser excitation wavelength of 532 nm. For XPS, a SPECS apparatus working at a pressure of 10^{-7} Pa and using a non-monochromatic Mg K_α X-ray source (11.81 kV, 100 W) was employed. Specimens for both Raman and XPS analysis were prepared by drop-casting graphene dispersions onto a metallic sample-holder pre-heated at ~50–60 ºC and allowing them to dry under ambient conditions until a uniform film was seen to cover the substrate. For the measurement of electrical conductivity, free-standing paper-like films were prepared by vacuum-filtration of graphene dispersions in NMP through a hydrophilic PTFE membrane filter (47 mm in diameter and 0.1 μm of pore size, from Merck Millipore). Then, 12 × 12 mm^2 square pieces were cut from the film and their conductivity determined by the van der Pauw method using a homemade setup (Agilent 6614C DC power source and Fluke 45 digital multimeter). The thickness of the films was estimated by FE-SEM and independently with a digital micrometer.

4.4. Testing of cathodically exfoliated graphene as a sorbent for oils/organic solvents and as an electrode for capacitive energy storage

The cathodic graphenes were tested as sorbents for organic solvents and oils, and as electrodes for electrochemical charge storage. Two types of graphene-based materials were tested as sorbents: (i) the as-expanded materials obtained with 0.3 M TPACl and 0.3 M HTMABr, i. e., the products directly obtained from the cathodic delamination process without a subsequent sonication step (only washed with water to remove remnants of the electrolyte), and (ii) cathodic graphene nanosheets extracted from the as-expanded product (0.3 M TPACl) through sonication and coated onto melamine foam. To prepare the graphene-coated melamine foam, a graphene dispersion at a concentration of ~0.25 mg mL^{-1} was first prepared by bath sonication of the as-expanded graphite in pyridine for 3 h. Then, a ~1 cm^3 cube of commercial melamine foam was soaked into the dispersion for 1 min and subsequently heated on a hot plate for 5 min to evaporate the solvent. The soaking/evaporation process was repeated three or four times up to graphene loadings of 4 mg cm^{-3} onto the foam. For the sorption of oils and organic solvents, a certain mass of powdery, expanded material (typically 10–15 mg) was first put in a 1.5 mL vial. Then, small known volumes of a given oil/solvent (usually ~50 μL) were successively dropped on the material, which took them up until a point was reached where the sorbent became saturated and the liquid was seen to overflow the powder by the naked eye. Such a saturation point allowed estimating the total volume of oil/solvent retained by the solvent. Similarly, the sorption capacity of the graphene-coated foams was calculated from the maximum volume of liquid taht they were seen to absorb without dripping, using the following densities for each liquid: toluene (0.865 g cm^{-3}), *n*- hexane (0.63 g cm^{-3}), dodecane (0.75 g cm^{-3}), tetrahydrofuran (0.886 g cm^{-3}), acetone (0.79 g cm^{-3}), chloroform (1.492 g cm^{-3}), olive oil (0.91 g cm^{-3}) and pump oil (0.86 g cm^{-3}). For the reusability tests, the foams were regenerated through extraction of the absorbed liquid by squeezing the foam between the handles of a pair of tweezers and gathering the desorbed liquid on absorbent paper.

The electrochemical energy storage experiments were carried out in a three-electrode configuration with a Swagelok-type cell, using either as obtained expanded graphite or cobalt oxide-coated expanded graphite as the working electrode, a commercial activated carbon fiber as the counter electrode, Hg/HgO (1 M NaOH) as the reference electrode and aqueous 6 M KOH as the electrolyte. Cobalt oxide-coated cathodically expanded

graphite was prepared by synthesizing cobalt oxide nanosheets in the confined 2D space of lamellar reverse micelles as reported elsewhere[67] but here in the presence of the cathodically expanded graphite. Specifically, 200 mg of Pluronic P123 were dissolved in 17.5 mL of a mixed ethanol/water (33/2, v/v) solvent under stirring. Subsequently, 250 mg of cobalt (II) acetate tetrahydrate, 70 mg of hexamethylenetetramine and 50 mg of cathodically expanded graphite were added to the resulting mixture. After 15 min, 13 mL of ethylene glycol were poured into the suspension. After 30 min of continuous stirring, the mixture was allowed to statically age for 24 h. The aged suspension was then transferred to a Teflon-lined autoclave (capacity: 40 mL) and heat-treated at 170 ºC for 2 h. The resulting slightly greenish solid product was thoroughly washed by repeated cycles of centrifugation (2000 g for 20 min, J.P. Selecta Meditronic centrifuge in 30 mL tubes) and re-suspension first in water and then in ethanol (3 cycles for each solvent), and finally dried at room temperature under a vacuum. The amount of cobalt oxide incorporated to the cathodically expanded graphite was determined from the difference between the elemental analyses of expanded graphite alone and combined with cobalt oxide (LECO Truspec Micro CHN microanalyses apparatus with a LECO Truspec Micro O accessory for direct O determination). For the electrochemical charge storage tests, the working electrode was prepared by pressing uncoated or cobalt oxide-coated expanded graphite powder onto circular graphite foil pieces (~1 cm in diameter). Typical loadings onto the graphite foil support were ~1 mg cm^{-2}. The counter electrode was obtained in the form of a paste that incorporated, in addition to the activated carbon fiber, polytetrafluoroethylene as a binder and carbon black as a conductive additive, in a weight ratio of 90:5:5. A circular piece (~1.3 cm in diameter) of nylon membrane filter (0.45 μm of pore size, from Whatman) was used as the electrode separator. Before the cell was assembled, the working and counter electrodes as well as the separator were individually soaked in 6 M KOH and vacuum- degassed. Prior to the measurements, the assembled cell with the electrolyte was also vacuum-degassed. The measurements were carried out in a VSP potentiostat (Bio-Logic Science Instruments), recording cyclic voltammograms at different voltage scan rates, and galvanostatic charge/discharge curves at different current densities. Electrochemical impedance spectra were also recorded for the fully discharged cell in the frequency region between 100 kHz and 10 mHz at a voltage amplitude of 10 mV.

Supporting Information. Additional XPS characterization of the materials; tables gathering a comparison of the sorption capacity and gravimetric capacitance values of the materials prepared in this work with those previously reported for other graphene-based materials.

Acknowledgements

Funding by the Spanish Ministerio de Economía y Competitividad (MINECO) and the European Regional Development Fund (ERDF) through project MAT2015-69844-R is gratefully acknowledged. S.G-D. and J.M.M. are grateful to MINECO and the Spanish Ministerio de Educación, Cultura y Deporte (MECD), respectively, for their pre-doctoral contracts (FPU14/00792 and BES/2016 077830, respectively).

References

[1] Geim, A.K.; Novoselov, K.S. *Nat. Mater.* The Rise of Graphene. **2007**, *6*, 183–191.

[2] Novoselov, K.S.; Fal´ko, V.I.; Colombo, L.; Gellert, P.R.; Schwab, M.G.; Kim, K. A Roadmap for Graphene. *Nature* **2012,** *490***,** 192–200.

[3] Ferrari, A. C.; Bonaccorso, F.; Fal'ko, V.; Novoselov, K. S.; Roche, S.; Boggild, P.; Borini, S.; Koppens, F. H. L.; Palermo, V.; Pugno, N.; Garrido, J. A.; Sordan, R.; Bianco, A.; Ballerini, L.; Prato, M.; Lidorikis, E.; Kivioja, J.; Marinelli, C.; Ryhanen, T.; Morpurgo, A.; Coleman, J. N.; Nicolosi, V.; Colombo, L.; Fert, A.; Garcia-Hernandez, M.; Bachtold, A.; Schneider, G. F.; Guinea, F.; Dekker, C.; Barbone, M.; Sun, Z.; Galiotis, C.; Grigorenko, A. N.; Konstantatos, G.; Kis, A.; Katsnelson, M.; Vandersypen, L.; Loiseau, A.; Morandi, V.; Neumaier, D.; Treossi, E.; Pellegrini, V.; Polini, M.; Tredicucci, A.; Williams, G. M.; Hee Hong, B.; Ahn, J.-H.; Min Kim, J.; Zirath, H.; van Wees, B. J.; van der Zant, H.; Occhipinti, L.; Di Matteo, A.; Kinloch, I. A.; Seyller, T.; Quesnel, E.; Feng, X.; Teo, K.; Rupesinghe, N.; Hakonen, P.; Neil, S. R. T.; Tannock, Q.; Lofwander, T.; Kinaret, J. Science and Technology Roadmap for Graphene, Related Two-Dimensional Crystals, and Hybrid Systems. *Nanoscale* **2015**, *7*, 4598–4810.

[4] Bonaccorso, F.; Lombardo, A.; Hasan, T.; Sun, Z.; Colombo, L.; Ferrari, A.C. Production and Processing of Graphene and 2D Crystals. *Mater. Today* **2012**, *15*, 564–589.

[5] Yang, Y.; Han, C.; Jiang, B.; Iocozzia, J.; He, C.; Shi, D.; Jiang, T.; Lin, Z. Graphene- Based Materials with Tailored Nanostructures for Energy Conversion and Storage. *Mater. Sci. Eng. R* **2016**, *102*, 1–72.

[6] Ye, M.; Zhang, Z.; Zhao, Y.; Qu, L. Graphene Platforms for Smart Energy Generation and Storage. *Joule* **2018**, *2*, 245–268.

[7] Han, T.-H.; Kim, H.; Kwon, S.-J.; Lee, T.-W. Graphene-based flexible electronic

devices. *Mater. Sci. Eng. R* **2017**, *118*, 1–43.

[8] Bao, Q.; Loh, K.P. Graphene Photonics, Plasmonics, and Broadband Optoelectronic Devices. *ACS Nano* **2012**, *6*, 3677–3694.

[9] Mao, H.Y.; Laurent, S.; Chen, W.; Akhavan, O.; Imani, M.; Ashkarran, A.A.; Mahmoudi,
M. Graphene: Promises, Facts, Opportunities, and Challenges in Nanomedicine. *Chem. Rev.*
2013, *113*, 3407–3424.

[10] Reina, G.; González-Domínguez, J.M.; Criado, A.; Vázquez, E.; Bianco, A.; Prato, M. Promises, Facts and Challenges for Graphene in Biomedical Applications. *Chem. Soc. Rev.* **2017**, *46*, 4400–4416.

[11] Tung, T.T.; Nine, Md.J.; Krebsz, M.; Pasinszki, T.; Coghlan, C.J.; Tran, D.N.H.; Losic,
D. Recent Advances in Sensing Applications of Graphene Assemblies and Their Composites.
Adv. Funct. Mater. **2017**, *27*, 1702891.

[12] Zhong, Y. L.; Tian, Z.; Simon, G. P.; Li, D. Scalable Production of Graphene Via Wet Chemistry: Progress and Challenges. *Mater. Today* **2015**, *18*, 73–78.

[13] Wang, X.-Y.; Narita, A.; Müllen, K. New Advances in Nanographene Chemistry. *Nat. Rev. Chem.* **2017**, *2*, 0100.

[14] Low, C.T.J.; Walsh, F.C.; Chakrabarti, M.H.; Hashim, M.A.; Hussain, M.A. Electrochemical Approaches to the Production of Graphene Flakes and their Potential Applications. *Carbon* **2013**, *54*, 1–21.

[15] Salavagione, H.J. Promising Alternative Routes for Graphene Production and Functionalization. *J. Mater. Chem. A* **2014**, *2*, 7138–7146.

[16] Abdelkader, A. M.; Cooper, A. J.; Dryfe, R. A. W.; Kinloch, I. A. How to Get Between the Sheets: a Review of Recent Works on the Electrochemical Exfoliation of Graphene Materials from Bulk Graphite. *Nanoscale* **2015**, *7*, 6944-6956.

[17] Yang, S.; Lohe, M. R.; Müllen, K.; Feng, X. New-Generation Graphene from Electrochemical Approaches: Production and Applications. *Adv. Mater.* **2016**, *28*, 6213–6221.

[18] Paredes, J. I.; Munuera, J. M. Recent Advances and Energy-Related Applications of High Quality/Chemically Doped Graphenes Obtained by Electrochemical Exfoliation Methods. *J. Mater. Chem. A* **2017**, *5*, 7228–7242.

[19] Chen, C.-H.; Yang, S.-W.; Chuang, M.-C.; Woon, W.-Y.; Su, C.-Y. Towards the Continuous Production of High Crystallinity Graphene Via Electrochemical Exfoliation with Molecular In Situ Encapsulation. *Nanoscale* **2015**, *7*, 15362–15373.

[20] Yang, S.; Brüller, S.; Wu, Z.-S.; Liu, Z.; Parvez, K.; Dong, R.; Richard, F.; Samorì, P.; Feng, X.; Müllen, K. Organic Radical-Assisted Electrochemical Exfoliation for the Scalable Production of High-Quality Graphene. *J. Am. Chem. Soc.* **2015**, *137*, 13927–13932.

[21] Munuera, J. M.; Paredes, J. I.; Villar-Rodil, S.; Ayán-Varela, M.; Martínez-Alonso, A.; Tascón, J. M. D. Electrolytic Exfoliation of Graphite in Water with Multifunctional Electrolytes: En Route Towards High Quality, Oxide-Free Graphene Flakes. *Nanoscale* **2016**, *8*, 2982–2998.

[22] Munuera, J. M.; Paredes, J. I.; Enterría, M.; Pagán, A.; Villar-Rodil, S.; Pereira, M.F.R.; Martins, J.I.; Figueiredo, J.L.; Cenis, J.L.; Martínez-Alonso, A.; Tascón, J. M. D, Electrochemical Exfoliation of Graphite in Aqueous Sodium Halide Electrolytes toward Low Oxygen Content Graphene for Energy and Environmental Applications. *ACS Appl. Mater.* Interfaces **2017**, *9*, 24085–24099.

[23] Wang, J.; Manga, K.K.; Bao, Q.; Loh, K.P. High-Yield Synthesis of Few-Layer Graphene Flakes through Electrochemical Expansion of Graphite in Propylene Carbonate Electrolyte. *J. Am. Chem. Soc.* **2011**, 133, 8888–8891.

[24] Cai, X.; Song, Y.; Sun, Z.; Guo, D.; Liu, X.-X. Rate Capability Improvement of Co−Ni Double Hydroxides Integrated in Cathodically Partially Exfoliated Graphite. *J. Power Sources* **2017**, *365*, 126–133.

[25] Zhou, M.; Tang, J.; Cheng, Q.; Xu, G.; Cui, P.; Qin, L.-C. Few-layer Graphene Obtained by Electrochemical Exfoliation of Graphite Cathode. *Chem. Phys. Lett.* **2013**, *572*, 61–65.

[26] Cooper, A. J.; Wilson, N. R.; Kinloch, I. A.; Dryfe, R. A. W. Single Stage Electrochemical Exfoliation Method for the Production of Few-Layer Graphene Via Intercalation of Tetraalkylammonium Cations. *Carbon* **2014**, *66*, 340–350.

[27] Ouhib, F.; Aqil, A.; Thomassin, J.-M.; Malherbe, C.; Gilbert, B.; Svaldo-Lanero, T.; Duwez, A.-S.; Deschamps, F.; Job, N.; Vlad, A.; Melinte, S.; Jérôme, C.; Detrembleur, C. A Facile and Fast Electrochemical Route to Produce Functional Few-Layer Graphene Sheets for Lithium Battery Anode Application. *J. Mater. Chem. A* **2014**, *2*, 15298–15302.

[28] Najafabadi, A.T.; Leeuwner, M.J.; Wilkinson, D.P.; Gyenge, E.L. Electrochemically Produced Graphene for Microporous Layers in Fuel Cells. *ChemSusChem* **2016**, *9*, 1689– 1697.

[29] Najafabadi, A. T.; Ng, N.; Gyenge, E. High-Yield Graphene Production by Electrochemical Exfoliation of Graphite: Novel Ionic liquid (IL)–Acetonitrile Electrolyte With Low IL Content. *Carbon*, **2014**, *71*, 58–69.

[30] Lei, H.; Tu, J.; Yu, Z.; Jiao, S. Exfoliation Mechanism of Graphite Cathode in Ionic Liquids. *ACS Appl. Mater. Interfaces* **2017**, *9*, 36702–36707. Yang, Y.; Lu, F.; Zhou, Z.; Song, W.; Chen, Q.; Ji, X. Electrochemically Cathodic Exfoliation of Graphene Sheets in Room Temperature Ionic Liquids N-Butyl, Methylpyrrolidinium Bis(trifluoromethylsulfonyl)imide and their Electrochemical Properties. *Electrochim. Acta* **2013**, *113*, 9–16.

[31] Najafabadi, A. T.; Gyenge, E. Synergistic Production of Graphene Microsheets by Simultaneous Anodic and Cathodic Electro-Exfoliation of Graphitic Electrodes in Aprotic Ionic Liquids. *Carbon*, **2015**, *84*, 449–459

[32] Morales, G.M.; Schifani, P.; Ellis, G.; Ballesteros, C.; Martínez, G.; Barbero, C.; Salavagione, H.J. High-Quality Few Layer Graphene Produced by Electrochemical Intercalation and Microwave-Assisted Expansion of Graphite. *Carbon* **2011**, *49*, 2809–2816.

[33] Jeon, I.; Yoon, B.; He, M.; Swager, T.M. Hyperstage Graphite: Electrochemical Synthesis and Spontaneous Reactive Exfoliation. *Adv. Mater.* **2018**, *30*, 1704538.

[34] Ejigu, A.; Miller, B.; Kinloch, I. A.; Dryfe, R. A. W., Optimisation of Electrolytic Solvents for Simultaneous Electrochemical Exfoliation and Functionalisation of Graphene with Metal Nanostructures. *Carbon* **2018**, *128*, 257–266.

[35] Yang, S.; Brüller, S.; Wu, Z.-S.; Liu, Z.; Parvez, K.; Dong, R.; Richard, F.; Samorì, P.; Feng, X.; Müllen, K. Organic Radical-Assisted Electrochemical Exfoliation for the Scalable Production of High-Quality Graphene. *J. Am. Chem. Soc.* **2015**, *137*, 13927–13932.

[36] Parvez, K.; Wu, Z.-S.; Li, R.; Liu, X.; Graf, R.; Feng, X.; Müllen, K. Exfoliation of Graphite into Graphene in Aqueous Solutions of Inorganic Salts. *J. Am. Chem. Soc.* **2014**, *136*, 6083–6091.

[37] Munuera, J. M.; Paredes, J. I.; Villar-Rodil, S.; Castro-Muñiz, A.; Martínez-Alonso, A.; Tascón, J. M. D. High Quality, Low-Oxidized Graphene via Anodic Exfoliation with Table Salt as an Efficient Oxidation-Preventing Co-Electrolyte for Water/Oil Remediation and Capacitive Energy Storage Applications *Appl. Mater. Today* **2018**, *11*, 246–254.

[38] Munuera, J. M.; Paredes, J. I.; Villar-Rodil, S.; Ayán-Varela, M.; Pagán, A.; Aznar- Cervantes, S. D.; Cenis, J. L.; Martínez-Alonso, A.; Tascón, J. M. D. High Quality, Low Oxygen Content and Biocompatible Graphene Nanosheets Obtained by Anodic Exfoliation of Different Graphite Types. *Carbon* **2015**, *94*, 729–739.

[39] Zhao, M.; Guo, X.-Y.; Ambacher, O.; Nebel, C.E.; Hoffmann, R. Electrochemical Generation of Hydrogenated Graphene Flakes, *Carbon* **2015**, *83*, 128–135.

[40] Wu, L.; Li, W.; Li, P.; Liao, S.; Qiu, S.; Chen, M.; Guo, Y.; Li, Q.; Zhu, C.; Liu, L. Powder, Paper and Foam of Few-Layer Graphene Prepared in High Yield by Electrochemical Intercalation Exfoliation of Expanded Graphite. *Small* **2014**, *10*, 1421–1429.

[41] Ossonon, B.D.; Bélanger, D. Synthesis and Characterization of Sulfophenyl-Functionalized Reduced Graphene Oxide Sheets. *Carbon* **2017**, *111*, 83–93.

[42] Boudon, C.; Gross, M.; Peter, F. Comparative Electrochemical Reduction of Ammonium and Potassium Chelates. *J. Electroanal. Chem. Interfacial Electrochem.* **1983**, *145*, 181–187.

[43] Berkh, O.; Shacham-Diamand, Y.; Gileadi, E. Reduction of Ammonium Ion on Pt Electrodes. *J. Electrochem. Soc.* **2008**, *155*, F223–F229.

[44] Dean, J.A. *Lange´s Handbook of Chemistry* (15th edition), McGraw-Hill, New

York, 1999; section 8.7.

[45] Vanýsek P. Ionic Conductivity and Diffusion at Infinite Dilution, In: D.R. Lide (Ed.),
CRC Handbook of Chemistry and Physics (83rd edition), CRC Press, Boca Raton, 2002.

[46] Butt, H.-J.; Graf, K.; Kappl, M. Physics and Chemistry of Interfaces, Wiley-VCH, Weinheim, 2003; chapter 12.

[47] Oremusová J. Micellization of Alkyl Trimethyl Ammonium Bromides in Aqueous Solutions–Part 1: Critical Micelle Concentration (CMC) and Ionization Degree. *Tenside Surf. Det.* **2012**, *49*, 231–240.

[48] Wang, T.; Quinn, M.D.J.; Notley S.M. Enhanced Electrical, Mechanical and Thermal Properties by Exfoliating Graphene Platelets of Larger Lateral Dimensions. *Carbon* **2018**, *129*, 191–198.

[49] Li, D.; Müller, M.B.; Gilje, S.; Kaner, R.B.; Wallace, G.G. Processable Aqueous Dispersions of Graphene Nanosheets. *Nat. Nanotech.* **2008**, *3*, 101–105.

[50] Seo, J.-W.T.; Green, A.A.; Antaris, A.L.; Hersam, M.C. High-Concentration Aqueous Dispersions of Graphene using Nonionic, Biocompatible Block Copolymers. *J. Phys. Chem. Lett.* **2011**, *2*, 1004–1008.

[51] Erickson, K.; Erni, R.; Lee, Z.; Alem, N.; Gannett, W.; Zettl, A. Determination of the Local Chemical Structure of Graphene Oxide and Reduced Graphene Oxide. *Adv. Mater.* **2010**, *22*, 4467–4472.

[52] Pimenta, M.A.; Dresselhaus, G.; Dresselhaus, M.S.; Cançado, L.G.; Jorio, A.; Saito, R. Studying Disorder in Graphite-Based Systems by Raman Spectroscopy. *Phys. Chem. Chem. Phys.* **2007**, *9*, 1276–1291.

[53] L. Guardia, M. J. Fernández–Merino, J. I. Paredes, P. Solís–Fernández, S. Villar–Rodil,
A. Martínez–Alonso, J. M. D. Tascón, Carbon, 2011, 49, 1653–1662

[54] Paton, K. R.; Varrla, E.; Backes, C.; Smith, R. J.; Khan, U.; O'Neil, A.; Boland, C.; Lotya, M.; Istrate, O. M.; King, P.; Higgins, T.; Barwich, S.; May, P.; Puczkarski, P.; Ahmed, I.; Moebius, M.; Pettersson, H.; Long, E.; Coelho, J.; O'Brien, S. E.; McGuire,

E. K.; Mendoza Sanchez, B.; Duesberg, G. S.; McEvoy, N.; Pennycook, T. J.; Downing, C.; Crossley, A.; Nicolosi, V.; Coleman, J. N. Scalable Production of Large Quantities of Defect- Free Few-Layer Graphene by Shear Exfoliation in Liquids. *Nat. Mater.* **2014**, *13*, 624–630.

[55] Ayán-Varela, M.; Paredes, J. I.; Guardia, L.; Villar-Rodil, S.; Munuera, J. M.; Díaz- González, M.; Fernández-Sánchez, C.; Martínez-Alonso, A.; Tascón, J. M. D. Achieving Extremely Concentrated Aqueous Dispersions of Graphene Flakes and Catalytically Efficient Graphene-Metal Nanoparticle Hybrids with Flavin Mononucleotide as a High-Performance Stabilizer. *ACS Appl. Mater. Interfaces* **2015**,

7, 10293–10307.

[56] Khan, U.; O´Neill, A.; Lotya, M.; De, S.; Coleman, J.N. High-Concentration Solvent Exfoliation of Graphene. *Small* **2010**, *6*, 864–871.

[57] Zhang, L.; Zhang, Z.; He, C.; Dai, L.; Liu, J., Wang L. Rationally Designed Surfactants for Few-Layered Graphene Exfoliation: Ionic Groups Attached to Electron-Deficient π- Conjugated Unit through Alkyl Spacers. *ACS Nano* **2014**, *8*, 6663-6670.

[58] F. Zhou, H. Huang, C. Xiao, S. Zheng, X. Shi, J. Qin, Q. Fu, X. Bao, X. Feng, K. Müllen, Z.-S. Wu, Electrochemically Scalable Production of Fluorine-Modified Graphene for Flexible and High-Energy Ionogel-Based Microsupercapacitors. *J. Am. Chem. Soc.* **2018**, *140*, 8198–8205.

[59] Zhong, Y.L.; Swager, T.M. Enhanced Electrochemical Expansion of Graphite for in Situ Electrochemical Functionalization. *J. Am. Chem. Soc.* **2012**, *134*, 17896–17899.

[60] Huang, H.; Xia, Y.; Tao, X.; Du, J.; Fang, J.; Gan, Y.; Zhang, W. Highly Efficient Electrolytic Exfoliation of Graphite into Graphene Sheets Based on Li Ions Intercalation– Expansion–Microexplosion Mechanism. *J. Mater. Chem.* **2012**, *22*, 10452–10456.

[61] Li, F.; Xue, M.; Zhang, X.; Chen, L.; Knowles, G.P.; MacFarlane, D.R.; Zhang, J. Advanced Composite 2D Energy Materials by Simultaneous Anodic and Cathodic Exfoliation. *Adv. Energy Mater.* **2018**, *8*, 1702794.

[62] Raccichini, R.; Varzi, A.; Passerini, S.; Scrosati, B. The Role of Graphene for Electrochemical Energy Storage. *Nat. Mater.* **2015**, *14*, 271–279.

[63] Sherrell, P. C.; Mattevi, C. Mesoscale Design of Multifunctional 3D Graphene Networks.
Mater. Today **2016**, *19*, 428−436.

[64] Nguyen, D. D.; Tai, N.-H.; Lee, S.-B.; Kuo, W.-S. Superhydrophobic and Superoleophilic Properties of Graphene-Based Sponges Fabricated Using a Facile Dip Coating Method. *Energy Environ. Sci.* **2012**, *5*, 7908–7912.

[65] Chen, B.; Ma, Q.; Tan, C.; Lim, T.-T.; Huang, L.; Zhang, H. Carbon-Based Sorbents with Three-Dimensional Architectures for Water Remediation, *Small* **2015**, *11*, 3319–3336.

[66] Sun, Z.; Liao, T.; Dou, Y.; Hwang, S. M.; Park, M.-S.; Jiang, L.; Kim, J. H.; Dou, S. X. Generalized Self-Assembly of Scalable Two-Dimensional Transition Metal Oxide Nanosheets. *Nat. Commun.* **2014**, *5*, 3813.

[67] Greenwood, N. N.; Earnshaw, A.. Chemistry of the Elements. Pergamon Press. Oxford, 1984; Chapter 26: Cobalt, Rhodium and Iridium.

[68] Cochran, S. J.; Larkins, F. P. Surface Reduction of some Transition-Metal Oxides. an X- Ray Photoelectron Spectroscopic Study of Iron, cobalt, Nickel and Zinc Oxides. *J. Chem. Soc., Faraday Trans.* **1985**, *81*, 2179–2190.

[69] Conway, B. E.. Electrochemical Supercapacitors. Scientific Fundamentals and Technological Applications. Kluwer Academic/Plenum Publishers, New York, 1999; pp. 401, 509.

Supplementary material for

An aqueous cathodic delamination route towards high quality graphene flakes for oil sorption and electrochemical charge storage applications

Sergio García-Dalí, Juan I. Paredes, José M. Munuera, Silvia Villar-Rodil, Amelia Martínez-Alonso, Juan M.D. Tascón

Instituto Nacional del Carbón, INCAR-CSIC, C/Francisco Pintado Fe 26, 33011 Oviedo, Spain

Contents

S1. Additional XPS characterization of cathodic graphene

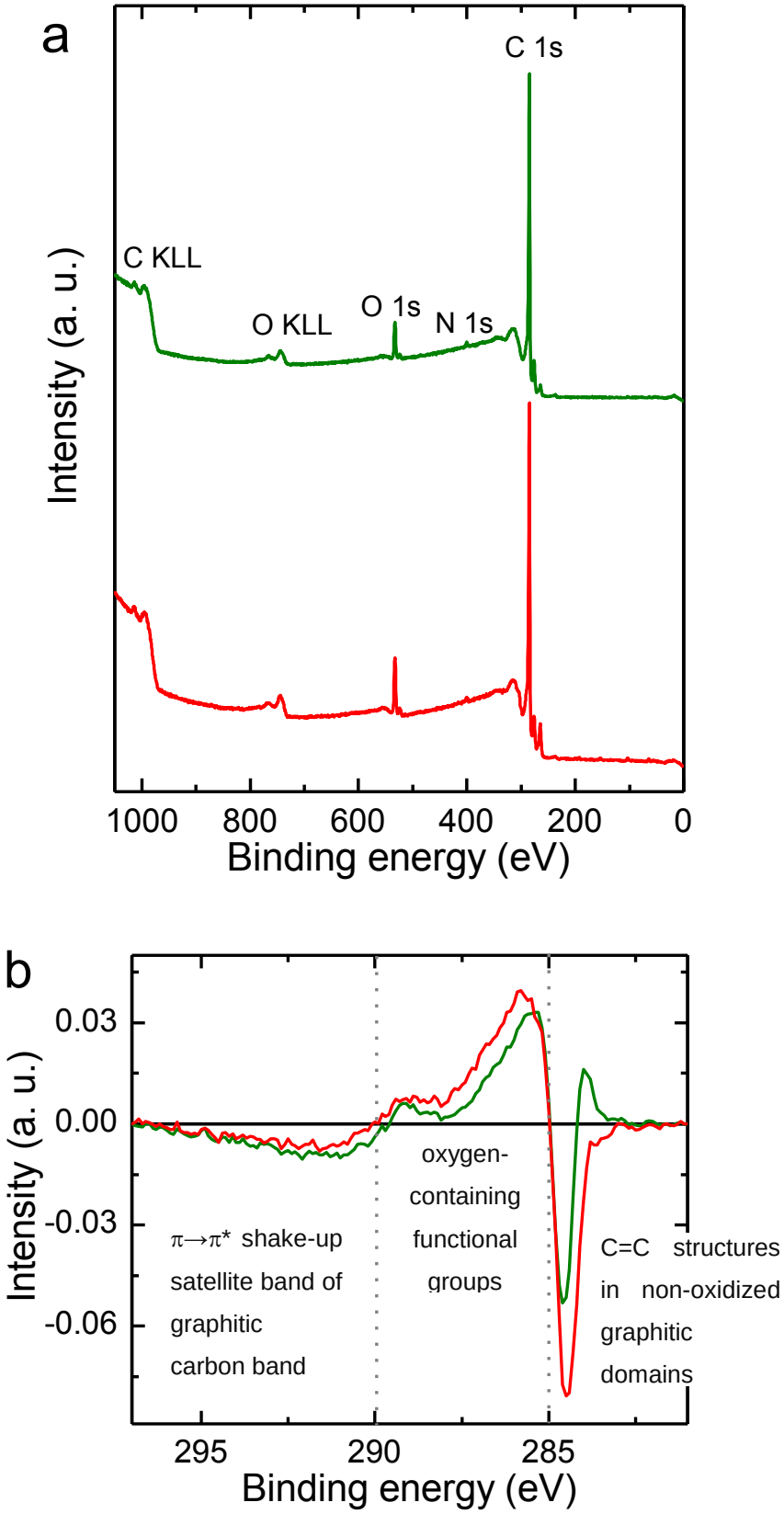

Figure S1. (a) Survey X-ray photoelectron (XPS) spectra for graphene paper-like films prepared from graphene dispersions obtained by sonication of graphite cathodically expanded with 0.3 M HTMABr (red trace) and 0.3 M TPACl (green trace). The detected XPS and Auger bands have been labeled for clarity. **(b)** High resolution C 1s difference spectra between 0.3 M HTMABr (red trace) and 0.3 M TPACl (green trace) and the starting graphite foil. The spectra are background-substracted and normalized. From the span of the y scale, the differences between cathodically expanded graphene and the starting graphite are seen to be minor.

S2. FE-SEM characterization of graphite foil and HOPG

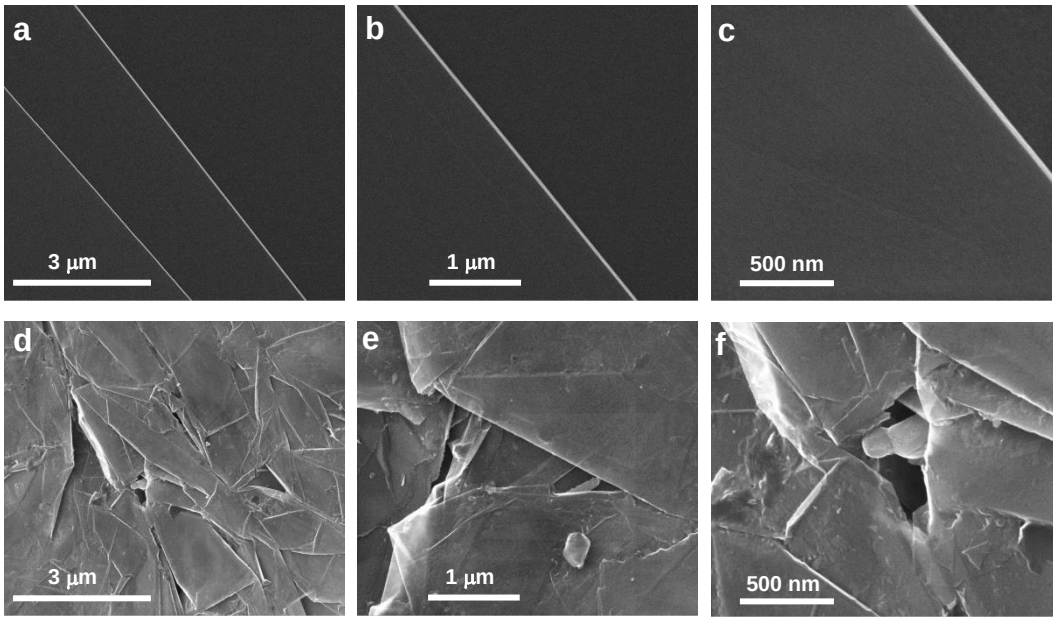

Figure S2. Representative FE-SEM micrographs at different magnifications of the surface of **(a–c)** HOPG, and **(d–f)** graphite foil observed at an angle of 45° in respect to the basal plane.

S3. Sorption capacities of graphene-based sorbents and other hydrophobic sorbents with similar densities

Table S1. Range of sorption capacities of different graphene-based sorbents and other hydrophobic sorbents with similar densities towards oils and organic solvents.

Material	**Density** (mg/cm^3)	**Sorption capacity** (g/g)	**Reference**
Graphene oxide (GO) foam	30	5–40	S1
GO 3D assembly	11	60–165	S2
Carbon nanotubes (CNT)	5–10	80–180	S3
GO and CNT	7	80–140	S4
N-doped graphene aerogel	10–20	40–110	S5
Poly(melamine formaldehyde)	8 –10	71–158	S6
Glucose	10	51–139	S7
Raw cotton	12	50–192	S8
As-expanded anodic graphene	30–40	15–30	S9
As-expanded cathodic graphene	30–45	8–20	This work
Graphene-coated melamine foam	12–14	60–150	This work

S4. Gravimetric capacitances of graphene-based electrodes

Table S2. Gravimetric capacitance values of a range of graphene-based electrodes determined with a three-electrode system at different current densities

Material	**Current density** (A/g)	**Capacity** (F/g)	**Reference**
Reduced graphene oxide (RGO)	1	276	S10
RGO	1	238	S11
Ruthenium oxide/RGO nanocomposite	0.5	82	S12
RGO/polyaniline noanocomposite	1	116	S13
RGO foam	5	125	S14
Highly crumpled N-doped graphene nanosheets	1	246	S15
As- expanded anodic graphene	0.3	105	S**¡Error! Marcador no definido.**
As-expanded anodic graphene	1	94	S**¡Error! Marcador no definido.**

As- expanded cathodic graphene	0.3	26	This work
As-expanded cathodic graphene	1	19	This work
As- expanded cathodic graphene combined with 5 wt% cobalt oxide nanosheets	0.3	140	This work
As-expanded cathodic graphene combined with 5 wt% cobalt oxide nanosheets	1	129	This work
As- expanded cathodic graphene combined with 5 wt% cobalt oxide nanosheets	5	94	This work

S5. References

[S1] Z. Niu , J. Chen , H. H. Hng , J. Ma , X. Chen , A Leavening Strategy to Prepare Reduced Graphene Oxide Foams, Adv. Mater. 24 (2012) 4144-4150.

[S2] D. D. Nguyen, N.-H. Tai, S.-B. Lee, W.-S. Kuo. Superhydrophobic and superoleophilic properties of graphene-based sponges fabricated using a facile dip coating method. Energy Environ. Sci. 5 (2012), 7908– 7912.

[S3] X. Gui, J. Wei, K. Wang, A. Cao, H. Zhu, Y. Jia, Q. Shu, D. Wu, Carbon Nanotube Sponges. Adv. Mater. 2010, 22, 617–621.

[S4] X. Dong, J. Chen, Y. Ma, J. Wang, M. B. Chan-Park, X. Liu, L. Wang, W. Huang, P. Chen, Superhydrophobic and superoleophilic hybrid foam of graphene and carbon nanotube for selective removal of oils or organic solvents from the surface of water. Chem. Commun. 2012, 48, 10660–10662.

[S5] H. Ren, X. Shi, J. Zhu, Y. Zhang, Y. Bi, L. Zhang, Facile synthesis of N-doped graphene aerogel and its application for organic solvent adsorption, J. Mater. Sci. 51 (2016) 6419–6427.

[S6] Y. Yang, Y. H. Deng, Z. Tong, C. Y. Wang, Multifunctional foams derived from poly(melamine formaldehyde) as recyclable oil absorbents. J. Mater. Chem. A 2014, 2, 9994–9999.

[S7] Z. Y. Wu, C. Li, H. W. Liang, Y. N. Zhang, X. Wang, J. F. Chen, S. H. Yu, Carbon nanofiber aerogels for emergent cleanup of oil spillage and chemical leakage under harsh

conditions. Sci. Rep. 2014, 4, 4079.

[S8] H. C. Bi, Z. Y. Yin, X. H. Cao, X. Xie, C. L. Tan, X. Huang, B. Chen, F. T. Chen, Q. L. Yang, X. Y. Bu, X. H. Lu, L. T. Sun, H. Zhang, Carbon Fiber Aerogel Made from Raw Cotton: A Novel, Efficient and Recyclable Sorbent for Oils and Organic Solvents. Adv. Mater. 2013, 25, 5916–5921.

[S9] J.M. Munuera, J.I. Paredes, S. Villar-Rodil, A. Castro-Muñiz, A. Martínez-Alonso, J.M.D. Tascón. High quality, low-oxidized graphene via anodic exfoliation with table salt as an efficient oxidation-preventing co-electrolyte for water/oil remediation and capacitive energy storage applications. Appl. Mater. Today 11 (2018) 246–254.

[S10] Z. Lin, Y. Liu, Y. Yao, O.J. Hildreth, Z. Li, K. Moon, C.-p. Wong. Superior Capacitance of Functionalized Graphene. J. Phys. Chem. C, 2011, 115, 7120–7125

[S11] D. Zhang, X. Zhang, Y. Chen, C. Wang, Y. Ma. An environment-friendly route to synthesize reduced graphene oxide as a supercapacitor electrode material Electrochim. Acta, 2012, 69, 364–370.

[S12] J.-Y. Kim, K.-H. Kim, S.-B. Yoon, H.-K. Kim, S.-H. Park, K.-B. Kim, In situ chemical synthesis of ruthenium oxide/reduced graphene oxide nanocomposites for electrochemical capacitor applications, Nanoscale, 5 (2013) 6804–6811.

[S13] Z. F. Li, H. Zhang, Q. Liu, L. Sun, L. Stanciu, J. Xie, Fabrication of High-Surface-Area Graphene/Polyaniline Nanocomposites and Their Application in Supercapacitors, ACS Appl. Mater. Interfaces, 5 (2013) 2685–2691.

[S14] J. Yan, Y. Ding, C. Hu, H. Cheng, N. Chen, Z. Feng, Z. Zhang, L. Qu, Preparation of multifunctional microchannel-network graphene foams, J. Mater. Chem. A, 2 (2014) 16786–16792.

[S15] Z. H. Wen, X. C. Wang, S. Mao, Z. Bo, H. Kim, S. M. Cui, G. H. Lu, X. L. Feng, J. H. Chen, Crumpled Nitrogen-Doped Graphene Nanosheets with Ultrahigh Pore Volume for High-Performance Supercapacitor, Adv. Mater. 24 (2012) 5610-5616.

ARTÍCULO II

An Aqueous Cathodic Exfoliation Strategy towards Solution-Processable and Phase-Preserved MoS_2 Nanosheets for Energy Storage and Catalytic Applications

Sergio García-Dalí,[†] Juan I. Paredes, [†,*] José M. Munuera,[†] Silvia Villar-Rodil, [†,*] Alaa Adawy,[‡] Amelia Martínez-Alonso, [†] Juan M.D. Tascón[†]

[†]*Instituto Nacional del Carbón, INCAR-CSIC, C/Francisco Pintado Fe 26, 33011 Oviedo, Spain*

[‡]*Laboratory of High-Resolution Transmission Electron Microscopy, Scientific and Technical Services, University of Oviedo-CINN, 33006, Oviedo, Spain*

* Corresponding author: paredes@incar.csic.es

* Corresponding author: silvia@incar.csic.es

Abstract

The production of MoS_2 nanosheets by electrochemical exfoliation routes holds great promise as a means to access this two-dimensional material in large quantities for different practical applications. Yet, the use of electrolytes based on synthetic organic salts and solvents, as well as issues related to the unwanted oxidation and/or phase transformation of the exfoliated nanosheets, constitute significant obstacles that hinder the industrial adoption of the electrochemical approach. Here, we introduce a safe and sustainable method for the cathodic delamination of MoS_2 that makes use of aqueous solutions of very simple and widely available salts, mainly KCl, as the electrolyte. Combined with an appropriate biomolecule- based solvent transfer protocol, such an electrolytic exfoliation route is shown to afford colloidally dispersed, oxide-free and phase-preserved MoS_2 nanosheets of a high structural quality in considerable yields. The mechanisms behind the efficient aqueous delamination of the bulk MoS_2 cathode are also discussed and rationalized on the basis of the penetration of hydrated cations from the electrolyte between its layers and the immediate reduction of the accompanying water molecules. An asymmetric supercapacitor assembled with a cathodic MoS_2 nanosheet-single walled carbon nanotube hybrid as the positive electrode and activated carbon as the negative electrode delivered energy densities (e.g., 26 W h kg^{-1} at 750 W kg^{-1} in 6 M KOH) that were competitive with those of other MoS_2-based asymmetric devices. When used as a catalyst for the reduction of nitroarenes, the present cathodically exfoliated nanosheets exhibited one of the highest activities reported so far with MoS_2 nanostructures, the origin of which is accounted for as well. Overall, by facilitating access to this two- dimensional material through a particularly simple, efficient and cost-effective technique, these results should expedite the practical implementation of MoS_2 nanosheets in energy, catalysis and beyond.

Keywords: Two-dimensional (2D) material; transition metal dichalcogenides (TMDs); MoS_2; electrochemical exfoliation; energy storage; catalysis

1. Introduction

The experimental isolation of graphene in 2004 and the subsequent discovery of its exceptional physical properties heralded a new era in materials research that to this day has been increasingly dominated by the broader family of two-dimensional (2D) solids.[1] In these materials, the spatial confinement of electrons and the large surface area available for interaction with the surrounding environment are the main drivers of novel and emerging characteristics that are generally absent from their three-dimensional counterparts, thus constituting the basis for their prospective use in many relevant technological applications.[1] While most research efforts on 2D materials were originally focused on graphene and its derivatives (e.g., graphene oxide), in recent years other members from this family have gained prominence on their own merit. This is particularly the case of layered transition metal dichalcogenides (TMDs), with MoS_2 being their most archetypal example.[2,3] Similar to graphite, bulk MoS_2 can be downsized to the 2D level to give single- or few-layer sheets that boast distinct and attractive properties, as well as a strong application potential in, e.g., electronics and optoelectronics,[4] energy conversion and storage,[5] catalysis[6] and photocatalysis,[7] chemical sensing[8] or biomedicine.[9]

As is usually the case with any novel material, the actual prospects of implementing 2D MoS_2 (as well as other TMDs) in real-life applications will critically depend on the availability of efficient and affordable strategies for the production of such a material in sufficient quantities and with targeted characteristics. Drawing again a parallel to the case of graphite/graphene, we note that both bottom-up and top-down (i.e., exfoliation) approaches have been explored for the preparation of different types of 2D MoS_2.[1,3,10] The former mostly include chemical vapor deposition and epitaxial growth methods that yield large-area, high quality wafers of 2D MoS_2 useful in (opto)electronic applications.[11] However, the need of costly (high temperature/high vacuum) equipment, suitable growth substrates and the relatively complex steps for the transfer of the 2D MoS_2 from the growth to the target substrate limits the potential of such methods towards large-scale implementation. On the other hand, strategies based on the exfoliation of the bulk layered solid are probably a better option when micrometer- and submicrometer-sized nanosheets (NSs) of MoS_2 are required in considerable amounts (e.g., in many energy-, catalysis- and biomedicine-related applications).[12,13]

So far, two main exfoliation routes have been extensively investigated to access 2D MoS_2 nanosheets in large quantities: (1) exfoliation induced by ultrasound or shear forces in organic solvents or water/surfactant solutions,[12–14] and (2) exfoliation triggered by lithium intercalation using organolithium compounds (e.g., *n*-butyllithium).[3,13,15,16] Nonetheless, both techniques are not without their own limitations. For example, while ultrasound- and shear force-induced methods are easy to implement and give few- and several-layer thick NSs of a high structural quality, they generally suffer from low exfoliation yields (< 5 wt%). By contrast, the lithium intercalation approach usually affords single-layer NSs in high yields (> 50 wt%), but it has to be carried out under stringent conditions (i.e., in the absence of oxygen and humidity). Also, such an intercalation causes a frequently unwanted transition from the original semiconducting 2H phase of MoS_2 to the metallic 1T´ phase. Although this transition can be reversed by different means,[15,16] it is usually associated to the generation of large numbers of defects and imperfections in the lattice (tears, pinholes, vacancies, etc) that cannot be readily healed.

Recently, electrochemical exfoliation has emerged as an alternative top-down approach for the production of MoS_2 NSs towards different applications.[17,18] Such an approach boasts the merits of simplicity and ease of operation, alacrity and scalability, and it is based on the application of a DC bias voltage to a bulk MoS_2 sample (working electrode) in an electrolytic solution to drive the intercalation of either cations (cathodic exfoliation) or anions (anodic exfoliation) and thus trigger the expansion and delamination of the electrode. Cathodic exfoliation has been typically accomplished using lithium salts (e.g., $LiPF_6$, $LiClO_4$ or LiCl) in organic solvents (ethyl/dimethyl carbonate mixtures or dimethylsulfoxide) as the electrolytic medium,[19–22] but the electrochemical intercalation of lithium also induces at least a partial 2H to 1T´ phase transition in MoS_2. This issue has been very recently circumvented by replacing lithium by tetraalkylammonium salts.[23,24] Still, the use of organic solvents (as opposed to water) as well as of relatively complex and expensive organic salts constitute a barrier for this method to become a competitive option in the industrial production of MoS_2 NSs. On the other hand, anodic exfoliation (or a combination of anodic and cathodic treatment) has been carried out in aqueous electrolytes using simple, sulfate-based salts (e.g., Na_2SO_4).[25,26] However, the exfoliation yields tend to be low to moderate (5–9 wt%)[25] and the generation of highly reactive oxygen species that is associated to such operating conditions promotes a substantial oxidation of the

resulting NSs, thus compromising their attractive properties and performance in applications.

To overcome the current drawbacks and limitations of electrochemical exfoliation and make this method truly competitive and viable for the large-scale fabrication of 2D MoS_2 NSs, electrolytic routes that are particularly simple, efficient, affordable and sustainable will be needed. More specifically, such routes should fulfill a number of important requirements:

(1) For safety, sustainability and economic reasons, exfoliation should be performed in water with readily available and inexpensive electrolytes. (2) To preserve the structural integrity of the lattice, and hence the properties of the corresponding 2D material, the electrolytic process should be able to avert any oxidation or phase transformation of the MoS_2 material. (3) For efficiency and processability reasons, substantial exfoliation yields should be attained and the exfoliated products should be easy to disperse in proper solvents, thus facilitating the preparation of MoS_2-based materials and devices. At present, none of the state-of-the-art electrochemical exfoliation strategies satisfies all these conditions.

Here, we report an electrochemical exfoliation route for MoS_2 that meets the above- mentioned requirements. More to the point, we demonstrate that using aqueous KCl solutions as the electrolytic medium, a fast and efficient cathodic delamination of bulk MoS_2 is possible. Furthermore, by way of a simple biomolecule-based protocol, the as-exfoliated products can be transferred to appropriate solvents (isopropanol, water, etc) with considerable yields (up to ~30 wt%), giving colloidal dispersions of oxide-free NSs of a high structural quality and retained phase that are readily processable for different practical purposes. These cathodically exfoliated MoS_2 NSs exhibit a competitive performance when used as an electrode material for asymmetric supercapacitors (e. g., energy density of 26 W h kg^{-1} at a power density of 750 W kg^{-1}) and also demonstrate an enhanced catalytic activity in the reduction of nitroarenes. Overall, by tackling several limitations associated to the known methods for electrochemical exfoliation of MoS_2, we believe that the present results will lower the barriers of industrial access to this 2D material for use in energy, catalysis and beyond.

2. Results and discussion

2.1.Cathodic exfoliation of MoS_2 in water with alkali metal ions: general aspects and exfoliation yields

In the search of an electrochemical exfoliation protocol for MoS_2 that can be potentially up-scaled, a number of stringent requirements should be met, which include working with readily available and inexpensive aqueous electrolytes, avoiding any substantial oxidation, phase transformation or structural degradation of the lattice, and attaining processable 2D NSs in competitive yields. Due to the propensity of MoS_2 to oxidize under varied conditions,[27,28] the application of anodic potentials toward exfoliation in water should be ruled out. Such conditions are expected to generate highly reactive oxygen species (e.g., ·OH radicals) from the anodic oxidation of water molecules, which would readily attack the MoS_2 electrode and lead eventually to the formation of molybdenum oxide particles and to etching of the material.[29] Oxidation issues are avoided in the intrinsically reductive environment associated to cathodic exfoliation, but in this case structural (phase) transformations of the MoS_2 material could be also of concern due to an excessive injection of electrons into the lattice, as it is the case when using lithium salts in organic solvents as the electrolyte.[19,21,24] It is then apparent that the selection of a suitable salt for cathodic exfoliation in water (i.e., a suitable intercalating cation) will be a critical aspect in the way of fulfilling the above-mentioned requirements. Working with organic ammonium salts (e.g., tetraalkylammonium halides) could offer a solution to the problem of phase transformation,[24] but their synthetic nature and relatively limited availability could be an obstacle to their widespread implementation.

As an alternative to lithium- and alkylammonium-based salts, we hypothesized that common salts of heavier alkali metals, such as NaCl or KCl, could be effective electrolytes for aqueous cathodic exfoliation. Both NaCl and KCl are widely available and inexpensive commodities (used as, e.g., table salt for human consumption), as well as highly soluble in water. Furthermore, the larger size of the Na^+ and K^+ cations (~0.19 and 0.26 nm, respectively) compared to Li^+ (~0.12 nm)[30] could in principle limit the number of such ions that get packed in the host MoS_2 lattice by intercalation, and so the number of electrons injected. As a result, the use of Na- or K-based electrolytes could be less conducive to phase transformations of the lattice.[24] To probe this hypothesis, we carried out cathodic exfoliation tests in a two-electrode configuration, using MoS_2 pieces (~5×5×0.5 mm^3 in size) as the working electrode,

platinum foil as the counter electrode and aqueous KCl solutions as the electrolytic medium [Fig. 1a; see Supporting Information (SI) for details on the experimental procedure]. Upon application of a negative voltage to the MoS_2 working electrode, the latter was seen to progressively swell and fan out starting from its free, submerged end. Visually, the extent of swelling and expansion of the MoS_2 piece clearly depended on both the magnitude of the applied cathodic voltage and the electrolyte concentration. Voltages of -10 V and below were required to induce substantial expansion of the cathode. At KCl concentrations in the 0.1–1 M range, such an expansion was relatively moderate, but it became much stronger at 2 and 4 M KCl, thus indicating the key role of the K^+ ion in the delamination process [see Fig. 1b and c for examples of initial (b) and expanded (c) MoS_2 pieces]. The expansion of the MoS_2 cathode was rather fast and it was completed after about 15–20 min. A control experiment in pure water, in the absence of any electrolyte, did not induce any expansion, as could be expected. Fig. 1d shows an overall field-emission scanning electron microscopy (FE-SEM) image of a well expanded sample, where an accordion-like structure of separated lamellae was already apparent. More detailed inspection (Fig. 1e) revealed that the lamellae were made up of very thin, wrinkled and/or rippled layers separated by micrometer- or submicrometer-sized voids. Such a morphology was very similar to that previously reported in, e.g., successful processes of anodic exfoliation of graphite,[31,32] suggesting that an efficient delamination was also attained in the present case for the cathodically treated MoS_2. For comparison, a FE-SEM image of a starting, untreated MoS_2 piece is presented in Fig. S1 of the SI, the morphology of which was dominated by non-expanded and close-packed layers.

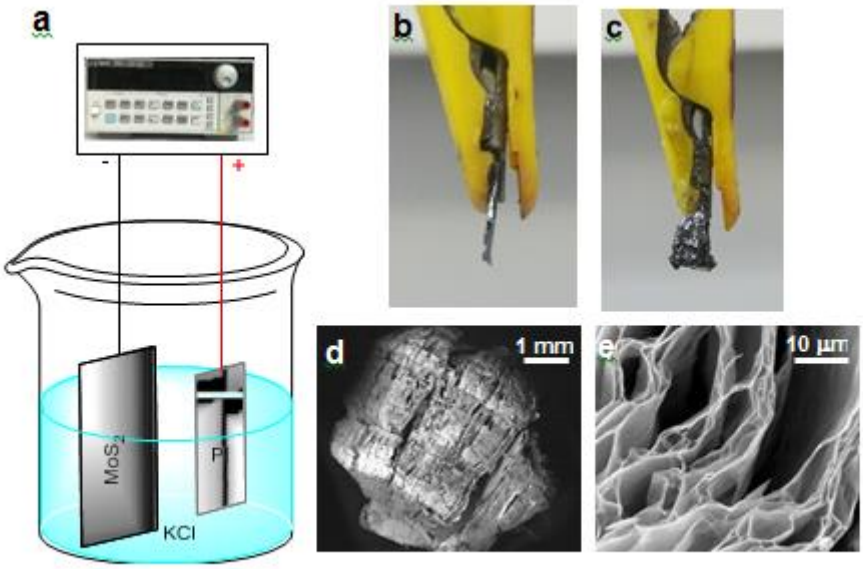

Figure 1. (a) Schematic of the cathodic exfoliation of MoS_2 using aqueous solutions of alkali metal salts (e. g., KCl) as the electrolytic medium. **(b, c)** Digital photographs of the initial (b) and cathodically expanded (c) MoS_2 piece using aqueous 4 M KCl solution as the electrolytic medium. **(d, e)** Representative FE-SEM images of the cathodically expanded MoS_2 piece at low (d) and high (e) magnification.

Individual, stand-alone MoS_2 NSs could be readily extracted from the cathodically exfoliated material by transferring it to the liquid phase followed by sonication. Different solvents were tested for this purpose, but the best results in terms of amount of extracted NSs were attained with solutions of the RNA nucleotides adenosine monophosphate (AMP) and guanosine monophosphate (GMP) in isopropanol (details of the liquid-phase dispersion protocol are given in the SI). As an example, Fig. 2a (left vial) shows a digital photograph of a 0.1 mg mL^{-1} MoS_2 dispersion in isopropanol assisted by GMP, where the greenish tone characteristic of nanostructured semiconducting MoS_2 could be noticed. Indeed, the UV-vis absorption spectrum of the dispersion (Fig. 2b) exhibited the four well-known exciton peaks of semiconducting 2H MoS_2, i.e, the A and B (C and D) peaks located in the 600–700 (400–500) nm wavelength range,[33] thus providing a first indication that the cathodic treatment largely preserved the original phase of the material (1T´-phase MoS_2 has featureless absorption in the visible range).[15,21,34] The UV-vis absorption spectra also allowed to estimate the MoS_2 concentration in the suspensions, and thus the amount of extracted NSs, on the basis of the Lambert-Beer law and using the extinction

coefficient (ε) previously determined for this material at the wavelength of 345 nm (ε ≈ 6900 mL mg^{-1} m^{-1}).[35] Values up to ~2–3 mg mL^{-1} in isopropanol with AMP and GMP could be attained by concentrating the as-extracted dispersions through consecutive cycles of sedimentation of the MoS_2 fraction via centrifugation and re-dispersion in smaller, 0.5 mg mL^{-1} AMP/GMP-containing isopropanol volumes.

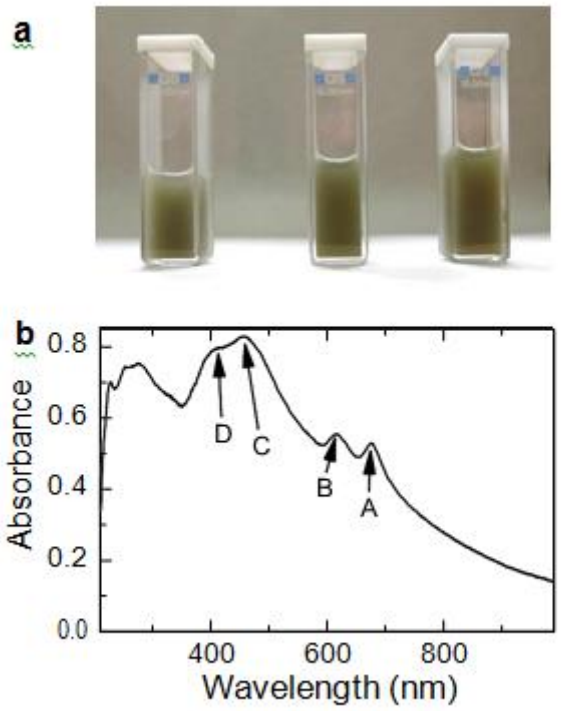

Figure 2. (a) Digital photograph of MoS_2 dispersions extracted from the cathodically exfoliated material with the assistance of GMP in different solvents (from left to right): isopropanol, DMF and NMP. **(b)** UV-vis absorption spectrum of a MoS_2 dispersion in isopropanol with GMP. The excitonic peaks A, B, C and D, characteristic of 2H-phase MoS_2 are indicated.

NS extraction with AMP or GMP was also possible in aqueous medium. However, while previous work has demonstrated that such nucleotides are efficient colloidal dispersants of MoS_2 and other TMD NSs in water,[36] here we found their performance towards the extraction of MoS_2 NSs from the cathodically exfoliated electrode to be higher (by a factor of ~10) in isopropanol. To rationalize such a result, we note that the colloidal stabilization of MoS_2 NSs by these biomolecules relies on the robust adsorption of the latter onto the NS surface, which in turn is thought to be driven by specific interactions of acid-base type between acidic sites on MoS_2 (e.g., sulfur

vacancies that are present in most MoS_2 materials) and the weakly basic nucleobases of the nucleotides.[36] It is thus reasonable to assume that in a solvent with a substantially protic character such as water, its conjugate base and acid (i.e., the OH^- and H_3O^+ ions, respectively) would partially screen (and hence weaken) the acid-base interaction between the nucleotide molecules and the MoS_2 surface, thus decreasing the ability of the biomolecule to transfer NSs from the cathodically exfoliated electrode to the olvent. Such a situation would not apply in aprotic or weakly protic solvents, e.g., isopropanol, where a more efficient extraction of NSs would therefore be expected. Indeed, the aprotic solvents *N*,*N*-dimethylformamide (DMF) and *N*-methyl-2-pyrrolidone (NMP) also boasted a considerable extracting ability with the assistance of AMP and GMP (second and third cuvettes from the left in Fig. 2a), although it was somewhat lower (about one half) than that of isopropanol. In the absence of the nucleotides, however, the amount of extracted NSs was much lower (by a factor of ~6–12) in any of these solvents, thus highlighting their critical role in the process. Other stabilizers were tested for NS extraction both in water and isopropanol, including polyvinylpyrrolidone and the Pluronic copolymer P123, as well as the anionic surfactants sodium deoxycholate and sodium dodecylbenzene sulfonate. In these cases, though, only weak dispersion interactions between the stabilizers and the MoS_2 surface were expected, and so their performance was much lower compared to that of AMP and GMP.

To provide quantitative estimates of the efficiency of the present cathodic exfoliation protocol, we determined the amount of NSs that could be extracted in isopropanol with GMP relative to the mass of cathodically expanded MoS_2 material, which was taken as a measure of the exfoliation yield (in weight percentage). Table 1 collects the results obtained with KCl and other electrolytes at different molar concentrations and applied cathodic voltages. For comparison, the exfoliation yield for the non-expanded material, i.e., for MoS_2 that was not subjected to any cathodic treatment but only to solvent sonication, is also given. As could be anticipated, a very low yield (~1 wt%) was attained in this case. The same result was obtained when the cathodic treatment was performed in the absence of any salt, i. e., in pure water. By contrast, cathodic treatment in aqueous KCl afforded a substantial amount of exfoliated product, thus highlighting the benefits of such an electrolytic delamination. Even at low to moderate electrolyte concentrations (i.e., 0.1–1 M KCl) and an applied voltage of -10 V, exfoliation yields around 10 wt% were achieved. These values could

be progressively improved up to a maximum of ~30 wt% by increasing the KCl concentration to 4 M and decreasing the cathodic voltage to -20 V. Qualitatively similar trends were observed with NaCl electrolyte, although the exfoliation yields were generally lower than those of their KCl counterparts (e.g., ~19 wt% at 4 M and -20 V). Only a slightly lower yield (~18 wt%) was attained with 4 M LiCl at -20 V, even though very little expansion of the MoS_2 cathode could be visually noticed with this electrolyte. On the other hand, tetraalkylammonium-based electrolytes [i.e., tetraethylammonium chloride (TEACl), tetrapropylammonium chloride (TPACl) and tetrabutylammonium chloride (TBACl)] gave good yields (~13–18 wt%) at the relatively limited concentrations that can be achieved in water with these salts (typically not much higher than 0.3 M). These results indicated that while such organic salts are efficient electrolytes for the cathodic exfoliation of MoS_2 not only in organic solvents[94] but also in water, a competitive alternative can be offered by much more affordable and widely available substances such as KCl, with a view to industrialize the production of 2D MoS_2 NSs.

Table 1. MoS_2 exfoliation yields calculated as the amount of NSs extracted in isopropanol with GMP by sonication of MoS_2 cathodically expanded under the indicated experimental conditions (applied voltage, type and concentration of electrolyte). The exfoliation yield for MoS_2 that was not subjected to any cathodic treatment but only to solvent sonication is given as a reference value.

Electrolyte	Concentration	Voltage	MoS_2 exfoliation yield
none	-	-	1
KCl	0.1	-10	13
	0.5	-10	10
	1	-10	13
	2	-10	15
	4	-10	22
		-20	30
NaCl	0.1	-10	2
	0.5	-10	9
	1	-10	8
	2	-10	11
	4	-10	7
		-20	19
LiCl	4	-20	18
TEACl	0.3	-20	17
TPACl	0.3	-20	18
TBACl	0.3	-20	13

2.2. Physicochemical characterization of the cathodically exfoliated products

Microscopic and spectroscopic analysis was carried out to confirm that the solvent- extracted material consisted of exfoliated, 2H MoS_2 NSs of a high structural quality. Fig. 3a–c shows representative scanning transmission electron microscopy (STEM) images of the product cathodically exfoliated in 4 M KCl (-20 V) and extracted in isopropanol with GMP, which was seen to be comprised of thin objects (NSs) having irregular polygonal profiles and typical lateral dimensions between a few and several hundreds of nanometers. Further STEM images of samples exfoliated in other electrolytes (NaCl, TPACl) can be found in Fig. S2 (SI). Atomic force microscopy (AFM, Fig. 3d) corroborated the STEM observations, but also revealed that the NSs were ~5–8 nm in (apparent) thickness. Taking into account that the thickness of a MoS_2 monolayer is about 0.7 nm and that a height offset of ~0.5 nm is usually present in AFM images of MoS_2 NSs on hydrophilic substrates,[37] we conclude the exfoliated NSs to be typically between 6 and 11 monolayers thick. This result was consistent with the average number of monolayers per NS (typical values ~7–10) that was determined from the position of the A exciton peak in the UV-vis absorption spectra using the formula previously derived by Coleman and co-workers.[35] In general, the exfoliated NSs possessed a high crystallinity, as evidenced by high resolution transmission electron microscopy (HR- TEM) in Fig. 3e and f, with the hexagonal symmetry of the MoS_2 lattice being made apparent in the selected-area electron diffraction patterns (SAED, inset to Fig. 3f).[24] However, point defects of the type marked by green arrows in Fig. 3e were frequently found in the images, although their density was not very high. Such defects were ascribed to sulfur vacancies, which are rather common in MoS_2 because they possess a low formation energy, and thus are present as an intrinsic feature of both natural and synthetic samples.[38] In our case, it is quite likely that the generation of sulfur vacancies was promoted by the intrinsically reductive conditions of the cathodic process.[39] Energy dispersive X-ray (EDX) analysis provided confirmation that the chemical composition of the observed NSs comprised Mo and S (see Fig. S3 in the SI).

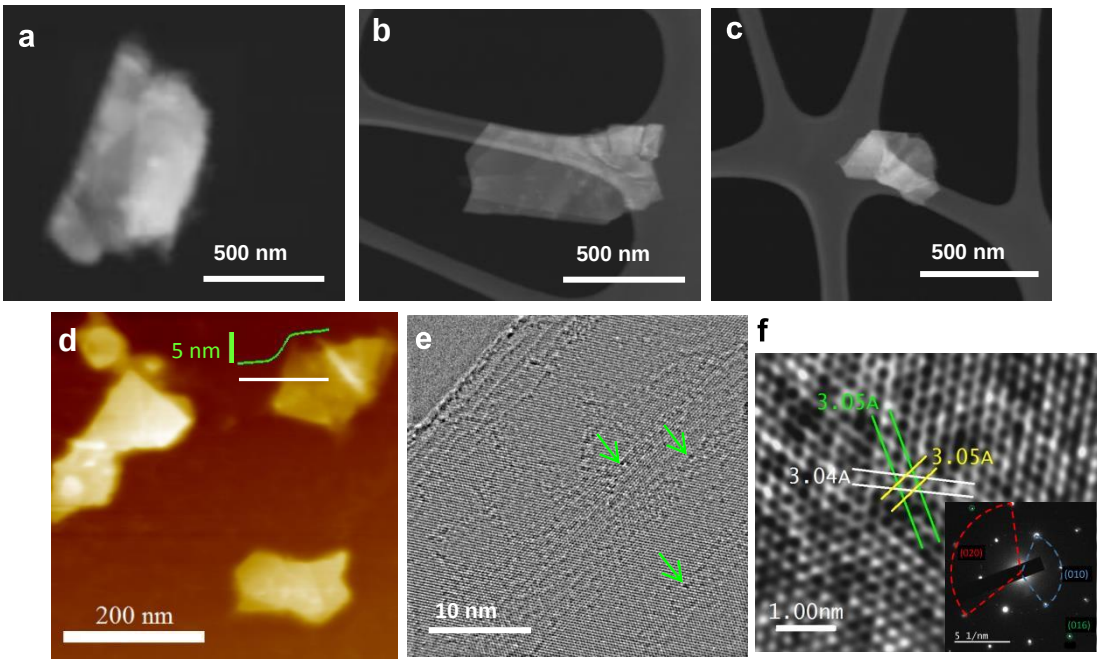

Figure 3. Microscopic characterization of MoS_2 cathodically exfoliated in 4 M KCl aqueous solution and extracted in isopropanol with the assistance of GMP. **(a–c)** Typical STEM images. **(d)** Typical AFM image of MoS_2 nanosheets deposited onto a mica substrate from their dispersion. A representative line profile (green line) taken along the marked white line is shown overlaid on the image. **(e,f)** Representative HR-TEM images of MoS_2 nanosheets. The green arrows in (e) mark some point defects in the MoS_2 lattice. The parallel lines in (f) assist in visualizing *a* and *b* cell parameters of the hexagonal unit cell in the MoS_2 crystal lattice. Inset to f: SAED pattern of the MoS_2 lattice with indication of the crystal planes involved in the observed diffractions.

The Raman spectra recorded at a laser wavelength of 532 nm (Fig. 4a, green trace) displayed two intense peaks at ~383 and 408 cm^{-1}, which correspond to the well-known E^1_{2g} and A_{1g} bands of 2H MoS_2.[40] Such spectra were essentially identical to that of the starting, bulk MoS_2 material (black trace), suggesting that any phase transformation or oxidation of the MoS_2 lattice was avoided during the cathodic exfoliation step. More specifically, no Raman peaks characteristic of 1T´ MoS_2 (i.e., at ~150, 200, 280 and 320 cm^{-1})[15] or molybdenum oxides (e.g., an intense doublet/broad band at ~285–295 cm^{-1})[41] could be detected. Likewise, the E^1_{2g} and A_{1g} bands retained their symmetrical shape and no substantial defect- related bands (mainly the LA(M) band at ~230 cm^{-1}) appeared after exfoliation, implying that defects were not introduced in large numbers in the lattice during the preparation of the MoS_2 NSs,112 in agreement with the HR-TEM results. The fact that a very weak and rather broad band appeared in the spectra of the extracted NSs at ~230 cm^{-1} (green trace in Fig. 4a),

which could therefore be ascribed to the defect-related LA(M) band, but was absent from the cathodically delaminated material before solvent extraction (spectrum not shown) suggested that such a band was associated to the presence of abundant edges due to the limited lateral size of the NSs (Fig. 3) rather than to basal plane lattice defects. Preservation of the 2H phase upon exfoliation was confirmed by X-ray photoelectron spectroscopy (XPS). Fig. 4b and c (green traces) shows high resolution Mo 3d (b) and S 2p (c) core level spectra of the exfoliated NSs. The corresponding spectra of the starting, bulk MoS_2 material (black traces) were mostly indistinguishable from those of the NSs. Regarding the Mo 3d doublet band, the symmetrical shape and position of its $3d_{5/2}$ and $3d_{3/2}$ components (~229.5 and 232.5 eV, respectively) indicated that only the 2H phase was present in both samples (for the 1T´ phase, a downshift of ~0.8 eV in the position of the two components should be expected).[15,24,34] Similarly, the shape and position of the S 2p doublet band was consistent with 2H phase-only materials.[15,36] For comparison, the spectra of chemically exfoliated MoS_2 NSs obtained by the *n*-butyllithium intercalation route, which possess a mixture of 2H and 1T´ phases (with predominance of the latter), are presented in Fig. S4 (SI).

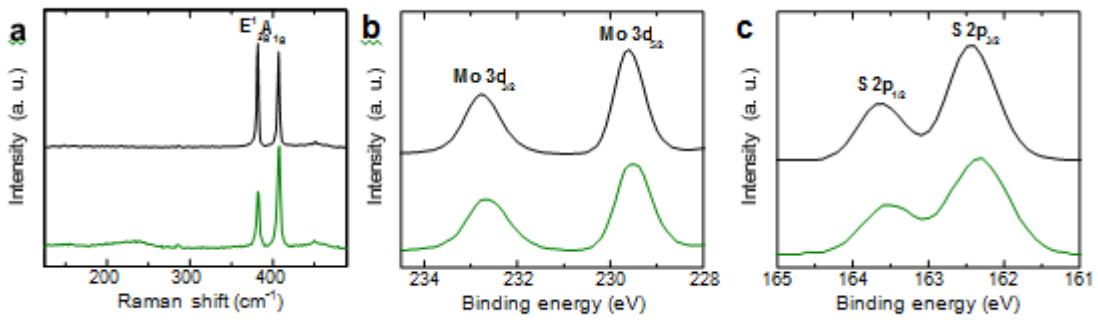

Figure 4. Spectroscopic characterization of cathodically exfoliated MoS_2 NSs. **(a)** Typical Raman spectra of the starting MoS_2 bulk material (black trace) and MoS_2 NSs cathodically exfoliated in 4 M KCl aqueous solution and extracted in isopropanol with the assistance of GMP (green trace). The main bands have been labeled for clarity. **(b, c)** Typical XPS spectra of (b) Mo 3d and (c) S 2p core levels for bulk MoS_2 (black trace) and cathodically exfoliated (green trace) MoS_2 NSs.

2.3. Rationalizing the cathodic exfoliation process of MoS_2 with aqueous alkali metal ions

Having demonstrated aqueous cathodic exfoliation with a very simple salt like KCl to be an efficient strategy for accessing high quality, 2H MoS_2 NSs in considerable yields, it is pertinent to examine the mechanisms that make such an exfoliation possible. First, it is apparent that exfoliation was largely due to intercalation of the MoS_2 electrode by K^+ ions, as the amount of exfoliated NSs tended to increase with increasing KCl concentration and magnitude of the cathodic potential (see Table 1). Second, as could be expected, intercalation was initiated at the edges of the MoS_2 crystal: this could be concluded from the fact that expansion of the cathode was seen to start from its free end (i.e., the one immersed in the electrolytic solution) and then progressed towards its opposite (non-immersed) end. Indeed, while recent work has demonstrated that intercalation of the smallest alkali metal ions (Li^+, Na^+) can take place through the basal surface of MoS_2 via lattice defects (e.g., sulfur vacancies), such a possibility was ruled out in the case of larger alkali ions (K^+), for which only intercalation through edges is feasible.[43] We note that, although it could be argued that just generation of hydrogen gas from water reduction in the external surface of the cathode, without the need of potassium intercalation, could explain the cathodic exfoliation of MoS_2, all the experimental facts suggested that this was not the case: (i) in a control experiment where the voltage was applied in pure water, water reduction was indeed detected by the bubbling of hydrogen but no expansion of the MoS_2 electrode was observed; (ii) the MoS_2 piece was seen to fan out in the presence of KCl (and with increasing extension with its concentration), i. e., the piece did not break down into small fragments but it expanded from the edges to the interior of the piece, as expected from the intercalation of the cations; (iii) when cathodic exfoliation of MoS_2 in 4 M KCl was carried out in a potentiostat in order to study the electrochemical processes involved (see Fig. S5 and the corresponding explanatory text in the SI), an abrupt reduction peak appeared only in the first voltage scan, during whose development the swelling of the MoS_2 cathode became apparent by bare eye. We interpret that this abrupt peak was originated by the intercalation of a large amount of hydrated potassium cations between the lamellae followed by the reduction of co-intercalated water. No reduction peaks were observed in subsequent cycles (grey traces), where just reaction of water on the surface could take place and,

correspondingly, no further swelling of the cathode occurred either.

In order to rationalize the distinct efficiencies of the alkali metal-based electrolytes towards exfoliation (in the order KCl > NaCl > LiCl), the actual nature of the ionic species that participate in the intercalation process needs to be considered. To this end, we note that in an aqueous medium, rather than existing as naked, stand-alone entities, ionic species are surrounded by a bound shell of water molecules (hydrated ions). For alkali metal-based salts, the hydrated cation would take the form $[M \cdot n(H_2O)]^+$, where M is the alkali metal (Li, Na, K) and *n* is the average number of bound water molecules that make up the hydrated cation. It is therefore reasonable to assume that the ability of the aqueous electrolyte to intercalate and expand the MoS_2 cathode efficiently will be dictated to a large extent by the characteristics of the $[M \cdot n(H_2O)]^+$ species, and not just by those of their naked M^+ counterparts. In particular, the value of *n* and thus the average size and mass of the hydrated cation decreases as the atomic weight of the alkali metal is increased, i.e., *n* has been estimated to be ~5.2, 3.5 and 2.6 for Li, Na and K, respectively,[44] and the corresponding hydrated cation diameters are 0.76, 0.72 and 0.66 nm.[30] As a result, the mobility of the hydrated cation under the applied electric field of an electrolytic cell should be larger for K and smaller for Li. Indeed, the molar conductivity of these alkali metal ions in water (at 25 ºC) has been determined to be 38.69, 50.11 and 73.5 S cm^2 mol^{-1} for Li, Na and K, respectively.[45] With a higher electrophoretic mobility and a smaller size, the hydrated K^+ ion will be expected to both reach and intercalate the MoS_2 cathode in larger numbers compared to their Na^+ and Li^+ counterparts, thus providing the basis for its higher exfoliation efficiency, as experimentally observed here.

The initial intercalation of the MoS_2 cathode can be assumed to take place at locally expanded sites (out-of-plane lattice distortions) that most likely exist at the very edges of the MoS_2 crystal due to the localized stress fields associated to such type of structural defect (see schematic representation in Fig. 5).[46] These expanded interlayer spaces at the MoS_2 edges should facilitate the incipient access of a number of hydrated cations, probably after some deformation of their hydration shells to allow accommodation into such constricted spaces.[47] Alternatively, an advance party of (partially) dehydrated cations could first intercalate at the edges, inducing a local increase in the interlayer distance and facilitating the subsequent entry of water molecules and/or fully hydrated cations.[48] We note that dehydration is a well-known phenomenon that can occur during the insertion of ionic species into spatially confined

pores of sub-nanometric dimensions.[49] For the latter scenario, the energy barrier to ion intercalation would be dictated, at least in part, by the binding energy of its hydration shell (hydration enthalpy), which is smaller for K^+ and larger for Li^+.[50] This suggests again a higher intercalation propensity for K^+ relative to Na^+ and Li^+, which would also contribute to its better exfoliation efficiency.

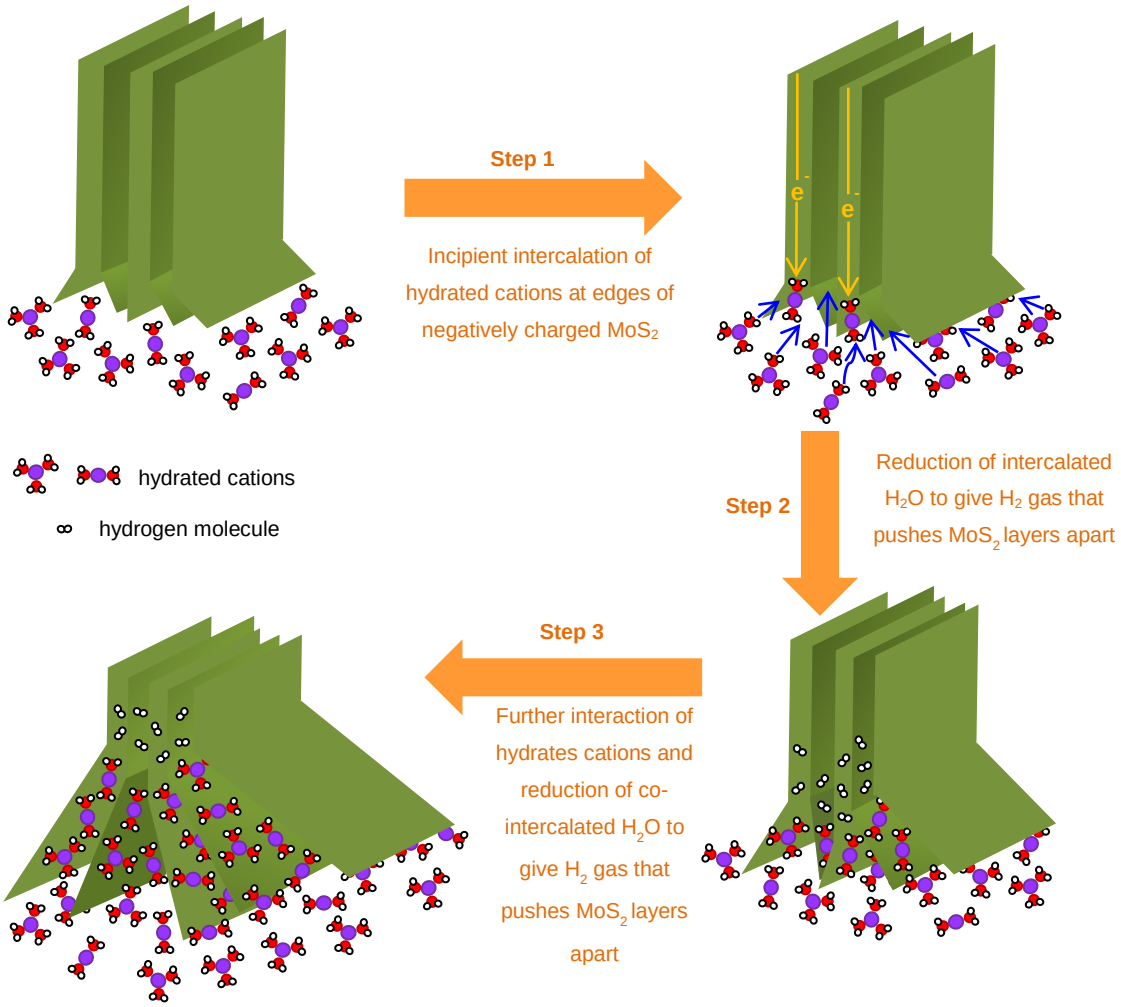

Figure 5. Squematic illustration of the cathodic delamination of MoS_2 in aqueous alkali metal-based electrolytes. Step 1: initial intercalation of hydrated cations at the edges of the negatively biased MoS_2 electrode. Step 2: hydrogen gas generated by co-intercalated water reduction pushes MoS_2 layers apart creating new accessible space for intercalation of additional hydrated cations. Step 3: progressive expansion of the MoS_2 crystal cathode starting from its edges and advancing towards inner regions by further intercalation of hydrated cations and reduction of co-intercalated water.

In either case, the hydrated cations will first intercalate in the edges of the MoS_2 crystal (step 1 in Fig. 5) and then the co-intercalated water molecules will reduce give hydrogen gas (step 2 in Fig. 5). These two steps can be condensed in the following electrochemical reaction (specified for the case of K^+)[51]

$$x[K\cdot n(H_2O)]^+ + MoS_2 + xe^- \rightarrow MoS_2 + x\text{KOH} + (x/2)H_2 + x(n\text{-}1)H_2O \qquad (1)$$

, where x is the number of hydrated cations inserted per unit formula of MoS_2 (step 1 in Fig. 5). Similar expressions can be written for Na^+ and Li^+, but with different values of x.

In turn, the pressure generated within the interlayer spaces by the accumulation of hydrogen gas should contribute to push the MoS_2 layers apart, thus creating new accessible space for the intercalation of additional hydrated cations further away from the edges and into the MoS_2 crystal (step 2 in Fig. 5). Iteration of steps 1 and 2 should then lead to the progressive expansion and delamination of the cathode starting from its edges and advancing towards its inner regions (step 3 in Fig. 5), as it was indeed observed in the experiments (Fig. 1). Moreover, because the hydrated K^+ ion is expected to reach and intercalate the MoS_2 cathode in larger numbers compared to Na^+ and Li^+, a more vigorous delamination of the crystal and hence a higher yield of extracted NSs should be attained with the former ion, which was also in agreement with the results reported here (Table 1). Finally, the fact that the cathodic intercalation process was able to fully retain the original 2H crystal phase of the material, avoiding its transformation to the 1T´ phase, usual when working in non-aqueous media, can be put down, at least in part, to the continuous transfer of electron charge from the negatively biased MoS_2 electrode to the co-intercalated water molecules.[48] Indeed, similar to the present case, A. Zak et al observed a lack of metallic behavior (an absence of 1T´ phase) in MoS_2 intercalated by exposure to potassium vapor, which was attributed to neutralization of part of the free carriers by water inserted during or after metal intercalation.[48] Thus, in addition to promoting electrode expansion and delamination as described above, this electron transfer would contribute to keeping the concentration of excess electron charge at the MoS_2 cathode below the critical threshold required to trigger the phase transformation.

2.4. Use of cathodically exfoliated MoS_2 as an electrode material for supercapacitors

Owing to their high surface area and propensity to ion adsorption/intercalation, 2D MoS_2 NSs are considered attractive candidates for electrochemical energy storage applications, including their use as electrodes for supercapacitors.[51] However, the relatively low electrical conductivity of the thermodynamically stable 2H phase of MoS_2 constitutes an obstacle in the path of high performance supercapacitor devices based on this material. Such an issue can be circumvented by using its metallic 1T-phase variant, which can be accessed either by lithium intercalation/exfoliation of bulk 2H-phase MoS_2 or by bottom-up (solvothermal) synthesis methods.[52] In addition to their high electrical conductivity, 1T-phase MoS_2 NSs are intrinsically hydrophilic, which favors a more extensive wetting of the electrode when using aqueous electrolytes. Unfortunately, the 1T phase is metastable, so that MoS_2 NSs having this polytype readily transform to the 2H phase under ambient conditions in a matter of weeks to months (or much faster under certain stimuli),[52] thus compromising the long-term workability of the corresponding MoS_2-based electrodes.

As an alternative, structurally stable 2H-phase MoS_2 NSs can be combined with highly conductive materials (e.g., carbon nanostructures such as graphene and carbon nanotubes) to give hybrid electrodes with improved electrical conductivity.[53] The present cathodically exfoliated MoS_2 NSs are good candidates for use as electrodes by this approach. Specifically, NSs derived from GMP-stabilized dispersions were mixed with single-walled carbon nanotubes (SWCNTs) that had been previously debundled by sonication in water with flavin mononucleotide (FMN) as a dispersant[54] (AMP and GMP were seen to be poor dispersants for SWCNTs). Details of electrode preparation and measurement can be found in the SI. Fig. 6a and b shows FE-SEM images of a hybrid electrode prepared with a MoS_2 to SWCNT weight ratio of 2:1, where the MoS_2 NSs were seen to be covered by a layer of intermingled SWCNTs. Thus, besides providing efficient conductive paths throughout the hybrid material, the nanotubes acted as spacers between the MoS_2 NSs, which should facilitate electrolyte access to inner regions of the electrode. Furthermore, the polar nature associated to the phosphate group in the GMP and FMN nucleotides adsorbed on MoS_2 and SWCNTs, respectively, should facilitate wetting of the electrode by aqueous electrolytes. Indeed, the contact angle of aqueous 6 M KOH solutions (i.e., the electrolyte used here) measured on vacuum-filtered films of bare MoS_2 NSs and GMP-adsorbed MoS_2 NSs

was ~130º and 110º, respectively (see Fig. S6 in the SI), which confirmed the increased wettability of the latter.

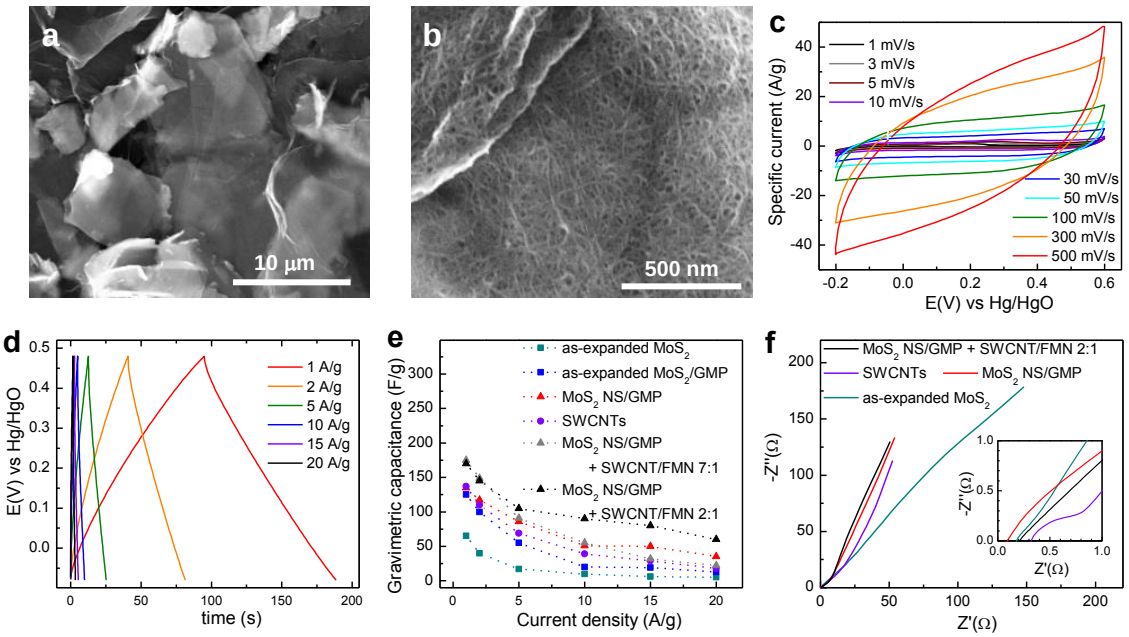

Figure 6. Microscopic and electrochemical characterization of a hybrid made up of cathodically exfoliated MoS_2 NSs and SWCNTs in a weight ratio of 2:1. **(a,b)** Representative FE-SEM images. **(c)** Cyclic voltammograms recorded in a three-electrode configuration at potential scan rates between 1 and 500 mV s^{-1}. **(d)** Galvanostatic charge/discharge profiles obtained at current densities between 1 and 20 A g^{-1}. **(e)** Capacitance values for (1) the product directly obtained from the cathodic treatment of MoS_2 without any post-processing (sample designated as "as-expanded MoS_2"); (2) as-expanded MoS_2 combined with GMP (sample denoted as "as-expanded MoS_2/GMP"); (3) MoS_2 NSs extracted from the as- expanded material by sonication with GMP (sample "MoS_2 NS/GMP"); (4) SWCNTs; GMP- adsorbed NSs mixed with SWCNTs at MoS_2 to SWCNT weight ratio of (5) 7:1 (sample "MoS_2 NS/GMP + SWCNT/FMN 7:1") and (6) 2:1 (sample "MoS_2 NS/GMP + SWCNT/FMN 2:1"). **(f)** Nyquist plots for the some of the materials in (e). Inset to f: detailed view of the high frequency region of the plots.

Fig. 6c shows cyclic voltammograms recorded in a three-electrode configuration with the hybrid material (MoS_2 to SWCNT weight ratio of 2:1) as the working electrode in 6 M KOH electrolyte at potential scan rates between 1 and 500 mV s^{-1}. Overall, the voltammograms tended to be rectangular (or quasi-rectangular) in shape, although broad redox peaks were observed at ~0.15–0.35 V vs Hg/HgO when scanning at the lowest rates (e.g., Fig. S7a in theI for 5 mV s^{-1}). Such peaks were ascribed to redox processes in the GMP and/or FMN molecules.[55,56] Despite the rectangular shape of the voltammograms, we note that the charge storage mechanism in these materials was not (pseudo)capacitive, but of a hybrid nature instead. More to the point, when writing the current measured at a given potential, *i*, as a function of the potential scan rate, in the form:

$$i = a\upsilon^b \tag{2}$$

, and fitting the actual current values for the present material to this equation (see Fig. S7b in the SI for anodic current values at 0.4 V vs Hg/HgO), the *b* exponent was neither 1, as would be the case of purely capacitive and pseudocapacitive processes, nor 0.5, which would indicate a pure battery-type behavior based on diffusion-controlled redox processes.[57] Rather, an intermediate *b* value was obtained ($b \approx 0.68$), indicating that both (pseudo)capacitive and battery-type mechanisms were at play. Furthermore, similar to the case of, e.g., orthorhombic Nb_2O_5, which exhibits a hybrid charge storage mechanism,[58] the current response was highly linear at scan rates below 30 mV s^{-1}, consistent with dominant (pseudo)capacitive processes, whereas it displayed a *b* exponent of ~0.66 in the 50–500 mV s^{-1} range that revealed a substantial battery-type behavior. We believe this mixed response arises from different contributions by the diverse components and characteristics of the hybrid electrode. On one hand, the relatively high surface area of the MoS_2 NSs and SWCNTs should afford capacitive processes through direct ion adsorption, whereas the redox-active nucleotides should deliver pseudocapacitance to the system. On the other hand, diffusion- limited intercalation and deintercalation of electrolyte ions into and out of the several-layer MoS_2 NSs can be expected to give a battery-type contribution to charge storage.

Typical galvanostatic charge/discharge profiles recorded for the hybrid electrode at current densities between 1 and 20 A g^{-1} are presented in Fig. 6d, which exhibited essentially triangular and symmetrical shapes. The corresponding capacitance values are plotted in Fig. 6e, together with those of other electrodes obtained from cathodically treated MoS_2 that was subjected to different post-processing conditions, as well as of SWCNTs without any MoS_2, which are shown for comparative purposes. First, we note that the as-expanded MoS_2 material, i.e., the product directly obtained from the cathodic treatment that was not post- processed in any form (only pressed under 1 ton to prepare the electrodes for measurement; sample denoted as "as-expanded MoS_2" in Fig. 6e), possessed limited capacitance values (e.g., 65 F g^{-1} at 1 A g^{-1}) and a poor rate capability (~15% of capacitance retention at 10 A g^{-1}). To a large extent, such a result was probably due to the hydrophobic nature of bare MoS_2 and to the particular morphology of this electrode (comprised of long and narrow 2D passages between large, re-stacked MoS_2 layers), which should hinder access of the electrolyte to the
bulk of the material.[59] Indeed, the Nyquist plot recorded for this sample by electrochemical impedance spectroscopy (EIS) and shown in Fig. 6e consisted of just an essentially straight line with a slope close to 45º (Warburg region), suggesting a very slow mass transfer into the electrode.[57,60]

The capacitance values improved significantly, mainly at low current densities, when the as-expanded MoS_2 was combined with GMP (sample denoted as "as-expanded MoS_2/GMP"), most likely owing to the improved wettability of the electrode and to the pseudocapacitance contribution of the GMP nucleotide. Some further improvement in capacitance was attained with electrodes made up of MoS_2 NSs extracted from the as-expanded material by sonication with GMP (sample "MoS_2 NS/GMP"), which can be ascribed to better electrolyte access through the larger number of voids and interstices present between the (sub)micrometer-sized NSs. This interpretation was consistent with the corresponding Nyquist plot for this sample (Fig. 6f), which exhibited a shorter Warburg region and a steeper line at lower frequencies compared to the case of as-expanded MoS_2, indicative of improved mass transfer into the electrode.[57,60] When the GMP-adsorbed NSs were mixed with a limited amount of SWCNTs (MoS_2 to SWCNT weight ratio of 7:1; sample "MoS_2 NS/GMP + SWCNT/FMN 7:1"), larger capacitance values were measured at low current densities, but not at high densities. By contrast, better results in the whole current density range

could be achieved with a MoS_2 to SWCNT weight ratio of 2:1 (sample "MoS_2 NS/GMP + SWCNT/FMN 2:1"), e.g., a capacitance of 170 F g^{-1} at 1 A g^{-1} with a ~53% retention at 10 A g^{-1} was measured, while the use of SWCNTs without any MoS_2 led to a poorer performance (see Table S1 in the SI for a comparison with the capacitances of other MoS_2-based electrodes reported in the literature) . Again, this behavior was reflected in the Nyquist plots of Fig. 6e. The hybrid electrode (weight ratio of 2:1) boasted the shortest Warburg region of all samples and a relatively steep profile at low frequencies, which was indicative of mass transfer processes with fewer restrictions, probably as a result of the SWCNTs acting as spacers between the NSs. We also notice from the high frequency region of the Nyquist plots (inset to Fig. 6f) that the semi- circular pattern commonly found in this region for many materials was only apparent in the SWCNT electrode (without MoS_2). Such an observation could again be related to the morphological features of the electrodes, as the absence of a semi-circle has been sometimes associated to electrodes with slit- and/or wedge-shaped pores/voids,[60] and this is the dominant type of void expected when using 2D materials.

To evaluate the performance of the cathodic MoS_2-based electrodes in practical energy storage applications, an asymmetric supercapacitor was assembled using the best-performing sample (i.e., the MoS_2-SWCNT hybrid prepared with a weight ratio of 2:1) as the positive electrode and a commercial activated carbon (Kurarai YP-50F) as the negative electrode, in aqueous 6 M KOH electrolyte. Fig. 7a shows cyclic voltammograms (potential scan rate: 50 mV s^{-1}) for both materials in the three-electrode configuration to illustrate the complementarity of their voltage windows. Stable scan windows between -1.1 and 0.0 V and between -0.2 and 0.6 V (vs Hg/HgO) were recorded for the activated carbon and the MoS_2- SWCNT hybrid, respectively. Cyclic voltammograms for the asymmetric, two-electrode cell could thus be reliably obtained in the 0–1.55 V range (Fig. 7b), the shape of which was reasonably well preserved up to potential scan rates of 500 mV s^{-1}, thus indicating that the device was able to cope with fast mass and electron transfer rates. The non-ideal rectangular shape of these voltammograms is believed to reflect the contribution of the diverse charge storage mechanisms that were discussed above. Galvanostatic charge/discharge curves for the asymmetric device at current densities between 1 and 10 A g^{-1} are presented in Fig. 7c, with the corresponding gravimetric capacitance values ranging between 83.3 and 26.7 F g^{-1} (at 1 and 10 A g^{-1}, respectively). Furthermore, the charge storage

capability of the supercapacitor remained essentially unaltered upon repeated cycling of the device, as demonstrated in the inset to Fig. 7c for 6000 consecutive charge/discharge cycles recorded at 3 A g^{-1}. From these results, the maximum energy density delivered by the cell was determined to be 26 W h kg^{-1} at a power density of 750 W kg^{-1}, and it was still 8.3 Wh kg^{-1} at 7500 W kg^{-1}. As can be noticed from Table S2 in the SI, these figures were competitive with those recently reported in the literature for a variety of asymmetric supercapacitors having MoS_2-based electrodes (typically the anode). We note that in most of these prior cases, the MoS_2 materials were obtained through hydrothermal synthesis at relatively low temperatures (generally < 200 ºC). However, MoS_2 prepared under such conditions tends to be of a limited crystalline quality and is particularly prone to oxidize under ambient conditions (especially in humid environments), which compromises its electrochemical and catalytic performance. [62] Oxidation issues, on the other hand, should be less severe when using MoS_2 samples with good crystallinity, such as those produced here by cathodic exfoliation.

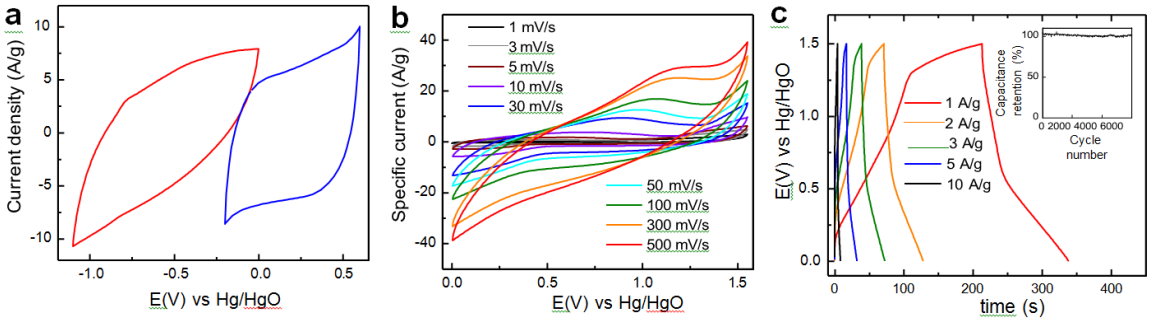

Figure 7. (a) Potential windows of cathodically exfoliated MoS_2 NS-SWCNT hybrid (positive electrode, blue trace) and activated carbon (negative electrode, red trace) at 50 mV s^{-1}. **(b)** Cyclic voltammograms recorded for the asymmetric two-electrode cell at potential scan rates between 1 and 500 mV s^{-1}. **(c)** Galvanostatic charge/discharge profiles obtained at current densities between 1 and 10 A g^{-1}. Inset to c: percentage of capacitance retention of the asymmetric cell measured at a current density of 3 A g^{-1} for consecutive charge/discharge cycles (up to 6000).

2.5 Use of cathodically exfoliated MoS_2 as a catalyst for the reduction of nitroarenes

Finally, we investigated the performance of the cathodic MoS_2 NSs as catalysts for the reduction of the nitroarenes 4-nitrophenol (4-NP) and 4-nitroaniline (4-NA) with $NaBH_4$ in aqueous medium. These reactions are of practical relevance in a number of industrial processes, such as the synthesis of certain antipyretic drugs (e.g., paracetamol), dyes or polymers, and while both are thermodynamically feasible, catalysts are typically required to circumvent significant kinetic barriers.[61] Noble metal (Pt, Pd, Au, etc) nanoparticles have been extensively employed to this end, but in recent years a shift in emphasis towards the exploration of more earth-abundant alternatives, i.e., non-noble metal132 or even metal-free catalysts (e.g, nitrogen-doped graphene),[63,64] has taken place. Different types of MoS_2 NSs are also effective catalysts for nitroarene reduction,[36,67] in particular 1T´-phase NSs produced by the lithium intercalation route, which exhibited a substantial activity that probably resulted from their metallic character.[67] However, the metastability of the 1T´ NSs and their tendency to irreversibly agglomerate in water compromise their long-term catalytic performance. These issues could be avoided with 2H- phase NSs produced in water/GMP solutions by direct ultrasound exfoliation, but at the expense of a considerable decrease in catalytic activities (for 2H MoS_2, catalytic sites are only located at edges and basal plane defects).[6,36] Here we show that the 2H-phase NSs produced by cathodic exfoliation and colloidally stabilized with GMP boast catalytic activities for nitroarene reduction that are comparable to those of 1T´ NSs, thus incorporating the best features of the two previously studied types of MoS_2 NSs.

The kinetics of both 4-NP and 4-NA reduction was followed with UV-vis absorption spectroscopy by recording the evolution of specific absorption peaks that are distinctive of the nitroarene molecules, but are absent from their reduced counterparts, so that their intensity reflects the nitroarene reactant concentration (see SI for details on the catalytic experiments). In the case of 4-NP, a peak at ~400 nm was monitored, which corresponded to the deprotonated form of the molecule, i.e, the 4-nitrophenoxide ion generated in the basic medium of the $NaBH_4$ reductant (Fig. 8a). For 4-NA, the peak at ~380 nm was recorded (Fig. 8b). Fig. 8c shows typical kinetic profiles for the reduction of 4-NP (blue trace) and 4-NA (red trace) with the cathodically exfoliated, GMP-stabilized MoS_2 NSs. An initial induction period of a few minutes was observed for the reduction of 4-NP, during which essentially no

change in the intensity of the absorption peak was measured even though the reducing agent and the catalyst were both present in the reaction medium. Such a behavior was probably related to the presence of oxygen dissolved in the solution, which was consumed during the induction period by oxidizing the reaction product back to its original unreduced form (i.e, the reactant and product molecules were in dynamic equilibrium).[68] Under this scenario, shorter induction periods were to be expected for faster reactions, such as the reduction of 4-NA, and this was indeed the case to the point that no induction period could be measured for 4-NA. After the induction period, if present, a steep and continuous decrease in absorbance was seen to occur, indicating that the forward (reduction) reaction became dominant. The absorbance does not drop down to zero but rather to a constant, finite value after the end of the reaction (see Fig. 8c), as the catalyst itself absorbs at the monitored wavelengths (see Fig. 2b). Similar to previous instances with MoS_2 NSs,[36,67] the kinetic profiles could be fitted to exponential decay functions, which was consistent with the reactions being pseudo-first-order with respect to nitroarene concentration ($NaBH_4$ was used in large excess and thus its concentration remained essentially constant throughout the reaction).

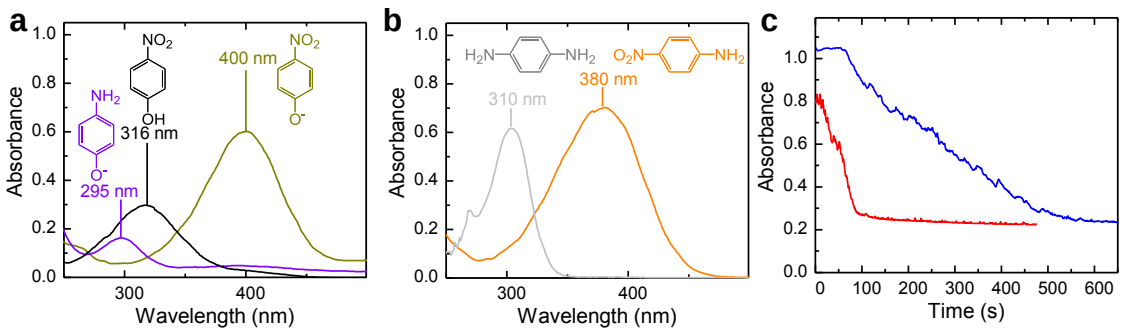

Figure 8. UV-vis absorption spectra of **(a)** 4-NP (black trace), 4-nitrophenoxide ion (dark yellow), and its reduced form, 4-aminophenoxide ion (violet); **(b)** 4-NA (orange) and its reduced form, *p*-phenylenediamine (gray). **(c)** Typical kinetic profiles for the reduction of 4- NP (blue trace) and 4-NA (red trace) with the cathodically exfoliated GMP-stabilized MoS_2 NSs as the catalyst.

To quantify the performance of the cathodically exfoliated NSs and compare it with that of other catalysts previously reported in the literature, their catalytic activity was calculated as the number of moles of reactant (4-NP or 4-NA) converted per unit

time per mole of MoS_2 used. Table S3 in the SI collects the results obtained for different types of MoS_2 NSs as well as some materials derived from graphene oxide. We note that the GMP molecules adsorbed on the MoS_2 surface had a significant effect on the catalytic activity of the nucleotide- stabilized NSs (both cathodically and ultrasound exfoliated), and therefore their amount had to be carefully optimized to obtain best results (see SI). If the amount of adsorbed GMP was too large, poor catalytic activities were attained, probably due to obstructed access of the 4- NP and 4- NA molecules to the catalytically active sites of the material, similar to the effect that the organic ligand shell has on the general catalytic activity of colloidal metal nanoparticles.[69] On the other hand, the colloidal stability of the NSs in the reaction medium was compromised when the amount of adsorbed GMP was too low, which also impacted negatively on the measured catalytic activities as a result of NS agglomeration.

The activity of the present GMP-stabilized, cathodic MoS_2 NSs was comparable to that measured for 1T´ NSs prepared by the lithium intercalation route, but several times higher than that of NSs produced by direct ultrasound exfoliation of bulk MoS_2 with GMP, even though 2H-phase NSs with similar lateral sizes and thicknesses were used for the two types of GMP-stabilized catalysts. We believe this result to be related to the particular processing history of the cathodically exfoliated product: (i) as discussed above, the reductive conditions of the cathodic treatment should be especially conducive to the generation of a certain amount of (catalytically active) sulfur vacancies in the NSs,[39] and (ii) the electrolytic delamination of the MoS_2 cathode introduces substantial strain in the expanded layers in the form of, e.g., wrinkles and ripples (see Fig. 1e), which is also expected to enhance the catalytic activity of the material.[70] Furthermore, the present catalytic activities were found to be ~2 orders of magnitude larger than those typical of graphene oxide-derived catalysts (Table S3 in the SI) and also compared favorably with those reported in recent years for catalysts based on non- noble metals, such as Cu, Ni or Co (Table S4 in the SI), indicating that the cathodic MoS_2 NSs developed here can be competitive catalysts for this application.

Conclusions

An efficient approach for the cathodic delamination of bulk MoS_2 into two-dimensional nanosheets has been demonstrated by resorting to aqueous solutions of very simple and widely available salts (most notably, KCl) as the electrolytic medium. In addition to its inherently safe and sustainable character associated to the use of such an electrolyte, this electrochemical route is able to avert any oxidation or phase transformation of the exfoliated products and, combined with a proper biomolecule-based solvent transfer protocol, affords colloidally dispersed MoS_2 nanosheets of a high structural quality in substantial yields that are suitable for further processing towards practical applications. The cathodically exfoliated MoS_2 nanosheets exhibited a competitive performance when used as the positive electrode for asymmetric supercapacitors and as a catalyst for the reduction of nitroarenes. Other prospective applications in the energy and catalysis realms where these cathodic MoS_2 nanosheets possess a strong potential include their use in different types of rechargeable batteries and as hydrogen evolution reaction electrocatalysts, which will be explored in the near future. Finally, it is also envisaged that the present cathodic exfoliation strategy can be extended to other transition metal dichalcogenides as well as other layered materials of current interest (e.g., black phosphorus).

Acknowledgements

Funding by the Spanish Ministerio de Economía y Competitividad (MINECO) and the European Regional Development Fund (ERDF) through project MAT2015-69844-R and Plan de Ciencia, Tecnología e Innovación (PCTI) 2013-2017 del Principado de Asturias and the ERDF (project IDI/2018/000233) are gratefully acknowledged. S.G-D. and J.M.M. are grateful to Spanish MINECO and Ministerio de Educación, Cultura y Deporte (MECD), respectively, for their respective pre-doctoral contracts (BES/2016 077830 and FPU14/00792). The University of Oviedo acknowledges the financial support from Spanish MINECO (MAT2016-78155-C2-1-R) and the Government of the Principality of Asturias (GRUPIN-IDI/2018/170).

Supporting Information. The Supporting Information is available free of charge on the ACS Publication website at DOI: 10.1021/acsami.9b13484. Experimental section, additional microscopic and spectroscopic characterization, .additional information related to the electrochemical characterization of cathodically exfoliated MoS_2,

comparison of the catalytic activity of GMP-stabilized cathodically exfoliated MoS_2 NSs towards the reduction of nitroarenes with $NaBH_4$ with that reported for other catalyst in the literature.

References

[1] Tan, C.; Cao, X.; Wu, X.-J.; He, Q.; Yang, J.; Zhang, X.; Chen, J.; Zhao, W.; Han, S.; Nam, G.-H.; Sindoro, M.; Zhang, H. Recent Advances in Ultrathin Two-Dimensional Nanomaterials, Chem. Rev. 2017, 117, 6225–6331.

[2] Choi, W.; Choudhary, N.; Han, G.H.; Park, J.; Akinwande, D.; Lee, Y.H. Recent Development of Two-Dimensional Transition Metal Dichalcogenides and their Applications, Mater. Today 2017, 20, 116–130.

[3] Samadi, M.; Sarikhani, N.; Zirak, M.; Zhang, H.; Zhang, H.-L.; Moshfegh, A.Z. Group 6 Transition Metal Dichalcogenide Nanomaterials: Synthesis, Applications and Future Perspectives, Nanoscale Horiz. 2018, 3, 90–204.

[4] Wang, Q.H.; Kalantar-Zadeh, K.; Kis, A.; Coleman, J.N.; Strano, M.S. Electronics and Optoelectronics of Two-Dimensional Transition Metal Dichalcogenides, Nat. Nanotechnol. 2012, 7, 699–712.

[5] Pumera, M.; Sofer, Z.; Ambrosi, A. Layered Transition Metal Dichalcogenides for Electrochemical Energy Generation and Storage, J. Mater. Chem. A 2014, 2, 8981–8987.

[6] Zhu, C.; Gao, D.; Ding, J.; Chao, D.; Wang, J. TMD-based Highly Efficient Electrocatalysts Developed by Combined Computational and Experimental Approaches, Chem. Soc. Rev. 2018, 47, 4332–4356.

[7] Quinn, M. D. J.; Ho, N. H.; Notley, S. M. Aqueous Dispersions of Exfoliated Molybdenum Disulfide for Use in Visible-Light Photocatalysis, ACS Appl. Mater. Interfaces 2013, 5, 12751–12756.

[8] Ping, J.; Fan, Z.; Sindoro, M.; Ying, Y.; Zhang, H. Recent Advances in Sensing Applications of Two-Dimensional Transition Metal Dichalcogenide Nanosheets and their Composites, Adv. Funct. Mater. 2017, 27, 1605817.

[9] Agarwal, V.; Chatterjee, K. Recent Advances in the Field of Transition Metal Dichalcogenides for Biomedical Applications, Nanoscale 2018, 10, 16365–16397.

[10] Yu, J.; Hu, X.; Li, H.; Zhou, X.; Zhai, T. Large-Scale Synthesis of 2D Metal Dichalcogenides, J. Mater. Chem. C 2018, 6, 4627.

[11] Y. Shi, H. Li and L.-J. Li, Recent Advances in Controlled Synthesis of Two-Dimensional Transition Metal Dichalcogenides via Vapour Deposition Techniques, Chem. Soc. Rev. 2015, 44, 2744–2756.

[12] Niu, L.; Coleman, J.N.; Zhang, H.; Shin, H.; Chhowalla, M.; Zheng, Z. Production of Two-Dimensional Nanomaterials via Liquid-Based Direct Exfoliation, Small 2016, 12, 272– 293.

[13] Cai, X.; Luo, Y.; Liu, B.; Cheng, H.-M. Preparation of 2D Material Dispersions and their Applications, Chem. Soc. Rev. 2018, 47, 6224–6266.

[14] Paredes, J.I.; Villar-Rodil, S. Biomolecule-Assisted Exfoliation and Dispersion of Graphene and other Two-Dimensional Materials: a Review of Recent Progress and Applications, Nanoscale 2016, 8, 15389–15413.

[15] Eda, G.; Yamaguchi, H.; Voiry, D.; Fujita, T., Chen, M.; Chhowalla, M. Photoluminescence from Chemically Exfoliated MoS_2, Nano Lett. 2011, 11, 5111–5116.

[16] Fan, X.; Xu, P.; Zhou, D.; Sun, Y.; Li, Y.C.; Nguyen, M.A.T.; Terrones, M.; Mallouk, T.E. Fast and Efficient Preparation of Exfoliated 2H MoS_2 Nanosheets by Sonication-Assisted Lithium Intercalation and Infrared Laser-Induced 1T to 2H Phase Reversion. Nano Lett. 2015, 15, 5956–5960.

[17] Ambrosi, A.; Pumera, M. Exfoliation of Layered Materials using Electrochemistry, Chem. Soc. Rev. 2018, 47, 7213–7224.

[18] Yang, Y.; Hou, H.; Zou, G.; Shi, W.; Shuai, H.; Li, J.; Ji, X. Electrochemical Exfoliation of Graphene-Like Two-Dimensional Nanomaterials, Nanoscale 2019, 11, 16–33.

[19] Zeng, Z.; Yin, Z.; Huang, X.; Li, H.; He, Q.; Lu, G.; Boey, F.; Zhang, H. Single-Layer Semiconducting Nanosheets: High-Yield Preparation and Device Fabrication, Angew. Chem. Int. Ed. 2011, 50, 11093–11097.

[20] Zeng, Z.; Sun, T.; Zhu, J.; Huang, X.; Yin, Z.; Lu, G.; Fan, Z.; Yan, Q.; Hng, H.H.; Zhang, H. An Effective Method for the Fabrication of Few-Layer-Thick Inorganic Nanosheets, Angew. Chem. Int. Ed. 2012, 51, 9052–9056.

[21] Ejigu, A.; Kinloch, I.A.; Prestat, E.; Dryfe, R.A.W. A Simple Electrochemical

Route to Metallic Phase Trilayer MoS_2: Evaluation as Electrocatalysts and Supercapacitors, J. Mater. Chem. A 2017, 5, 11316–11330.

[22] El Garah, M.; Bertolazzi, S.; Ippolito, S.; Eredia, M.; Janica, I.; Melinte, G.; Ersen, O.; Marletta, G.; Ciesielski, A.; Samorì, P. MoS_2 nanosheets via Electrochemical Lithium-Ion Intercalation under Ambient Conditions, FlatChem 2018, 9, 33–39.

[23] Li, F.; Xue, M.; Zhang, X.; Chen, L.; Knowles, G.P.; MacFarlane, D.R.; Zhang, J. Advanced Composite 2D Energy Materials by Simultaneous Anodic and Cathodic Exfoliation, Adv. Energy Mater. 2018, 8, 1702794.

[24] Lin, Z.; Liu, Y.; Halim, U.; Ding, M.; Liu, Y.; Wang, Y.; Jia, C.; Chen, P.; Duan, X.; Wang, C.; Song, F.; Li, M.; Wan, C.; Huang, Y.; Duan, X. Solution-Processable 2D Semiconductors for High Performance Large-Area Electronics, Nature 2018, 562, 254–258.

[25] Liu, N.; Kim, P.; Kim, J.H.; Ye, J.H.; Kim, S.; Lee, C.J. Large-Area Atomically Thin MoS_2 Nanosheets Prepared Using Electrochemical Exfoliation, ACS Nano 2014, 8, 6902– 6910.

[26] Ambrosi, A.; Pumera, M. Electrochemical Exfoliation of MoS_2 Crystal for Hydrogen Electrogeneration, Chem. Eur. J. 2018, 24, 18551–18555.

[27] Jaegermann, W.; Schmeisser, D. Reactivity of Layer Type Transition Metal Chalcogenides towards Oxidation, Surf. Sci. 1986,165, 143–160.

[28] Pető, J.; Ollár, T.; Vancsó, P.; Popov, Z.I.; Magda, G.Z.; Dobrik, G.; Hwang, C.; Sorokin, P.B.; Tapasztó, L. Spontaneous Doping of the Basal Plane of MoS_2 Single Layers through Oxygen Substitution under Ambient Conditions, Nat. Chem. 2018, 10, 1246–1251.

[29] Spychalski, W.L.; Pisarek, M.; Szoszkiewicz, R. Microscale Insight into Oxidation of Single MoS_2 Crystals in Air, J. Phys. Chem. C 2017, 121, 26027–26033.

[30] Zhong, C.; Deng, Y.; Hu, W.; Qiao, J.; Zhang, L.; Zhang, J. A Review of Electrolyte Materials and Compositions for Electrochemical Supercapacitors, Chem. Soc. Rev. 2015, 44, 7484–7539.

[31] Xia, Z.Y.; Pezzini, S.; Treossi, E.; Giambastiani, G.; Corticelli, F.; Morandi, V.;

Zanelli, A.; Bellani, V.; Palermo, V. The Exfoliation of Graphene in Liquids by Electrochemical, Chemical, and Sonication-Assisted Techniques: A Nanoscale Study, Adv. Funct. Mater. 2013, 23, 4684–4693.

[32] Munuera, J.M.; Paredes, J.I.; Villar-Rodil, S.; Ayán-Varela, M.; Pagán, A.; Aznar- Cervantes, S.D.; Cenis, J.L.; Martínez-Alonso, A.; Tascón, J.M.D. High Quality, Low Oxygen Content and Biocompatible Graphene Nanosheets Obtained by Anodic Exfoliation of Different Graphite Types, Carbon 2015, 94, 729–739.

[33] Li, B.L.; Zou, H.L.; Lu, L.; Yang, Y.; Lei, J.L.; Luo, H.Q.; Li, N.B. Size-Dependent Optical Absorption of Layered MoS_2 and DNA Oligonucleotides Induced Dispersion Behavior for Label-Free Detection of Single-Nucleotide Polymorphism, Adv. Funct. Mater. 2015, 25, 3541–3550.

[34] Paredes, J.I.; Munuera, J.M.; Villar-Rodil, S.; Guardia, L.; Ayán-Varela, M.; Pagán, A.; Aznar-Cervantes, S.D.; Cenis, J.L.; Martínez-Alonso, A.; Tascón, J.M.D. Impact of Covalent Functionalization on the Aqueous Processability, Catalytic Activity, and Biocompatibility of Chemically Exfoliated MoS_2 Nanosheets, ACS Appl. Mater. Interfaces 2016, 8, 27974– 27986.

[35] Backes, C.; Smith, R.J.; McEvoy, N.; Berner, N.C.; McCloskey, D.; Nerl, H.C.; O´Neill, A.; King, P.J.; Higgins, T.; Hanlon, D.; Scheuschner, N.; Maultzsch, J.; Houben, L.; Duesberg, G.S.; Donegan, J.F.; Nicolosi, V.; Coleman, J.N. Edge and Confinement Effects Allow in situ Measurement of Size and Thickness of Liquid-Exfoliated Nanosheets, Nat. Commun. 2014, 5, 4576.

[36] Ayán-Varela, M.; Pérez-Vidal, Ó.; Paredes, J.I.; Munuera, J.M.; Villar-Rodil, S.; Díaz- González, M.; Fernández-Sánchez, C.; Silva, V.S.; Cicuéndez, M;. Vila, M.; Martínez- Alonso, A.; Tascón, J.M.D. Aqueous Exfoliation of Transition Metal Dichalcogenides Assisted by DNA/RNA Nucleotides: Catalytically Active and Biocompatible Nanosheets Stabilized by Acid−Base Interactions, ACS Appl. Mater. Interfaces 2017, 9, 2835–2845.

[37] Li, H.; Lu, G.; Yin, Z.; He, Q.; Li, H.; Zhang, Q.; Zhang, H. Optical Identification of Single-and Few-Layer MoS_2 Sheets, Small 2012, 8, 682–686.

[38] Hong, J.; Hu, Z.; Probert, M.; Li, K.; Lv, D.; Yang, X.; Gu, L.; Mao, N.; Feng, Q.; Xie, L.; Zhang, J.; Wu, D.; Zhang, Z.; Jin, C.; Ji, W.; Zhang, X.; Yuan, J.; Zhang, Z.

Exploring Atomic Defects in Molybdenum Disulphide Monolayers, Nat. Commun. 2015, 6, 6293.

[39] Tsai, C.; Li, H.; Park, S.; Park, J.; Han, H.S.; Nørskov, J.K.; Zheng, X.; Abild-Pedersen, F. Electrochemical Generation of Sulfur Vacancies in the Basal Plane of MoS_2 for Hydrogen Evolution, Nat. Commun. 2017, 8, 15113.

[40] Zhang, X.; Qiao, X.-F.; Shi, W.; Wu, J.-B.; Jiang, D.-S.; Tan, P.-H. Phonon and Raman Scattering of Two-Dimensional Transition Metal Dichalcogenides from Monolayer, Multilayer to Bulk Material, Chem. Soc. Rev. 2015, 44, 2757–2785.

[41] Dieterle, M.; Weinberg, G.; Mestl, G. Raman Spectroscopy of Molybdenum Oxides. Part I. Structural Characterization of Oxygen Defects in MoO_{3-x} by DR UV/VIS, Raman Spectroscopy and X-Ray Diffraction, Phys. Chem. Chem. Phys. 2002, 4, 812–821.

[42] Mignuzzi, S.; Pollard, A.J.; Bonini, N.; Brennan, B.; Gilmore, I.S.; Pimenta, M.A.; Richards, D.; Roy, D. Effect of disorder on Raman scattering of single-layer MoS_2, Phys. Rev. B, 2015, 91, 195411.

[43] Zhang, J.; Yang, A.; Wu, X.; van de Groep, J.; Tang, P.; Li, S.; Liu, B.; Shi, F.; Wan, J.; Li, Q.; Sun, Y.; Lu, Z.; Zheng, X.; Zhou, G.; Wu, C.-L.; Zhang, S.-C.; Brongersma, M.L.; Li, J.; Cui, Y. Reversible and Selective Intercalation through the Top Surface of Few-Layer MoS_2, Nat. Commun. 2018, 9, 5289.

[44] Marcus, Y. Thermodynamics of Solvation of Ions. Part 5.—Gibbs Free Energy of Hydration at 298.15 K, J. Chem. Soc. Faraday Trans. 1991, 87, 2995–2999.

[45] Dean, J.A. Lange´s Handbook of Chemistry, 15^{th} edition, McGraw-Hill, New York, 1999, section 8.7.

[46] Tinoco, M.; Maduro, L.; Masaki, M.; Okunishi, E.; Conesa-Boj, S. Strain-Dependent Edge Structures in MoS_2 Layers, Nano Lett. 2017, 17, 7021–7026.

[47] Kalluri, R.K.; Biener, M.M.; Suss, M.E.; Merrill, M.D.; Stadermann, M.; Santiago, J.G.; Baumann, T.F.; Biener, J.; Striolo, A. Unraveling the Potential and Pore-Size Dependent Capacitance of Slit-Shaped Graphitic Carbon Pores in Aqueous Electrolytes, Phys. Chem. Chem. Phys. 2013, 15, 2309–2320.

[48] Zak, A.; Feldman, Y.; Lyakhovitskaya, V.; Leitus, G.; Popovitz-Biro, R.;

Wachtel, E.; Cohen, H.; Reich, S.; Tenne, R. Alkali Metal Intercalated Fullerene-Like MS_2 (M = W, Mo) Nanoparticles and their Properties, J. Am. Chem. Soc. 2002, 124, 4747–4758.

[49] Sahu, S.; Ventra, M.D.; Zwolak, M. Dehydration as a Universal Mechanism for Ion Selectivity in Graphene and Other Atomically Thin Pores, Nano Lett. 2017, 17, 4719–4724.

[50] Housecroft, C.E.; Jenkins, H.D.B. Absolute Ion Hydration Enthalpies and the Role of Volume within Hydration Thermodynamics, RSC Adv. 2017, 7, 27881–27894.

[51] Schöllhorn; R.; Weiss, A. Cation Exchange Reactions and Layer Solvate Complexes of Ternary Phases M_xMoS_2, J. Less-Common Met. 1974, 36, 229–236.

[52] Wang, T.; Chen, S.; Pang, H.; Xue, H.; Yu, Y. MoS_2-Based Nanocomposites for Electrochemical Energy Storage, Adv. Sci. 2017, 4, 1600289.

[53] Jiao, Y.; Hafez, A.M.; Cao, D.; Mukhopadhyay, A.; Ma, Y.; Zhu, H. Metallic MoS_2 for High Performance Energy Storage and Energy Conversion, Small 2018, 14, 1800640.

[54] Choudhary, N.; Islam, M.A.; Kim, J.H.; Ko, T.-J.; Schropp, A.; Hurtado, L.; Weitzman, D.; Zhai, L.; Jung, Y. Two-Dimensional Transition Metal Dichalcogenide Hybrid Materials for Energy Applications, Nano Today 2018, 19, 16–40.

[55] Ju, S.-Y.; Doll, J.; Sharma, I.; Papadimitrakopoulos, F. Selection of Carbon Nanotubes with Specific Chiralities Using Helical Assemblies of Flavin Mononucleotide, Nat. Nanotechnol. 2008, 3, 356–362.

[56] Goyal, R.N.; Puri, B.K.; Jain, N. Electrochemical Oxidation of Guanosine-5′-Monophosphate at the Pyrolytic Graphite Electrode, J. Chem. Soc., Perkin Trans. 2001, 2, 832–837.

[57] Ayán-Varela, M.; Paredes, J.I.; Guardia, L.; Villar-Rodil, S.; Munuera, J.M.; Díaz- González, M.; Fernández-Sánchez, C.; Martínez-Alonso, A.; Tascón, J.M.D. Achieving Extremely Concentrated Aqueous Dispersions of Graphene Flakes and Catalytically Efficient Graphene-Metal Nanoparticle Hybrids with Flavin Mononucleotide as a High-Performance Stabilizer, ACS Appl. Mater. Interfaces 2015, 7, 10293–10307.

[58] Noori, A.; El-Kady, M.F.; Rahmanifar, M.S.; Kaner, R.B.; Mousavi, M.F. Towards Establishing Standard Performance Metrics for Batteries, Supercapacitors and Beyond, Chem. Soc. Rev. 2019, 48, 1272–1341.

[59] Augustyn, V.; Come, J.; Lowe, M.A.; Kim, J.W.; Taberna, P.-L.; Tolbert, S.H.; Abruña, H.D.; Simon, P.; Dunn, B. High-rate Electrochemical Energy Storage through Li^+ Intercalation Pseudocapacitance, Nat. Mater. 2013, 12 , 518–522.

[60] Munuera, J.M.; Paredes, J.I.; Villar-Rodil, S.; Castro-Muñiz, A.; Martínez-Alonso, A.; Tascón, J.M.D. High Quality, Low-Oxidized Graphene via Anodic Exfoliation with Table Salt as an Efficient Oxidation-Preventing Co-Electrolyte for Water/Oil Remediation and Capacitive Energy Storage Applications, Appl. Mater. Today 2018, 11, 246–254.

[61] Conway, B.E. Electrochemical supercapacitors. Scientific fundamentals and technological applications, Kluwer Academic/Plenum Publishers, New York, 1999, ch. 14.

[62] Afanasiev, P.; Lorentz, C. Oxidation of Nanodispersed MoS_2 in Ambient Air: The Products and the Mechanistic Steps, J. Phys. Chem. C 2019, 123, 7486−7494.

[63] Aditya, T.; Pal, A.; Pal, T. Nitroarene Reduction: a Trusted Model Reaction to Test Nanoparticle Catalysts, Chem. Commun. 2015, 51, 9410–9431.

[64] Formenti, D.; Ferretti, F.; Scharnagl, F.K.; Beller, M. Reduction of Nitro Compounds Using 3d-Non-Noble Metal Catalysts, Chem. Rev. 2019, 119, 2611–2680.

[65] Song, J.; Kang, S.W.; Lee, Y.W.; Park, Y.; Kim, J.-H.; Han, S.W. Regulating the Catalytic Function of Reduced Graphene Oxides Using Capping Agents for Metal-Free Catalysis, ACS Appl. Mater. Interfaces 2017, 9, 1692–1701.

[66] Liu, J.; Yan, X.; Wang, L.; Kong, L.; Jian, P. Three-Dimensional Nitrogen-Doped Graphene Foam as Metal-Free Catalyst for the Hydrogenation Reduction of p-Nitrophenol, J. Colloid Interface Sci. 2017, 497, 102–107.

[67] Guardia, L.; Paredes, J.I.; Munuera, J.M.; Villar-Rodil, S.; Ayán-Varela, M.; Martínez- Alonso, A.; Tascón, J.M.D. Chemically Exfoliated MoS_2 Nanosheets as an Efficient Catalyst for Reduction Reactions in the Aqueous Phase, ACS Appl. Mater. Interfaces 2014, 6, 21702– 21710.

[68] Menumerov, E.; Hughes, R.A.; Neretina, S. Catalytic Reduction of 4-Nitrophenol: A Quantitative Assessment of the Role of Dissolved Oxygen in Determining the Induction Time, Nano Lett. 2016, 16, 7791–7797.

[69] Smith, J.G.; Jain, P.K. The Ligand Shell as an Energy Barrier in Surface Reactions on Transition Metal Nanoparticles, J. Am. Chem. Soc. 2016, 138, 6765–6773.

[70] Tan, Y.; Liu, P.; Chen, L.; Cong, W.; Ito, Y.; Han, J.; Guo, X.; Tang, Z.; Fujita, T.; Hirata, A.; Chen, M.W. Monolayer MoS_2 Films Supported by 3D Nanoporous Metals for High-Efficiency Electrocatalytic Hydrogen Production, Adv. Mater. 2014, 26, 8023–8028

Supporting Information for

Aqueous Cathodic Exfoliation Strategy toward Solution-Processable and Phase-Preserved MoS_2 Nanosheets for Energy Storage and Catalytic Applications

Sergio García-Dalí,[†] Juan I. Paredes, [†,*] José M. Munuera,[†] Silvia Villar-Rodil, [†,*] Alaa Adawy,[‡] Amelia Martínez-Alonso, [†] Juan M.D. Tascón[†]

[†]*Instituto Nacional del Carbón, INCAR-CSIC, C/Francisco Pintado Fe 26, 33011 Oviedo, Spain*

[‡]*Laboratory of High-Resolution Transmission Electron Microscopy, Scientific and Technical Services, University of Oviedo-CINN, 33006, Oviedo, Spain*

* Corresponding author: paredes@incar.csic.es

* Corresponding author: silvia@incar.csic.es

Contents

S1. Experimental section

S1.1. Materials and reagents

Pieces of MoS_2 crystals (approximate dimensions: ~10×10×0.5 mm^3) were obtained from SPI Supplies and used throughout the study. Platinum foil (25×25×0.025 mm^3) was purchased from Sigma-Aldrich. The inorganic salts KCl, NaCl and LiCl (purity >99.5%), the alkylammonium salts tetraethylammonium chloride (TEACl), tetrapropylammonium chloride (TPACl) and tetrabutylammonium chloride (TBACl), the nucleotides adenosine 5´-monophosphate disodium salt (AMP) and guanosine 5´monophosphate disodium salt (GMP), the nitroarenes 4-nitrophenol (4-NP) and 4- nitroaniline (4-NA) as well as the solvents isopropanol, *N*,*N*-dimethylformamide (DMF) and *N*-methyl-2-pyrrolidone (NMP) were also obtained from Sigma-Aldrich and used as received. Milli-Q deionized water (Millipore Corporation; resistivity: 18.2 MΩ·cm) was employed in all the experiments.

S1.2. Electrochemical exfoliation experiments

The electrochemical exfoliation of TMDs was carried out in a two-electrode setup under cathodic conditions, using a piece of the TMD crystal and platinum foil as the working and counter electrodes, respectively, and an aqueous solution of a given salt as the electrolytic medium. MoS_2 was the TMD of choice in most of the experiments, although $MoSe_2$ and WS_2 were also probed to demonstrate the suitability of the present exfoliation approach to other layered TMDs. Likewise, although KCl-based electrolytes yielded the best results in terms of efficiency of delamination, other salts (namely, NaCl, LiCl, TEACl, TPACl and TBACl) were tested for comparative purposes. In a typical cathodic exfoliation experiment, a ~5×5×0.5 mm^3 piece of MoS_2 was cut from the as-received crystal and immersed, together with the platinum foil piece, in an aqueous KCl solution (20 mL). Both electrodes were connected to a dc power supply (Agilent 6614C) using crocodile clips and kept at a distance of ~2 cm from each other in the solution. In this configuration, about two-thirds of the MoS_2 electrode were immersed in the electrolyte. A negative voltage was then applied to the MoS_2 electrode for 30 min, during which the MoS_2 piece was generally seen to swell and fan out starting from the free (non-clipped) end of the electrode. The extent of expansion and thus the efficiency of delamination depended on both the electrolyte molar concentration and the magnitude of the cathodic voltage, with the yield of exfoliated MoS_2 NSs being maximized at 4 M and -20 V, respectively. After the electrochemical

treatment, the most expanded part of the cathode, which roughly corresponded to the lower half of the MoS_2 piece, was recovered, thoroughly washed with water, dried overnight at room temperature under reduced pressure and finally stored in glass vials for subsequent use.

In order to gain insight into the exfoliation process, it was also carried out in a VSP potentiostat (Bio-Logic Science Instruments) in a three-electrode configuration, using the MoS_2 piece as the working electrode, Pt foil as the counter electrode, and Hg/HgO (1 M NaOH) as the reference electrode, with either pure water or 4 M KCl as electrolytic medium. Cyclic voltammograms (CVs) were recorded at voltage scan rate of 10 mV s^{-1}.

S1.3. Post-processing of the as-exfoliated products: nanosheet extraction and dispersion in solvents

To obtain individualized MoS_2 NSs from the as-exfoliated material, the latter was first cut into smaller pieces with the aid of a scalpel and then transferred to a solution of the nucleotides AMP or GMP (5 mg mL^{-1}) in isopropanol, where it was bath-sonicated (J.P. Selecta Ultrasons system, 40 kHz) for 3 h. The starting concentration of the as- exfoliated material in the isopropanol-nucleotide solution was 0.3-0.4 mg mL^{-1}. The nucleotides played the role of efficient dispersing agents to aid in the colloidal stabilization of MoS_2 NSs in the liquid phase. After standing undisturbed for 24 h to allow sedimentation of the poorly exfoliated fraction of the material, the upper ~75% of the supernatant volume was collected from the sonicated dispersion and kept for subsequent use. The retained supernatant was a solution (suspension) containing MoS_2 NSs colloidally stabilized by adsorbed nucleotides (AMP or GMP) as well as free (non- adsorbed) nucleotide molecules. To remove a majority of the latter, the dispersion was subjected to two cycles of sedimentation of the MoS_2 fraction via centrifugation (20000 *g*, 20 min; Eppendorf 5424 and 5430 microcentrifuges), removal of the upper supernatant liquid containing the free nucleotides, and re-dispersion of the MoS_2 sediment in neat isopropanol with the help of a brief sonication step. Using this protocol, NS dispersions with concentrations up to ~0.1 mg mL^{-1} were obtained, but suspensions of increasing concentration could be procured by consecutive cycles of sedimentation through centrifugation and re-dispersion in smaller isopropanol volumes. MoS_2 dispersions in other solvents, such as water, DMF or NMP, could also be obtained by using these solvents instead of isopropanol in the aforementioned protocol. Alternatively, NS extraction from the cathodically exfoliated electrode could be made in isopropanol, as described above, but in the final process of removal of the free nucleotides the target solvent was used to re-disperse the MoS_2 sediments instead of neat isopropanol. The concentration of NSs in the dispersions was

estimated through UV-vis absorption spectroscopy on the basis of the Lambert-Beer law by measuring the extinction of the dispersion at a wavelength of 345 nm and using the extinction coefficient [ε(345 nm) ≈ 6900 mL mg^{-1} m^{-1}] previously derived for MoS_2 by Coleman and co-workers [1].

S1.4. Characterization techniques

The materials were analyzed by UV-vis absorption spectroscopy, field-emission scanning electron microscopy (FE-SEM), scanning transmission electron microscopy (STEM), high resolution transmission electron microscopy (HR-TEM), selected-area electron diffraction (SAED), atomic force microscopy (AFM), Raman spectroscopy, X- ray photoelectron spectroscopy (XPS), as well as by measurement of contact angles. UV-vis absorption spectra were obtained for colloidal dispersions of the exfoliated MoS_2 material on a double-beam Heλios α spectrophotometer (Thermo Spectronic) using quartz cuvettes with an optical path length of 1 cm. FE-SEM and STEM images were recorded on a Quanta FEG apparatus (FEI Company) operated at 30 kV, whereas HR-TEM and SAED were accomplished in a JEM-2100F system (JEOL) working at an acceleration voltage of 200 kV. The HR-TEM was also equipped with STEM and energy dispersive X-ray (EDX) detector (Oxford Instruments, silicon drift detector (SDD) 80 mm^2), which allowed chemical mapping. Specimens for FE-SEM were directly mounted on the sample holder using double-sided carbon adhesive tape, while for imaging exfoliated NSs by STEM and HR-TEM, their dispersion in isopropanol was drop-cast (~40 μL) onto copper grids (200 mesh) covered with either a lacey or a continuous carbon film (acquired from EMS and SPI Supplies, respectively). To avoid damage by high energy electron bombardment, the HR-TEM measurements were performed under cryogenic conditions, using a double tilt cooling sample holder (GATAN model 636) maintained at -180 °C. AFM measurements were carried out with a Nanoscope IIIa Multimode apparatus (Veeco Instruments) in the tapping mode of operation, using silicon cantilevers with nominal spring constant and resonance frequency of ~40 N m^{-1} and 250–300 kHz, respectively. Samples for AFM were prepared by drop-casting a small volume (~20 μL) of a low-concentration MoS_2 NS dispersion in isopropanol (~0.01–0.03 mg mL^{-1}) onto SiO_2(300 nm)/Si wafers and allowing it to dry under ambient conditions. Raman spectra were recorded on a Horiba Jobin-Yvon LabRam instrument at a laser excitation wavelength of 532 nm (green line). A low incident laser power (~0.5 mW) was employed to avoid damage to the NSs. XPS was accomplished on a SPECS system, working at a pressure of 10^{-7} Pa with a monochromatic Al

K_α X-ray source (1486.7 eV) operated at 14.00 kV and 150 W. For both Raman spectroscopy and XPS, specimens were prepared in the form of thin films by vacuum-filtering MoS_2 NS dispersions in isopropanol through silver membrane filters (diameter: 25 mm in diameter; pore size: 0.2 μm; acquired from Whatman). Contact angles were measured on vacuum-filtered films by dropping 2 μL of 6 M KOH solution with a pipette and immediately taking images of the droplet with a standard digital camera, which had a macro lens attached. Analysis of the recorded images with ImageJ software was then carried out to determine contact angle values.

S1.5. Testing of cathodically exfoliated MoS_2 as an electrode material for energy storage

The performance of different samples derived from the cathodically treated MoS_2 material was evaluated in their role as electrodes for electrochemical energy storage in 6 M KOH electrolyte. Three-electrode tests were carried out using a commercial activated carbon fiber (ACF A20) as the counter electrode [paste consisting of a mixture of ACF A20, polytetrafluoroethylene (PTFE) as a binder and carbon black as a conducting additive in a weight ratio of 90:5:5] and Hg/HgO (1 M NaOH) as the reference electrode. The following materials were tested as working electrodes: (1) As-expanded MoS_2, which was directly obtained from the cathodic treatment (4 M KCl, -20 V) without any further processing. (2) As-expanded MoS_2 combined with guanosine 5´- monophosphate disodium salt (GMP), which was prepared by first stirring the as- expanded material in an aqueous GMP solution (5 mg mL^{-1}) and then drying the resulting product under a vacuum at 60 ºC overnight. (3) MoS_2 nanosheets extracted from the as-expanded material in isopropanol with GMP as described in section S1.3. The GMP-stabilized MoS_2 dispersion in isopropanol was sedimented via centrifugation (20000 *g*, 20 min) and then the precipitate was dried under a vacuum at 60 ºC overnight to finally obtain a loose powder. (4) MoS_2 NSs combined with single walled-carbon nanotubes (SWCNTs) in a weight ratio of 2:1. The MoS_2 component was prepared as described for sample no. 3. The carbon nanotube component was prepared by first debundling commercial SWCNTs (0.7–1.3 nm in diameter, from Sigma-Aldrich) in an aqueous flavin mononucleotide (FMN) solution (1 mg mL^{-1} SWCNT, 1 mg mL^{-1} FMN) via sonication and subsequent centrifugation (20000 *g*, 40 min). The resulting supernatant (a dispersion of debundled SWCNTs) was mixed with an equal volume of ethanol to colloidally destabilize the nanotubes, which agglomerated at the air-liquid interface. The agglomerated nanotubes were then collected and dried under a vacuum at 60 ºC overnight to give a loose powder.

Finally, the MoS_2 nanosheet and SWCNT powders were combined in the desired proportion and hand-ground with a mortar and pestle until a visually homogenous powder was attained. (5) MoS_2 nanosheets combined with SWCNTs in a weight ratio of 7:1, obtained using the same protocol as described for sample no. 4. (6) SWCNTs in the absence of any MoS_2 material, obtained in powder form as described in the case of sample no. 4. For the electrochemical measurements, the working electrode materials were pressed (1 ton for 10 s) at typical mass loadings of 1.0-1.3 mg cm^{-2} onto a graphite foil support (Papyex I980, from Mersen) by means of a hydraulic press. The electrodes were assembled in a Swagelok-type cell, using a piece of nylon membrane filter (0.45 μm of pore size, from Whatman) as the electrode separator. Before mounting the cell, the working electrode, counter electrode and separator were soaked in the electrolytic solution and vacuum-degassed. The measurements were conducted in a Biologic VSP potentiostat, recording both cyclic voltammograms and different potential scan rates and galvanostatic charge/discharge curves at different current densities. The best-performing sample (MoS_2-SWCNT hybrid in a weight ratio of 2:1) was also tested in a two-electrode, asymmetric supercapacitor configuration. To this end, a commercial powdered activated carbon (YP-50F, from Kuraray) was used in the form of a paste (mixture of YP-50F, PTFE and carbon black in a weight ratio of 90:5:5) as the negative electrode, whereas the MoS_2- SWCNT hybrid was used as the positive electrode, with 6 M KOH as the electrolyte.

S1.6. Testing of cathodically exfoliated MoS_2 as a catalyst for nitroarene reduction

The catalytic activity of the cathodically exfoliated MoS_2 NSs was tested for the reduction of 4-nitrophenol (4-NP) and 4-nitroaniline (4-NA) to 4-aminophenol (4-AP) and *p*-phenylenediamine (*p*-PDA), respectively, in aqueous medium at room temperature and using $NaBH_4$ as the reducing agent. To this end, GMP-stabilized NSs dispersed in water by the procedure described above were used. Nevertheless, for best results the as-obtained aqueous dispersions were subjected first to a centrifugation step (5000 *g*, 20 min) to retain in the supernatant those NSs with smaller mean lateral size (< 200 nm) and then to an additional step of free GMP removal by sedimentation (20000 *g*, 20 min) and re-dispersion in water. Omitting the latter step led to lower catalytic activities, likely as a result of an excessive amount of nucleotide adsorbed on the MoS_2 NSs, while additional washing steps caused agglomeration of the dispersed NS and hence also a decrease in the measured catalytic activities. Following previously reported procedures [2], the catalytic tests were carried out by

preparing aqueous solutions (2.5 mL) containing a small amount of the MoS_2 NSs (~5–10 μg mL^{-1}), either 4-NP (0.12 mM) or 4-NA (0.11 mM), as well as $NaBH_4$ [72 (110) mM when testing 4-NP (4-NA)]. Right after their preparation, the solutions were loaded onto an UV-vis absorption spectrophotometer and the progress of the reaction was recorded by monitoring the intensity of an absorption peak characteristic of the reactant molecule, i.e., the peak located at ~400 nm for 4-NP and at ~382 nm for 4-NA.

S2. Additional microscopic characterization

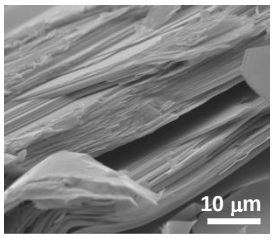

Figure S1. Representative FE-SEM image of a starting, untreated MoS2 crystal.

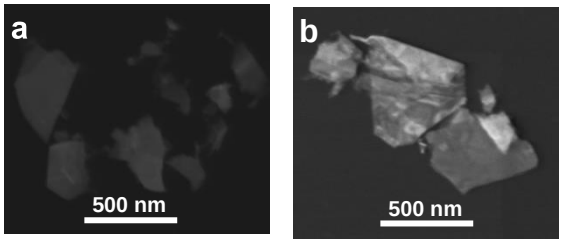

Figure S2. Representative STEM images of MoS2 exfoliated in (a) 4 M NaCl and (b) 0.3 M TPACl.

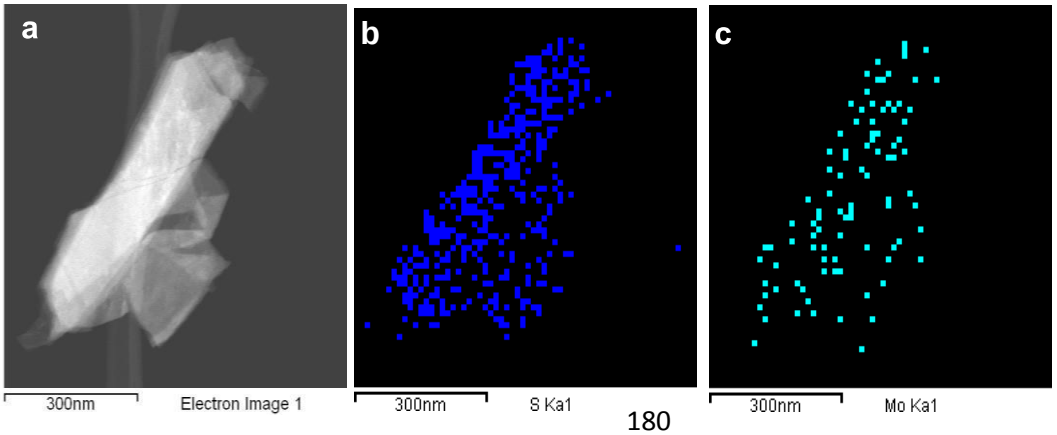

Figure S3. (a) STEM image of MoS_2 exfoliated in 4 M KCl and **(b,c)** the corresponding energy dispersive X-ray (EDX) area mapping of (b) sulfur and (c) molybdenum.

S3. Additional spectroscopic characterization

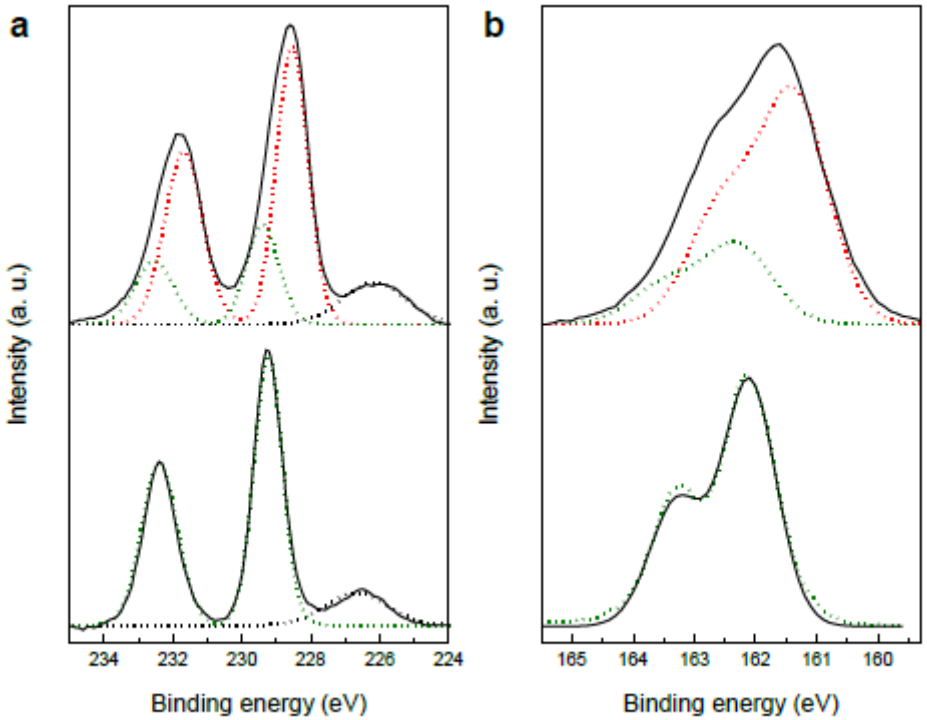

Figure S4. Typical XPS spectra of **(a)** Mo 3d (and S 2s, black dotted line), and **(b)** S 2p core levels of chemically exfoliated MoS_2 nanosheets obtained by the n-butyllithium intercalation route as reported in Paredes et al. [3] (top), and MoS_2 cathodically exfoliated in 4 M KCl and extracted with isopropanol (bottom). Mo 3d and S 2p XPS core level doublet bands are deconvoluted into two components assigned to the 2H (green dotted line) and 1T phases (red dotted line). For this comparison, the XPS spectra of the present cathodically exfoliated materials were acquired under the same conditions used in [3], i. e., with a non–monochromatic Mg Kα X-ray source operated at a power of 100 W. The high resolution spectra were taken at a pass energy of 10 eV with an energy step of 0.1 eV. The binding energy scale of all spectra was referenced to the maximum of the C 1s band for adventitious carbon.

S4. Electrochemical study of the cathodic exfoliation of MoS_2

Cathodic exfoliation of MoS_2 was carried out in a potentiostat in order to study the electrochemical processes involved. Fig. S5 shows four consecutive CVs recorded at a potential scan rate of 10 mV s^{-1} in the widest potential range available in the current equipment (8 V), using pure water (blue trace) and 4 M KCl (black trace: first cycle; grey traces: following cycles) as electrolytic medium. When the potential range from 0 to -8 V was swept using pure water as electrolytic medium, the current remained near 0 A (blue trace) and no change was observed in the MoS_2 cathode morphology. However, when the same process was carried out in 4 M KCl, an abrupt reduction peak was observed in the first CV cycle (black trace). Throughout the few minutes during which this peak developed, the progressive swelling of the MoS_2 cathode became apparent by bare eye. We interpret that this abrupt peak was originated by the intercalation of a large amount of hydrated potassium cations followed by the reduction of co-intercalated water between the lamellae. As explained in the main text, the pressure exerted by the hydrogen generated upon water reduction separated the layers. No reduction peaks were observed in subsequent cycles (grey traces), and no further swelling of the cathode occurred either. Intercalation and expansion having already taken place, only water reduction on the surface remained. The noise observed in the CVs came from the variation of the surface of the cathode during the measurement, which in turn originated in the lack of rigidity of the exfoliated MoS_2 layers.

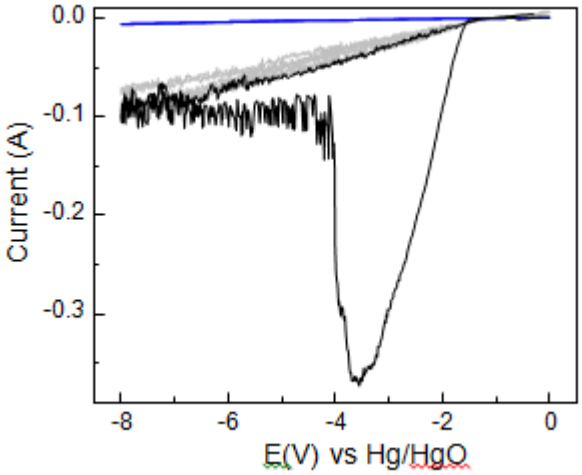

Figure S5. Cyclic voltammograms recorded in a three-electrode configuration, using an MoS2 piece as the working electrode, Pt foil as the counter electrode, and Hg/HgO (1 M NaOH) as the reference electrode with either pure water (blue trace) or 4 M KCl (black trace:

first cycle; grey traces: following cycles) as electrolytic medium (potential scan rate:10 mV s^{-1}).

S5. Additional information related to the electrochemical characterization of cathodically exfoliated MoS_2

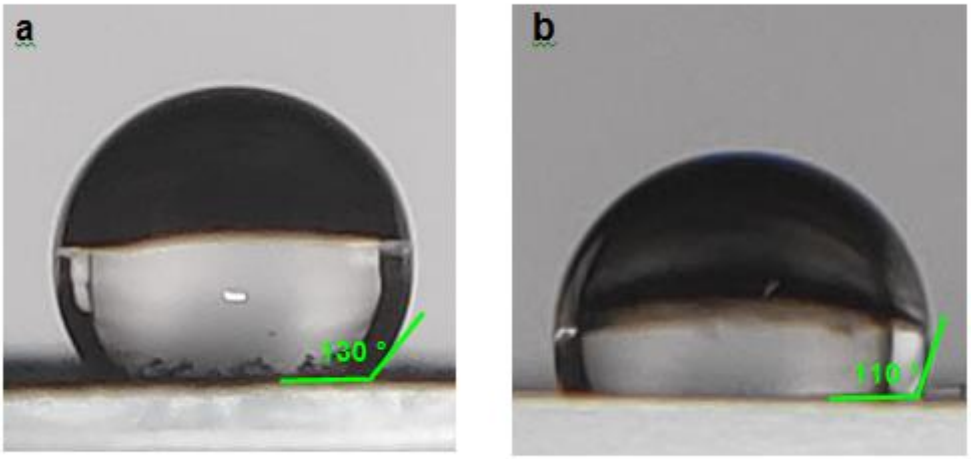

Figure S6. Digital pictures of droplets of electrolyte (aqueous 6 M KOH solution) deposited on (a) the surface of vacuum-filtered films of bare MoS2 nanosheets and (b) GMP-adsorbed MoS2 nanosheets, with indication of the contact angle.

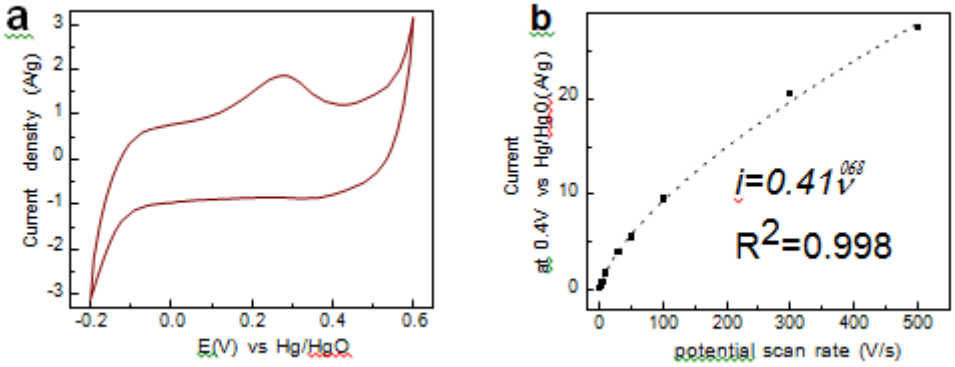

Figure S7. (a) Cyclic voltammogram recorded in a three-electrode configuration with the hybrid material (MoS2 to SWCNT weight ratio of 2:1) as the working electrode in 6 M KOH electrolyte at a potential scan rate of 5 mV s^{-1}. **(b)** Fitting of the anodic current, i, measures at a potential of 0.4 V vs Hg/HgO as a function of the potential scan rate, □, to the equation $i = a□^{b}$.

Table S1. Gravimetric capacitance values of a range of MoS_2-based electrodes determined with a three-electrode system at current density of 1 A g^{-1}.

Material	Electrolyte	Capacitance (F g^{-1})	Ref.
Li-intercalated 1T' MoS_2 NSs	Phosphate buffer solution	10–15	4
Hydrothermally synthesized MoS_2 NSs	1 M Na_2SO_4	129.2	5
Hydrothermally synthesized 2H MoS_2 NSs	1 M Na_2SO_4	194	6
Hydrothermally synthesized 2H MoS_2 NSs/carbon nanotube hybrid	1 M Na_2SO_4	402	6
Hydrothermally synthesized flower-like MoS_2	1M KCl	235	7
Hydrothermally synthesized flower-like 2H MoS_2 NSs	1M KCl	168	8
Hydrothermally synthesized few-layer MoS_2 NSs embedded in porous carbon matrix	1 M H_2SO_4	472	9
1 T' MoS_2 NSs confined on TiO_2 nanotube arrays	1 M Na_2SO_4	345	10
1 T' MoS_2 NSs	0.5 M Li_2SO_4/Na_2SO_4/ K_2SO_4	100	11
Li-exfoliated MoS_2 NSs	2 M Na_2SO_4	117	12
Li-exfoliated MoS_2 NSs/poly(ethyleneimine)-modified graphene oxide hybrid	2 M Na_2SO_4	154	12
Reduced graphene oxide (RGO)-ultrafine 2H MoS_2 powder aerogel	1M NaCl	69	13
Hydrothermally synthesized 1T-2H mixed phase MoS_2 sheet-RGO aerogel	1M NaCl	416	13
Low-temperature deposited MoS_2 thin films	1 M Na_2SO_4	180	14
Hydrothermally synthesized MoS_2/RGO@polyaniline hybrid	1 M H_2SO_4	216	15
Hydrothermally synthesized porous tubular carbon/MoS_2 nanocomposite	3 M KOH	210	16
Hydrothermally synthesized, interlayer expanded MoS_2 NSs	1 M Na_2SO_4	231	17

Table S2. Maximum energy densities reported in the literature for a variety of asymmetric supercapacitors having MoS_2-based electrodes (except for the case of a $MoSe_2$-based electrode).

Positive electrode	**Negative electrode**	**Electrolyte**	**Maximum energy density, in W h kg^{-1} (power density, in W kg^{-1})**	**Ref.**
Li-exfoliated MoS_2/reduced graphene oxide (RGO)	Reduced graphene oxide (RGO)	1 M Na_2SO_4	23	19
Hollow carbon spheres decorated with hydrothermally synthesized MoS_2 NSs	RGO	3 M KOH	13.7 (61.6)	20
Hydrothermally synthesized MoS_2 NSs on graphene foam	Activated carbon (AC)	6 M KOH	16 (758)	21
Solvent-exfoliated MoS_2 NSs on graphene foam	AC	3 M KOH	36.4 (400)	22
Solvent-exfoliated MoS_2 NSs-NiO hybrid	Solvent-exfoliated MoS_2 NSs-Fe_2O_3 hybrid	6 M KOH	39.6 (807)	23
Hydrothermally synthesized nickel sulfide/MoS_2 NSs on carbon nanotubes	AC	3 M KOH	40 (400)	24
Hydrothermally synthesized MoS_2/NiS yolk–shell Microspheres	AC	6 M KOH	31 (156)	25
AC	Hydrothermally synthesized and di-exfoliated MoS_2/graphene oxide hybrid	2 M Na_2SO_4	19.3 (450)	26
Hydrothermally synthesized MoS_2-carbon-$NiCo_2S_4$ hybrid	AC	6 M KOH	27.7 (400)	27
Hydrothermally synthesized V_2O_3@MoS_2 composite tubes	AC	1 M Na_2SO_4	31.8 (370)	28
Thermally synthesized MoS_2-WS_2-RGO hetrostructure	RGO	3 M KOH	15 (373)	29
MnO_2 on carbon fiber	Hydrothermally synthesized MoS_2 NSs on carbon fiber	1 M Na_2SO_4	22.5 (750)	30
Ultrasound-exfoliated $MoSe_2$-RGO hybrid	AC	6 M KOH	26.6 (800)	31
Cathodically exfoliated MoS_2 NSs-SWCNT hybrid	AC	6 M KOH	26 (750)	This work

S6. Comparison of the catalytic activity of GMP-stabilized cathodically exfoliated MoS_2 NSs towards the reduction of nitroarenes with $NaBH_4$ with those reported for other catalysts in the literature

Table S3. Catalytic activity (defined as number of moles of reactant converted per mole of catalyst used per unit time) of GMP-stabilized cathodically exfoliated MoS_2 NSs towards the reduction of 4-NP and 4-NA compared with that of different types of MoS_2 NSs and graphene-derived materials reported in the literature.

Catalytic system	**Catalytic activity (h^{-1})**	**Ref.**
Reduction of 4- NP		
GMP-stabilized cathodically exfoliated MoS_2 NSs	21.4	Present work
GMP-stabilized sonicated MoS_2 NSs	2.6–7.8	32
Li-exfoliated 1T'-phase MoS_2 NSs	44.4	33
Hydrothermally synthesized MoS_2 NSs supported onto Fe_3O_4 particles	2.4	34
Co-doped MoS_2 NSs	8.4	35
Hydrothermally synthesized MoS_2 NSs intercalated in pillared montomorillonite	24	36
RGO NSs capped with poly(diallyldimethylammonium chloride)	0.10	37
N-doped RGO foam	0.07	38
Reduction of 4-NA		
GMP-stabilized cathodically exfoliated MoS_2 NSs	140	Present work
GMP-stabilized sonicated MoS_2 NSs	3.4–14.4	32
Li-exfoliated 1T'-phase MoS_2 NSs	83.4	33
Co-doped MoS_2 NSs	3.2	35
N-doped RGO NSs	0.08	33

Table S4. Catalytic activity (defined as number of moles of substrate converted per mole of catalyst used) of catalysts based on non-noble metals towards the reduction of 4-NP with $NaBH_4$.

Catalytic system	**Catalytic activity (h^{-1})**	**Ref.**
Cu and Sn sponges/dendrites	1.2–1.8	39
Cu nanoparticles on carbon microspheres	0.2	40
Graphene stabilized CuNi nanocomposite	12	41
MOF-derived Ni based N-doped mesoporous carbon	2.4	42
Co nanoparticles embedded in hierarchically porous N-doped carbon frameworks	18	43
Co nanocrystals on RGO	0.6	44
Hexagonal Ni plates on RGO	0.44	45
Hollow porous Cu particles from silica-encapsulated Cu_2O nanoparticle aggregates	3	46
Co@BN core–shell nanoparticles	0.38	47
Co nanoparticles embedded into ordered mesoporous Carbon	7.8	48
Ni nanoparticles on silica nanotubes	1.8	49
Ultrafine Cu_2O nanoparticles on cubic mesoporous carbon	9.6	50
Cu nanoparticles on oxidized boron nitride	27	51
NiO hollow nanospheres	4.2	52

S7.References

[1] C. Backes, R.J. Smith, N. McEvoy, N.C. Berner, D. McCloskey, H.C. Nerl, A. O´Neill, P.J. King, T. Higgins, D. Hanlon, N. Scheuschner, J. Maultzsch, L. Houben, G.S. Duesberg, J.F. Donegan, V. Nicolosi, J.N. Coleman, Nat. Commun. 5 (2014), 4576.

[2] L. Guardia, J.I. Paredes, J.M. Munuera, S. Villar-Rodil, M. Ayán-Varela, A. Martínez-Alonso, J.M.D. Tascón, ACS Appl. Mater. Interfaces 6 (2014), 21702-21710.

[3] J.I. Paredes, J.M. Munuera, S. Villar-Rodil, L. Guardia, M. Ayán-Varela, A. Pagán, S.D. Aznar-Cervantes, J.L. Cenis, A. Martínez-Alonso, J.M.D. Tascón, Impact of Covalent Functionalization on the Aqueous Processability, Catalytic Activity, and Biocompatibility of Chemically Exfoliated MoS_2 Nanosheets, ACS Appl. Mater. Interfaces 8 (2016), 27974-27986.

[4] C. C. Mayorga-Martínez, A Ambrosi, A. Y. S. Eng, Z. Sofer, M. Pumera, Transition metal dichalcogenides (MoS_2, $MoSe_2$, WS_2 andWSe_2) exfoliation technique has strong influence upon their capacitance, Electrochem. Commun. 56 (2015) 24–28.

[5] K.-J. Huang, J.-Z. Zhang, G.-W. Shi, Y.-M. Liu, Hydrothermal synthesis of molybdenum disulfide nanosheets as supercapacitors electrode material, Electrochim. Acta 132 (2014) 397–403.

[6] X. Chen, J. Ding, J. Jiang, G. Zhuang, Z. Zhang, Peizhi Yang, Preparation of a MoS_2/carbon nanotube composite as an electrode material for high-performance supercapacitors, RSC Adv. 2018, 8, 29488–29494.

[7] G. Ma, H. Peng, J. Mu, H. Huang, X. Zhou, Z. Lei, In situ intercalative polymerization of pyrrole in graphene analogue of MoS_2 as advanced electrode material in supercapacitor, J. Power Sources 229 (2013) 72–78.

[8] X. Wang, J. Ding, S. Yao, X. Wu, Q. Feng, Z. Wang, B. Geng, High supercapacitor and adsorption behaviors of flower-like MoS_2 nanostructures. : J. Mater. Chem. A, 2014, 2, 15958–15963.

[9] H. Ji, C. Liu, T. Wang, J. Chen, Z. Mao, J. Zhao, W. Hou, G. Yang, Porous Hybrid Composites of Few-Layer MoS_2 Nanosheets Embedded in a Carbon Matrix with an Excellent Supercapacitor Electrode Performance, Small 2015, 11, 6480–6490.

[10] J. Zhou, M. Guo, L. Wang, Y. Ding, Z. Zhang, Y. Tang, C. Liu, S. Luo, 1T-MoS_2 nanosheets confined among TiO_2 nanotube arrays for high performance supercapacitor, Chem. Eng. J. 366 (2019) 163–171.

[11] M. Acerce, D. Voiry, M. Chhowalla, Metallic 1T phase MoS_2 nanosheets as supercapacitor electrode materials, Nat. Nanotechnol. 10 (2015) 313–318.

[12] M.-C. Liu, Y. Xu, Y.-X. Hu, Q.-Q. Yang, L.-B. Kong, W.-W. Liu, W.-J. Niu, Y.-L. Chueh, Electrostatically Charged MoS_2/Graphene Oxide Hybrid Composites for Excellent Electrochemical Energy Storage Devices, ACS Appl. Mater. Interfaces 2018, 10, 35571−35579.

[13] A. Gigot, M. Fontana, M. Serrapede, M. Castellino, S. Bianco, M. Armandi, B. Bonelli, C. F. Pirri, E. Tresso, P. Rivolo, Mixed 1T−2H Phase MoS_2/Reduced Graphene Oxide as Active Electrode for Enhanced Supercapacitive Performance, ACS Appl. Mater. Interfaces 2016, 8, 32842−32852.

[14] R.B. Pujari, A.C. Lokhande, A.R. Shelke, J.H. Kim, C.D. Lokhande, Chemically deposited nano grain composed MoS_2 thin films for supercapacitor application. J. Colloid Interf. Sci. 496 (2017) 1–7

[15] X. Li, C. Zhang, S. Xin, Z. Yang, Y. Li, D. Zhang, P. Yao,Facile Synthesis of MoS_2/Reduced Graphene Oxide@Polyaniline for High-Performance Supercapacitors, ACS Appl. Mater. Interfaces 2016, 8, 21373−21380.

[16] B. Hu, X. Qin, A. M. Asiri, K. A. Alamry, A. O. Al-Youbi, X, Sun, Synthesis of porous tubular C/MoS_2 nanocomposites and their application as a novel electrode material for supercapacitors with excellent cycling stability, Electrochim. Acta 100 (2013) 24–28.

[17] H. Xiao, S. Wang, S. Zhang , Y. Wang, Q. Xu, W. Hu, Y. Zhou, Z. Wang, C. An, J. Zhang, Interlayer expanded molybdenum disulfide nanosheets assembly for electrochemical supercapacitor with enhanced performance, Mater. Chem. Phys. 192 (2017) 100–107.

[18] K.-J. Huang, L. Wang, J.-Z. Zhang, K. Xing, Synthesis of molybdenum disulfide/carbon aerogel composites for supercapacitors electrode material application, J. Electroanal. Chem. 752 (2015) 33–40.

[19] U. M. Patil, M. S. Nam, S. Kang, J. S. Sohn, H. B. Sim, S. Kanga and S. C. Jun, Fabrication of ultra-high energy and power asymmetric supercapacitors based on hybrid

2D MoS_2/graphene oxide composite electrodes: a binder-free approach, RSC Adv., 2016, 6, 43261–43271.

[20] T.-W. Lin, M.-C. Hsiao, A.-Y. Wang and J.-Y. Lin, Hollow Hierarchical Carbon Spheres Decorated with Ultrathin Molybdenum Disulfide Nanosheets as High-Capacity Electrode Materials for Asymmetric Supercapacitors, ChemElectroChem, 2017, 4, 620–627.

[21] T. M. Masikhwa, M. J. Madito, A. Bello, J. K. Dangbegnon and N. Manyala, High performance asymmetric supercapacitor based on molybdenum disulphide/graphene foam and activated carbon from expanded graphite, J. Colloid Interf. Sci., 2017, 488, 155–165.

[22] R. Zhou, C.-J. Han and X.-M. Wang, Hierarchical MoS_2-coated three-dimensional graphene network for enhanced supercapacitor performances, J. Power Sources, 2017, 352, 99–110.

[23] K. Wang, J. Yang, J. Zhu, L. Li, Y. Liu, C. Zhang and T. Liu, General solution-processed formation of porous transition-metal oxides on exfoliated molybdenum disulfides for high-performance asymmetric supercapacitors, J. Mater. Chem. A, 2017, 5, 11236–11245.

[24] X. Yang, L. Zhao and J. Lian, Arrays of hierarchical nickel sulfides/MoS_2 nanosheets supported on carbon nanotubes backbone as advanced anode materials for asymmetric supercapacitor, J. Power Sources, 2017, 343, 373–382.

[25] Q. Qin, L. Chen, T. Wei and X. Liu, Yolk–Shell Microsphere-Based Electrodes for Overall Water Splitting and Asymmetric Supercapacitor, Small, 2018, 15, 1803639.

[26] M.-C. Liu, Y. Xu, Y.-X. Hu, Q.-Q. Yang, L.-B. Kong, W.-W. Liu, W.-J. Niu and Y.-L. Chueh, Electrostatically Charged MoS_2/Graphene Oxide Hybrid Composites for Excellent Electrochemical Energy Storage Devices, ACS Appl. Mater. Interfaces, 2018, 10, 35571−35579.

[27] D. Wang, W. Zhu, Y. Yuan, G. Du, J. Zhu, X. Zhu and G. Pezzotti, Kelp-like structured $NiCo_2S_4$-C-MoS_2 composite electrodes for high performance supercapacitor, J. Alloy. Comp., 2018, 735, 1505–1513.

[28] H. Peng, T. Liu, Y. Li, X. Wei, X. Cui, Y. Zhang and P. Xiao, Hierarchical MoS_2-coated V_2O_3 composite nanosheet tubes as both the cathode and anode materials for pseudocapacitors, Electrochim. Acta, 2018, 277, 218–225.

[29] T.-W. Lin, T. Sadhasivam, A.-Y. Wang, T.-Y. Chen, J.-Y. Lin and L.–D. Shao, Ternary Composite Nanosheets with MoS_2/WS_2/Graphene Heterostructures as High-Performance Cathode Materials for Supercapacitors, ChemElectroChem, 2018, 5, 1024–1031.

[30] Y.-P. Gao, K.-J. Huang, X. Wu, Z.-Q. Hou and Y.-Y. Liu, MoS_2 nanosheets assembling three-dimensional nanospheres for enhanced-performance supercapacitor, J. Alloy. Comp., 2018, 741, 174–181.

[31] B. Kirubasankar, S. Vijayan and S. Angaiah, Sonochemical synthesis of a 2D–2D $MoSe_2$/graphene nanohybrid electrode material for asymmetric supercapacitors, Sustain. Energ. Fuels, 2019, 3, 467–477.

[32] M. Ayán-Varela, Ó. Pérez-Vidal, J.I. Paredes, J.M. Munuera, S. Villar-Rodil, M. Díaz-González, C. Fernández-Sánchez, V.S. Silva, M. Cicuéndez, M. Vila, A. Martínez-Alonso and J.M.D. Tascón, Aqueous Exfoliation of Transition Metal Dichalcogenides Assisted by DNA/RNA Nucleotides: Catalytically Active and Biocompatible Nanosheets Stabilized by Acid−Base Interactions, ACS Appl. Mater. Interfaces, 2017, 9, 2835–2845.

[33] L. Guardia, J.I. Paredes, J.M. Munuera, S. Villar-Rodil, M. Ayán-Varela, A. Martínez-Alonso and J.M.D. Tascón, Chemically Exfoliated MoS_2 Nanosheets as an Efficient Catalyst for Reduction Reactions in the Aqueous Phase, ACS Appl. Mater. Interfaces, 2014, 6, 21702–21710.

[34] T. Lin, J. Wang, L. Guo and F. Fu, Fe_3O_4@MoS_2 Core–Shell Composites: Preparation, Characterization, and Catalytic Application, J. Phys. Chem. C, 2015, 119, 13658–13664.

[35] C. Nethravathi, J. Prabhu, S. Lakshmipriya and M. Rajamathi, Magnetic Co-Doped MoS_2 Nanosheets for Efficient Catalysis of Nitroarene Reduction, ACS Omega, 2017, 2, 5891–5897.

[36] K. Peng, L. Fu, H. Yang, J. Ouyang and A. Tang, Hierarchical MoS_2 intercalated clay hybrid nanosheets with enhanced catalytic activity, Nano Res., 2017, 10, 570–583.

[37] J. Song, S.W. Kang, Y.W. Lee, Y. Park, J.-H. Kim and S.W. Han, egulating the Catalytic Function of Reduced Graphene Oxides Using Capping Agents for Metal-Free Catalysis, ACS Appl. Mater. Interfaces, 2017, 9, 1692–1701.

[38] J. Liu, X. Yan, L. Wang, L. Kong and P. Jian, hree-dimensional nitrogen-doped graphene foam as metal-free catalyst for the hydrogenation reduction of *p*-nitrophenol, J. Colloid Interface Sci., 2017, 497, 102–107.

[39] B. K. Barman, K. K. Nanda, Uninterrupted galvanic reaction for scalable and rapid synthesis of metallic and bimetallic sponges/dendrites as efficient catalysts for 4-nitrophenol reduction, Dalton Trans., 2015, 44, 4215–4222.

[40] X. Cheng, A. Fu, H. Li, Y. Wang, P. Guo, J. Liu, J. Zhang, X. S, Zhao, Sustainable Preparation of Copper Particles Decorated Carbon Microspheres and Studies on Their Bactericidal Activity and Catalytic Properties ACS Sustainable Chem. Eng. 2015, 3, 2414−2422.

[41] H. Fang, M. Wen, Hanxing Chen, Qingsheng Wu and Weiying Li, Graphene stabilized ultra-small CuNi nanocomposite with high activity and recyclability toward catalysing the reduction of aromatic nitro-compounds, Nanoscale. 2016, 8, 536–542.

[42] W. Zuo, G. Yu and Z. Dong A MOF-derived nickel based N-doped mesoporous carbon catalyst with high catalytic activity for the reduction of nitroarenes, RSC Adv., 2016, 6, 11749–11753.

[43] X. Li, C. Zeng, J. Jiang, L. Ai, Magnetic cobalt nanoparticles embedded in hierarchically porous nitrogen-doped carbon frameworks for highly efficient and well-recyclable catalysis, J. Mater. Chem. A, 2016, 4, 7476–7482.

[44] M. Guo, Y. Zhao, F. Zhang, L. Xu, H. Yang, X. Song, Y. Bu, Reduced graphene oxide-stabilized copper nanocrystals with enhanced catalytic activity and SERS properties, RSC Adv., 2016, 6, 50587–50594.

[45] Z. Ji, Y. Wang, X. Shen, H. Ma, J. Yang, A. Yuan, H. Zhou, Facile synthesis and enhanced catalytic performance of reduced graphene oxide decorated with hexagonal structure Ni nanoparticles, J. Colloid Interf. Science 487 (2017) 223–230.

[46] J. Jiang, Y. S. Lim, S. Park, S.-H. Kim, S. Yoon, L. Piao. Hollow porous Cu particles from silica-encapsulated Cu_2O nanoparticle aggregates effectively catalyze 4- nitrophenol reduction, Nanoscale, 2017,9, 3873–3880.

[47] M. Du, Q. Liu, C. Huang, X. Qiu, One-step synthesis of magnetically recyclable Co@BN core–shell nanocatalysts for catalytic reduction of nitroarenes, RSC Adv., 2017, 7, 35451–35459.

[48] J. Liu, Z. Wang, X. Yan, P. Jian, Metallic cobalt nanoparticles imbedded into ordered mesoporous carbon: A non-precious metal catalyst with excellent hydrogenation performance, J. Colloid Interf. Sci. 505 (2017) 789–795.

[49] S. Zhang, S. Gai, F. He, S. Ding, L. Lia, P. Yang, In situ assembly of well-dispersed Ni nanoparticles on silica nanotubes and excellent catalytic activity in 4-nitrophenol reduction, Nanoscale, 2014,6, 11181-11188.

[50] P. C. Rath, D. Saikia, M. Mishra, H.-M. Kao, Exceptional catalytic performance of ultrafine Cu_2O nanoparticles confined in cubic mesoporous carbon for 4-nitrophenol reduction, Appl. Surf. Sci. 427 (2018) 1217–1226.

[51] X. Jiang, B. Han, C. Zhou, K. Xia, Q. Gao, J. Wu. Cu Nanoparticles Supported on Oxygen-Rich Boron Nitride for the Reduction of 4‑Nitrophenol. ACS Appl. Nano Mater. 2018, 1, 6692–6700.

[52] G. Wu, X. Liang, L. Zhang, Z. Tang, M. Al-Mamun, H. Zhao, X. Su, Fabrication of Highly Stable Metal Oxide Hollow Nanospheres and Their Catalytic Activity toward 4‑Nitrophenol Reduction, ACS Appl. Mater. Interfaces 2017, 9, 18207–18214.

5.2. Activación de MoS_2 mediante formación de vacantes

Artículo III

Activation of two-dimensional MoS_2 nanosheets by wet-chemical sulfur vacancy engineering for the catalytic reduction of nitroarenes and organic dyes, S. García-Dalí, J.I. Paredes, B. Caridad, S. Villar-Rodil, M. Díaz-González, C. Fernández-Sánchez, A. Adawy, A. Martínez- Alonso, J.M.D. Tascón, *Applied Materials Today*, 2020, 20, 100678.

Las láminas de MoS_2 2D en fase 2H pueden ser utilizadas como catalizador para la reducción de nitroarenos y colorantes orgánicos. Sin embargo, su superficie basal es mayormente inerte, lo que supone una seria limitación en su actividad catalítica. Se sabe que las vacantes de azufre en la superficie basal del MoS_2 son centros químicamente reactivos que facilitan determinadas reacciones catalíticas. Por ello, el objetivo de este trabajo consiste en la generación de vacantes de azufre en la superficie que provoquen un aumento en su actividad catalítica para la reducción de nitroarenos y colorantes manteniendo, además, la estabilidad de dichas láminas en dispersión acuosa, medio en el que se realizan los estudios catalíticos.

Para ello, se descartan procesos de generación de vacantes de azufre que requieran que el MoS_2 esté soportado sobre un sustrato (tratamiento por plasma, radiación iónica, etc) y tratamientos con agentes reductores ($NaBH_4$ o hidracina) en condiciones muy agresivas (alta temperatura e intensa sonicación). En su lugar, se realiza el tratamiento de generación de vacantes de azufre en MoS_2 en dispersión en IPA con hidracina a temperatura moderada (70 ºC). La dispersión original de MoS_2 se obtiene mediante sonicación del material *bulk* en polvo en IPA.

La caracterización mediante espectroscopías UV-Vis, XPS y Raman muestra que solo se encuentra presente la fase 2H, indicando que no ha habido cambio de fase durante el tratamiento con hidracina. Mediante STEM se observan láminas de apariencia y dimensiones similares a las del MoS_2 sin tratar, lo que indica que dicho tratamiento no ha provocado ningún cambio morfológico ni estructural radical a la muestra.

Por otro lado, las imágenes obtenidas por TEM de alta resolución muestran una clara diferencia entre la conformación atómica del MoS_2 tratado con hidracina y sin tratar. Mientras que en el MoS_2 sin tratar se observa un patrón triangular ordenado a largo alcance, indicativo de la ausencia de defectos atómicos significativos, en el MoS_2 tratado con hidracina el patrón se vuelve más irregular y discontinuo, observándose huecos que sugieren la ausencia de átomos de azufre. Esta idea queda reforzada con los valores de la relación atómica S/Mo obtenidos por XPS, donde se observa una disminución desde ~2 (MoS_2 inicial) hasta ~1.7 para MoS_2 tratado con la mayor cantidad de hidracina.

Sin embargo, la presencia de un mayor número de vacantes de azufre en una muestra no significa necesariamente que tenga que ser más activa catalíticamente, ya que la distribución espacial de esas vacantes puede tener un efecto importante. No tiene por qué tener el mismo efecto que las vacantes sean monoatómicas a que sean multiatómicas o

que las vacantes estén distribuidas homogéneamente por la superficie del material a que estén agrupadas en determinadas zonas. Esto es así en el caso de la reacción de evolución de hidrogeno, en el que la catálisis mejora con la presencia de vacantes de azufre solo hasta una cierta densidad. Para los estudios cinéticos realizados, los centros no saturados de molibdeno asociados a vacantes de azufre son centros donde se puede estabilizar el anión hidruro que permite reducir al nitroareno, favoreciendo la catálisis. En base a los resultados de EPR, parece que esos centros son más abundantes en muestras con un número moderado de vacantes de azufre que en muestras con números altos de vacantes, teniendo a quedar más sitios donde estabilizar el hidruro y por tanto más sitios donde propiciar la catálisis. De hecho, los estudios cinéticos de reducción de nitroarenos y colorantes orgánicos muestran una clara mejora en la actividad catalítica de los materiales con número moderado de vacantes de azufre, corroborando así la hipótesis establecida previamente de que no sólo es importante el número de vacantes, sino también la distribución de éstas.

ARTÍCULO III

Activation of two-dimensional MoS_2 nanosheets by wet-chemical sulfur vacancy engineering for the catalytic reduction of nitroarenes and organic dyes

S. García-Dalí[a], J.I. Paredes[a,*], B. Caridad[a], S. Villar-Rodil[a,*], M. Díaz-González[b], C. Fernández-Sánchez[b], A. Adawy[c], A. Martínez-Alonso[a], J.M.D. Tascón[a]

[a]*Instituto Nacional de Ciencia y Tecnología del Carbono, C/Francisco Pintado Fe 26, 33011 Oviedo, Spain*

[b]*Instituto de Microelectrónica de Barcelona, IMB-CNM (CSIC), Campus UAB, 08193 Bellaterra, Barcelona, Spain*

[c]*Laboratory of High-Resolution Transmission Electron Microscopy, Institute for Scientific and Technological Resources, University of Oviedo, 33006 Oviedo, Spain*

Corresponding authors:

E-mail addresses:

paredes@incar.csic.es (J. I. Paredes), silvia@incar.csic.es (S. Villar-Rodil).

Abstract

Two-dimensional 2H-phase MoS_2 nanosheets can be used as a non-noble metal-based catalyst for nitroarene and organic dye reduction, thus being of potential utility towards the treatment of industrial wastewater. However, their activity is severely limited by the inertness of their pristine basal surface. We report here a simple approach for the catalytic activation of solvent-dispersed MoS_2 nanosheets based on the introduction of sulfur vacancies by hydrazine treatment. MoS_2 nanosheets boasting markedly improved catalytic activities in the reduction of 4-nitrophenol, 4-nitroaniline, methyl orange and methylene blue by $NaBH_4$ could be obtained, outperforming many prior non-noble metal-based catalysts developed for such reactions. Notably, the improvement in catalytic activity was not compromised by the use of a proper dispersant to colloidally stabilize the activated nanosheets in the aqueous reaction medium. Substrate-supported catalysts could be prepared by immobilizing the nanosheets on melamine foam, facilitating their handling and reutilization. The chemical processes taking place between the investigated reagents and the MoS_2 catalyst were also discussed and rationalized, based on which a mechanism for nitroarene/dye reduction mediated by the sulfur vacancies was proposed.

Keywords:

Two-dimensional material, MoS_2, catalytic reduction, 4-nitrophenol, organic dye degradation.

1. Introduction

Transition metal dichalcogenides (TMDs) in two-dimensional (2D) form, such as MoS_2, $MoSe_2$ or WS_2, have in recent years become the focus of intensive research endeavors due to their strong potential for application in many technological fields,[1,2]

including that of catalysis[3-5]. Although bulk layered TMDs, especially MoS_2, have long been known to be catalytically active towards certain reactions of industrial interest (mainly, hydrodesulfurization reactions),[6,7] their downsizing into 2D nanosheets (NSs) can bring a number of benefits when used in catalysis.[3,4] First, the large surface-to- volume ratio of 2D TMDs provides a greatly increased density of catalytic active sites (either native or intentionally generated) that are accessible to reactants. Second, the electronic structure of TMDs undergoes considerable changes when their dimensionality is reduced to the single-/few-layer level, which can be exploited to modulate the reactivity of their catalytic sites. Third, while not acting as catalysts themselves, TMD nanosheets supported onto catalytic substrates afford two-dimensionally confined spaces where the rate of chemical reactions may be accelerated, a phenomenon referred to as "catalysis under cover".[8]

To this day, most efforts on the application of 2D TMDs in catalysis have been directed to the area of electrochemical energy conversion, where they have been mainly explored as electrocatalysts for the hydrogen evolution reaction (HER) and, to a lesser extent, the oxygen reduction/evolution reactions.[4,5,9] In the meantime, however, a number of studies have disclosed the high catalytic activity of 2D and nanostructured TMDs towards other, environmentally relevant chemical processes, such as CO_2 methanation[10] and the reduction of nitroarenes and organic dyes.[11] In particular, the reduction of nitroarenes/dyes is carried out in the liquid phase (mainly water)[11–19] and bears a considerable practical relevance in addition to its interest as model reaction for the testing of catalytic systems.[20-23] For example, nitrophenols and their derivatives are highly toxic and recalcitrant pollutants generated as by-products by many chemical industries (e.g., those manufacturing pesticides, herbicides or dyes). Therefore, they need to be degraded before they are discharged to the aquatic environment. The reduction of nitrophenols into

biodegradable and much less toxic anilines is one of the possible solutions.[22,24,25] Similarly, the degradation of organic dyes found in industrial wastewater effluents, such as methyl orange and methylene blue,[26] by reduction processes is also relevant from an environmental remediation perspective.[25,27,28] In addition, the reduction of nitrophenols into their corresponding anilines is an essential step in the synthesis of certain pharmaceutical compounds (e.g., antipyretic and analgesic drugs) and polymers.[21]

Though the reduction of nitroarenes and other aromatic compounds has been traditionally accomplished with precious metal (Pt, Pd, Au, etc) nanoparticles as the catalyst,[29,30] the high cost and scarcity of the latter has driven a search for more affordable alternatives based on the use of non-noble metals (e.g., Co, Ni and Cu).[22,31,32] Metal compounds such as transition metal oxides and sulfides, including 2D MoS_2, are also being explored.[21] Indeed, early work demonstrated that 1T-phase MoS_2 NSs produced via the Li intercalation/exfoliation route are efficient catalysts in the reduction of a number of nitroarenes and dyes by $NaBH_4$ in water.[11,14] The metallic character of the 1T phase was believed to be largely responsible for the good catalytic behavior of the NSs; indeed, their activity decreased markedly when the 1T phase was converted to the semiconducting 2H phase.[11] Unfortunately, 1T phase is metastable and reverts to the thermodynamically stable 2H phase in a matter of weeks to months,[33,34] and is also prone to environmental oxidation.[35,36] Such instability compromises the practical use of the 1T-phase material in catalysis and beyond. While this problem can be alleviated through covalent functionalization of the 1T NSs,[37] both the chemical derivatization and the Li intercalation process itself require long reaction times (days) and/or inert atmospheres, which challenges the feasibility of this route for the industrial production of 2D MoS_2-based catalysts.

Alternatively, 2H-phase NSs can be easily prepared in large quantities by direct,

ultrasound- or shear force-induced exfoliation of bulk MoS_2 in the liquid phase.[38-40] This solvent-exfoliated MoS_2 is also catalytically active towards the reduction of nitroarenes, but its activity is substantially lower than that of 1T-phase NSs derived from Li intercalation.[41] Such a comparatively meager performance can be attributed to the fact that, similar to other MoS_2-catalyzed processes (e.g., HER),[4,5,9] the catalytic active sites for these reduction reactions are located for the most part at the edges of the 2H NSs, their basal planes being largely inert.[41] Finding simple and efficient ways to activate the basal plane of 2H NSs for these catalytic reactions would thus be highly desirable to foster their industrial use, but such an issue is yet to be addressed. We hypothesized that introducing sulfur vacancies on the surface of 2H MoS_2 NSs could be an effective way to activate their basal planes toward the reduction of nitroarenes and organic dyes. Although this type of lattice defect has in recent years been demonstrated to be catalytically very active for the electrochemical HER,[42] it is currently unknown whether the same holds true for the abovementioned reduction reactions. However, since the latter are essentially electron transfer processes[11,19] and sulfur vacancies in MoS_2 are known to behave as electron donors,[43] it is quite likely that such defects will also be catalytically active in this case. Very recent and limited evidence seems to support this idea,[44] but the question has not yet been systematically investigated and demonstrated.

Here, we investigate a simple wet chemical method based on hydrazine treatment for the controlled generation of sulfur vacancies in solvent-exfoliated MoS_2 NSs, which is shown to activate them for the catalytic reduction of nitroarenes and organic dyes. Through proper adjustment of the treatment conditions, the catalytic activity of the material can be markedly increased, becoming comparable or even higher than that of metallic 1T MoS_2 and other catalysts based on non-noble metals. The central role played by the introduced sulfur vacancies in the enhanced catalytic performance is

mechanistically discussed and substantiated through experiments whereby these defects are deactivated by well-known vacancy passivation methods, as well as through comparison with the activity of the NSs as electrocatalysts for HER. Likewise, easily recoverable and reusable catalysts based on the vacancy-decorated MoS_2 NSs are obtained by resorting to melamine foam as a supporting scaffold for the NSs. Overall, the present results may provide a viable route to implement activated 2D MoS_2 in industrial catalytic processes of environmental relevance.

2. Materials and methods

2.1. Materials and reagents

The following materials and chemicals were acquired from Sigma-Aldrich and used as received: MoS_2 powder, isopropanol, hydrazine monohydrate, $NaBH_4$, 4-nitrophenol (4-NP), 4-nitroaniline (4-NA), methyl orange (MO), methylene blue (MB), guanosine monophosphate (GMP) and 1-pentanethiol. Milli-Q deionized water (Millipore Corporation; resistivity: 18.2 MΩ cm) was used throughout the experiments.

2.2.Preparation and hydrazine treatment of 2D MoS_2 nanosheets

MoS_2 NSs were obtained from the direct exfoliation of bulk MoS_2 powder in isopropanol with the assistance of sonication. In a typical procedure, 3 g of MoS_2 powder were added to 100 mL of isopropanol in a vial and bath-sonicated (J.P. Selecta Ultrasons system, 40 kHz) for 5 h. The resulting mixture was then centrifuged (Eppendorf 5424 microcentrifuge) at 2000 *g* for 20 min to retain only the thinnest (i.e., few/several-layer) exfoliated NSs in the supernatant, which was collected for further use, while the rest of the MoS_2 material (i.e., thicker exfoliated NSs as well as poorly and non-exfoliated particles) was sedimented. The average lateral size and thickness of the dispersed NSs along with

their concentration in the supernatant suspension were estimated by means of UV-vis absorption (extinction) spectroscopy using the metrics developed by Backes et al specifically for this 2D material.[45] These MoS_2 suspensions were used in all the subsequent experiments. To generate sulfur vacancies in the exfoliated MoS_2 NSs, their colloidal dispersions in isopropanol were subjected to hydrazine treatment, which was carried out as follows: in a test tube, a given volume of hydrazine monohydrate was added to 20 mL of MoS_2 dispersion with a concentration of 0.1 mg mL^{-1}. The test tube was then capped with a rubber septum having a small perforated orifice to allow gas release and heated at 70 ºC for 2 h. The reacted product was then washed to remove any hydrazine monohydrate remaining in the solution by applying three consecutive cycles of MoS_2 NS sedimentation via centrifugation (20000 *g*, 20 min), replacement of all the supernatant volume by neat isopropanol and re-dispersion of the NSs by a brief (2 min) sonication step. When the MoS_2 material was required in a dry state, the sediment from the last centrifugation cycle was collected and dried overnight at room temperature under reduced pressure. Different samples of hydrazine-treated MoS_2 NSs were obtained depending on the amount of hydrazine monohydrate used for the treatment. These samples were denoted as MoS_2-x%, where x% stands for the volume percentage of hydrazine monohydrate added relative to the volume of MoS_2 dispersion used (e.g., MoS_2-2% indicates that 0.4 mL of hydrazine monohydrate were added to 20 mL of the MoS_2 dispersion in isopropanol). For comparison purposes, hydrazine treatments at room temperature (~20 ºC) and 150 ºC were also carried out. The reaction at 150 ºC was not conducted in a capped test tube. A Teflon-lined autoclave heated in a conventional laboratory oven was used instead.

2.3. *Catalytic reduction of nitroarenes and organic dyes with activated MoS_2 nanosheets*

The hydrazine-treated MoS_2 NSs were investigated as catalysts for the reduction of the nitroarenes 4-NP and 4-NA as well as the organic dyes MO and MB in aqueous medium at room temperature, using $NaBH_4$ as the reducing agent. Two main sets of catalysts were tested: (1) bare, uncapped 2D MoS_2, i.e., NSs that were transferred from their original isopropanol dispersion to the aqueous reaction medium without resorting to any stabilizer or surfactant, and (2) GMP-stabilized 2D MoS_2, i.e., NSs that were transferred to the aqueous medium with the aid of the GMP nucleotide as a colloidal stabilizer. For the bare NSs, solvent transfer was accomplished by two cycles of sedimentation of their original dispersion in isopropanol via centrifugation (20000 *g*, 20 min), replacement of the supernatant liquid by water and re-dispersion by a brief sonication treatment (2 min). The colloidal stability of the resulting aqueous dispersions of bare MoS_2 was limited to several hours. For this reason, the corresponding catalytic tests were carried out immediately after the solvent transfer step. For the GMP-stabilized NSs, the solvent transfer protocol was similar, with the exception that, in the second cycle, the sedimented NSs were re-dispersed in an aqueous solution of the nucleotide (GMP concentration: 2 mg mL^{-1}). This gave a mixed solution containing MoS_2 NSs colloidally stabilized by adsorbed GMP molecules together with free, non-adsorbed GMP. To remove the free molecules and retain only the GMP-adsorbed NSs, the latter were sedimented by 2 iterative cycles of centrifugation (20000 *g*, 20 min), replacement of ~75% of the supernatant volume by pure water and re-dispersion of the sedimented NSs by a brief (2 min) sonication step. The different hydrazine-treated, GMP-stabilized MoS_2 samples were denoted as GMP-MoS_2-x%, where x% has the same meaning as that defined for their bare MoS_2 counterparts.

For the catalytic tests, aqueous aliquots (2.5 mL) containing a given MoS_2 catalyst (~7 μg mL^{-1}), the substrate molecule, i.e., either 4-NP (0.12 mM), 4-NA (0.11 mM), MO (0.07 mM) or MB (0.06 mM), as well as $NaBH_4$ at a concentration of 72, 110, 180 and 100 mM for 4- NP, 4-NA, MO and MB, respectively, were prepared in quartz cuvettes with an optical path length of 1 cm. Immediately after preparation, the cuvettes were transferred to a double-beam Heλios α UV-vis absorption spectrophotometer (Thermo Spectronic) and the reaction progress was monitored by recording the corresponding kinetic profiles. The latter were obtained by measuring the temporal evolution of absorbance at the wavelength of a characteristic peak of the substrate molecule, namely, at 400 (4-NP), 382 (4-NA), 461 (MO) and 675 nm (MB).

Catalyst deactivation tests were carried out by reaction of the hydrazine-treated MoS_2 NSs with alkanethiol molecules. Specifically, 0.1 mg mL^{-1} MoS_2 dispersion in isopropanol that had been previously treated with 4% hydrazine monohydrate (i.e., sample MoS_2-4%) was mixed with 1-pentanethiol. The concentration of the alkanethiol in the dispersion was set to 5 mM. After the mixture was allowed to stand at room temperature for 24 hours, the excess thiol was removed from the reacted MoS_2 NSs through three consecutive cycles of sedimentation via centrifugation (20000 *g*, 20 min), replacement of the supernatant liquid by neat isopropanol and re-suspension of the NSs through a brief (2 min) sonication step. To examine their catalytic activity, the resulting alkanethiol- and hydrazine-treated MoS_2 NSs were transferred to the aqueous phase with the assistance of GMP, following the procedure described above.

To facilitate their recovery and re-use, the activated MoS_2 NSs were immobilized onto commercial melamine foam. To this end, the foam was first cut into ~1 cm edge cubes and cleaned by bath-sonication in ethanol and acetone (15 min in each solvent). After drying under ambient conditions, the melamine foam cubes were soaked into a 0.1 mg mL^{-1} MoS_2

dispersion in isopropanol and then dried at room temperature under reduced pressure. To increase the amount of loaded NSs, the soaking/drying process was carried out several times (typically three), after which the original white color of the melamine foam turned into an olive green tone. For the catalytic tests, the MoS_2-loaded foam cubes were simply immersed into the substrate/$NaBH_4$ reaction mixture and then 0.25 mL aliquots were taken from the mixture at specific intervals for measurement in the UV-vis spectrophotometer. After reaction completion, the cubes were removed from the solution, rinsed with water and allowed to dry before being used in the next catalytic cycle.

2.4. Characterization of the 2D MoS_2 nanosheets

The materials were analyzed by UV-vis absorption spectroscopy, field-emission scanning electron microscopy (FE-SEM), scanning transmission electron microscopy (STEM), high resolution transmission electron microscopy (HR-TEM), atomic force microscopy (AFM), Raman spectroscopy, X-ray photoelectron spectroscopy (XPS) and electron paramagnetic resonance (EPR). UV-vis absorption spectra were obtained in the same equipment used for the catalytic tests. FE-SEM and STEM images were recorded on a Quanta FEG apparatus (FEI Company) operated at 25 kV, whereas HR-TEM was accomplished in a JEM-2100F system (JEOL) working at an acceleration voltage of 200 kV. For the preparation of specimens for STEM and HR-TEM, their dispersion in isopropanol was drop-cast (~40 μL) onto copper grids (200 mesh) covered with either continuous or lacey carbon film (acquired from SPI supplies and EMS, respectively). To avoid damage by high energy electron bombardment, the HR-TEM measurements were performed under cryogenic conditions (-180 °C), using a double tilt, cooled sample holder (GATAN model 636). AFM measurements were carried out with a Nanoscope IIIa Multimode apparatus (Veeco Instruments) in the tapping mode of operation, using silicon

cantilevers with nominal spring constant and resonance frequency of ~40 N m^{-1} and 250–300 kHz, respectively. Samples for AFM were prepared by drop-casting a small volume (~20 μL) of a low-concentration MoS_2 NS dispersion in isopropanol (~0.01–0.03 mg mL^{-1}) onto SiO_2 (300 nm)/Si wafers and allowing it to dry under ambient conditions. Raman spectra were recorded on a Horiba Jobin-Yvon LabRam instrument at a laser excitation wavelength of 532 nm (green line). A low incident laser power (~0.2 mW) was employed to avoid damage to the NSs. XPS was accomplished on a SPECS system, working at a pressure of 10^{-7} Pa with a non-monochromatic Mg K_α X-ray source operated at 11.81 kV and 150 W. For both Raman spectroscopy and XPS, specimens were prepared by drop-casting MoS_2 NS dispersions in isopropanol onto stainless steel disks until a thin, continuous film became visible to the naked eye. EPR spectra were collected at room temperature using a Bruker EMX spectrometer equipped with a EMX premium X microwave bridge with X band frequency of ~9 GHz. Spectra were recorded with a magnetic field modulation amplitude of 1.86 G, a modulation frequency of 100 kHz and a microwave power of ~20 mW. EPR data treatment was carried out with Bruker WinEPR Procesing software.

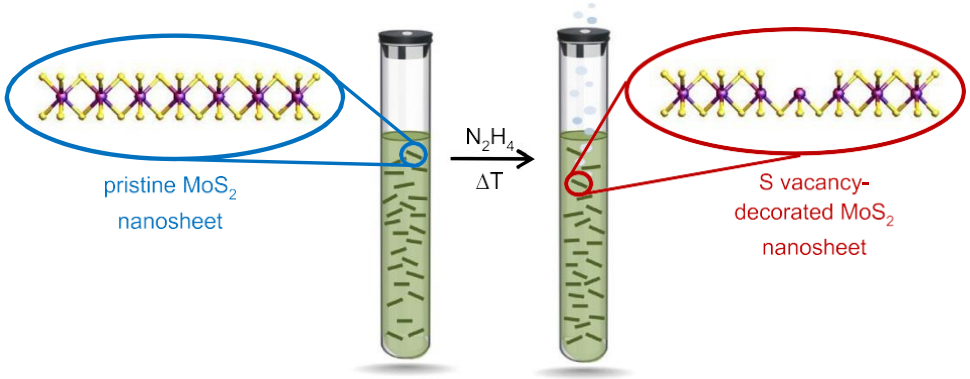

Fig. 1. Schematic of the generation of sulfur vacancies in MoS2 nanosheets by a wet-chemical route. Isopropanol-dispersed MoS2 nanosheets are reacted with hydrazine at 70 °C to generate sulfur vacancies on their surface.

3. Results and discussion

3.1. Preparation and characterization of MoS_2 nanosheets activated by hydrazine treatment

Our aim was to activate the basal plane of MoS_2 NSs suspended in solution toward the catalytic reduction of nitroarenes and organic dyes by the removal of sulfur atoms from their surface. The strategies proposed in recent years for generating sulfur vacancies in 2D MoS_2, e.g., plasma treatment,[42,46,47] ion irradiation,[48,49] vacuum annealing[50] or electrochemical reduction,[51] were only applicable for NSs supported onto substrates. A wet-chemical treatment appeared as a more suitable option for MoS_2 NSs dispersed in solution. Specifically, a reduction treatment with a sufficiently strong reducing agent seemed appropriate given that the removal of a sulfur atom from the MoS_2 lattice is formally a reduction process (to give MoS_{2-x}). Indeed, a few recent reports on the liquid-phase exfoliation of bulk MoS_2 through treatment with well-known reductants (hydrazine and its derivatives, $NaBH_4$) under harsh conditions (e.g., high temperatures or intensive sonication) have revealed the formation of sulfur vacancies or even holes in the resulting exfoliated NSs.[52-54] However, such aggressive treatments easily led to an extensive structural modification of the 2D NSs,[52-54] making it difficult to fine-tune the introduction of defects in their lattice, and thus to control and optimize their performance as electron transfer catalysts. For our purpose, the implementation of milder treatments appeared as a more attractive alternative. Fig. 1 shows a schematic representation of the strategy followed here for generating sulfur vacancies in solution-dispersed MoS_2 NSs, which

relied on reacting them with hydrazine in isopropanol solvent at a moderate temperature (70 ºC).

First of all, we obtained (non-activated) MoS_2 dispersions in isopropanol from the MoS_2 bulk powder by a sonication/centrifugation procedure (see Materials and Methods for details and Fig. 2a for a photograph of an as-prepared dispersion). UV-vis absorption spectroscopy (Fig. 2b) revealed features that were typical of semiconducting 2H MoS_2.[55] Both XPS (Fig. 2g) and Raman spectroscopy (Fig. 2h) confirmed that the structural phase of the MoS_2 NSs was exclusively 2H, with no sign of the metallic 1T phase.[56,57] Quantitative analysis of the UV-vis spectrum (Fig. 2b) afforded estimates of the concentration (~0.1 mg mL^{-1}) as well as average lateral size (~190–200 nm) and layer number (~7–8) of the suspended NSs.[45] Such results agreed with those obtained from the direct observation of the solvent-dispersed objects by scanning transmission electron microscopy (STEM; Fig. 2c) and atomic force microscopy (AFM; Fig. 2d), and summarized in the histograms of Fig. 2e (distribution of NS lateral size) and f (distribution of NS layer number).

Then, MoS_2 dispersions in isopropanol at a concentration of 0.1 mg mL^{-1} were treated with hydrazine monohydrate in capped test tubes at a moderate temperature (70 ºC) to generate sulfur vacancies in their lattice (details of the procedure are given in the Materials and Methods). Different treated samples were obtained by adding different hydrazine monohydrate volumes to the MoS_2 dispersion, resulting in samples denoted as MoS_2-x%, where *x* indicates the hydrazine monohydrate to MoS_2 dispersion volume ratio (in percentage). Volume ratios in the 1–10% range were investigated. Upon mixing the reducing agent with the MoS_2 suspension and heating at 70 ºC, some convection developed in the liquid and, after several minutes, the MoS_2 NSs started to agglomerate and sediment, and at the same time small gas bubbles were seen to rise through the liquid.

After two hours the mixture was cooled to room temperature and the treated NSs were washed to remove any remnants of the reducing agent and then re-dispersed in neat isopropanol. Several control experiments described in the Electronic Supplementary Material (ESM) allowed concluding that the gas bubbles were generated as a result of reactions between the MoS_2 NSs and the reducing agent. Temperature appeared to play a central role in the evolution of the gas bubbles, that is, in the reduction of MoS_2 by hydrazine. For instance, no bubbles (nor NS agglomeration) were observed to form when the MoS_2 dispersion/hydrazine monohydrate mixtures were kept at room temperature (~20 ^{o}C), implying that the processes leading up to gas generation were kinetically hindered by a non-negligible activation barrier. The effect of treatment temperature on the catalytic performance of the NSs will be discussed below.

The hydrazine-treated MoS_2 NSs retained their overall morphology and structural phase. Indeed, the lamellar appearance and dimensions of the typical dispersed objects from samples MoS_2-2%, MoS_2-4%, MoS_2-6% and MoS_2-10% (see STEM images in Fig. S1 of the ESM) were very similar to those of the starting, untreated dispersion (Fig. 2c). Likewise, results from UV-vis absorption spectroscopy, XPS and Raman spectroscopy (Fig. S2 in the ESM) indicated a virtually complete preservation of the semiconducting 2H phase after the treatments, with no sign of the metallic 1T phase (a discussion on the reasons for the lack of phase transformation upon reduction is included in the ESM).

On the other hand, the atomic-scale conformation of the MoS_2 NSs underwent noticeable changes with hydrazine treatment. Fig. 3a-c shows HR-TEM images of the starting exfoliated material (a) as well as samples MoS_2-4% (b) and MoS_2-10% (c). Whereas the former generally exhibited a long-range ordered triangular pattern,

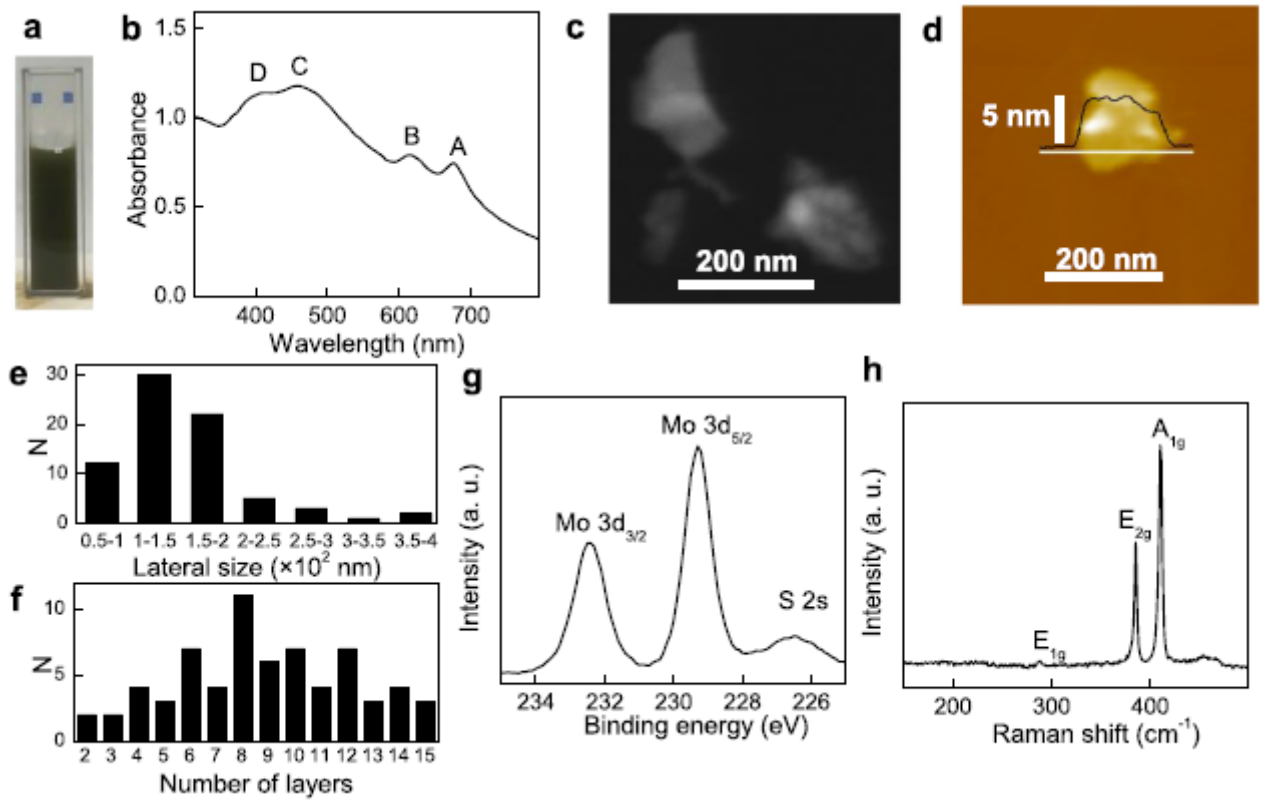

Fig. 2. Characterization of the starting MoS2 nanosheets. (a) Digital photograph of MoS2 dispersion obtained in isopropanol and (b) its corresponding UV–vis absorption spectrum. The excitonic bands A, B, C and D characteristic of 2H-phase MoS2 are indicated. (c) Representative STEM image recorded for MoS2 flakes. (d) Typical AFM image of MoS2 flakes deposited from their dispersion. A representative line profile (black line) taken along the marked white line is shown overlaid on the image. Histograms of nanosheet (e) lateral size and (f) layer number. (g) Background-subtracted, high resolution XPS Mo 3d spectrum and (h) Raman spectrum of a MoS2 film drop-cast from dispersion. The main bands of the spectra in g and h are labeled for clarity. (For interpretation of the references to color in this figure legend, the reader is referred to the web version of this article.)

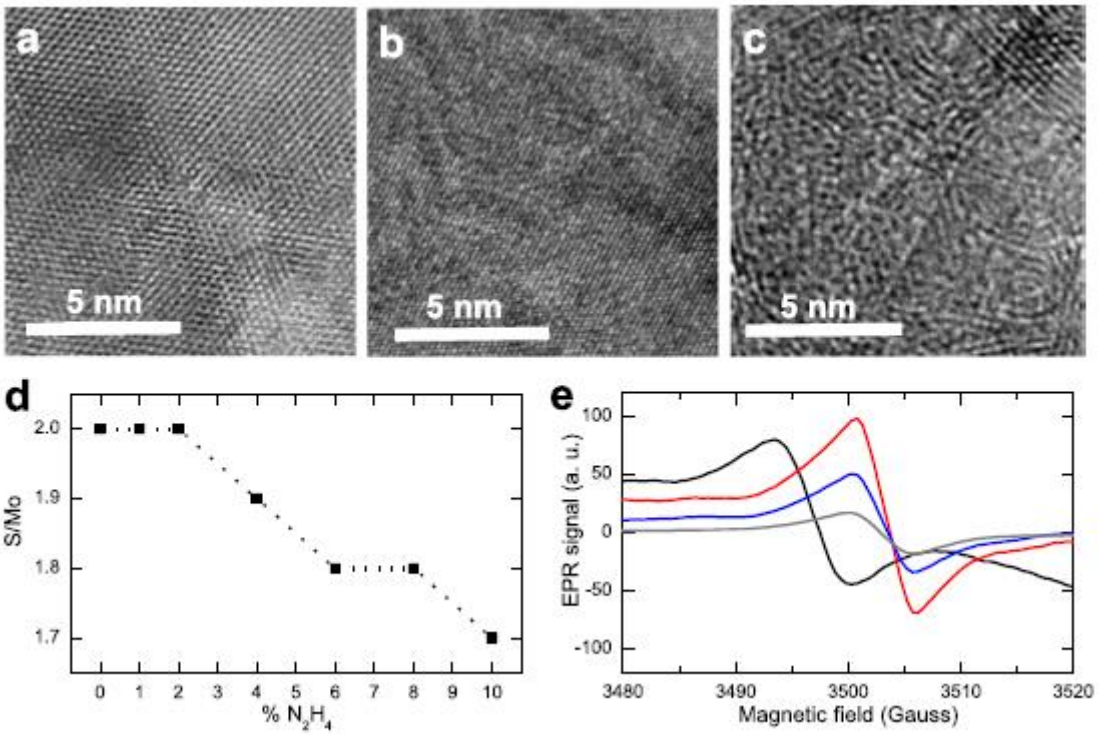

Fig. 3. Characterization of the hydrazine-treated MoS2 nanosheets. High resolution TEM images of: (a) the starting exfoliated material, (b) MoS2 -4%, and (c) MoS2 -10%. (d) S/Mo atomic ratio calculated from XPS data for the different materials versus the amount of hydrazine monohydrate used for their preparation. (e) Representative first-derivative X-band EPR spectra of the bulk, non-exfoliated MoS2 powder (gray trace), starting MoS2 nanosheets (black trace) as well as MoS2 -4% (red trace) and MoS2 -10% (blue trace). (For interpretation of the references to color in this figure legend, the reader is referred to the web version of this article.)

which is indicative of a MoS_2 lattice with no or very few atomic defects, the hydrazine-treated NSs appeared more irregular and discontinuous. For example, the presence of dark spots in MoS_2-4% sample suggested that some atoms were missing from the lattice. Furthermore, treatment with larger hydrazine volumes (i.e., sample MoS_2-10%) led to more distinct and widespread lattice distortions. We interpret these structural

changes to be mostly related to the removal of sulfur atoms upon reaction of the MoS_2 NSs with hydrazine. Indeed, as can be seen from Fig. 3d, the S/Mo atomic ratio values estimated for the different samples from XPS data tended to decrease with increasing amount of hydrazine monohydrate used, more specifically, from ~2.0 for the starting, untreated MoS_2 NSs to 1.7 for sample MoS_2-10%. These figures implied that moderate total numbers of sulfur vacancies were generated in the NSs by the different hydrazine treatments. Additional information on the determination of S/Mo atomic ratios by XPS is provided in the ESM.

Electron paramagnetic resonance (EPR) spectroscopy provided further insight into the introduction of sulfur vacancies in the MoS_2 lattice. Mo-S dangling bonds in MoS_2 give rise to an EPR signal at a magnetic field of ~3500 G, and hence the introduction of sulfur vacancies should in principle lead to an enhanced intensity of this signal.[58,59] Fig. 3e shows EPR spectra recorded for the starting MoS_2 NSs (black trace) as well as samples MoS_2-4% (red) and MoS_2-10% (blue). The spectrum for the bulk, non-exfoliated MoS_2 powder is also shown for comparison (gray). The fact that the EPR signal was already substantial for the starting exfoliated sample relative to its non-exfoliated counterpart can be ascribed to the presence of a sizable amount of dangling bonds associated to edges in MoS_2 NSs of a limited lateral size (~100–300 nm; see Fig. 2).[59] A stronger EPR signal was measured for sample MoS_2-4%, which was consistent with the introduction of sulfur vacancies and hence of new dangling bonds in the lattice. Still, an even stronger signal was not observed for sample MoS_2-10%, but rather a noticeably weaker one. This result appeared to be at odds with the fact that, according to XPS, the latter possessed a lower S/Mo ratio and thus a larger number of sulfur vacancies. We stress that these features were reproducible, as independently prepared batches of the same type of sample yielded the same quantitative results. A very similar behavior has been recently reported for MoS_2 NSs that had a

variable fraction of their sulfur atoms removed by hydrogen annealing at different temperatures, and put down to a change in the nature of the resulting defects as the S/Mo ratio was decreased,[59] which led to fewer Mo-S dangling bonds per defect and thus to weaker EPR signals. As will be discussed below, these EPR results provide a basis for rationalizing the catalytic activity trends of our hydrazine-treated MoS_2 NSs.

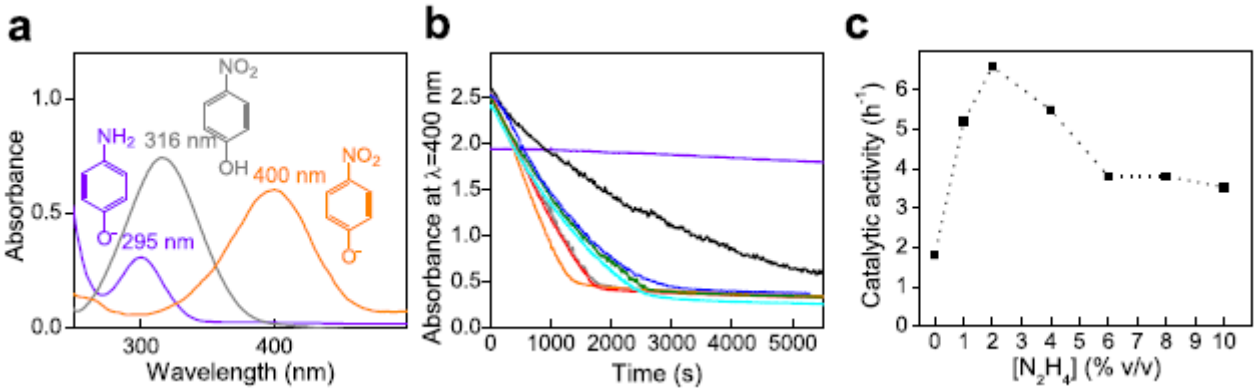

Fig. 4. Hydrazine-treated, solvent-exfoliated bare MoS2 nanosheets as catalysts for 4-NP reduction. (a) Chemical structure and UV–vis spectra of 4-NP (gray trace), 4-nitrophenoxide ion (orange trace), and 4-aminophenoxide ion (violet trace). (b) Typical kinetic profiles using the starting MoS2 nanosheets (black trace), MoS2 -1% (gray trace), MoS2 -2% (orange trace), MoS2 -4% (red trace), MoS2 -6% (green trace), MoS2 -8% (cyan trace), and MoS2 -10% (blue trace) as catalyst for the reduction of 4-NP. The kinetic profile of a blank experiment (no catalyst added) is also included (violet trace). (c) Catalytic activity values of the different MoS2 materials, which were calculated as the number of moles of 4-NP converted per mole of MoS2 catalyst per unit time.(For interpretation of the references to color in this figure legend, the reader is referred to the web version of this article.)

3.2. Catalytic performance of the activated MoS_2 nanosheets towards nitroarene and organic dye reduction

Having demonstrated the generation of sulfur vacancies in solvent-exfoliated MoS_2 NSs by hydrazine treatment, we set out to investigate the influence of such defects on the performance of the NSs as a catalyst for the reduction of nitroarenes and organic dyes. As

the main benchmark reaction, we selected the reduction of 4-nitrophenol (4-NP) to 4-aminophenol (4-AP) with $NaBH_4$ in aqueous medium at room temperature. This reaction is known to be thermodynamically favored but kinetically hindered by a significant activation barrier, and thus relies on the assistance of a proper catalyst to proceed at a fast rate.[21] As noticed in Fig. 4a, the reaction progress can be conveniently followed with UV-vis absorption spectroscopy by monitoring the absorption band located at a wavelength of ~400 nm that is distinctive of the 4-nitrophenoxide anion (i.e., the deprotonated form of 4-NP in the basic medium induced by $NaBH_4$).[11,20] This band is not present in the corresponding reduced species (i.e., 4-aminophenoxide anion), which in turn is characterized by an absorption peak located at ~295 nm. Details on the implementation of the catalytic tests can be found in the Materials and Methods section. Fig. 4b presents typical kinetic profiles measured using the starting, untreated MoS_2 NSs as the catalyst, as well as NSs treated with different amounts of hydrazine monohydrate, where the temporal evolution of absorbance at 400 nm for the reaction mixture (reflecting changes in 4-NP concentration as it is reduced to 4-AP) was plotted. In all cases, the absorbance was seen to monotonously decrease with time until a plateau was reached, which marked completion of the reduction reaction. The kinetic profiles of the hydrazine-treated samples generally exhibited a linear decay. Because $NaBH_4$ was used in a large excess relative to 4-NP, this implied that the reaction was pseudo-zero-order with respect to the latter and hence that the catalytic active sites in the NSs were fully occupied during the reaction. By contrast, exponential decay profiles were recorded for the untreated MoS_2 NSs, i.e., the reaction was pseudo-first-order in this case (for a detailed discussion of the order of the catalytic reaction, see section 3.3 and Fig. S6 in the ESM). Such a discrepancy in the reaction order can be ascribed to a different nature of the active sites in the catalysts. Specifically, the main active sites can be associated to sulfur vacancies in the hydrazine-treated MoS_2

samples and to edges in their untreated counterpart, the former being probably less abundant but catalytically much more active than the latter in the hydrazine-treated NSs, and largely absent from the untreated NSs.

It can be noticed from Fig. 4b that hydrazine treatment had a substantial positive effect on the catalytic performance of the MoS_2 NSs, as evidenced by the shorter times required to reaction completion relative to that of the untreated material. Such an effect was already significant for the sample prepared with the smallest amount of hydrazine monohydrate (MoS_2-1%), but peaked for sample MoS_2-2%. By contrast, the use of larger hydrazine monohydrate volumes (i.e., 4, 6, 8 and 10%) led to a gradual decrease in the observed reaction rates, although they were still considerably faster than that obtained with the untreated NSs. These trends could be quantitatively confirmed by comparing the overall catalytic activity of the different MoS_2 samples, which was calculated as the number of moles of 4-NP converted per mole of MoS_2 catalyst used per unit time. The results are plotted in Fig. 4c, where the most efficient hydrazine-treated samples were seen to be more active than their non-treated counterpart by a factor of about 3–4 (e.g., 6.6 h^{-1} for MoS_2-2% vs 1.8 h^{-1} for untreated MoS_2). Such an improved activity made these 2H-phase NSs to be on a par with, or even significantly outperform, 1T-phase 2D MoS_2 as well as other catalysts based on non- noble metal nanoparticles previously investigated for nitrophenol reduction (see Table S1 in the ESM for a comparison of catalytic activity values).

We note that the plateau region in the kinetic profiles was associated to a finite absorbance value (around 0.4–0.5), which was not due to the presence of unreacted 4-NP but mostly originated from the MoS_2 NSs themselves, as the latter exhibit strong absorption at 400 nm (see Fig. 2b). Indeed, the absorbance measured for a MoS_2 dispersion having the same concentration as that used in the catalytic tests (i.e., ~7 μg mL^{-}

[1]) was about 0.5. In the absence of any MoS_2 in the reaction mixture, a constant kinetic profile was recorded (also plotted in Fig. 4b), indicating that no reduction of 4-NP was taking place, as expected. When the MoS_2 dispersion used for the catalytic tests was replaced by the supernatant solution resulting from sedimentation of the NSs via centrifugation, constant kinetic profiles were obtained as well. This suggested that the MoS_2 NSs were the actual catalyst for the process, rather than any possible molecular species that could have leached from the NSs. Although not shown in Fig. 4b, an initial induction period of a few to several minutes was usually observed in the recorded profiles (see Fig. S3a in the ESM), during which the absorbance value remained constant or changed very little. Such an induction period was attributed to oxidation of the reaction product back to 4-NP by oxygen molecules dissolved in the reaction solution. Support for this assignment is provided in section S3.1 of the ESM.

The results of the catalytic tests reported in Fig. 4b and c for the different 2D MoS_2 samples were obtained in all cases using bare, uncapped NSs. While such conditions afforded the intrinsic activity of the catalysts to be determined without the possible interference of foreign adsorbed species,[61] their practical utility was compromised by the limited colloidal stability of the bare 2D material in the aqueous reaction medium. To conduct the investigated catalytic reactions, a simple protocol (see Materials and Methods section for details) was first applied to transfer the untreated and hydrazine-treated MoS_2 NSs from isopropanol, where they formed stable colloidal dispersions on their own, to water. In the latter medium, and at the low concentrations used for the catalytic experiments (< 0.01 mg mL^{-1}), the bare NSs were colloidally stable only within a narrow time interval of several hours,[62,63] after which the material started to form visible aggregates. Hence, to avoid the negative effects of NS agglomeration on the catalytic activity, the tests were run immediately after the MoS_2 material was transferred to the

aqueous phase, the results of which are reported in Fig. 4b and c. Likewise, as could be anticipated, the measured catalytic activity values were seen to decrease substantially when the experiments were run several hours after the catalyst was transferred to the aqueous phase.

To circumvent these problems and attain 2D MoS_2 catalysts with sustained activity in water, the transferred NSs were colloidally stabilized by the use of a proper dispersing agent. Among the known range of dispersants/surfactants for MoS_2 NSs,[64] we selected guanosine monophosphate (GMP), which has been recently shown to act as an effective stabilizer of TMDs (including MoS_2).[41] Compared to other dispersants, a particularly attractive feature of this RNA nucleotide rests on its ability to colloidally stabilize the NSs at relatively low GMP/MoS_2 mass ratios, and hence the use of GMP should be less conducive to interfering with the catalytic reactions. Fig. 5 shows representative kinetic profiles (a) and corresponding catalytic activity values (b) for the reduction of 4-NP with the different GMP-stabilized MoS_2 samples, denoted as GMP-MoS_2 (untreated NSs) and GMP-MoS_2-x% (hydrazine-treated NSs). Again, the latter outperformed their untreated counterpart in terms of reaction rates, but in this case the most efficient samples were those prepared with a larger amount of hydrazine, i.e., samples GMP-MoS_2-4% and GMP-MoS_2-6% in Fig. 5b vs sample MoS_2-2% in Fig. 4c.

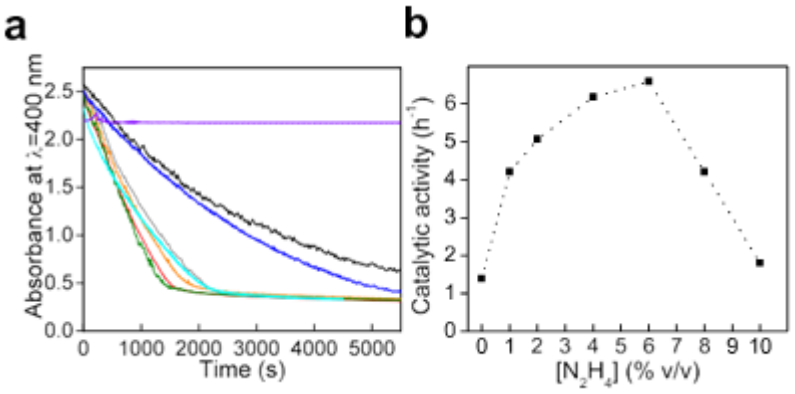

Fig. 5. GMP-stabilized MoS2 nanosheets as catalysts for 4-NP reduction. (a) Representative kinetic profiles using GMP-MoS2 (black trace), GMP-MoS2-1% (gray trace), GMP-MoS2 -2% (orange trace), GMP-MoS2 -4% (red trace), GMP-MoS2 -6% (green trace), GMP-MoS2-8% (cyan trace), and GMP-MoS2-10% (blue trace) as cat- alyst for the reduction of 4-NP. The kinetic profile of a blank experiment in the absence of MoS2 NSs but in the presence of GMP (violet trace) is included for com- parison. (b) Catalytic activity values of the different MoS2 materials.(For interpre- tation of the references to color in this figure legend, the reader is referred to the web version of this article.)

Such a result is reasonable considering that GMP molecules adsorbed onto the MoS_2 NSs probably hinder access of the reactants to surface sulfur vacancies, which are regarded the main catalytic active sites in the material. GMP itself does not possess any catalytic effect, as shown by the flat kinetic profile obtained for a blank experiment performed in the absence of MoS_2 NSs but in the presence of GMP (violet trace in Fig. 5a). According to previous work, this nucleotide adsorbs preferentially at sulfur vacancy sites on the MoS_2 surface due to specific interactions of acid-base type between its nucleobase moiety and the vacancy,[41] which in turn should impair the catalytic activity of the latter, at least in the case of isolated single vacancies. More specifically, for NSs having low vacancy densities (i.e., those treated with small amounts of hydrazine), a significant fraction of their vacancies are expected to be blocked by adsorbed GMP, yielding catalytic activity values below those of their bare NS counterparts. On the other hand, as the vacancy density is increased (NSs treated with increasing amounts of hydrazine), the blocking effect of GMP on the newly added vacancies will probably vanish. This is because the extra vacancies will tend to form next to pre-existing ones,[43] and therefore their blockage by adsorbed nucleotide molecules will be likely inhibited by electrostatic (and possibly also steric) repulsion from GMP molecules already adsorbed at

adjacent, pre-existing vacancies. As a result, the catalytic activity of the GMP- stabilized MoS_2 NSs can be expected to peak for more extensive hydrazine treatments relative to the case of the bare NSs, as it was indeed the case (compare Figs. 4c and 5b). What is quite remarkable, however, is that the highest catalytic activity values afforded with the GMP-stabilized NSs (sample GMP-MoS_2-4%) were very similar to those achieved with the bare material (sample MoS_2-2%), implying that the improvements in catalytic performance attainable by hydrazine treatment were not compromised by the presence of the GMP dispersant.

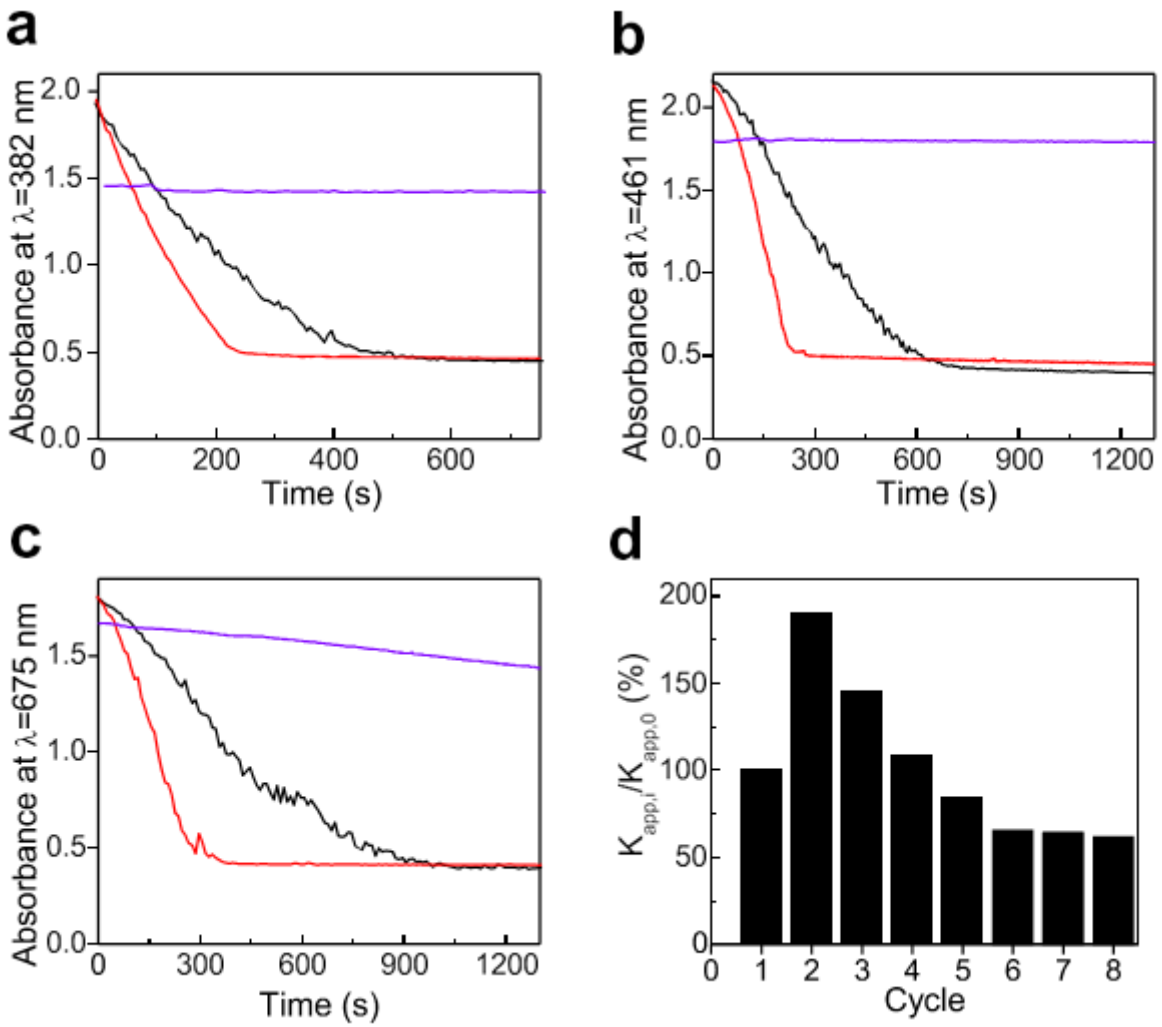

Fig. 6. GMP-stabilized MoS2 nanosheets as catalysts for different reduction reactions. Kinetic profiles for the reduction of (a) 4-nitroniline, (b) methyl orange, and (c) methylene blue using GMP-MoS2 (black trace) and GMP-MoS2-4% (red trace) as catalyst. The kinetic profile for the reduction in the absence of catalyst (blank experiment) is also included (violet trace). (d) Reusability experiments of GMP-MoS2-4% catalyst in the reduction of MO.(For interpretation of the references to color in this figure legend, the reader is referred to the web version of this article.)

The substantially improved catalytic activity of hydrazine-treated MoS_2 NSs was not restricted to 4-NP reduction. Indeed, similar effects were observed for the reduction of 4-nitroaniline (4-NA) as well as the organic dyes methyl orange (MO) and methylene blue (MB), which demonstrated more generally the benefits of the present MoS_2 activation strategy in this type of reduction reactions (more examples of nitroarene reduction reactions catalyzed by these materials are given in fig. S8 in the ESM). Such benefits are illustrated in Fig. 6, where the kinetic profiles recorded for the GMP-stabilized, untreated MoS_2 NSs (sample GMP-MoS_2) are compared with those of sample GMP-MoS_2-4% for the different reactions: 4-NA (a), MO (b) and MB (c). The chemical structures and UV-vis absorption spectra of these compounds and their reduced counterparts are given in Fig. S4 of the ESM. Fig. S5 shows the temporal evolution of the whole UV-vis absorption spectra of the catalytic media of the reduction of the four substrates using GMP-MoS_2-4% as catalyst. Likewise, as exemplified in Fig. 6d for sample GMP-MoS_2-4% and the MO dye, the colloidally stabilized catalysts could be reutilized several times without experiencing a large decline in their activity. Indeed, similar to a previous study with 1T-phase MoS_2 NSs,[11] the measured activity increased in the second reaction cycle and then monotonously decreased in subsequent cycles. Although the origin of such a behavior is not understood at present, this result demonstrated both the positive effect of the GMP dispersant and the overall stability of the NSs as an active catalyst (see Fig. S7 and the corresponding text in

the ESM for information on the effect of the amount of GMP on the recyclability of the catalyst). As stated above, the enhanced catalytic performance of the hydrazine-treated NSs was attributed to the introduction of surface sulfur vacancies in the MoS_2 lattice, which would act as highly active catalytic sites for the investigated reduction reaction. Such a hypothesis was reasonable because sulfur vacancies are known to behave as local electron donors in MoS_2,[43,65] a feature that should be generally conducive to facilitating electron transfer processes in redox reactions, like those investigated here. This conclusion would be in line with previous work that pointed to the donor properties of molybdenum centers in MoS_2 as being highly relevant to the catalytic activity of the material in, e.g., hydrodesulfurization reactions.[66] In that prior case, the greater local availability of electrons at the Fermi level that is associated to the exposed (undercoordinated) molybdenum center next to a sulfur vacancy was concluded to be a main driver of its high catalytic activity, and a similar mechanism can be arguably invoked for the present case. Moreover, the same reasoning can be applied to account for the catalytic activity of edges, which are believed to be the main active sites in MoS_2 NSs lacking sulfur vacancies and other basal plane defects, both for nitroarene reduction[41] and HER.[9] These edges usually possess a metallic character,[67,68] implying that they are richer in electron density at the Fermi level than the semiconducting, defect-free basal planes, which in turn should favor electron transfer processes in catalyzed reactions. Consistent with these ideas, very recent work has determined sulfur vacancies and certain edge terminations to be the main catalytic active sites for nitroarene reduction with H_2 using a similar TMD material, namely, nanostructured WS_2.[69]

The hydrazine-treated samples obtained by the present protocol became also more active towards the electrochemical HER. This was apparent from linear sweep voltammograms recorded in 0.5 M H_2SO_4 solution for different bare MoS_2 NSs that were

deposited onto glassy carbon electrodes (Fig. S9 of the ESM). Lower onset potentials (in absolute value) were measured for the hydrazine-treated samples relative to their untreated counterpart, demonstrating the improved activity of the former. We ascribed such improvement to the introduction of sulfur vacancies in the MoS_2 NSs.

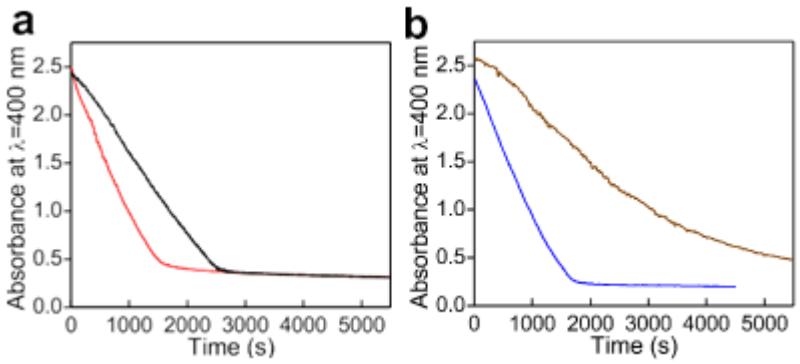

Fig. 7. Further insight into the catalytic activity of hydrazine-treated, solvent-exfoliated MoS2 nanosheets. (a) Kinetic profiles recorded for 4-NP reduction using GMP-MoS2 -4% (red trace), GMP-MoS2-4% modified with pentanethiol (black trace), as well as (b) GMP-MoS2-4%-RT (brown trace) and GMP-MoS2-4%-150 (blue trace) as catalysts.(For interpretation of the references to color in this figure legend, the reader is referred to the web version of this article.)

Attribution of the improved catalytic activity of our hydrazine-treated NSs to the generation of sulfur vacancies was supported through experiments whereby these defects became deactivated by a well-known passivation method that relies on their reaction with alkanethiols.[70-72] Although the exact mechanism and products of the alkanethiol-sulfur vacancy interaction in MoS_2 are still debated, it is widely agreed that the overall result is the passivation of the vacancy by way of its filling with the sulfur atom from the thiol,[73,74] which in turn should lead to its deactivation as a catalytic site. To probe into this idea, MoS_2 NSs dispersed in isopropanol that had been previously treated with 4% hydrazine monohydrate were reacted with 1-pentanethiol (see Materials and Methods section for

details). Fig. 7a shows kinetic profiles recorded for NSs modified with the alkanethiol as well as for unmodified NSs taken as a reference (sample GMP-MoS_2-4%). Much slower reaction rates were measured with the thiol-modified NSs, thus confirming that the sulfur vacancies act as the main catalytic active sites (see Fig. S10 in the ESM and the accompanying text for additional support for such attribution).

An issue of relevance in the activation of MoS_2 NSs towards the investigated reduction reactions concerned the fact that the actual extent of catalytic activation depended sensitively on the intensity of the hydrazine treatment, those of intermediate intensity being the most effective. This was apparent from the observation that the catalytic activity values peaked for treatments with hydrazine hydrate volume ratios of 2–4% (Figs. 4 and 5) and decreased when larger ratios were used. Proper treatment temperatures were also required to optimize the activation of the NSs. The results reported here were obtained with NSs exposed to hydrazine at 70 ºC. However, catalysts prepared at room temperature exhibited a lower activity (e.g., sample GMP-MoS_2-4%-RT in Fig. 7b), being indeed akin to that of the untreated NSs, which suggested that no or very few sulfur vacancies were generated under such conditions and thus agreed with the lack of gas bubble evolution noted above in this case. The use of higher treatment temperatures, such as 150 ºC, did not significantly improve the catalytic behavior, as was noticed for the corresponding sample obtained at 150 ºC (i.e., GMP-MoS_2-4%-150 in Fig. 7b).

With a view to facilitating their recovery and further use in subsequent catalytic cycles, the activated MoS_2 NSs were immobilized onto commercial melamine foam by a simple procedure, namely, the foam was soaked into an isopropanol dispersion of a given MoS_2 sample (e.g., MoS_2-2%) and then dried (see Materials and Methods section for details). Compared to the white color of the starting foam (Fig. 8a, inset), the MoS_2-treated foam displayed an olive green tone (Fig. 8b, inset), suggesting a successful incorporation

of the NSs. Indeed, as revealed by field-emission scanning electron microscopy (FE-SEM) imaging, the smooth and featureless surface typical of the original melamine scaffold (Fig. 8a) became rough and NS-decorated after exposure to the MoS_2 dispersion (Fig. 8b and c). As could be anticipated, while the neat foam was catalytically inactive, its MoS_2 NS-coated counterpart was able to catalyze, e.g., the reduction of 4-NP. After reaction completion, the foam could be readily removed from the solution, washed with water and re-used. Fig. 8d shows the evolution of the catalytic activity of the foam coated with MoS_2-2% NSs for consecutive cycles of 4-NP reduction, where a substantial retention of the activity was achieved.

3.3. Rationalizing the catalytic activity of sulfur vacancies in MoS_2 for nitroarene/organic dye reduction: proposal of a reaction mechanism

The results presented in the previous section allow us to draw two main conclusions. First, as postulated above, to make the most of sulfur vacancy engineering to activate MoS_2 NSs for this type of reduction reactions, the treatment conditions need to be carefully tuned. In particular, relatively harsh treatments leading to extensive NS modification should be avoided, as they do not generally result in catalysts with optimum performance. Second, the most active catalysts appear to be those having intermediate concentrations of sulfur vacancies, rather than those with the highest concentrations as could be a priori assumed. We note that this behavior was similar to that previously reported for the electrochemical HER with sulfur vacancy-decorated MoS_2, which was rationalized by relying on the free energy of hydrogen adsorption (ΔG_H) as an accurate descriptor for predicting the HER activity of these and other catalysts.[42,51] ΔG_H turned out to be zero or very close to zero (i.e., the most favorable for HER) for intermediate sulfur vacancy concentrations (~13–15% sulfur atoms missing from a monolayer), while lower

(higher) concentrations yielded positive (negative) values of ΔG_H. Our hydrazine-treated NSs revealed an analogous trend towards the HER, in that the activity peaked for sample MoS_2-6% but was lower for both more and less extensively treated samples (see Fig. S9 in the ESM). In this case, such a trend can also be reasonably ascribed to the effect of increasing sulfur vacancy concentration that is attained with increasing intensity of hydrazine treatment.

It can be argued that the catalytic activity trends for the reduction reactions with $NaBH_4$ reported here are the result of hydrogen operating as the actual reducing agent. This would not be an unlikely prospect: in aqueous solution, the BH^- anion hydrolyzes spontaneously to give H_2 molecules as one of its reaction products.[75,76] Prior work has indicated that the H_2 molecule undergoes dissociative adsorption at sulfur vacancies in MoS_2,[77,78] so that the resulting adsorbed H atoms could in principle react with a nitroarene/dye molecule to trigger its reduction. In this scenario, the ability of the H atoms to combine with nitroarene/dye molecules at the vacancy sites would be at least partly dictated by the ΔG_H parameter, therefore leading to catalytic activity trends that would roughly mirror those characteristic of HER. However, such a reduction reaction will most probably be inhibited by the fast recombination of the adsorbed H atoms into H_2 molecules, which is a very favorable process at the catalytic sites of MoS_2 (i.e., the Tafel step of HER).[5,9] Indeed, we have previously shown that neither H_2 nor the BH^- anion itself actually function as the reductant in the hydrogenation of nitroarenes with $NaBH_4$ using MoS_2 catalysts, but instead that role is played by an intermediate hydrolysis product, i.e. the BH_3OH^- anion, which is readily oxidizes.[11,79] Also, recent theoretical calculations have revealed that the strength and geometry of adsorption of nitroarenes on WS_2 catalysts, which should have a direct impact on their hydrogenation rates, are highly dependent on the concentration of sulfur vacancies,[69] so a similar effect can be expected for MoS_2.

Hence, the specific configuration of the sulfur vacancies on the MoS_2 surface (e.g., low vs high concentration, single vacancy vs multivacancy, evenly distributed vs clustered vacancies) should dictate the availability of the nitroarene/dye and BH_3OH^- species (or some of their key intermediate products) at such catalytic active sites by determining their adsorption strength and geometry. Such different vacancy configurations should therefore result in different rates for the reduction reaction, as it was indeed observed here.

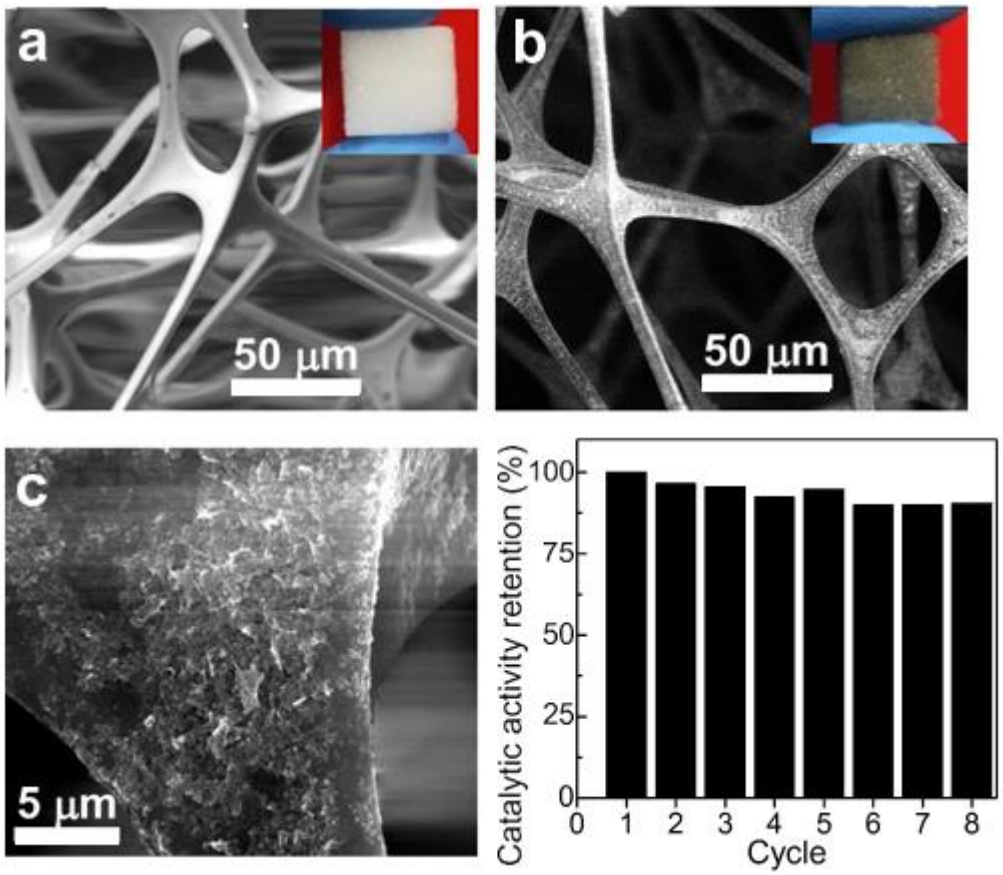

Fig. 8. Melamine foam-supported MoS2 nanosheets as catalyst. (a–c) FE-SEM images of (a) the neat, non-coated melamine foam and (b,c) melamine foam coated with MoS2 -2%. Insets to a and b: digital photographs of cubes with 1 cm edge of the corresponding foams. (d) Reusability experiments of melamine foam-supported MoS2 -2% nanosheets in the catalytic reduction of 4-NP.

As to the actual reduction mechanism occurring at the active sites of the MoS_2 NSs, the following can be put forward as a plausible pathway for the specific case of 4-NP, which is also schematically depicted in Fig. 9. First, in the basic medium of the reaction, the BH_3OH^- species is oxidized at a sulfur vacancy site on the MoS_2 surface with the assistance of hydroxide anions, to release the metaborate anion (BO_2^-), water, hydrogen and electrons [reaction (1) in Fig. 9].[80] While BO_2^- is most certainly inactive as a reductant and thus will not participate in the hydrogenation of 4-NP,[11] the generated hydrogen can be activated by the released electrons to give a negatively charged hydride (H^-),[81] which would be adsorbed at the sulfur vacancy [reaction (2)]. Indeed, prior studies have shown that the H^- species is very unstable, and thus cannot form, on the surface of defect-free MoS_2, but becomes stabilized at sulfur vacancies by transferring excess electron charge to their neighboring unsaturated molybdenum atoms.[82] As a highly active moiety, the vacancy- anchored, negatively charged hydride should readily trigger the hydrogenation of the nitro group in the 4-NP molecule through the well-known three-step sequence;[21,83] i.e., the nitro group is first converted to the nitroso group [reaction (3)], which is then reduced to a hydroxylamine species [reaction (4)] and finally to the amino group [reaction (5)]. In the overall reaction (illustrated graphically in Fig. 9), two BH_3OH^- anions combine with one 4- NP molecule to yield two BO_2^- anions, three H_2 molecules and one 4-AP molecule. The same mechanism should apply in the case of other nitroarenes, such as 4-NA, 2-NA and nitrobencene (see Figs. S4a and S8 in the ESM). For the reduction of other organic molecules (e.g., the dyes MO and MB; see Fig. S4b and c), the generation of highly active hydride species at the sulfur vacancy sites by way of reactions (1) and (2) in Fig. 9, which would subsequently trigger hydrogenation of the substrate, should also be applicable.

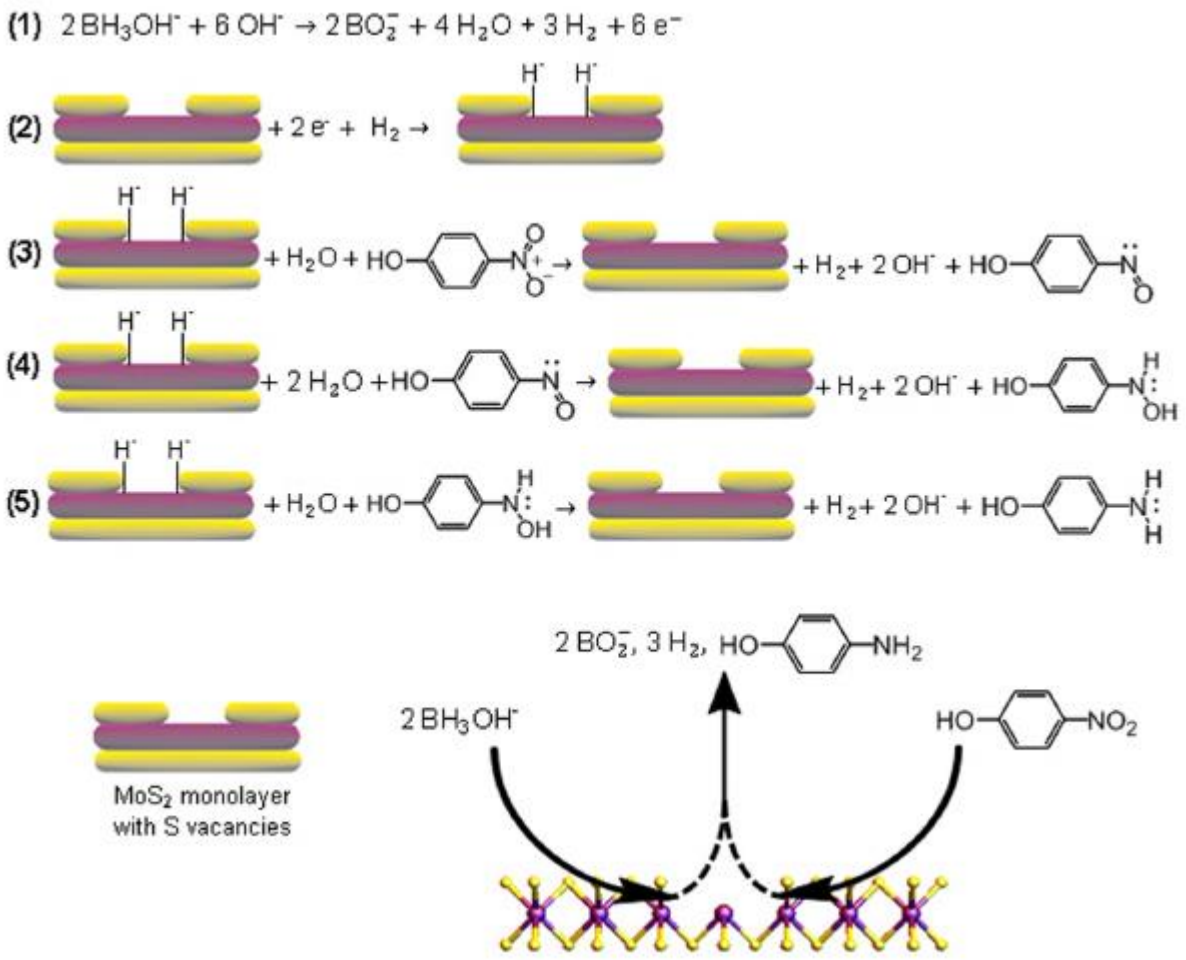

Fig. 9. Proposed reduction mechanism of 4-NP at the active sites of the MoS2 nanosheets. Reaction (1): the hydrolysis product of NaBH4 , i. e., the BH3 OH− anion, is oxidized at a sulfur vacancy site on the MoS2 surface with the assistance of hydroxide anions from the basic medium of the reaction, to release metaborate anion (BO2 −), water, hydrogen and electrons. Reaction (2): the generated hydrogen is activated by the released electrons to give a negatively charged hydride (H−), which adsorbs at the sulfur vacancy. The negatively charged hydride triggers the hydrogenation of the nitro group in the 4-NP molecule through the following three-step sequence: the nitro group is first converted to the nitroso group [reaction (3)], which is then reduced to a hydroxylamine species [reaction (4)] and finally to the amino group [reaction (5)]. The overall reaction is illustrated at the bottom.

Under the proposed mechanism, the catalytic activity of a MoS_2 NS would be largely determined by the availability of stable adsorption sites for the H^- species. For a sulfur vacancy-free NS, the pristine basal plane would be inert and only the edges would be expected to exhibit some activity, as the latter also possess unsaturated molybdenum atoms where the hydride could be stabilized. When sulfur vacancies are introduced in the NS, stable adsorption sites become available at its basal plane, which should result in a catalyst with a higher overall activity, as it was indeed observed here. Furthermore, the degree of stabilization of the hydride at the vacancies, and thus the actual contribution of these defects to the increased catalytic activity, should depend on the specific vacancy configuration as outlined above (i.e., vacancy concentration, spatial distribution and/or type). Thus, MoS_2 NSs with different vacancy configurations (generated, e.g., by hydrazine treatments of varied intensity) can be expected to possess distinct catalytic activities. Although the detailed atomic structure of the vacancy defects in our hydrazine-treated samples remains unknown at this time, making it difficult to understand the ultimate cause of their different activities, we note that sample MoS_2-10% displayed a weaker EPR signal than that of sample MoS_2-4% (Fig. 3e). This implies that the former should possess a smaller number of unsaturated molybdenum atoms and, according to the above mechanism, a smaller number of sites for hydride stabilization than the latter. Consequently, it should exhibit a lower catalytic activity, which was indeed in agreement with our results (Fig. 4c).

4. Conclusions

An effective strategy for the wet-chemical activation of two-dimensional MoS_2 NSs towards the catalytic reduction of nitroarenes (4-nitrophenol, 4-nitroaniline) and organic dyes (methyl orange, methylene blue) has been demonstrated. Such an activation relied on the mild treatment of solvent-dispersed NSs with hydrazine, which was thought to trigger the generation of sulfur vacancies on their surface as highly active catalytic sites for the investigated reduction reactions. By carefully controlling the treatment conditions (mainly, the amount of hydrazine used and choice of a moderate treatment temperature), activated NSs having catalytic activities for nitroarene/dye reduction with $NaBH_4$ ~3-4 times higher than that of their untreated counterpart could be obtained, with values that were among the highest ever reported using non-noble metal-based catalysts. The poor colloidal stability of the bare MoS_2 NSs in aqueous medium, which was highly detrimental to their sustained catalytic performance, could be overcome by resorting to a proper dispersant, namely, the RNA nucleotide guanosine monophosphate. Significantly, the use of this stabilizer did not critically compromise the catalytic activity of the hydrazine-treated NSs. The activated NSs could also be immobilized onto melamine foam, thus facilitating their handling and re-utilization as demonstrated by their sustained activity in consecutive catalytic cycles. The central role played by sulfur vacancies in enhancing the catalytic performance of the hydrazine-treated MoS_2 NSs was made apparent by passivating such defects with alkylthiol molecules, which led to substantially deactivated catalysts. Finally, a mechanism for the reduction of nitroarenes/dyes with $NaBH_4$ at the activated MoS_2 NSs, which relied on the formation and stabilization of hydride species at sulfur vacancy defects, was proposed and discussed. Overall, the present work should strengthen the prospects of two-dimensional MoS_2 as a competitive and inexpensive catalyst for use in industrial reactions

of environmental relevance (e.g., treatment of wastewater effluents polluted by nitroarenes and/or dyes).

Acknowledgements

Funding by the Spanish Ministerio de Economía y Competitividad (MINECO) and the European Regional Development Fund (ERDF) through project MAT2015-69844-R, the Spanish Ministerio de Ciencia, Innovación y Universidades (MICINN), Agencia Estatal de Investigación (AEI) and the ERDF through project RTI2018-100832-B-I00, and Plan de Ciencia, Tecnología e Innovación (PCTI) 2013-2017 del Principado de Asturias and the ERDF (project IDI/2018/000233) is gratefully acknowledged. S.G.-D. is grateful to the Spanish MINECO for his pre-doctoral contract (BES/2016 077830). A.A. acknowledges the financial support from Spanish MINECO (MAT2016-78155-C2-1-R) and the Government of the Principality of Asturias (GRUPIN-IDI/2018/170).

Appendix A. Supplementary data

Supplementary material related to this article can be found, in the online version, at doi: 10.1016/j.apmt.2020.100678

Data availability

The data that support the findings of this study are available from the corresponding authors,

J. I. P and S. V.-R., upon reasonable request.

References

[1] W. Choi, N. Choudhary, G.H. Han, J. Park, D. Akinwande, Y.H. Lee, Recent development of two-dimensional transition metal dichalcogenides and their applications, Mater. Today 20 (2017), 116-130.

[2] Z. Wei, B. Li, C. Xia, Y. Cui, J. He, J.-B. Xia, J. Li, Various structures of 2D transition-metal dichalcogenides and their applications, Small Methods 2 (2018), 1800094.

[3] D. Deng, K.S. Novoselov, Q. Fu, N. Zheng, Z. Tian, X. Bao, Catalysis with two-dimensional materials and their heterostructures, Nat. Nanotechnol. 11 (2016), 218-230.

[4] X. Chia, M. Pumera, Characteristics and performance of two-dimensional materials for electrocatalysis, Nat. Catal. 1 (2018), 909-921.

[5] C. Zhu, D. Gao, J. Ding, D. Chao, J. Wang, TMD-based highly efficient electrocatalysts developed by combined computational and experimental approaches, Chem. Soc. Rev. 47 (2018), 4332-4356.

[6] P. Grange, B. Delmon, The role of cobalt and molybdenum sulphides in hydrodesulphurisation catalysts: a review, J. Less-Common Met. 36 (1974), 353-360.

[7] F. Delannay, High resolution electron microscopy of hydrodesulfurization catalysts: a review, Appl. Catal. 16 (1985), 135-152.

[8] Q. Fu. X. Bao, Surface chemistry and catalysis confined under two-dimensional materials, Chem. Soc. Rev. 46 (2017), 1842-1874.

[9] S. Jayabal, G. Saranya, J. Wu, Y. Liu, D. Geng, X. Meng, Understanding the high-electrocatalytic performance of two-dimensional MoS_2 nanosheets and their composite materials, J. Mater. Chem. A 5 (2017), 24540-24563.

[10] A. Primo, J. He, B. Jurca, B. Cojocaru, C. Bucur, V.I. Parvulescu, H. Garcia, CO_2 methanation catalyzed by oriented MoS_2 nanoplatelets supported on few layers graphene, Appl. Catal. B: Environ. 245 (2019), 351-359.

[11] L. Guardia, J.I. Paredes, J.M. Munuera, S. Villar-Rodil, M. Ayán-Varela, A. Martínez-Alonso, J.M.D. Tascón, Chemically exfoliated MoS_2 nanosheets as an efficient catalyst for reduction reactions in the aqueous phase, ACS Appl. Mater. Interfaces 6 (2014), 21702-21710.

[12] T. Lin, J. Wang, L. Guo, F. Fu, Fe_3O_4@MoS_2 core-shell composites: preparation, characterization and catalytic application, J. Phys. Chem. C 119 (2015), 13658-13664.

[13] K. Peng, L. Fu, J. Ouyang, H. Yang, Emerging parallel dual 2D composites: natural clay mineral hybridizing MoS_2 and interfacial structure, Adv. Funct. Mater. 26 (2016), 2666-2675.

[14] A.A. Jeffery, S.R. Rao, M. Rajamathi, Preparation of MoS_2-reduced graphene oxide (rGO) hybrid paper for catalytic applications by simple exfoliation-costacking, Carbon 112 (2017), 8-16.

[15] K. Peng, L. Fu, H. Yang, J. Ouyang, A. Tang, Hierarchical MoS_2 intercalated clay hybrid nanosheets with enhanced catalytic activity, Nano Res. 10 (2017), 570-583.

[16] N. Meng, J. Cheng, Y. Zhou, W. Nie, P. Chen, Green synthesis of layered 1T-MoS_2/reduced graphene oxide nanocomposite with excellent catalytic performances for 4-nitrophenol reduction, Appl. Surf. Sci. 396 (2017), 310-318.

[17] C. Nethravathi, J. Prabhu, S. Lakshmipriya, M. Rajamathi, Magnetic Co-doped MoS_2 nanosheets for efficient catalysis of nitroarene reduction, ACS Omega 2 (2017), 5891-5897.

[18] Y. Li, Q. Chen, Z. Zhang, Q. Li, X. Qiao, Effects of morphology and crystallinity of MoS_2 nanocrystals on the catalytic reduction of p-nitrophenol, J. Nanopart. Res. 20 (2018), 327.

[19] C. Nethravathi, A.D. Manganahalli, M. Rajamathi, Bi_2Te_3-MoS_2 layered nanoscale heterostructures for electron transfer catalysis, ACS Appl. Nano Mater. 2 (2019), 2005-2012.

[20] P. Hervés, M. Pérez-Lozano, L.M. Liz-Marzán, J. Dzubiella, Y. Lubc, M. Ballauf, Catalysis by metallic nanoparticles in aqueous solution: model reactions, Chem. Soc. Rev. 41 (2012), 5577-5587.

[21] T. Aditya, A. Pal, T. Pal, Nitroarene reduction: a trusted model reaction to test nanoparticle catalysts, Chem. Commun. 51 (2015), 9410-9431.

[22] H. Hu, J.H. Xin, H. Hu, X. Wang, D. Miao, Y. Liu, Synthesis and stabilization of metal nanocatalysts for reduction reactions – a review, J. Mater. Chem. A 3 (2015), 11157-11182.

[23] K. Zhang, J.M. Suh, J.-W. Choi, H.W. Jang, M. Shokouhimehr, R.S. Varma, Recent advances in the nanocatalyst-assisted $NaBH_4$ reduction of nitroaromatics in water, ACS Omega 4 (2019), 483-495.

[24] Z. Xiong, H. Zhang, W. Zhang, B. Lai, G. Yao, Removal of nitrophenols and their derivatives by chemical redox: a review, Chem. Eng. J. 359 (2019), 13-31.

[25] M. Shahid, Z. H. Farooqi, R. Begum, M. Arif, W. Wu, A. Irfan, Hybrid microgels for catalytic and photocatalytic removal of nitroarenes and organic dyes from aqueous medium: a review. Crit. Rev. Anal. Chem. (2019) DOI: 10.1080/10408347.2019.1663148

[26] R. Begum, J. Najeeb, A. Sattar, K. Naseem, A. Irfan, A. G. Al-Sehemi, Z. H. Farooqi, Chemical reduction of methylene blue in the presence of nanocatalysts: a critical review. Rv. Chem. Eng. (2019) DOI: 10.1515/revce-2018-0047

[27] M.M. Khan, J. Lee, M.H. Cho, Au@TiO_2 nanocomposites for the catalytic degradation of methyl orange and methylene blue: an electron relay effect, J. Ind. Eng. Chem. 20 (2014), 1584-1590.

[28] S. Li, H. Li, J. Liu, H. Zhang, Y. Yang, Z. Yang, L. Wang, B. Wang, Highly efficient degradation of organic dyes by palladium nanoparticles decorated on 2D magnetic reduced graphene oxide nanosheets, Dalton Trans. 44 (2015), 9193-9199.

[29] Z. Medříková, P. Jakubec, V. Ranc, A. Bakandritsos, J. Kašlík, R. Zbořil, Carboxymethylcellulose-based magnetic Au or Ag nanosystems: Eminent candidates in catalysis, sensing applications based on SERS, and electrochemistry, Appl. Mat. Today 14 (2019), 143–150.

[30] R. Begum, Z. H. Farooqi, A. H. Aboo, E. Ahmed, A. Sharif, J. Xiao, Reduction of nitroarenes catalyzed by microgel-stabilized silver nanoparticles, J. Hazard. Mater. 377 (2019), 399-408.

[31] J. Xia, G. He, L. Zhang, X. Sun, X. Wang, Hydrogenation of nitrophenols catalyzed by carbon black-supported nickel nanoparticles under mild conditions, Appl. Catal. B: Environ. 180 (2016), 408-415.

[32] C. Chu, S. Rao, Z. Ma, H. Han, Copper and cobalt nanoparticles doped nitrogen-containing carbon frameworks derived from CuO-encapsulated ZIF-67 as high-efficiency catalyst for hydrogenation of 4-nitrophenol, Appl. Catal. B: Environ. 256 (2019), 117792.

[33] Y. Jiao, A.M. Hafez, D. Cao, A. Mukhopadhyay, Y. Ma, H. Zhu, Metallic MoS_2 for high performance energy storage and energy conversion, Small 14 (2018), 1800640.

[34] S. Shi, Z. Sun, Y.H. Hu, Synthesis, stabilization and applications of 2-dimensional 1T metallic MoS_2, J. Mater. Chem. A 6 (2018), 23932-23977.

[35] Z Wang, Y.-J. Zhang, M. Liu, A. Peterson, R. H. Hurt, Oxidation suppression during hydrothermal phase reversion allows synthesis of monolayer semiconducting MoS_2 in stable aqueous suspension, Nanoscale 9 (2017) 5398-5403.

[36] T.-W. Lee, C.-C. Chen, C. Chen, Chemical stability and transformation of molybdenum disulfide nanosheets in environmental media, Environ. Sci. Technol. 53 (2019), 6282-6291.

[37] J.I. Paredes, J.M. Munuera, S. Villar-Rodil, L. Guardia, M. Ayán-Varela, A. Pagán, S.D. Aznar-Cervantes, J.L. Cenis, A. Martínez-Alonso, J.M.D. Tascón, Impact of covalent functionalization on the aqueous processability, catalytic activity, and biocompatibility of chemically exfoliated MoS_2 nanosheets, ACS Appl. Mater. Interfaces 8 (2016), 27974-27986.

[38] J.N. Coleman, M. Lotya, A. O´Neill, S.D. Bergin, P.J. King, U. Khan, K. Young, A. Gaucher, S. De, R.J. Smith, I.V. Shvets, S.K. Arora, G. Stanton, H.-Y. Kim, K. Lee, G.T. Kim, G.S. Duesberg, T. Hallam, J.J. Boland, J.J. Wang, J.F. Donegan, J.C. Grunlan, G. Moriarty, A. Shmeliov, R.J. Nicholls, J.M. Perkins, E.M. Grieveson, K. Theuwissen, D.W. McComb, P.D. Nellist, V. Nicolosi, Two-dimensional nanosheets produced by liquid exfoliation of layered materials, Science 331 (2011), 568-571.

[39] R.J. Smith, P.J. King, M. Lotya, C. Wirtz, U. Khan, S. De, A. O´Neill, G.S. Duesberg, J.C. Grunlan, G. Moriarty, J. Chen, J. Wang, A.I. Minett, V. Nicolosi, J.N. Coleman, Large-scale exfoliation of inorganic layered compounds in aqueous surfactant solution, Adv. Mater. 23 (2011), 3944-3948.

[40] E. Varrla, C. Backes, K.R. Paton, A. Harvey, Z. Gholamvand, J. McCauley, J.N. Coleman, Large-scale production of size-controlled MoS_2 nanosheets by shear exfoliation, Chem. Mater. 27 (2015), 1129-1139.

[41] M. Ayán-Varela, Ó. Pérez-Vidal, J.I. Paredes, J.M. Munuera, S. Villar-Rodil, M. Díaz-González, C. Fernández- Sánchez, V.S. Silva, M. Cicuéndez, M. Vila, A. Martínez-Alonso, J.M.D. Tascón, Aqueous exfoliation of transition metal dichalcogenides assisted by DNA/RNA nucleotides: catalytically active and biocompatible nanosheets stabilized by acid-base interactions, ACS Appl. Mater. Interfaces 9 (2017), 2835-2845.

[42] H. Li, C. Tsai, A.L. Koh, L. Cai, A.W. Contryman, A.H. Fragapane, J. Zhao, H.S. Han, H.C. Manoharan, F. Abild-Pedersen, J.K. N¢rskov, X. Zheng, Activating and optimizing MoS_2 basal planes for hydrogen evolution through the formation of strained sulphur vacancies, Nat. Mater. 15 (2016), 48-53.

[43] S. Wang, A. Robertson, J.H. Warner, Atomic structure of defects and dopants in 2D layered transition metal dichalcogenides, Chem. Soc. Rev. 47 (2018), 6764-6794.

[44] S. García-Dalí, J.I. Paredes, J.M. Munuera, S. Villar-Rodil, A. Adawy, A. Martínez-Alonso, J.M.D. Tascón, Aqueous cathodic exfoliation strategy toward solution-processable and phase-preserved MoS_2 nanosheets for energy storage and catalytic applications, ACS Appl. Mater. Interfaces 11 (2019), 36991-37003.

[45] C. Backes, R.J. Smith, N. McEvoy, N.C. Berner, D. McCloskey, H.C. Nerl, A. O´Neill, P.J. King, T. Higgins, D. Hanlon, N. Scheuschner, J. Maultzsch, L. Houben, G.S. Duesberg, J.F. Donegan, V. Nicolosi, J.N. Coleman, Edge and confinement effects allow in situ measurement of size and thickness in liquid-exfoliated nanosheets, Nat. Commun. 5 (2014), 4576.

[46] H. Nan, Z. Wang, W. Wang, Z. Liang, Y. Lu, Q. Chen, D. He, P. Tan, F. Miao, X. Wang, J. Wang, Z. Ni, Strong photoluminescence enhancement of MoS_2 through defect engineering and oxygen bonding, ACS Nano 8 (2014), 5738-5745.

[47] C.-C. Cheng, A.-Y. Lu, C.-C. Tseng, X. Yang, M.N. Hedhili, M.-C. Chen, K.-H. Wei, L.-J. Li, Activating basal-plane catalytic activity of two-dimensional MoS_2 monolayer with remote hydrogen plasma, Nano Energy 30 (2016), 846-852.

[48] M. Ghorbani-Asl, S. Kretschmer, D.E. Spearot, A.V. Krasheninikov, Two-dimensional MoS_2 under ion irradiation: from controlled defect production to electronic structure engineering, 2D Mater. 4 (2017), 025078.

[49] Z. He, R. Zhao, X. Chen, H. Chen, Y. Zhu, H. Su, S. Huang, J. Xue, J. Dai, S. Cheng, M. Liu, X. Wang, Y. Chen, Defect engineering in single-layer MoS_2 using heavy ion irradiation, ACS Appl. Mater. Interfaces 10 (2018), 42524-42533.

[50] M. Donarelli, F. Bisti, F. Perrozzi, L. Ottaviano, Tunable sulfur desorption in exfoliated MoS_2 by means of thermal annealing in ultra-high vacuum, Chem. Phys. Lett. 588 (2013), 198-202.

[51] C. Tsai, H. Li, S. Park, J. Park, H.S. Han, J.K. N¢rskov, X. Zheng, F. Abild-Pedersen, Electrochemical generation of sulfur vacancies in the basal plane of MoS_2 for hydrogen evolution, Nat. Commun. 8 (2017), 15113.

[52] T. Daeneke, R.M. Clark, B.J. Carey, J.Z. Ou, B. Weber, M.S. Fuhrer, M. Bhaskaran, K. Kalantar-zadeh, Reductive exfoliation of substoichiometric MoS_2 bilayers using hydrazine salts, Nanoscale 8 (2016), 15252-15261.

[53] C. Wei, W. Wu, H. Li, X. Lin, T. Wu, Y. Zhang, Q. Xu, L. Zhang, Y. Zhu, X. Yang, Z. Liu, Q. Xu, Atomic plane-vacancy engineering of transition-metal dichalcogenides with

enhanced hydrogen evolution capability, ACS Appl. Mater. Interfaces 11 (2019), 25264-25270.

[54] J. Zhang, Y. Wang, J. Cui, J. Wu, Y. Li, T. Zhu, H. Kang, J. Yang, J. Sun, Y. Qin, Y. Zhang, P.M. Ajayan, Y. Wu, Water-soluble defect-rich MoS_2 ultrathin nanosheets for enhanced hydrogen evolution, J. Phys. Chem. Lett. 10 (2019), 3282-3289.

[55] K.F. Mak, C. Lee, J. Hone, J. Shan, T.F. Heinz, Atomically thin MoS_2: a new direct-gap semiconductor, Phys. Rev. Lett. 105 (2010), 136805.

[56] G. Eda, H. Yamaguchi, D. Voiry, T. Fujita, M. Chen, M. Chhowalla, Photoluminiscence from chemically exfoliated MoS_2, Nano Lett. 11 (2011), 5111-5116.

[57] Z. Lei, J. Zhan, L. Tang, Y. Zhang, Y. Wang, Recent development of metallic (1T) phase of molybdenum disulfide for energy conversion and storage, Adv. Energy Mater. 8 (2018), 1703482.

[58] L. Cai, J. He, Q. Liu, T. Yao, L. Chen, W. Yan, F. Hu, Y. Jiang, Y. Zhao, T. Hu, Z. Sun, S. Wei, Vacancy-induced ferromagnetism of MoS_2 nanosheets, J. Am. Chem. Soc. 137 (2015), 2622-2627.

[59] L. Li, Z. Qin, L. Ries, S. Hong, T. Michel, J. Yang, C. Salameh, M. Bechelany, P. Miele, D. Kaplan, M. Chhowalla, D. Voiry, Role of sulfur vacancies and undercoordinated Mo regions in MoS_2 nanosheets toward the evolution of hydrogen, ACS Nano 13 (2019), 6824-6834.

[60] J.R. González, R. Alcántara, J.L. Tirado, A.J. Fielding, R.A.W. Dryfe, Electrochemical interaction of few-layer molybdenum disulfide composites vs sodium: new insights on the reaction mechanism, Chem. Mater. 29 (2017), 5886-5895.

[61] J.G. Smith, P.K. Jain, The ligand shell as an energy barrier in surface reactions on transition metal nanoparticles, J. Am. Chem. Soc. 138 (2016), 6765-6773.

[62] J. Kim, S. Kwon, D.-H. Cho, B. Kang, H. Kwon, Y. Kim, S.O. Park, G.Y. Jung, E. Shin, W.-G. Kim, H. Lee, G.H. Ryu, M. Choi, T.H. Kim, J. Oh, S. Park, S.K. Kwak, S.W. Yoon, D. Byun, Z. Lee, C. Lee, Direct exfoliation and dispersion of two-dimensional materials in pure water via temperature control, Nat. Commun. 6 (2015), 8294.

[63] V. Forsberg, R. Zhang, J. Bäckström, C. Dahlström, B. Andres, M. Norgren, M. Andersson, M. Hummelgård, H. Olin, Exfoliated MoS_2 in water without additives, PLoS ONE 11 (2016), e0154522.

[64] E.D. Grayfer, M.N. Kozlova, V.E. Fedorov, Colloidal 2D nanosheets of MoS_2 and other transition metal dichalcogenides through liquid-phase exfoliation, Adv. Colloid Interface Sci. 245 (2017), 40-61.

[65] H. Qiu, T. Xu, Z. Wang, W. Ren, H. Nan, Z. Ni, Q. Chen, S. Yuan, F. Miao, F. Song, G. Long, Y. Shi, L. Sun, J. Wang, X. Wang, Hopping transport through defect-induced localized states in molybdenum disulfide, Nat. Commun. 4 (2013), 2642.

[66] S. Harris, R.R. Chianelli, Theoretical studies of transition metal sulfide hydrodesulfurization catalysts, in J.B. Moffat (ed.), Theoretical aspects of heterogeneous catalysts, Van Nostrand Reinhold, New York, 1990, ch. 6.

[67] M.V. Bollinger, J.V. Lauritsen, K.W. Jacobsen, J.K. Nørskov, S. Helveg, F. Besenbacher, One-dimensional metallic edge states in MoS_2, Phys. Rev. Lett. 87 (2001), 196803.

[68] C. Zhang, A. Johnson, C.-L. Hsu, L.-J. Li, C.-K. Shih, Direct imaging of band profile in single layer MoS_2 on graphite: quasiparticle energy gap, metallic edge states, and edge band bending, Nano Lett. 14 (2014), 2443-2447.

[69] Y. Sun, A.J. Darling, Y. Li, K. Fujisawa, C.F. Holder, H. Liu, M.J. Janik, M. Terrones, R.E. Schaak, Defect-mediated selective hydrogenation of nitroarenes on nanostructured WS_2, Chem. Sci. 10 (2019), 10310-10317.

[70] M. Makarova, Y. Okawa, M. Aono, Selective adsorption of thiol molecules at sulfur vacancies on MoS_2(0001), followed by vacancy repair via S-C dissociation, J. Phys. Chem. C 116 (2012), 22411-22416.

[71] Z. Yu, Y. Pan, Y. Shen, Z. Wang, Z.-Y. Ong, T. Xu, R. Xin, L. Pan, B. Wang, L. Sun, J. Wang, G. Zhang, Y.W. Zhang, Y. Shi, X. Wang, Towards intrinsic charge transport in monolayer molybdenum disulfide by defect and interface engineering, Nat. Commun. 5 (2014), 5290.

[72] K. Cho, M. Min, T.-Y. Kim, H. Jeong, J. Pak, J.-K. Kim, J. Jang, S.J. Yun, Y.H. Lee, W.-K. Hong, T. Lee, Electrical and optical characterization of MoS_2 with sulfur vacancy passivation by treatment with alkanethiol molecules, ACS Nano 9 (2015), 8044-8053.

[73] Q. Li, Y. Zhao, C. Ling, S. Yuan, Q. Chen, J. Wang, Towards a comprehensive understanding of the reaction mechanisms between defective MoS_2 and thiol molecules, Angew. Chem. Int. Ed. 56 (2017), 10501-10505.

[74] A. Förster, S. Gemming, G. Seifert, D. Tománek, Chemical and electronic repair mechanism of defects in MoS_2 monolayers, ACS Nano 11 (2017), 9989-9996.

[75] E.Y. Marrero-Alfonso, A.M. Beaird, T.A. Davis, M.A. Matthews, Hydrogen generation from chemical hydrides, Ind. Eng. Chem. Res. 48 (2009), 3702-3712.

[76] J. Andrieux, U.B. Demirci, J. Hannauer, C. Gervais, C. Goutaudier, P. Miele, Spontaneous hydrolysis of sodium borohydride in harsh conditions, Int. J. Hydrogen Energy 36 (2011), 224-233.

[77] S.W. Han, G.-B. Cha, Y. Park, S.C. Hong, Hydrogen physisorption based on the dissociative hydrogen chemisorption at the sulphur vacancy of MoS_2 surface, Sci. Rep. 7 (2017), 7152.

[78] N.P. Rezende, A.R. Cadore, A.C. Gadelha, C.L. Pereira, V. Ornelas, K. Watanabe, T. Taniguchi, A.S. Ferlauto, A. Malachias, L.G. Campos, R.G. Lacerda, Probing the electronic properties of monolayer MoS_2 via interaction with molecular hydrogen, Adv. Electron. Mater. 5 (2019), 1800591.

[79] B.M. Concha, M. Chatenet, C. Coutanceau, F. Hahn, In situ infrared (FTIR) study of the borohydride oxidation reaction, Electrochem. Commun. 11 (2009), 223-226.

[80] D.A. Finkelstein, N. Da Mota, J.L. Cohen, H.D. Abruña, Rotating disk electrode (RDE) investigation of BH_4^- and BH_3OH^- electro-oxidation at Pt and Au: implications for BH_4^- fuel cells, J. Phys. Chem. C 113 (2009), 19700-19712.

[81] Y. Fu, T. Huang, B. Jia, J. Zhu, X. Wang, Reduction of nitrophenols to aminophenols under concerted catalysis by Au/g-C_3N_4 contact system, Appl. Catal. B: Environ. 202 (2017), 430-437.

[82] Y. Cai, Z. Bai, H. Pan, Y.P. Feng, B.I. Yakobson, Y.-W. Zhang, Constructing metallic nanoroads on a MoS_2 monolayer via hydrogenation, Nanoscale 6 (2014), 1691-1697.

[83] S. Bae, S. Gim, H. Kim, K. Hanna, Effect of $NaBH_4$ on properties of nanoscale zero-valent iron and its catalytic activity for reduction of *p*-nitrophenol, Appl. Catal. B: Environ. 182 (2016), 541-549.

Supplementary material for

Activation of two-dimensional MoS_2 nanosheets by wet-chemical sulfur vacancy engineering for the catalytic reduction of nitroarenes and organic dyes

S. García-Dalí[a], J.I. Paredes[a,*], B. Caridad[a], S. Villar-Rodil[a,*], M. Díaz-González[b], C. Fernández-Sánchez[b], A. Adawy[c], A. Martínez-Alonso[a], J.M.D. Tascón[a]

[a]*Instituto Nacional de Ciencia y Tecnología del Carbono, C/Francisco Pintado Fe 26, 33011 Oviedo, Spain*

[b]*Instituto de Microelectrónica de Barcelona, IMB-CNM (CSIC), Campus UAB, 08193 Bellaterra, Barcelona, Spain*

[c]*Laboratory of High-Resolution Transmission Electron Microscopy, Institute for Scientific and Technological Resources, University of Oviedo, 33006 Oviedo, Spain*

Corresponding authors:

E-mail addresses:

paredes@incar.csic.es (J. I. Paredes), silvia@incar.csic.es (S. Villar-Rodil).

Table of contents

S1. Preparation of activated MoS_2 nanosheets: control experiments

As explained in the main text, after mixing the MoS_2 suspension with the reducing agent (hydrazine monohydrate) and heating at 70 ºC, some convection developed in the liquid and, several minutes later, the MoS_2 nanosheets started to agglomerate and sediment. At the same time small gas bubbles were seen to rise through the liquid. The following control experiments allowed concluding that the gas bubbles were generated as a result of reactions between the MoS_2 nanosheets and the reducing agent

1) When the MoS_2 dispersion was heated in the absence of hydrazine monohydrate, no bubbles or nanosheet agglomeration were noticed.

2) When a solution of the reductant in isopropanol was heated in the absence of MoS_2, no bubbles formed.

3) When hydrazine monohydrate was added to isopropanol containing a large amount of bulk MoS_2 powder at the bottom of the heated test tube, gas bubbles were seen to arise directly from the MoS_2 material.

S2. Characterization of hydrazine-treated MoS_2 nanosheets

S2.1 Microscopic characterization

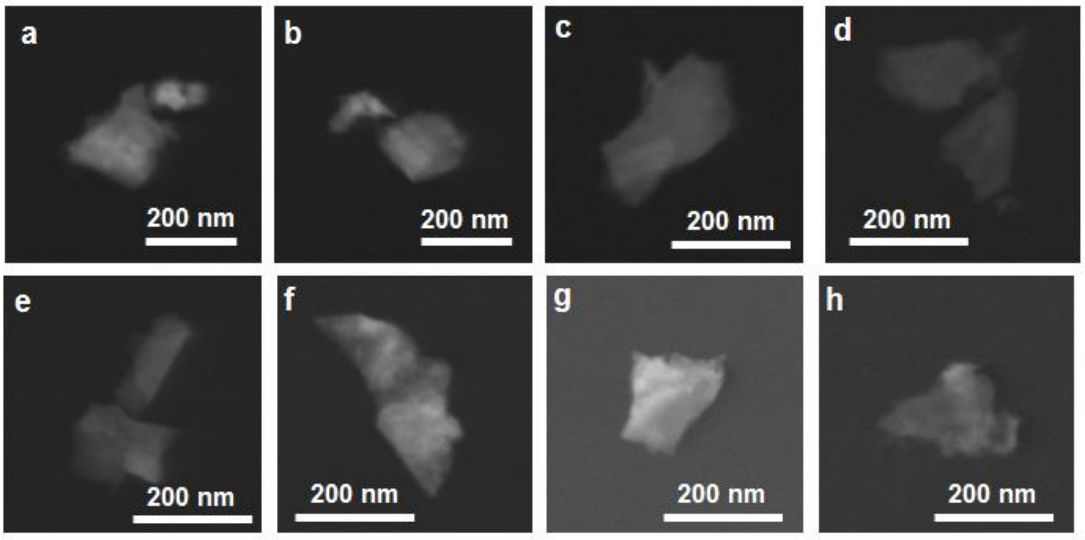

Figure S1. Morphology of the MoS_2 nanosheets after hydrazine treatment. Typical STEM images of flakes deposited from dispersions of: **(a, b)** MoS_2-2%, **(c, d)** MoS_2-4%, **(e, f)** MoS_2-6% and **(g, h)** MoS_2-10%.

S2.2 Spectroscopic characterization

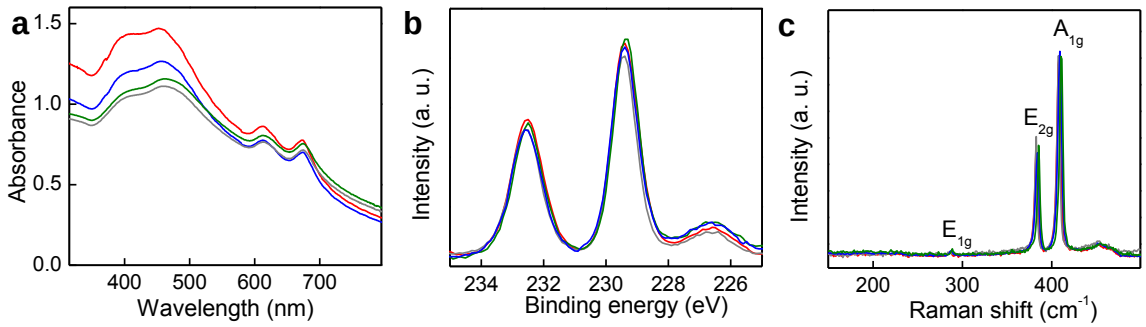

Figure S2. Spectroscopic characterization of the hydrazine-treated MoS_2 nanosheets. **(a)** UV-vis absorption spectra of MoS_2 dispersions in isopropanol. **(b)** High resolution XPS Mo 3d and S 2s core level spectra and **(c)** Raman spectra of MoS_2 films drop-cast from the corresponding dispersions. Color code: MoS_2-1% (gray trace), MoS_2-4% (red trace), MoS_2-6% (green trace), and MoS_2-10% (blue trace).

Explanation on the lack of transformation from 2H to 1T phase upon reducing treatment

We note that the prospect of a 2H to 1T phase transformation upon hydrazine treatment in the MoS_2 NSs was not unreasonable. In fact, this transformation is known to be triggered by the build-up of excess electrons in the MoS_2 lattice [1,2] and a reducing agent like hydrazine can potentially donate electronic charge to the MoS_2 NSs [3]. On the flip side, the 2H to 1T phase conversion in the MoS_2 NSs can also be brought about by the presence of sulfur vacancies at a sufficiently large concentration [4,5]. However, such a phase conversion did not take place under the present conditions. It is quite likely that a much stronger reducing environment (e.g., the well-known treatment with *n*-butyllithium in *n*-hexane) and/or larger numbers of sulfur vacancies are required to induce the structural phase transition in the material (the XPS S/Mo ratios of our hydrazine-treated materials indicate that moderate total numbers of sulfur vacancies are generated in this case).

Limitations of the determination of S/Mo atomic ratios by XPS

We note that the accuracy in determining atomic ratios by the XPS technique is somewhat limited. Therefore, making out differences between samples that have similar ratios (e.g., within 5%) is probably unrealistic. However, this did not prevent the technique from

revealing a clear trend of decreasing S/Mo atomic ratio with increasing intensity of the hydrazine treatment.

S3. Additional data on the use of hydrazine-treated MoS_2 nanosheets as catalysts of reduction reactions

S3.1 Induction period

Although not shown in Fig. 4b of the main text, an initial induction period of a few to several minutes was usually observed in the kinetic profiles for the reduction 4-NP with hydrazine, during which the absorbance value remained constant or changed very little. Fig. S3a shows the initial part of the recorded profiles including the induction period. Such an induction period has been attributed to oxidation of the reaction product back to 4-NP by oxygen molecules dissolved in the reaction solution, so that the concentration of 4-NP (and hence the absorbance at 400 nm) will only start to decline at a significant rate after all the dissolved oxygen is exhausted and a net conversion of 4-NP to 4-AP sets in [6]. The fact that shorter induction periods tended to be associated to those samples boasting shorter times to reaction completion (see combined results from Figs. 4b in the main text and S3a below) is in agreement with this interpretation, because the faster the rate of 4-NP reduction, the faster the consumption of dissolved oxygen can be expected to occur.

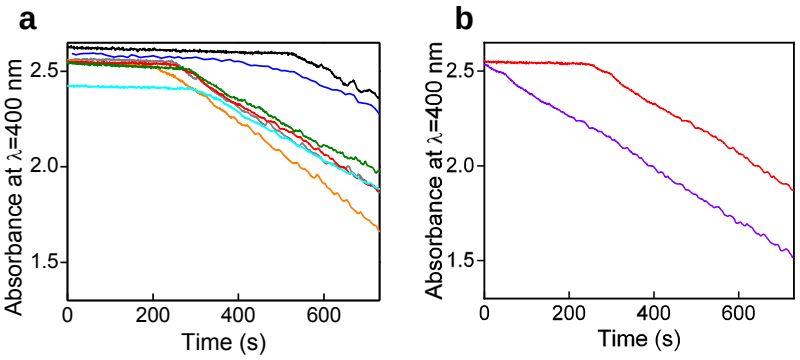

Figure S3. Induction period for the reduction of 4-NP using hydrazine-treated MoS_2 as catalyst. (a) Initial part of the kinetic profiles (including the induction period) for the reduction of 4-NP using the starting MoS_2 nanosheets (NSs) (black trace), MoS_2-1% (gray trace), MoS_2-2% (orange trace), MoS_2-4% (red trace), MoS_2-6% (green trace), MoS_2-8% (cyan trace), and MoS_2-10% (blue trace) as catalyst. **(b)** Initial part of the kinetic profiles

for the reduction of 4-NP using MoS_2-4% as catalyst after removal of dissolved oxygen from the reaction medium.

Further support to this interpretation was provided by control experiments where dissolved gases were swept away from the reaction medium. This was done by bubbling an inert gas (nitrogen) flow for half an hour through both the catalyst dispersion and the reagents solution before mixing them. Indeed, the induction period disappeared after oxygen was removed from the reaction medium, as can be seen in Fig. S3b, thus confirming its effect.

S3.2. Monitoring of different reduction reactions

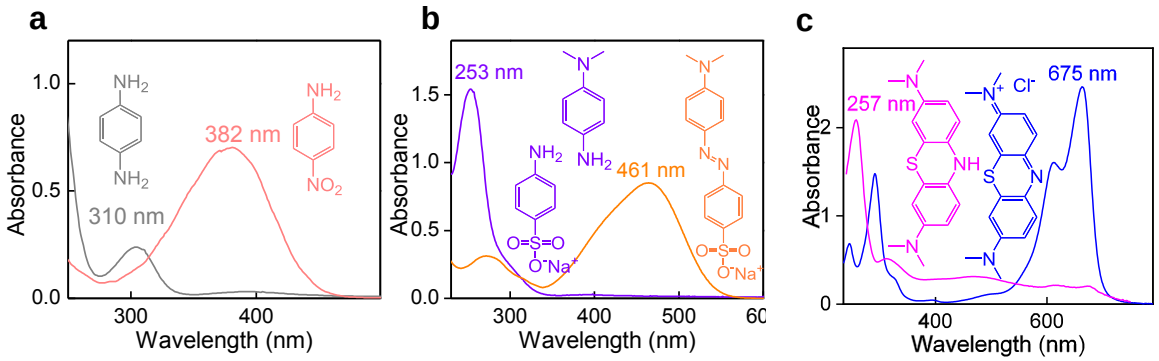

Figure S4. UV-Vis absorption spectra of the reagents and products of different reduction reactions. Chemical structures and UV-vis absorption spectra obtained before and after the different reduction reactions where the hydrazine treated MoS_2 NSs were tested as catalysts: **(a)** 4-nitroaniline (sepia trace) and p-phenylendiamine (gray trace); **(b)** methyl orange (orange trace) is first reduced to the corresponding azo product (not shown) [7], which is followed by -HN-NH- bond dissociation to yield N,N-dimethyl-benzene-1,4-diamine and 4-amino-benzenesulfonate (violet trace) [8]; **(c)** methylene blue (blue trace) and its reduction product, leucomethylene blue (magenta trace) [9,10]. The wavelengths at the maxima of the substrates and their reduced counterparts are indicated in the figures. In all cases, the wavelength at the maximum of a band characteristic of the substrate was chosen to monitor the reduction reactions.

The combined results of Fig. 4a of the main text and Fig. S5a below confirm the gradual conversion of 4-nitrophenolate into 4-aminophenol. Indeed, the UV–vis spectrum of the catalytic media gradually transforms from that of 4-nitrophenolate to that characteristic of the reduced product (see Fig. 4a). The gradual decrease in the intensity of the absorption

band centered at ~400 nm (characteristic of 4-nitrophenolate, see Fig. 4a) and the simultaneous increase in the intensity of that centered ~ 295 nm (characteristic of the reduced product, see Fig. 4a) are indicated by the arrows in Fig. S5a for clarity. Analogously, the combined results of Fig. S4a and Fig. S5b, Fig. S4b and Fig. S5c, and Fig S4c and S5d confirm the gradual conversion of 4-NA, MO and MB, respectively, into their corresponding reduced counterparts.

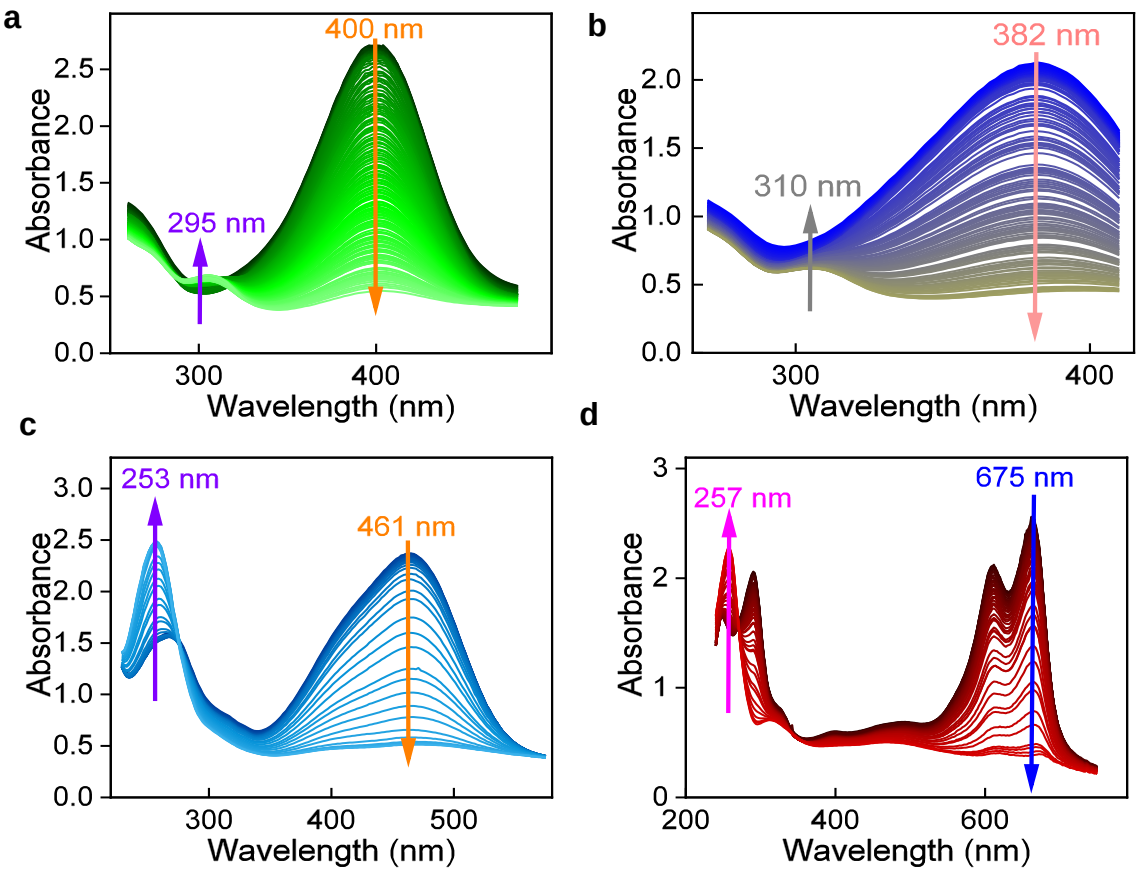

Figure S5. UV-Vis absorption monitoring of different benchmark reduction reactions. UV–vis spectra of the catalytic media for the reduction of **(a)** 4-NP, **(b)** 4-NA, **(c)** MO and **(d)** MB. As the reaction progresses, the UV-vis absoption spectra traces vary from dark to light green in (a), from blue to dark yellow in (b), from darker to lighter blue in (c), and from dark brown to red in (d). The absorption maxima corresponding to the substrates and their reduced counterparts (see Fig. 4a in the main text and S4 above) are labeled in the spectra for clarity. The arrows indicate the decreasing and increasing trend of their intensities, respectively.

S3.3. Fitting of the kinetic profiles and calculation of the apparent reaction rates

As long as the number of catalytic sites is large enough in relation to the number of reactant molecules, i. e., as long as the progress of the reaction is not limited by the number of free catalytic sites available, the reaction rate *v* of the catalytic reduction of 4-NP with $NaBH_4$ will depend on the concentrations of both reactants. This comes from the fact that the reactants have at least to meet for the reaction to occur. Such dependence is expressed as follows:

$$v = -\frac{d[4-NP]}{dt} = -\frac{d[NaBH_4]}{dt} = k[4-NP][NaBH_4] \quad (1)$$

, where *k* is the reaction rate constant. Hence, the global reaction order will be two. For a given [4-NP], the reaction rate *v* increases monotonically with [$NaBH_4$] until a plateau is reached [11] at certain concentration $[NaBH_4]_{plateau}$. This means that, above a certain [$NaBH_4$]/[4-NP] ratio, there will be always $NaBH_4$ molecules nearby any 4-NP available to react and thus the reaction rate will only depend on [4-NP]. Here, $NaBH_4$ was used in a sufficiently large excess to be within the plateau region and thus *v* is not dependent on the specific amount of reductant. Indeed, as specified in Materials and Methods section of the main text, [4-NP]=0.12 mM and [$NaBH_4$]=72 mM, i.e., there is a 1:600 ratio. $[NaBH_4]_{plateau}$, which remains approximately constant during the reaction, can be integrated into a new constant k_{app} so-called apparent reaction rate constant:

$$k_{app} = k[NaBH_4]_{plateau} \quad (2)$$

Thus, equation 1 can be rewritten as follows:

$$v = -\frac{d[4-NP]}{dt} = k_{app}[4-NP] \quad (3)$$

And the kinetics of the reduction of 4-NP can be considered as pseudo-first order, as long as the number of catalytic sites is large enough in relation to the number of reactant molecules, as we said above. Integrating equation 3 over the reaction time:

$$[4-NP]_f - [4-NP]_i = Ae^{-k_{app}t} \quad (4)$$

, where $[4\text{-NP}]_i$ and $[4\text{-NP}]_f$ are the 4-NP concentration at the initial and final instants of the reaction, respectively. This means that [4-NP] displays exponential decay dependence with time t for pseudo-first order kinetics. Thus, the apparent reaction rate constant k_{app} can be directly obtained as the exponent of the fitting [4-NP] vs. t data to an exponential decay function. Its units are of reciprocal time.

Here, we have monitored the progress of the reaction by following the variation in the absorbance at an adsorption maximum characteristic of 4-NP (λ=400 nm). By the Beer-Lambert's equation, we can correlate the absorbance value obtained at an absorption maximum (*Abs*) of 4-NP with its concentration by the Lambert-Beer's equation:

$$Abs = \varepsilon b[4\text{-}NP] \quad (5)$$

, where b is the optical path and ε is the extinction coefficient at the wavelength of the absorption maximum for 4-NP.

Thus, substituting (5) in (3):

$$\frac{1}{\varepsilon b}\frac{dAbs}{dt} = -k_{app}\frac{Abs}{\varepsilon b} \Longrightarrow \frac{dAbs}{dt} = -k_{app}Abs \quad (6)$$

And integrating over time:

$$Abs_f - Abs_i = A' e^{-k_{app}t} \quad (7)$$

, where Abs_i and Abs_f are the absorbance recorded at the beginning and the end of the reaction, respectively. As clearly seen, the expressions for the dependence of concentration and absorbance versus time (equations 4 and 7, respectively) are analogous. The rate constant k_{app} is the very same coefficient of the exponent found in the fitting of absorbance versus time, i. e., we can either fit the concentration or the absorbance to an exponential decay function to directly obtain k_{app}. As can be seen in Fig. 4b in the main text and Fig. S6a below, the temporal evolution of the absorbance of the starting, untreated MoS_2 nanosheets suggested exponential decay dependence with time.

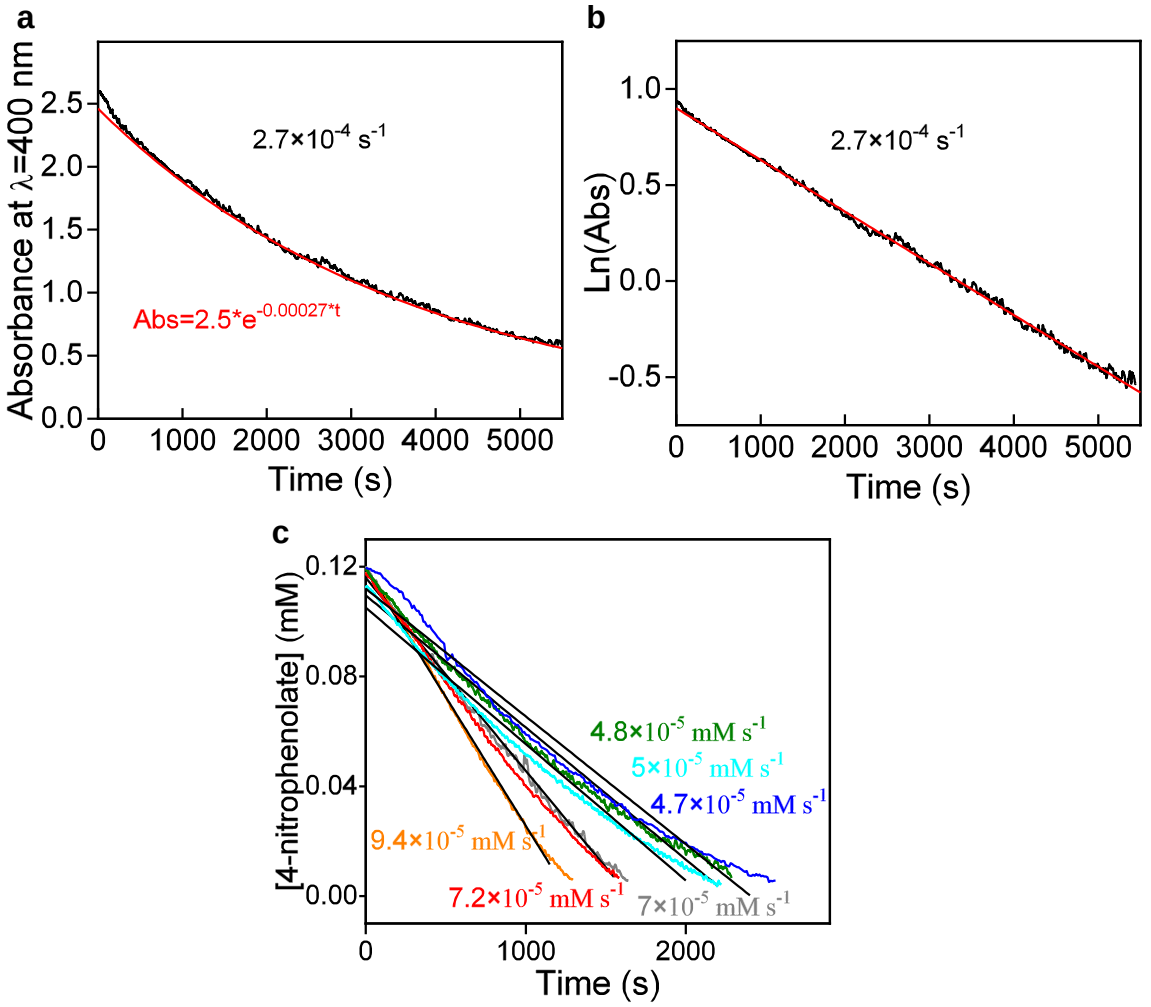

Fig. S6. **Kinetic profiles and their fitting to different kinetic models.** Kinetic profiles using the starting MoS_2 nanosheets (black trace) shown as **(a)** absorbance at 400 nm versus post-induction time and **(b)** natural logarithm of the absorbance of 4-nitrophenolate versus post-induction time. The fittings of (a) to an exponential decay function and (b) to a straight line are shown overlaid (red traces). The equation of the fitted exponential function is shown in red in (a), while the value of k_{app} deduced from the fittings is shown in both graphs. **(c)** Kinetic profiles of the reduction of 4-NP using the hydrazine-treated samples as catalysts: MoS_2-1% (gray trace), MoS_2-2% (orange trace), MoS_2-4% (red trace), MoS_2-6% (green trace), MoS_2-8% (cyan trace), and MoS_2-10% (blue trace). The linear fittings are shown as black traces overlaid on the corresponding profiles. The values of K_{app} (the slopes of the linear fittings) for each profile are indicated with the same color code as the corresponding data sets.

Let us thus fit the kinetic profile to an exponential decay function to calculate k_{app}. Traditionally, this has been done by linearizing the exponential equation 7 as follows:

$$Ln\frac{Abs_i}{Abs_f} = LnA' - k_{app}t \quad (8)$$

And thus obtaining k_{app} as the slope of the linear fitting of *LnAbs* vs post-induction time [12-14]. This is shown in Fig. S6b where LnAbs data appear as a black trace and the linear fit of the data is shown overlaid as a red line. The regression coefficient of the fitting was greater than 0.99. However, there is no need for linearization, given that nowadays non-linear fitting routines are so widely available in common data analysis software packages as linear fitting routines are. The direct fitting to an exponential decay function is shown in Fig. S6a as red trace overlaid on the experimental set of data (black trace). Of course, the resulting k_{app} is the same whether we linearize or not (2.7×10^{-4} s^{-1}, as indicated in Figs. S6a and b) but the direct fitting is more straightforward and gives a better grasp of its quality at bare eye.

By contrast, the kinetic profiles of the hydrazine-treated samples generally exhibited a linear decay (see Fig. 4b in the main text and Fig. S6c above), obeying the following equation:

$$\frac{d[4-NP]}{dt} = -k_{app} \quad (9)$$

As clearly seen, in this case, the reaction rate constant is equivalent to the reaction rate and its units are of concentration and reciprocal time. Once more, because $NaBH_4$ was used in a large excess relative to 4-NP, its concentration could be reasonably assumed to remain constant throughout the reaction, and for this reason the corresponding term was not explicitly included in the right-hand side of eq. 9. The reaction was pseudo-zero-order with respect to [4-NP]. Integrating over time:

$$[4-NP]_f - [4-NP]_i = -k_{app}t \quad (10)$$

Thus, the slope of the linear fit of [4-NP] vs. t yields k_{app}.

Again, we have monitored the reaction progress by measurement of the temporal evolution of the absorbance at an absorption maximum of 4-NP. Combining Lambert-Beer's law (eq. 5) with eq. 10:

$$\frac{dAbs}{dt} = -\varepsilon b k_{app} \quad (11)$$

Integrating over time:

$$Abs_f - Abs_i = -\varepsilon b k_{app}t \quad (12)$$

Thus, contrary to the case of the pseudo-first order kinetics, in this case we need to know the relation between *Abs* and [4-NP] to calculate k_{app}, i. e., we need to know the value of *b* and ε. As stated in the Materials and Methods section in the main text, the optical path *b* is 1 cm in our UV-Vis spectrophotometer. The extinction coefficient for nitrophenolate at 400 nm has been reported to be 17,500 cm^{-1} M^{-1} in the literature. We can either transform absorbance data into concentration first (multiplying by εb) and then fit linearly [4-NP] vs. *t* to directly obtain k_{app} as the slope of the fitted line (eq. 10) or we can fir *Abs* vs. *t* and calculate k_{app} from the slope of the fitted line (eq. 12) by dividing into εb). We have chosen the first option to display directly the values of k_{app} on the graph. While in Fig. 4b of the main text the profiles were expressed as the absorbance at 400 nm of the catalytic media versus post-induction time, the profiles in Fig. S6c above are shown as concentration of 4-nitrophenolate versus post-induction time. We have selected the data for conversion below 95 %. At higher conversions, near the end of the reaction, the concentration of the products would be high and the rate of the opposite reaction or other possible processes involving the products would have to be taken into account to calculate the global reaction rate. The linear fittings are overlaid on the profiles as black traces. The values of k_{app} of the kinetic profiles (the slopes of the linear fitting) are indicated in the graph using the same color code. The regression coefficients were 0.99 for MoS_2-1%, MoS_2-2%, and MoS_2-4%, and MoS_2-8%. The fittings were slightly worse for MoS_2-6% and MoS_2-8%, showing regression coefficients ~0.98, which is still acceptable according to the literature [**¡Error! Marcador no definido.**]. It must be noted that if the profiles of the hydrazine-treated were fitted to an exponential decay, the regression coefficient was lower or equal to 0.95 for any of them. This confirms that pseudo-zero order kinetics match them better than pseudo-first order kinetics, as was visible to the naked eyed. In contrast, if the kinetic profile obtained using the starting, untreated sample MoS_2-0%, i. e., that shown in Fig. S6a was fitted as pseudo-zero order, the regression coefficient was ~0.96, confirming it agreed better with pseudo-first order behavior, for which it showed a regression coefficient greater than 0.99, as said above. The characteristic k_{app} values for the hydrazine-treated materials were on the order of 10^{-5} mM s^{-1}, as corresponds to their catalytic activity values (defined as number of moles of reactant converted per mole of catalyst used per hour) on the order of h^{-1} (see main text and Table S1 below). Specifically, they were 7.0×10^{-5} (MoS_2-1%), 9.4×10^{-5} (MoS_2-2%), 7.2×10^{-5} (MoS_2-4%), 4.8×10^{-5} (MoS_2-6%), 5.0×10^{-5} (MoS_2-8%), and 4.8×10^{-5} mM s^{-1} (MoS_2-10%).

S3.4 Catalytic activity of MoS_2 and graphene nanostructures and non-noble metal-based catalysts for the reduction of 4-NP

Table S1. Catalytic activity (defined as number of moles of reactant converted per mole of catalyst used per unit time) of the hydrazine-treated MoS_2 NSs towards the reduction of 4-NP compared with that of different types of MoS_2 nanostructures, graphene-derived materials and catalysts based on non-noble metals reported in the literature.

Catalytic system	**Catalytic activity (h^{-1})**	**Ref.**
Hydrazine-treated MoS_2 NSs	6.6	Present work
Li-exfoliated 1T'-phase MoS_2 NSs	44.4	**¡Error! arcador no definido.**
Hydrothermally synthesized MoS_2 NSs supported onto Fe_3O_4 particles	2.4	15
GMP-stabilized sonicated MoS_2 NSs	2.6–7.8	16
GMP-stabilized cathodically exfoliated MoS_2 NSs	21.4	17
Co-doped MoS_2 NSs	8.4	18
N-doped RGO foam	0.07	19
RGO NSs capped with poly(diallyldimethylammonium chloride)	0.10	20
Hydrothermally synthesized MoS2 NSs intercalated in	24	21

pillared montomorillonite		
Hydrothermally synthesized MoS_2 NSs	21	22
Bi_2Te_3−MoS_2 heterostructure	67.2–100.8	**¡Error! arcador no definido.**
Hydrogel network with embedded Co nanoparticles (NPs)	16.2	23
Ni nanoparticles on silica nanotubes	1.8	24
Hybrid Ni nanoparticles/N doping carbon on diatomite	0.85	25
Cu NPs on carbon microspheres	0.2	26
Cu and Sn sponges/dendrites	1.2–1.8	27
Co particles-decorated carbon microspheres	0.06–0.24	28
Co nanocrystals on reduced graphene oxide (RGO)	0.6	29
Ni NPs supported onto carbon black	26.4	30
Nanostructured zero-valent iron	78	31
Graphene stabilized CuNi nanocomposite	12	32
MOF-derived Ni based N-doped mesoporous carbon	2.4	33
Co NPs embedded in hierarchically porous N-doped carbon frameworks	18	34
Hexagonal Ni plates on RGO	0.44	35
Hollow porous Cu particles from silica-encapsulated	3	36

Cu_2O nanoparticle aggregates		
Co@BN core–shell nanoparticles	0.38	37
Co NPs embedded into ordered mesoporous carbon	7.8	38
NiO hollow nanospheres	4.2	39
Ultrafine Cu_2O nanoparticles on cubic mesoporous carbon	9.6	40
Cu NPs on oxidized boron nitride	27	41
Cu NPs immobilized by layered Ti_3C_2 MXene	51	42
Cu and Co NPs doped N-containing carbon frameworks	63	43

S3.5 Effect of GMP content on the recyclability

Fig. 6d in the main text gathers the results of reusability experiments of GMP-MoS2-4% catalyst in the reduction of MO. This catalyst, as explained in Materials and Methods of the main text, was prepared from MoS_2 dispersions in isopropanol by:

1st) solvent transfer: two cycles of sedimentation were applied to the original dispersion in isopropanol via centrifugation (20000 g, 20 min), replacement of the supernatant liquid by an aqueous solution of the nucleotide and re-dispersion by a brief sonication treatment (2 min).

2nd) free GMP removal by sedimentation (20000 g, 20 min) and re-dispersion in water.

The effect of the GMP molecules adsorbed on the MoS2 surface has been already explored and discussed by us in a previous paper [**¡Error! Marcador no definido.**]. Indeed, the amount of GMP molecules adsorbed on the surface has been shown to have a significant effect on the catalytic activity of nucleotide-estabilized MoS_2 nanosheets, and therefore, their amount has to be optimized. If the amount of adsorbed GMP is too large, poor catalytic activities are attained, due to obstructed access of the substrate molecules to the catalytically active sites of the material, similar to the effect that the organic ligand shell

has on the general catalytic activity of colloidal metal nanoparticles [44] On the other hand, the colloidal stability of the NSs in the reaction medium is compromised when the amount of adsorbed GMP is too low, which also impacts negatively on the measured catalytic activities as a result of NS agglomeration. Thus, ideally, the amount of GMP should be the minimum amount needed to impart good colloidal stability in water.

To explore the effect of the amount of stabilizer on reciclability, we have tried performing the tests on MoS_2 NSs with the maximum GMP amount possible, i. e., omitting the 2nd step in their preparation. The results of the ciclability tests are shown in Fig. S7. As can be ascertained by comparing Fig. 6d and Fig S7, a higher amount of GMP does not lead to an improvement.

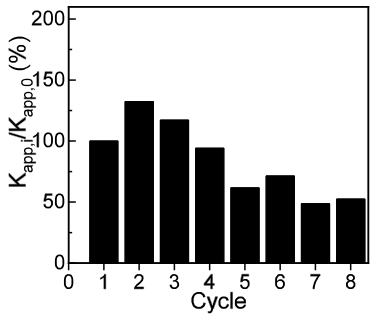

Fig. S7. **Effect of GMP content on the recyclability.** Reusability experiments of GMP-MoS_2-4% catalyst, where free GMP removal by sedimentation and re-dispersion in water have been omitted from its preparation, in the reduction of MO.

S3.6 MoS_2 nanosheets as catalysts of nitroarene reduction reactions

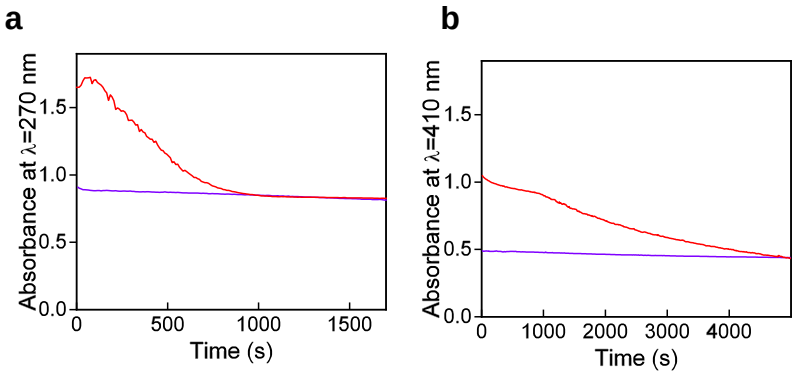

Fig. S8. **Catalytic reduction of other nitroarenes.** Kinetic profiles for the reduction of **(a)** nitrobenzene and **(b)** 2-nitroniline, using MoS_2-4% (red trace) as catalyst. The kinetic profile for the reduction in the absence of catalyst (blank experiment) is also included (violet trace).

S4. Hydrazine-treated MoS_2 nanosheets as electrocatalysts for the HER

The hydrazine-treated samples obtained by the present protocol became also more active towards the electrochemical HER. This was apparent from linear sweep voltammograms recorded in 0.5 M H_2SO_4 solution for different bare MoS_2 nanosheets that were deposited onto glassy carbon electrodes shown in Fig. S8 below. Lower onset potentials (in absolute value) were measured for the hydrazine-treated samples relative to their untreated counterpart, demonstrating the improved activity of the former.

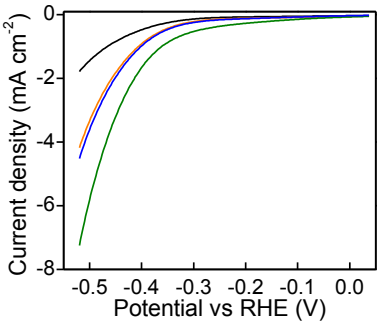

Figure S9. Hydrazine-treated MoS_2 nanosheets as electrocatalysts for the HER. Linear sweep voltammograms for different MoS_2 NSs deposited onto glassy carbon electrodes: starting MoS_2 NSs (black trace), MoS_2-2% (orange trace), MoS_2-6% (green trace) and MoS_2-10% (blue trace).

While ascribing the catalytic activation of the MoS_2 nanosheets upon hydrazine treatment to the generation of sulfur vacancies is plausible, an alternative explanation behind the observed behavior could arise from charge transfer processes taking place between the hydrazine molecules (or their decomposition products) and the nanosheets. Indeed, such a mechanism was previously shown to be in place for MoS_2 nanostructures exposed to dilute hydrazine solutions at room temperature [45]. In that case, amine-type moieties dissociated from hydrazine and adsorbed on the MoS_2 surface acted as electron dopants for the

material. Albeit this doping effect was not strong enough to trigger a 2H to 1T phase transition, it was deemed responsible for the improved performance of the MoS_2 nanostructures when used as an electrocatalyst for the HER. It is thus conceivable that a similar electron doping effect from hydrazine-derived species, rather than increased amounts of sulfur vacancies, could be driving the activation of the MoS_2 nanosheets towards the reduction reactions reported here. However, the electron doping effect derived from hydrazine exposure should be associated to an adsorbed amine-type phase that would be readily detectable by XPS in the form of an intense N1s band at a binding energy of ~400 eV [**¡Error! Marcador no definido.**]. As noticed from Fig. S9 below, such an intense band was not present in any of our hydrazine-treated MoS_2 samples. In fact, the XPS signal recorded at 400 eV was virtually negligible even for the most extensively treated materials (i.e., sample MoS_2-10%), indicating that their enhanced activity in the reduction reactions and HER was not related to electron doping processes.

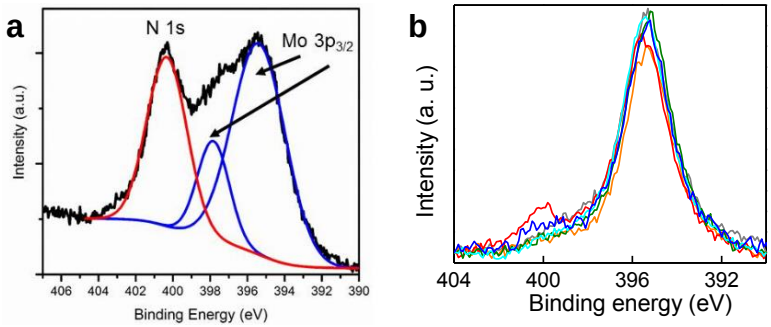

Figure S10. Checking MoS_2 surface for adsorbed hydrazine by XPS (a) XPS of nitrogen species in hydrazine-treated MoO_x/MoS_2 core-shell nanowires where hydrazine molecules (or their decomposition products) adsorbed on the MoS_2 surfaces and acted as electron dopants. The adsorbed amine-based phase appeared as an intense N 1s band at binding energy of ~400 eV. This figure was taken from Supplementary Information of Efficient hydrogen evolution in transition metal dichalcogenides via a simple one-step hydrazine reaction by D. R. Cummins et al, where it appears as Supplementary Figure 11b. It is licensed under a Creative Commons Attribution 4.0 International License. **(b)** Background-subtracted, high resolution XPS spectra of the Mo $3p_{3/2}$ and N 1s binding energy range for films drop-cast from dispersions of MoS_2-1% (gray trace), MoS_2-2% (orange trace), MoS_2-4% (red trace), MoS_2-6% (green trace), MoS_2-8% (cyan trace), and

MoS_2-10% (blue trace). The absence of an intense N 1s signal allows discarding charge transfer processes between the hydrazine molecules (or their decomposition products) and the NSs as the origin of the catalytic activation of the MoS_2 NSs.

S5. References

[1] M. Chhowalla, H.S. Shin, G. Eda, L.-J. Li, K.P. Loh, H. Zhang, The chemistry of two-dimensional layered transition metal dichalcogenide nanosheets, Nat. Chem. 5 (2013), 263-275.

[2] G. Gao, Y. Jiao, F. Ma, Y. Jiao, E. Waclawik, A. Du, Charge mediated semiconducting-to-metallic phase transition in molybdenum disulfide monolayer and hydrogen evolution reaction in new 1T´ phase, J. Phys. Chem. C 119 (2015), 13124-13128.

[3] H. Li, S. Chen, X. Jia, B. Xu, H. Lin, H. Yang, L. Song, X. Wang, Amorphous nickel-cobalt complexes hybridized with 1T-phase molybdenum disulfide via hydrazine-induced phase transformation for water splitting, Nat. Commun. 8 (2017), 15377.

[4] X. Gan, L.Y.S. Lee, K. Wong, 2H/1T phase transition of multilayer MoS_2 by electrochemical incorporation of S vacancies, ACS Appl. Energy Mater. 1 (2018), 4754-4765.

[5] D.-H. Nam, J.-Y. Kim, S. Kang, W. Joo, S.-Y. Lee, H. Seo, H.G. Kim, I.-K. Ahn, G.-B. Lee, M. Choi, E. Cho, M. Kim, K.T. Nam, S. Han, Y.-C. Joo, Anion extraction-induced polymorph control of transition metal dichalcogenides, Nano Lett. (2019), DOI: 10.1021/acs.nanolett.9b03240.

[6] E. Menumerov, R.A. Hughes, S. Neretina, Catalytic reduction of 4-nitrophenol: a quantitative assessment of the role of dissolved oxygen in determining the induction time, Nano Lett. 16 (2016), 7791-7797.

[7] A. Furst, R. C. Berlo, S. Hooton, Hydrazine as a Reducing Agent for Organic Compounds (Catalytic Hydrazine Reductions). Chem. Rev. 1965, 65, 1, 51–68. DOI:10.1021/cr60233a00

[8] L.-Q. Zheng, X.-D. Yu, J.-J. Xu and H.-Y. Chen, Reversible catalysis for the reaction between methyl orange and $NaBH_4$ by silver nanoparticles. Chem. Commun., 2015, 51, 1050–1053.

[9] S. Pande, S. Jana, S. Basu, A. K. Sinha, A. Datta, T. Pal, Nanoparticle-Catalyzed Clock Reaction. J. Phys. Chem. C 2008, 112, 10, 3619-3626. DOI: 10.1021/jp7106999

[10] A. Mignani, S. Fazzini, B. Ballarin, E. Boanini, M. C. Cassani, C. Maccato, D. Barreca, D. Nanni. Mild fabrication of silica-silver nanocomposites as active platforms for environmental remediation, RSC Adv., 2015, 5, 9600–9606. DOI: 10.1039/C4RA14069A

[11] L. Guardia, J. I. Paredes, J. M. Munuera, S. Villar-Rodil, M. Ayán-Varela, A. Martínez-Alonso and J. M. D. Tascón, Chemically exfoliated MoS_2 nanosheets as an efficient catalyst for reduction reactions in the aqueous phase, ACS Appl. Mater. Interfaces, 2014, 6, 21702–21710.

[12] S. Ashraf, R. Begum, R. Rehan, W. Wu, Z. H. Farooqi, Synthesis and Characterization of pH-Responsive Organic–Inorganic Hybrid Material with Excellent Catalytic Activity, J. Inorg. Organomet. Polym. Mater. 28 (2018), 1872-1884.

[13] H. Farooqi, R. Khalid, R. Begum, U. Farooq, Q. Wu, W. Wu, M. Ajmal, A. Irfan, K. Naseem, Facile synthesis of silver nanoparticles in a crosslinked polymeric system by in situ reduction method for catalytic reduction of 4-nitroaniline. Environ. Technol. 40(2019), 2027-2036.

[14] K. Naseem, R. Begum, W. Wu, A. Irfan, A. G. Al-Sehemi, Z. H. Farooqi. Catalytic reduction of toxic dyes in the presence of silver nanoparticles impregnated core-shell composite microgels, J. Clean. Prod. 211 (2019), 855-864.

[15] T. Lin, J. Wang, L. Guo and F. Fu, Fe_3O_4@MoS_2 Core–shell composites: preparation, characterization, and catalytic application, J. Phys. Chem. C, 2015, 119, 13658–13664.

[16] M. Ayán-Varela, Ó. Pérez-Vidal, J. I. Paredes, J. M. Munuera, S. Villar-Rodil, M. Díaz-González, C. Fernández-Sánchez, V. S. Silva, M. Cicuéndez, M. Vila, A. Martínez-Alonso and J. M. D. Tascón, Aqueous Exfoliation of Transition Metal Dichalcogenides Assisted by DNA/RNA Nucleotides: Catalytically Active and Biocompatible Nanosheets Stabilized by Acid−Base Interactions, ACS Appl. Mater. Interfaces, 2017, 9, 2835–2845.

[17] S. García-Dalí, J. I. Paredes, J. M. Munuera, Silvia Villar-Rodil, A. Adawy, A. Martínez-Alonso, J. M.D. Tascón. Aqueous cathodic exfoliation strategy toward solution-processable and phase-preserved MoS_2 nanosheets for energy storage and catalytic applications. ACS Appl. Mater. Interfaces 2019, 11, 40, 36991–37003.

[18] C. Nethravathi, J. Prabhu, S. Lakshmipriya and M. Rajamathi, Magnetic co-doped MoS_2 nanosheets for efficient catalysis of nitroarene reduction, ACS Omega, 2017, 2, 5891–5897.

[19] J. Liu, X. Yan, L. Wang, L. Kong and P. Jian, Three-dimensional nitrogen-doped graphene foam as metal-free catalyst for the hydrogenation reduction of *p*-nitrophenol, J. Colloid Interface Sci., 2017, 497, 102–107.

[20] J. Song, S.W. Kang, Y.W. Lee, Y. Park, J.-H. Kim and S.W. Han, Regulating the Catalytic Function of Reduced Graphene Oxides Using Capping Agents for Metal-Free Catalysis, ACS Appl. Mater. Interfaces, 2017, 9, 1692–1701.

[21] K. Peng, L. Fu, H. Yang, J. Ouyang and A. Tang, Hierarchical MoS2 intercalated clay hybrid nanosheets with enhanced catalytic activity, Nano Res., 2017, 10, 570–583.

[22] C. Nethravathi, A.D. Manganahalli, M. Rajamathi, Bi_2Te_3-MoS_2 layered nanoscale heterostructures for electron transfer catalysis, ACS Appl. Nano Mater., 2019, 2, 2005–2012.

[23] N. Sahiner, H. Ozay, O. Ozay, N. Aktas, A soft hydrogel reactor for cobalt nanoparticle preparation and use in the reduction of nitrophenols, Appl. Catal. B-Environ. 101 (2010) 137–143.

[24] S. Zhang, S. Gai, F. He, S. Ding, L. Lia, P. Yang, In situ assembly of well-dispersed Ni nanoparticles on silica nanotubes and excellent catalytic activity in 4-nitrophenol reduction, Nanoscale, 2014, 6, 11181-11188.

[25] D. B. Jiang, X. Liu, Y. Yuan, L. Feng, J. Ji, J. Wang, D. Losic, H.-C. Yao, Y. X. Zhang, Biotemplated top-down assembly of hybrid Ni nanoparticles/N doping carbon on diatomite for enhanced catalytic reduction of 4-nitrophenol, Chem. Eng. J. 383 (2020) 123156.

[26] X. Cheng, A. Fu, H. Li, Y. Wang, P. Guo, J. Liu, J. Zhang, X. S, Zhao, Sustainable Preparation of Copper Particles Decorated Carbon Microspheres and Studies on Their Bactericidal Activity and Catalytic Properties ACS Sustainable Chem. Eng. 2015, 3, 2414−2422.

[27] B. K. Barman, K. K. Nanda, Uninterrupted galvanic reaction for scalable and rapid synthesis of metallic and bimetallic sponges/dendrites as efficient catalysts for 4-nitrophenol reduction, Dalton Trans., 2015, 44, 4215–4222.

[28] X. Cheng, A. Fu, H. Li, Y. Wang, P. Guo, J. Liu, J. Zhang, X. S. Zhao, Sustainable Preparation of Copper Particles Decorated Carbon Microspheres and Studies on Their Bactericidal Activity and Catalytic Properties, ACS Sustainable Chem. Eng. 2015, 3, 2414–2422.

[29] M. Guo, Y. Zhao, F. Zhang, L. Xu, H. Yang, X. Song, Y. Bu, Reduced graphene oxide-stabilized copper nanocrystals with enhanced catalytic activity and SERS properties, RSC Adv., 2016, 6, 50587–50594.

[30] J. Xia, G. He, L. Zhang , X. Sun, X. Wang, Hydrogenation of nitrophenols catalyzed by carbon black-supported nickel nanoparticles under mild conditions, Appl. Catal. B-Environ. 180 (2016) 408–415.

[31] S. Bae , S. Gim , H. Kim , K. Hanna. Effect of $NaBH_4$ on properties of nanoscale zero-valent iron and its catalytic activity for reduction of p-nitrophenol. Appl. Catal. B-Environ. 182 (2016) 541–549.

[32] H. Fang, M. Wen, Hanxing Chen, Qingsheng Wu and Weiying Li, Graphene stabilized ultra-small CuNi nanocomposite with high activity and recyclability toward catalysing the reduction of aromatic nitro-compounds, Nanoscale. 2016, 8, 536–542.

[33] W. Zuo, G. Yu and Z. Dong A MOF-derived nickel based N-doped mesoporous carbon catalyst with high catalytic activity for the reduction of nitroarenes, RSC Adv., 2016, 6, 11749–11753.

[34] X. Li, C. Zeng, J. Jiang, L. Ai, Magnetic cobalt nanoparticles embedded in hierarchically porous nitrogen-doped carbon frameworks for highly efficient and well-recyclable catalysis, J. Mater. Chem. A, 2016, 4, 7476–7482.

[35] Z. Ji, Y. Wang, X. Shen, H. Ma, J. Yang, A. Yuan, H. Zhou, Facile synthesis and enhanced catalytic performance of reduced graphene oxide decorated with hexagonal structure Ni nanoparticles, J. Colloid Interf. Science 487 (2017) 223–230.

[36] J. Jiang, Y. S. Lim, S. Park, S.-H. Kim, S. Yoon, L. Piao. Hollow porous Cu particles from silica-encapsulated Cu_2O nanoparticle aggregates effectively catalyze 4-nitrophenol reduction, Nanoscale, 2017, 9, 3873–3880.

[37] M. Du, Q. Liu, C. Huang, X. Qiu, One-step synthesis of magnetically recyclable Co@BN core–shell nanocatalysts for catalytic reduction of nitroarenes, RSC Adv., 2017, 7, 35451–35459.

[38] J. Liu, Z. Wang, X. Yan, P. Jian, Metallic cobalt nanoparticles imbedded into ordered mesoporous carbon: A non-precious metal catalyst with excellent hydrogenation performance, J. Colloid Interf. Sci. 505 (2017) 789–795.

[39] G. Wu, X. Liang, L. Zhang, Z. Tang, M. Al-Mamun, H. Zhao, X. Su, Fabrication of Highly Stable Metal Oxide Hollow Nanospheres and Their Catalytic Activity toward 4‑Nitrophenol Reduction, ACS Appl. Mater. Interfaces 2017, 9, 18207–18214.

[40] P. C. Rath, D. Saikia, M. Mishra, H.-M. Kao, Exceptional catalytic performance of ultrafine Cu_2O nanoparticles confined in cubic mesoporous carbon for 4-nitrophenol reduction, Appl. Surf. Sci. 427 (2018) 1217–1226.

[41] X. Jiang, B. Han, C. Zhou, K. Xia, Q. Gao, J. Wu. Cu Nanoparticles Supported on Oxygen-Rich Boron Nitride for the Reduction of 4‑Nitrophenol. ACS Appl. Nano Mater. 2018, 1, 6692–6700.

[42] L. Liu, Q. Zhao, R. Liu, L. Zhu. Hydrogen adsorption-induced catalytic enhancement over Cu nanoparticles immobilized by layered Ti_3C_2 MXene, Appl. Catal. B-Environ. 252 (2019) 198–204.

[43] C. Chu, S. Rao, Z. Ma, H. Han, Copper and cobalt nanoparticles doped nitrogen-containing carbon frameworks derived from CuO-encapsulated ZIF-67 as high-efficiency catalyst for hydrogenation of 4-nitrophenol, Appl. Catal. B-Environ. 256 (2019) 117792.

[44] J. G Smith, P. K. Jain, The Ligand Shell as an Energy Barrier in Surface Reactions on Transition Metal Nanoparticles. J. Am. Chem. Soc. 2016, 138, 6765−6773.

[45] D.R. Cummins, U. Martinez, A. Sherehiy, R. Kappera, A. Martinez-Garcia, R.K. Schulze, J. Jasinski, J. Zhang, R.K. Gupta, J. Lou, M. Chhowalla, G. Sumanasekera, A.D. Mohite, M.K. Sunkara, G. Gupta, Efficient hydrogen evolution in transition metal dichalcogenides via a simple one-step hydrazine reaction, Nat. Commun. 7 (2016), 11857.

6. Conclusiones

Tras los estudios realizados y los resultados obtenidos y presentados en esta tesis, podemos llegar a las siguientes conclusiones:

- Mediante exfoliación catódica y optimizando factores como el tipo de grafito de partida y el electrolito acuoso, se pueden obtener láminas de grafeno de alta calidad estructural con rendimientos considerables (hasta un ~40-50 % en peso) en producto expandido. El material exfoliado presenta buenas prestaciones como adsorbente para la eliminación de aceites y disolventes orgánicos al recubrir con él una esponja de melamina. Asimismo, el material expandido combinado con una pequeña cantidad de láminas de óxido de cobalto da lugar a un híbrido que funciona satisfactoriamente como supercondensador.
- La exfoliación catódica de MoS_2 *bulk* en láminas bidimensionales es posible utilizando disoluciones acuosas de diferentes sales muy simples y comunes (como el KCl) como electrolito. Mediante este método, se evita tanto la oxidación como el cambio de fase del producto exfoliado, obteniéndose láminas con alta calidad estructural, con buen rendimiento en producto expandido. El material obtenido resulta competitivo tanto en su uso como electrodo positivo para supercondensadores asimétricos, como en su aplicación como catalizador en la reducción de nitroarenos.
- Es posible activar nanoláminas de MoS_2 a través de la generación de vacantes de azufre por tratamiento con hidracina, controlando para ello de manera cuidadosa la cantidad de hidracina y la temperatura aplicada. De hecho, el material activado muestra actividades catalíticas para la reducción de nitroarenos y colorantes en medio acuoso hasta ~3-4 veces mayores que las del material sin tratar. El uso de un estabilizador natural (GMP, nucleótido del ARN) permite aumentar su estabilidad coloidal en medio acuoso sin afectar críticamente a su actividad catalítica. Las nanoláminas de MoS_2 activadas pueden ser inmovilizadas en una esponja de melamina para facilitar su manejo y reutilización.

6. Conclusions

After carrying out the studies and obtaining the results which have been presented in this PhD. Thesis, the following can be concluded:

- High quality graphene nanosheets can be obtained in substantial yields (up to ~40-50 wt%) through cathodic exfoliation, optimizing parameters such as the starting graphite and the electrolyte. A useful adsorbent for the removal of oils and organic solvents from water could be obtained by covering melamine foam with exfoliated graphene material. Furthermore, combination of the expanded material with a small amount of vertically oriented cobalt oxide nanosheets afforded hybrids with good capacitive charge storage characteristics.
- The cathodic delamination of bulk MoS_2 into two-dimensional nanosheets was shown to be possible just using an aqueous solution of very simple and common salts (such as KCl) as the electrolyte. Using this straightforward method, no oxidation or phase transformation of the exfoliated products was seen to take place, affording two-dimentional MoS_2 nanosheets with a high structural quality in substantial yields. The resulting material exhibits a competitive performance as positive electrode (in combination with carbon nanotubes) for asymmetric supercapacitors and as a catalyst for the reduction of nitroarenes.
- Two-dimentional MoS_2 nanosheets have been activated through the generation of sulfur vacancies via hydrazine treatment by carefully controlling the concentration of hydrazine and the temperature of the process. The activated nanosheets exhibited catalytic activities for nitroarene/dye reduction with $NaBH_4$ ~3-4 times higher than that of their untreated counterpart. The use of a stabilizer (GMP, an RNA nucleotide) did not critically compromise the catalytic activity of the hydrazine-treated nanosheets. In order to facilitate their handling and re-utilization, the activated nanosheets could be immobilized onto melamine foam. Indeed, the resulting low-density macroscopic structure preserved its activity along consecutive catalytic cycles.

ANEXO

A lo largo de esta tesis doctoral se realizaron otra serie de publicaciones que no están incluídas en esta memoria pero cuya temática está estrechamente relacionada:

- Munuera J.; Paredes J.I.; Villar-Rodil S.; García-Dalí S.; Castro-Muñiz A.; Martínez-Alonso A.; Tascón J. M. D. A direct route to activated two-dimensional cobalt oxide nanosheets for electrochemical energy storage, catalytic and environmental applications. Journal of Colloid and Interface Science. 2019, 539, 263 - 276.
- García-Dalí S.; Paredes J. I.; Villar-Rodil S.; Martínez-Jódar A.; Martínez-Alonso A.; Tascón J. M. D. Molecular functionalization of 2H-phase MoS2 nanosheets via an electrolytic route for enhanced catalytic. ACS Applied Materials and Interfaces (Enviado para su publicación). 2021.

Participaciones en congresos:

- García-Dalí S.; Paredes J. I.; Munuera J.; Villar-Rodil S.; Martínez-Alonso A.; Tascón J. M. D. High quality graphene in competitive yield via cathodic exfoliation of graphite in aqueous medium with efficient ammonium-based electrolytes. XV Simposio Jóvenes Investigadores Químicos, Toledo, 11/2018, Oral flash and poster, presentada por S. García-Dalí.
- García-Dalí S.; Paredes J. I.; Munuera J.; Villar-Rodil S.; Martínez-Alonso A.; Tascón J. M. D. Efficient cathodic exfoliation of graphite in aqueous electrolytes towards high quality graphene for energy and environmental applications. Graphene 2019, Roma, 06/2019, Oral communication, presentada por S. García-Dalí.
- García-Dalí S.; Paredes J. I.; Munuera J.; Villar-Rodil S.; Martínez-Alonso A.; Tascón J. M. D. Efficient cathodic exfoliation of graphite in aqueous electrolytes towards high quality graphene for energy and environmental applications. Carbon for Energy Storage and Environment Protection (CESEP), Alicante, 10/2019, Keynote, presentada por S. García-Dalí.

- García-Dalí S.; Paredes J. I.; Munuera J.; Villar-Rodil S.; Adawy A.; Martínez-Alonso A.; Tascón J. M. D. High quality and Solution-Processable MoS2 Nanosheets obtained by electrochemical exfoliation for Energy Storage and Catalytic Applications. Graphene 2020 International Online Conference, 10/2020, Oral communication, presentada por S. García-Dalí.